

SELECTED TOPICS IN NOVEL OPTICAL DESIGN

by

Yufeng Yan

Copyright © Yufeng Yan 2019

A Dissertation Submitted to the Faculty of the

JAMES C. WYANT COLLEGE OF OPTICAL SCIENCES

In Partial Fulfillment of the Requirements

For the Degree of

DOCTOR OF PHILOSOPHY

In the Graduate College

THE UNIVERSITY OF ARIZONA

2019

THE UNIVERSITY OF ARIZONA
GRADUATE COLLEGE

As members of the Dissertation Committee, we certify that we have read the dissertation prepared by *Yufeng Yan*, titled *Selected Topics in Novel Optical Design* and recommend that it be accepted as fulfilling the dissertation requirement for the Degree of Doctor of Philosophy.

Jose Sasian

Jose Sasian

Date: 11/18/2019

James Schwiegerling

James Schwiegerling

Date: 11/18/2019

Rongguang Liang

Rongguang Liang

Date: 11/18/2019

Final approval and acceptance of this dissertation is contingent upon the candidate's submission of the final copies of the dissertation to the Graduate College.

I hereby certify that I have read this dissertation prepared under my direction and recommend that it be accepted as fulfilling the dissertation requirement.

Jose Sasian

Jose Sasian
Dissertation Committee Chair
Optical Sciences

Date: 12-8-2019



ACKNOWLEDGEMENTS

I would like to first thank my parents in China for their support that encouraged me to pursue both bachelor's, master's and doctorate degree abroad. I would also like to thank my girlfriend Jie Feng for her strong support and being the first reader of each chapter of this dissertation. I am very grateful to my adviser, Dr. Jose Sasian. This project would not have been possible without his constant support and mentoring. I would also like to acknowledge the members of my committee, Dr. Rongguang Liang and Dr. Jim Schwiegerling, who took their time to review this dissertation and gave me valuable suggestions.

In addition, I would like to thank Zemax for giving me permission to use their software for designing and evaluating the optical systems in this project. I would also like to thank Dr. Liang for his funding and support to the project "Optical performance evaluation and chromatic aberration correction of a focus tunable lens used for 3D microscopy", which is included in Chapter 4 of this dissertation.

DEDICATION

To my parents Xueping and Zhiming, and to my love Jie

TABLE OF CONTENTS

LIST OF FIGURES	7
LIST OF TABLES	14
ABSTRACT.....	15
1 Introduction.....	16
2 Photographic Fisheye Lens Design for 35mm Format Cameras.....	19
2.1 Introduction to Fisheye Lenses	20
2.1.1 The History behind Fisheye Lenses	21
2.1.2 Diagonal and Circular Fisheye Lens for Photographic Purpose	27
2.2 Projection Methods of Fisheye Lenses	30
2.2.1 Tangential and Sagittal Magnification.....	31
2.2.2 Equidistant Projection.....	33
2.2.3 Orthographic Projection.....	35
2.2.4 Stereographic Projection.....	36
2.2.5 Equisolid Angle Projection.....	38
2.2.6 Projection Difference and their Practice Use.....	40
2.3 Special Properties and Design Issues of Photographic Fisheye Lenses	42
2.3.1 Negative Meniscus Lens and Pupil Shift.....	43
2.3.2 Inverted Telephoto Structure and Minimum BFD Requirement	46
2.3.3 Depth of Field	48
2.3.4 Relative Illumination and Image Space Chief Ray Angle	51
2.4 Design of a Zoom Fisheye Lens for 35mm Format DSLR Cameras.....	53
2.4.1 Motivation and Current Designs of Zoom Fisheye Lenses	54
2.4.2 Design Specifications and Lens Construction	56
2.4.3 Aberration Control.....	60
2.4.4 Lens Optimization.....	65
2.4.5 Performance Evaluation.....	66
2.4.6 Tolerance Analysis.....	73
2.5 Conclusion	74
3 Miniature Camera Lens Design with a Freeform Surface.....	77
3.1 Design Challenges of a Miniature Camera Lens	79

3.2 Aspherical and Freeform Surfaces.....	84
3.2.1 Conventional Aspherical Surfaces.....	85
3.2.2 Freeform Surface based on Pedal Curve to the Ellipse.....	88
3.3 First Lens Comparison.....	92
3.3.1 Nominal Performance Comparison.....	93
3.3.2 Tolerance Sensitivity	94
3.4 Second Lens Comparison	99
3.4.1 Performance Comparison.....	100
3.4.2 Reversed Asphere Design	107
3.5 Conclusion	111
4 Applications and Optical Performance Consideration of Liquid Lenses	114
4.1 Development and Principles of Focus Tunable Lenses	115
4.2 A Review of Application Utilizing Liquid Lenses	121
4.2.1 Focus Sweeping.....	121
4.2.2 Zoom System based on Liquid Lens.....	130
4.2.3 Nonmechanical Beam Steering.....	139
4.3 Optical Performance Evaluation of Liquid Lens used for 3D microscopy.....	142
4.3.1 Simulation and Experiment Setup	143
4.3.2 Simulation and Experiment Results.....	147
4.4 Correction of Chromatic Aberration.....	154
4.5 Conclusion	162
5 Conclusion	165
APPENDIX A – LENS DATA I.....	167
APPENDIX B – LENS DATA II	171
REFERENCES.....	179

LIST OF FIGURES

Figure 2.1. Modern fisheye lens applications such as (a) the “Bird’s-eye” visual system [6] and (b) a Samsung “360-degree” camera for virtual reality displays [7].	21
Figure 2.2. Refraction of a ray at critical angle	23
Figure 2.3. (a) Water camera designed by R.W.Wood, (b) photo took by Wood’s camera, (c) fisheye camera designed by W.N.Bond and (d) entire sky captured by Bond’s camera	23
Figure 2.4. The layout of ‘the Hill sky lens’ designed by R. Hill	24
Figure 2.5. The comparison between the (a) AEG fisheye lens and (b) Nikkor’s first fisheye lens	26
Figure 2.6. A sample Image taken by a diagonal fisheye lens	29
Figure 2.7. A sample Image taken by a circular fisheye lens	29
Figure 2.8. The object hemisphere of a fisheye lens system	31
Figure 2.9. The image space of a fisheye lens system	32
Figure 2.10. Image height vs. field angle for different fisheye projection system	40
Figure 2.11. Same object under (a) stereographic projection, (b) equidistant projection, (c) equisolid angle projection and (d) orthographic projection	41
Figure 2.12. The projection curve fitting for the Nikkor 16mm F/2.8D fisheye lens	42
Figure 2.13. The Nikkor 6mm F/2.8 220-degree fisheye lens with 3 negative meniscus lenses	44
Figure 2.14. The pupil shift effect of the Nikkor 8mm F/8 fisheye lens	45
Figure 2.15. A fisheye lens with ray aiming turned on (top) and off (bottom) in Zemax	46
Figure 2.16. The structure of the telephoto lens and the inverted telephoto lens	47
Figure 2.17. For a fisheye lens without sufficient BFD, (a) the folding mirror needs to be held at upright position and (b) an attachable viewfinder is needed to provide live view [20]	48
Figure 2.18. Illustration of depth of field L	49
Figure 2.19. Coma aberration of the entrance pupil. Black solid lines indicate the paraxial entrance pupil with grid. The red dashed lines indicate the off-axis entrance pupil with corresponding grid.	53
Figure 2.20. A monochromatic fisheye lens design with 104% edge relative illumination (compare to center illumination)	53

LIST OF FIGURES - Continued

Figure 2.21. (a) Size comparison between a 35mm sensor and an APS-C sensor, (b) zoom fisheye lens at its shortest focal length, (c) zoom fisheye lens providing diagonal fisheye image for APS-C sensor, (d) zoom fisheye lens at its longest focal length.	54
Figure 2.22. Lens structure at extreme zoom positions.....	58
Figure 2.23. Cam curve of the zoom lens	58
Figure 2.24. Image space CRA vs. HFOV at (a) wide-angle position, (b) intermediate zoom position, and (c) telephoto zoom position.....	66
Figure 2.25. Optical path difference for 0 deg, 30 deg, 60 deg, and 90 deg half field at (a) wide angle zoom position, (b) intermediate zoom position, and (c) telephoto zoom position. Scale is ± 2 waves	67
Figure 2.26. Astigmatic field curves at (a) wide angle zoom position, (b) intermediate zoom position, and (c) telephoto zoom position.....	67
Figure 2.27. Longitudinal aberration at (a) wide angle zoom position, (b) intermediate zoom position, and (c) telephoto zoom position.....	68
Figure 2.28. Longitudinal aberration at (a) wide angle zoom position, (b) intermediate zoom position, and (c) telephoto zoom position.....	68
Figure 2.29. Lateral color at (a) wide angle zoom position, (b) intermediate zoom position, and (c) telephoto zoom position.....	69
Figure 2.30. MTF versus spatial frequency at (a) wide angle zoom position, (b) intermediate zoom position, and (c) telephoto zoom position.....	71
Figure 2.31. MTF versus field at (a) wide angle zoom position, (b) intermediate zoom position, and (c) telephoto zoom position.	71
Figure 2.32. Entrance pupil shape at its maximum at (a) wide angle zoom position, (b) intermediate zoom position, and (c) telephoto zoom position.....	72
Figure 2.33. Relative illumination at (a) wide angle zoom position, (b) intermediate zoom position, and (c) telephoto zoom position.....	73
Figure 2.34. Effect of 1-arc min surface/element tilt, and 10- μ m surface/element decenter, at all three critical zoom positions, based upon the root-sum-square method.....	74
Figure 3.1. Global digital still camera shipments in pieces from 2010 to 2018.....	77

LIST OF FIGURES - *Continued*

Figure 3.2. Layout comparison between the Nikon 28mm conventional camera lens and Apple 4mm miniature camera lens	80
Figure 3.3. Sideview of a typical CMOS sensor, large angle off-axis ray bundle may cause light leakage into the neighboring pixels and results in color crosstalk	81
Figure 3.4. Comparison of relative illumination between Nikon 28mm camera lens and Apple 4mm miniature lens.....	82
Figure 3.5. An example pedal curve to the ellipse, $a = 2$, $b = 1$	89
Figure 3.6. An elliptical-like curve on the x-y plane for sag equation derivation	90
Figure 3.7. Layout and OPD plots of the benchmark lens. The maximum scales of OPD plots are ± 1 wave.....	93
Figure 3.8. Layout and OPD plots of the evaluation lens. The maximum scales of OPD plots are ± 1 wave.....	94
Figure 3.9. Nominal MTF plots of benchmark lens (left) and evaluation lens (right).....	94
Figure 3.10. MTF plots of benchmark lens (left) and evaluation lens (right) under $5 \mu\text{m}$ decenter of surface 7 in Y direction.....	95
Figure 3.11. MTF plots of benchmark lens (left) and evaluation lens (right) under $5 \mu\text{m}$ decenter of surface 8 in Y direction.....	95
Figure 3.12. MTF plots of benchmark lens (left) and evaluation lens (right) under $5 \mu\text{m}$ decenter of surface 9 in Y direction.....	96
Figure 3.13. MTF plots of benchmark lens (left) and evaluation lens (right) under $5 \mu\text{m}$ decenter of surface 10 in Y direction.....	96
Figure 3.14. MTF plots of benchmark lens (left) and evaluation lens (right) under $5 \mu\text{m}$ decenter of element 4 in Y direction.....	96
Figure 3.15. MTF plots of benchmark lens (left) and evaluation lens (right) under $5 \mu\text{m}$ decenter of element 5 in Y direction.....	97
Figure 3.16. MTF plots of benchmark lens (left) and evaluation lens (right) under $5 \mu\text{m}$ decenter of surface 7 in X direction.....	97
Figure 3.17. MTF plots of benchmark lens (left) and evaluation lens (right) under $5 \mu\text{m}$ decenter of surface 8 in X direction.....	97

LIST OF FIGURES - *Continued*

Figure 3.18. MTF plots of benchmark lens (left) and evaluation lens (right) under 5 μm decenter of surface 9 in X direction.....	98
Figure 3.19. MTF plots of benchmark lens (left) and evaluation lens (right) under 5 μm decenter of surface 10 in X direction.....	98
Figure 3.20. MTF plots of benchmark lens (left) and evaluation lens (right) under 5 μm decenter of element 4 in X direction.....	98
Figure 3.21. MTF plots of benchmark lens (left) and evaluation lens (right) under 5 μm decenter of element 5 in X direction.....	99
Figure 3.22. Lens layout of the even asphere lens, the Q-type polynomial lens and the pedal freeform lens.....	101
Figure 3.23. Nominal OPD plots of the even sphere lens.....	101
Figure 3.24. Nominal OPD plots of the Q-type polynomial lens.....	102
Figure 3.25. Nominal OPD plots of the pedal freeform lens	102
Figure 3.26. Nominal MTF plots of the even asphere lens, the Q- type polynomial lens and the pedal freeform lens.....	103
Figure 3.27. MTF plots under 5 μm decenter of surface 7 in Y direction for the even asphere lens, the Q- type polynomial lens and the pedal freeform lens.....	104
Figure 3.28. MTF plots under 5 μm decenter of surface 8 in Y direction for the even asphere lens, the Q- type polynomial lens and the pedal freeform lens.....	104
Figure 3.29. MTF plots under 5 μm decenter of surface 9 in Y direction of the even asphere lens, the Q- type polynomial lens and the pedal freeform lens.....	105
Figure 3.30. MTF plots under 5 μm decenter of surface 10 in Y direction of the even asphere lens, the Q- type polynomial lens and the pedal freeform lens.....	105
Figure 3.31. MTF plots under 5 μm decenter of element 4 in Y direction of the even asphere lens, the Q- type polynomial lens and the pedal freeform lens.....	106
Figure 3.32. MTF plots under 5 μm decenter of element 5 in Y direction of the even asphere lens, the Q- type polynomial lens and the pedal freeform lens.....	106
Figure 3.33. Layout of the pedal freeform lens (left) and the reversed asphere lens (right).....	108

LIST OF FIGURES - *Continued*

Figure 3.34. Nominal MTF plots of the pedal freeform lens (left) and the reversed asphere lens (right)	108
Figure 3.35. MTF plots of the pedal freeform lens (left) and the reversed asphere lens (right) under 5 μm decenter of surface 7 in Y direction	109
Figure 3.36. MTF plots of the pedal freeform lens (left) and the reversed asphere lens (right) under 5 μm decenter of surface 8 in Y direction	109
Figure 3.37. MTF plots of the pedal freeform lens (left) and the reversed asphere lens (right) under 5 μm decenter of surface 9 in Y direction	110
Figure 3.38. MTF plots of the pedal freeform lens (left) and the reversed asphere lens (right) under 5 μm decenter of surface 10 in Y direction	110
Figure 3.39. MTF plots of the pedal freeform lens (left) and the reversed asphere lens (right) under 5 μm decenter of element 4 in Y direction	110
Figure 3.40. MTF plots of the pedal freeform lens (left) and the reversed asphere lens (right) under 5 μm decenter of element 10 in Y direction	111
Figure 4.1. Working principle of the “butterfly cup” from Song dynasty.	116
Figure 4.2. Working principle of LC tunable lens with inhomogeneous cell cap	117
Figure 4.3. Electrode designs for LC lenses with homogeneous cell gap, including (a) hole-patterned electrode, (b) curved electrode and (c) planar electrodes.	118
Figure 4.4. Working principle of a liquid lens based on electrowetting.	119
Figure 4.5. Working principle of a liquid lens with polymer membrane, lens shape is changed by applying pressure on membrane.	120
Figure 4.6. Figure of an example patented variable focus liquid ophthalmic lens. Optical power of liquid lens is tunable by adjusting the rotatable impeller	122
Figure 4.7. Example of presbyopia correction using liquid lens. (a) A relaxed eye looking at infinity through liquid lens, (b) a relaxed eye looking at a near object through liquid lens, (c) a relaxed eye looking at infinity without liquid lens, (d) an eye looking at a near object with eye lens accommodation.	123
Figure 4.8. Demonstration of VAC in HMDs.	125
Figure 4.9. A “bird bath” type HMD with a tunable lens to reduce VAC	126

LIST OF FIGURES - *Continued*

Figure 4.10. A wide FOV HMD with commercial off-the-shelf liquid lens.....	127
Figure 4.11. A focus-tunable near-eye HMD based on commercially off-the-shelf components [71]	128
Figure 4.12. Light propagation through (a) a conventional infinite conjugate objective with a fixed focus plane and (b) an infinite conjugate objective pairs with a liquid lens.....	129
Figure 4.13. System comparison between putting liquid lens at conjugated pupil of aperture stop (top) and putting liquid lens directly above microscope objective close to the aperture stop (bottom).	129
Figure 4.14. An afocal zoom system. Both objective and eye piece are liquid lenses introduced by Nickolaos Savidis	132
Figure 4.15. A 4x zoom laparoscope presented by Lee.	134
Figure 4.16. A 1.7x zoom camera lens presented by Kuiper [78].....	134
Figure 4.17. A 2x zoom camera lens presented by Zhao [79].	135
Figure 4.18. A 2x zoom camera lens with chromatic aberration correction.	137
Figure 4.19. Optical performance of the 2x zoom lens based on liquid lenses.....	138
Figure 4.20. 2.5x hybrid zoom lens presented by Wippermann (left) and 2.6x hybrid zoom lens presented by Sun [82, 83]	139
Figure 4.21. A 9.8x hybrid zoom lens patented by Canon [84]	139
Figure 4.22. A non-mechanical beam steering system using liquid lenses.....	140
Figure 4.23. An ultra-wide angle non-mechanical beam steering system using liquid lenses presented by Zohrabi [87].....	141
Figure 4.24. A camera lens with liquid lens optical image stabilizer [88].....	142
Figure 4.25. Simulation setup in Zemax	144
Figure 4.26. A Twyman-Green interferometer to measure the spherical aberration and chromatic focal shift of the 3D microscopy setup in vertical direction.....	145
Figure 4.27. Setup to measure the image contrast with a USAF 1951 target to evaluate system resolution.	146
Figure 4.28. Setup to measure aberration and contrast of the 3D microscopy in horizontal direction to exam gravity effect.	147

LIST OF FIGURES - *Continued*

Figure 4.29. On-axis MTF of the liquid lens and OL paired with Thorlabs 2X refractive objective.	148
Figure 4.30. On-axis MTF of the liquid lens and OL paired with Thorlabs 4X refractive objective.	148
Figure 4.31. On-axis MTF of the liquid lens and OL paired with Thorlabs 15X reflective objective.	149
Figure 4.32. On-axis MTF of the liquid lens and OL paired with Thorlabs 40X reflective objective.	149
Figure 4.33. Chromatic focal shifts between F-line and C-line (blue bar) and between F-line and d- line (orange bar) for 4 chosen objectives with liquid lens and OL.	150
Figure 4.34. Chromatic focal shift plots for the objectives with and without liquid lens.	151
Figure 4.35. Optical performance evaluation of 3D microscopy setup in vertical direction	152
Figure 4.36. Optical performance evaluation of 3D microscopy setup in horizontal direction	154
Figure 4.37. Optical setup for equation derivation.....	155
Figure 4.38. An achromatic liquid lens system with 2 thin doublets	161
Figure 4.39. An apochromatic 3D microscopy system.	162

LIST OF TABLES

Table 2.1. Design specification of the zoom fisheye lens at different zoom positions.....	57
Table 2.2. Lens data with aspherical coefficients.....	59
Table 2.3. Aberration coefficients upon object shift according to the object shift parameter S ...	60
Table 2.4. Zoom lens aberration coefficients in waves for a semi-field of 30 degrees	62
Table 3.1. Lens data for the Nikon lens, Apple lens and Nikon lens scaled to same focal length with the Apple lens	80
Table 3.2. Some example patent lenses with strongly aspherical rear elements.	85
Table 3.3. Design specification of the first benchmark lens and evaluation lens.....	92
Table 3.4. Design specification of the even asphere lens, the Q-type polynomial lens, and the pedal freeform lens.....	100
Table 3.5. Number of polynomial coefficients, including the conic number, of all 3 lenses under evaluation.....	107
Table 4.1. Comparison between Zemax solution and derived conditions.	159
Table A.1. Lens data for benchmark lens in section 3.3.....	167
Table A.2. Aspherical coefficients for benchmark lens in section 3.3	168
Table A.3. Lens data for evaluation lens in section 3.3.....	169
Table A.4. Pedal Surface data for evaluation lens in section 3.3.....	170
Table B.1. Lens data for the even asphere lens in section 3.4	171
Table B.2. Aspherical coefficients for the even asphere lens in section 3.4.....	172
Table B.3. Lens data for the Q-type polynomial lens in section 3.4.....	173
Table B.4. Aspherical coefficients for the Q-type polynomial lens in section 3.4.....	174
Table B.5. Lens data for the freeform lens in section 3.4.....	175
Table B.6. Pedal Surface data for the freeform lens in section 3.4.....	176
Table B.7. Lens data for the reversed even asphere lens in section 3.4.....	177
Table B.8. Aspherical coefficients for the reversed even asphere lens in section 3.4	178

ABSTRACT

This dissertation discusses various selected topics in novel optical design and engineering, including photographic fisheye lens design for 35mm format cameras, miniature camera lens design with a freeform surface, applications and optical performance consideration of liquid lenses.

For the topic of photographic fisheye lens design for 35mm format cameras, a state-of-art large aperture (F/2.8 – F/3.5) zoom fisheye lens for 35mm DSLR cameras is presented with optical performance evaluation. The design philosophy and aberration control are explained in detail, along with the background of fisheye lenses in general.

Other than state-of-art optical systems, novel methods to improve tolerance performance of current designs are also desired. For the topic of miniature camera lens design, the author introduced a new freeform surface that has been never used in imaging system based on pedal curve to the ellipse. Via two different sets of tolerance performance comparison with conventional aspherical surfaces, the newly presented freeform surface is proved to efficiently desensitize the current miniature camera designs without a significant change in structure.

In the last topic, author explain the use of liquid lenses in detail. As a recently developed novel optical component, liquid lenses introduce new degrees of freedoms for optical designers, along with new design problems. For this topic, the author will explain various potential applications of liquid lenses. The optical performance of a motion-free 3D microscope objective based on liquid lens is analyzed in both simulation and experiment set up. In the end, the author will introduce a novel method to correct chromatic aberration of a liquid lens setup, which has been a challenge for previous applications with liquid lenses.

1 Introduction

Novel optical design is always an interesting topic in the optics community. The topics on novel optical design are not only limited to novel optical systems, but also includes new design method and utilization of novel optical components. This dissertation contains a collection of topics on novel optical system design, innovative optical design methods and performance assessments on novel optical components. Each topic is presented independently as a self-explanatory chapter. For each chapter, the author gives an introduction, a detailed historical background, a comprehensive description of the proposed work with practical examples, and a thorough conclusion. The goal of this dissertation is to supply useful designs to extent capability of current optical systems, propose new design methods to further optimize the design and improve tolerance performance, provide assessments on novel optical components and potential solutions to the challenges when utilizing these components.

The chapter by chapter structure of this dissertation is as below.

Chapter 2 focuses on the design of photographic fisheye lenses. A thorough historic background on photographic fisheye lenses is given to show the evolution on the design forms of fisheye lenses. Then the author explains different fisheye lens mapping methods and shows how the images with different mapping methods would look like via deriving magnification equation in both tangential and sagittal direction. Special properties of fisheye lenses and the design challenges are also discussed in this chapter. In the end of this chapter, a state-of-art large aperture zoom fisheye lens designed by the author is presented. Aberration control of the zoom fisheye lens throughout the zoom range is explained in a new perspective. Optical performance, along with system tolerance is also provided by the author.

In Chapter 3, a freeform surface type based on pedal curve to the ellipse is presented for the purpose of miniature camera lens design. Conventional miniature lens design usually uses even aspherical surfaces up to the 20th order to maintain good correction for high order aberrations. The abuse of such many aspherical orders results strong waviness that are sensitive to decenter tolerances, thus results in low yield. However, the freeform surface presented by the author naturally has the desired shape for miniature lens design and is able to achieve similar surface shape with much fewer polynomial terms. Two sets of comparison between the proposed freeform surface and conventional even aspherical surface are provided in this chapter to show the tolerance improvement by using this freeform surface. A Q-type polynomial surface is also included in the second comparison.

Chapter 4 focuses on utilization of liquid lens in modern optical systems. An introduction with historical background on various types of focus tunable lens followed by a survey on liquid lens applications is given in this chapter. Then the author focuses on optical performance of 3D microscopes using liquid lenses. Liquid lens is often used recently to provide motion free 3D scanning when pairing with an infinite conjugate microscope. However, the optical performance impact caused by adding the liquid lens was rarely discussed before. The author thus discussed the optical performance issues by using both software simulation and lab experiment.

One of the key optical performance impacts caused by the liquid lens is chromatic aberration correction at different liquid lens power setting. Since the liquid lens changes power while maintaining the material dispersion at different power setting, conventional achromatic methods would not be adequate. Thus, the author provides a novel method to correct chromatic change of focus throughout the entire focus tunable range of the liquid lens.

Some of the materials included in this dissertation have been previously published as journal papers, conference proceedings and author's master thesis. Such references are clearly cited in the corresponding chapters.

2 Photographic Fisheye Lens Design for 35mm Format Cameras

A fish's eye underwater can see the entire hemisphere above the water, as such, the field of view (FOV) of this eye in object space can reach 180 degrees. With appropriate optical design, humans may acquire the same 180 degrees and even larger FOV using special lenses. Lenses that are capable of capturing extremely large FOV are referred to as "fisheye lenses".

Since the first fisheye lens, the "Hill Sky Lens" [1] that was introduced in 1924, fisheye lenses have been in development for almost an entire century. Many great fisheye lenses were designed in the past century, and the designs have been improved, especially on image quality. Due to the poor aberration control, the maximum aperture of the 'Hill Sky Lens' was only F/22. In addition, only monochromatic images can be captured by this lens due to the lack of color correction. Today, modern fisheye lenses for commercial cameras can capture very sharp polychromatic image with a maximum aperture of F/2.8. However, despite the great development of fisheye lenses in the past century, there were not many references other than the patents on the topics of fisheye lens design. Even in the standard books for lens design, such as *Lens Design* (Milton Laikin, 2006) [2] and *Modern Lens Design* (Warren J. Smith, 2004) [3], the topics of fisheye lens were only mentioned in few sentences, while the topics of other lens designs were discussed in detail. Besides that, the corresponding English patents are also hard to acquire. The current photographic lens designs are almost completely dominated by the Japanese companies such as Nikkor (Nikon), Canon, Minolta (Sony), Sigma, Fuji, Pentax and Olympus. Many of their fisheye lens designs were only patented in Japan. A good reference that specifically talks about fisheye lens designs in English is in need.

In this chapter, a detailed discussion on design and optimize photographic fisheye lenses for 35mm format cameras are provided. Section 1 provide an introduction of fisheye lenses,

includes some fascinated history about the development of fisheye lenses, and a discussion on different types of photographic fisheye lenses. Section 2 describe the four different fisheye projection methods with detailed mathematical derivation. Section 3 discusses the unique properties and design issues specifically for a photographic fisheye lens. In section 4, the author discusses about zoom fisheye lenses. Aberration control of a 2 group zoom lens is explained from a new perspective where the front group is treated as a shifting object. Author's design of a zoom fisheye lens is introduced in this section along with the performance evaluations. Finally, a conclusion that summarizes this chapter is given in section 5. The study introduced in this chapter is a continuation of author's previous research that is presented in the author's master's thesis "Photographic fisheye lens design for 35mm format cameras" [4]. Some of the materials from the thesis are reused in this chapter as necessary backgrounds of fisheye lenses.

2.1 Introduction to Fisheye Lenses

Although the initial purpose of fisheye lenses is to record the cloud in the sky, due to their special properties, fisheye lenses are also widely used in many other different areas today, such as creative photography, sky projection and dome movie projection in the planetariums, surveillance cameras, and military defense. The applications of fisheye lenses are still expanding today. For example, the "Bird's-eye" visual system that stitches multiple fisheye image together to provide vehicle surrounding monitoring is becoming a popular feature in many luxury cars [Fig 2.1 (a)]. Many of the "360-degree cameras" that combines 2 fisheye lenses to provide true panoramic images are also becoming popular due to the recent trend of virtual reality (VR) technology [Fig 2.1 (b)]. The global market of panoramic camera is expected to reach at USD 36 billion in 2022 [5].

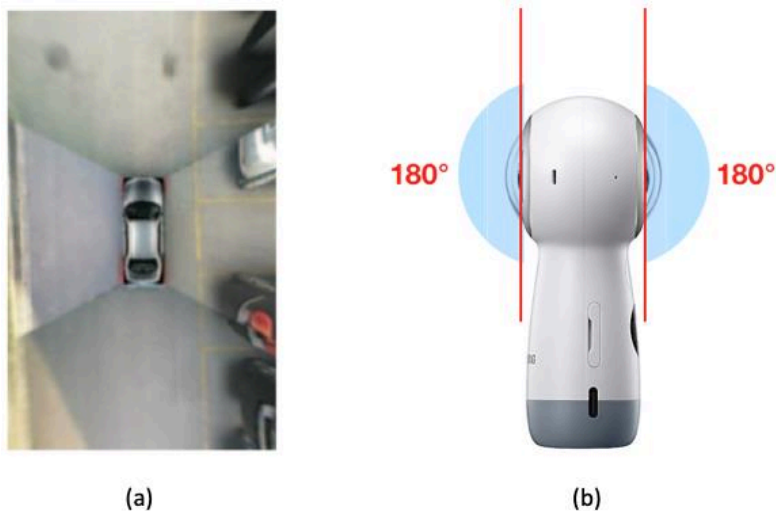


Figure 2.1. Modern fisheye lens applications such as (a) the “Bird’s-eye” visual system [6] and (b) a Samsung “360-degree” camera for virtual reality displays [7].

Before fisheye lenses are widely used in many different areas, the famous ‘Hill sky lens’ designed in 1924 that is used for could recording is commonly recognized as the first fisheye lens. But the fisheye photography based on a bionic device inspired by the fishes under water can be traced to 18 years before R. Hill published the ‘Hill sky lens’. The history of the fisheye lens is briefly discussed in the next subsection.

2.1.1 The History behind Fisheye Lenses

As well known, a submerged fish points its eye directly at the surface of water sees objects above the water surface compressed into a circular image. The image would be severely distorted towards the edge, however, it does contain everything embraced within the complete hemisphere above the water surface. The 180 degrees field of view of a fisheye can be explained by Snell’s law, which is

$$n \sin \theta = n' \sin \theta' \quad (2.1)$$

where n = refractive index of the incident material

n' = refractive index of the emergent material

θ = angle of incidence

θ' = angle of emergence

When light travels from the water to air [Fig 2.2(a)], since the refractive index of water ($n = 1.333$) is larger than the refractive index of air ($n = 1$), the angle of emergence θ' is always larger than the angle of incidence θ . According to Eq. (2.1), if $\theta' = 90^\circ$, the corresponding angle of incidence is called the critical angle θ_c , which can be calculated by

$$\theta_c = \sin^{-1} \frac{n'}{n} \quad (2.2)$$

If we substitute the refraction indexes with the indexes of water and air to the equation above, then the critical angle can be calculated

$$\theta_c = 48.6^\circ$$

Based on the fact that rays are reversible, the light enters the water with an angle of incidence of 90 degrees has an angle of emergence equal to the critical angle θ_c [Fig 2.2(b)]. Thus, putting an image sensor under the water can record the entire hemisphere above the water, just like a fisheye. Such bionics design simply based on Snell's law is first introduced by R.W.Wood in 1906 [Fig 2.3 (a)] [8]. He put a photographic plate (image plane) in a water-tight box and filled the box with water. On the top of the box, there was a small pinhole covered by a glass, which made the entire box a water filled pinhole camera. He took the world's first fisheye photo [Fig 2.3 (b)] and pointed out that this kind of fisheye camera can be used as a sunshine recorder.

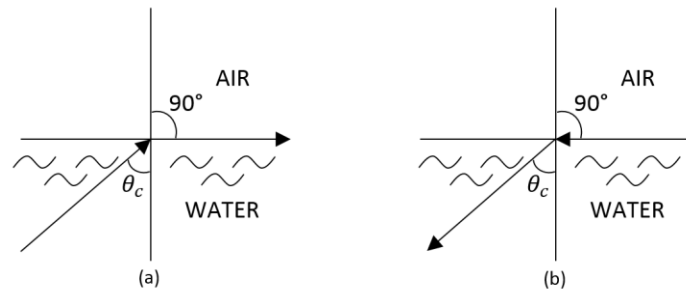


Figure 2.2. Refraction of a ray at critical angle

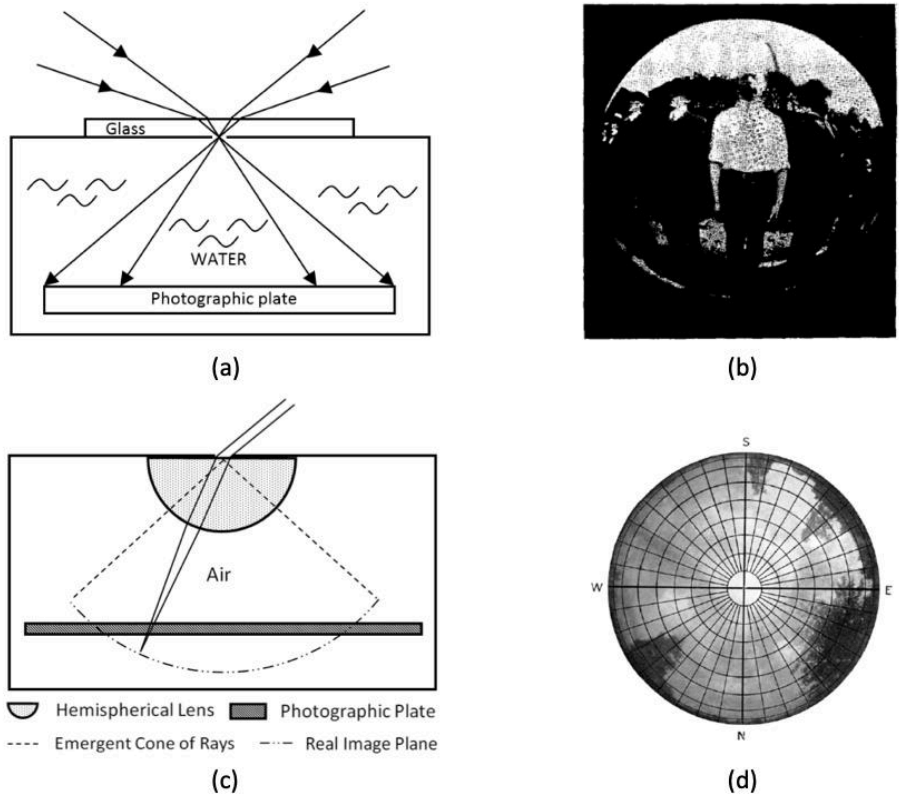


Figure 2.3. (a) Water camera designed by R.W.Wood, (b) photo took by Wood's camera, (c) fisheye camera designed by W.N.Bond and (d) entire sky captured by Bond's camera

Mr. Wood's water camera has proved that the process of light entering a fisheye could be reproduced by human and such fisheye camera could be beneficial to people. A more practical design of fisheye camera that contains no water was later introduced by W.N.Bond in 1922 [9]. He used a single piece of glass with the shape of a hemisphere to replace the water in Wood's design [Fig 2.3 (c)]. The aperture of the cameras was located at the center of the hemisphere, and

this camera also had a full FOV of 180 degrees. A photo of the entire sky captured by this fisheye camera is showed in Fig 2.3 (d).

From the modern lens design point of view, Bond's fisheye camera had a very poor optical performance. With a single hemisphere lens, the aberrations are poorly controlled, so the aperture of the system is set to be very small (F/50) in order to produce a fairly low aberrated image. Also, the image plane is almost a hemisphere, such large field curvature is only compensated by using defocus. Besides that, both Wood's and Bond's design failed to consider the relative illumination at the edge of the image. With a flat first surface, the relative illumination would drop rapidly towards the edge of the image, thus made the effective FOV of these two lenses smaller than 180 degrees. In the end of Bond's paper, he did propose that a plano-convex lens can be placed in front of the aperture to increase the FOV and improve the relative illumination. However, with no follow up from Mr. Bond, this issue was not solved until 2 years later.

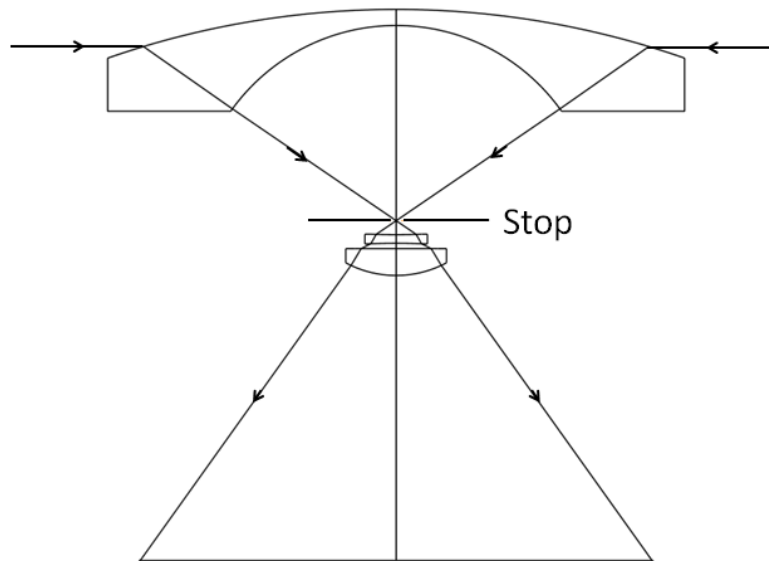


Figure 2.4. The layout of 'the Hill sky lens' designed by R. Hill

In 1924, R. Hill presented a much improved fisheye lens system [Fig 2.4]. Unlike Wood's and Bond's fisheye camera, Hill's fisheye lens was not only a simple simulation of a fisheye anymore. In his design, Hill attempted to improve the image quality by controlling the aberration and maintaining the relative illumination. He used a negative meniscus lens in front of the stop to reduce the maximum ray angle from ± 90 degrees to about ± 60 degrees, which makes aberrations correction easier with 2 singlet lenses behind the stop. The meniscus lens also helped preventing the relative illumination from falling off too much towards the edge of the image. Coma, astigmatism and field curvature were well controlled in this lens. However, the lack of control of the spherical aberration was constraining the speed of lens to a maximum of F/22 without serious image quality fall off. The speed of this lens is not acceptable today, but it was still about 5.4 times faster than Bond's fisheye camera and was fast enough for cloud recording purpose. Hill's lens, also referred as the "Hill sky lens", was the first mass production fisheye lens that is commercially available [10]. This lens is the greatest milestone of the fisheye lens history and is credited as the first prototype of the modern fisheye lens. Its negative meniscus shape of the first lens element is still used in every fisheye lens design ever since. However, his contribution to modern fisheye lens design did not stop there, in his paper, he also pointed out three mapping methods that can be used for fisheye lenses, which are stereographic projection, equidistant projection and orthographic projection. These projection methods, along with another mapping method called equisolid angle projection, will be further explained in detail in section 2.

Hill's fisheye lens showed significant improvement in optical performance compare to previous fisheye cameras. However, lack of control of spherical aberration and chromatic aberration were still a problem, which caused the aperture to be very small and only monochromatic photos can be taken. In 1932, a more elaborate fisheye lens design is published as

a patent by the AEG Company in Berlin [Fig 2.5 (a)] [11]. This lens used 2 meniscus lenses in the front so the FOV can be extended to a maximum of 210 degree according to the patent. For the first time, an achromatic doublet was used behind the stop so the chromatic aberration, along with other aberrations are well controlled, which leads to a fast F/6.3 design (about 11 times faster than the Hill sky lens). The larger aperture allows much shorter exposure time than the previous fisheye lens designs so it can be eventually used for normal photography rather than just meteorological photography.

The AEG fisheye lens is a remarkable design in the fisheye lens history, however, it was rarely mentioned in any other literatures. Many people also believed that this design was shared by the German government to their ally Japan and used by the former Imperial Japanese Navy for meteorological observation in 1938. This lens was still listed on Nikon's website as their first fisheye lens [12]. Although no evidence can be found to prove that the first Nikon fisheye lens was a modification of the AEG fisheye lens, however, the layout of these two designs were almost identical [Fig 2.5(b)].

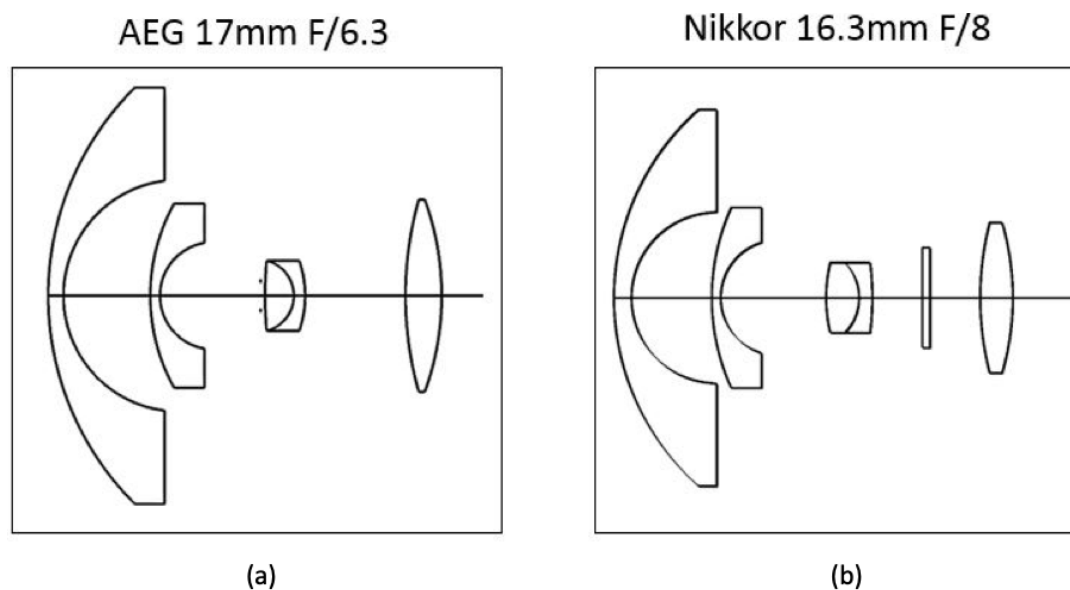


Figure 2.5. The comparison between the (a) AEG fisheye lens and (b) Nikkor's first fisheye lens

Since 1960s, with the help of computer optimization, fisheye lenses were well developed. In 1964, K. Miyamoto published the first fisheye lens that controls lateral color [13]. In 1968, Nikkor released the world's first interchangeable orthographic projection fisheye lens, which is also the first 35mm format camera lens with aspherical element [14]. During the same year, Nikon filed a patent on a 270-degree FOV fisheye lens [15]. In 1972, Nikon's F/2.8 220-degree FOV fisheye lens [16] went to mass production, it is still the world's widest FOV fisheye lens ever went to mass production until today. In February 2019, C-4 Optics introduced a prototype 4.9mm f/3.5 fisheye lens with a maximum FOV of 270 degree [17].

Lately, a few zoom fisheye lenses appeared on the market. Canon and Nikon both released their zoom fisheye lens in 2010 and 2017. Zoom fisheye lenses allow photographers to change the focal length to capture both a fulfilled image or a circular image without changing lenses. Detailed explanation of these image types will be covered in the next subsection. A zoom fisheye lens designed by the author is also presented in this chapter.

2.1.2 Diagonal and Circular Fisheye Lens for Photographic Purpose

Although the initial purpose of fisheye lenses is to record the cloud in the sky and other scientific uses, the special fisheye effect with large distortion also drew attentions from the photographers. As a result, fisheye lenses for photographic purposes were introduced since 1960s, and became one of the most common use of a fisheye lens today.

Based on how the image fulfills the cameras sensor, photographic fisheye lenses can be categorized by two different types, including the diagonal fisheye lens and the circular fisheye lens. A diagonal fisheye lens refers to a fisheye lens that has its image circle just fulfills the entire

camera sensor. In another word, the image height is equal to the length of the sensor diagonal and the lens achieves 180-degree FOV over its diagonal. However, the horizontal and vertical FOVs are smaller than 180 degrees due to the rectangular shape of the image sensors. A sample image taken by a diagonal fisheye lens is provided in Fig 2.6.

A circular fisheye lens refers to a fisheye lens that fits its entire image circle on the camera sensor. For circular fisheye lenses, the image height is equal or slightly less than the sensor height, so the entire hemisphere in front of the camera can be captured. Fig 2.7 demonstrates a photo taken by a circular fisheye lens. The entire circular image achieves 180-degree FOV, while the areas outside the image circle appear to be black on the final rectangular image.

For a camera with a constant sensor size, switching between diagonal fisheye image and circular fisheye image requires the change of lens focal length. One solution to provide both types of fisheye image without switching lenses is a zoom fisheye lens. The design of a zoom fisheye lens is covered in section 5 of this chapter.



Figure 2.6. A sample Image taken by a diagonal fisheye lens



Figure 2.7. A sample Image taken by a circular fisheye lens

2.2 Projection Methods of Fisheye Lenses

For a typical non-fisheye camera lens, the half image height from optical axis Y , effective focal length f and semi field angle in object space θ obey the following projection relationship:

$$Y = f \tan \theta \quad (2.3)$$

This projection is often named gnomonic projection. The camera lenses that use this projection are called rectilinear lenses. For ideal rectilinear lenses, the magnification is constant through the entire field, so the final image has no distortion. However, this projection will fail at extreme FOV. According to the projection equation, the image height will start to increase rapidly and become unrealistic when the semi FOV is larger than 70 degrees. Furthermore, the half image height would become infinity if the semi FOV reaches 90 degrees. Thus, it is impossible for a fisheye lens to fill the entire hemisphere onto the camera sensor without introducing large amount of barrel distortion. Other projection methods are needed for fisheye lenses. The earliest fisheye lenses, including the Hill sky lens, use equidistant projection [Eq. (2.4)]. Other projection methods that were used on fisheye lenses includes orthographic projection [Eq. (2.5)], stereographic projection [Eq. (2.6)] and equisolid angle projection [Eq. (2.7)]. This projection methods are explained in detail in this section.

$$Y = f\theta \quad (2.4)$$

$$Y = f \sin \theta \quad (2.5)$$

$$Y = 2f \tan(\theta/2) \quad (2.6)$$

$$Y = 2f \sin(\theta/2) \quad (2.7)$$

2.2.1 Tangential and Sagittal Magnification

In order for a fisheye lens to capture the entire hemisphere with a fisheye lens, huge barrel distortion towards the edge of the image is needed. This means the image close to the edge is somehow compressed compare to the center of the image. Thus, the magnification is not constant across the field as the gnomonic projection. The magnification change of a fisheye lens varies with the projection method and impacts the appearance of the image. Thus, to understand what the images look like for each projection method, one need to first understand how the magnification changes in each projection method.

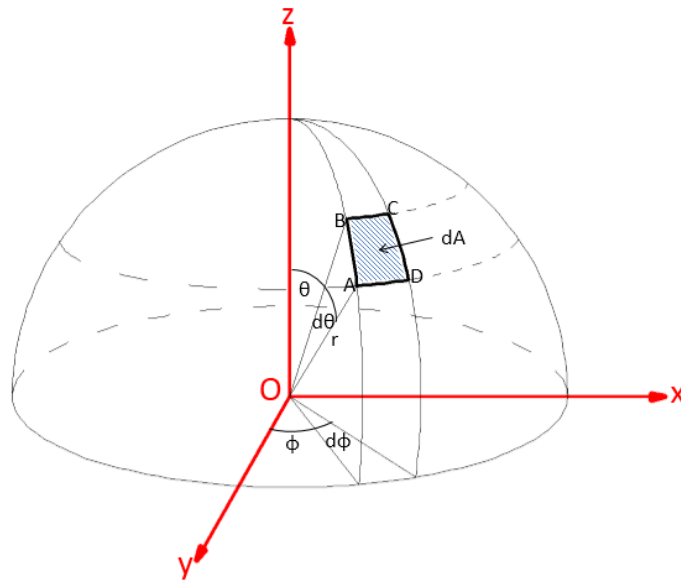


Figure 2.8. The object hemisphere of a fisheye lens system

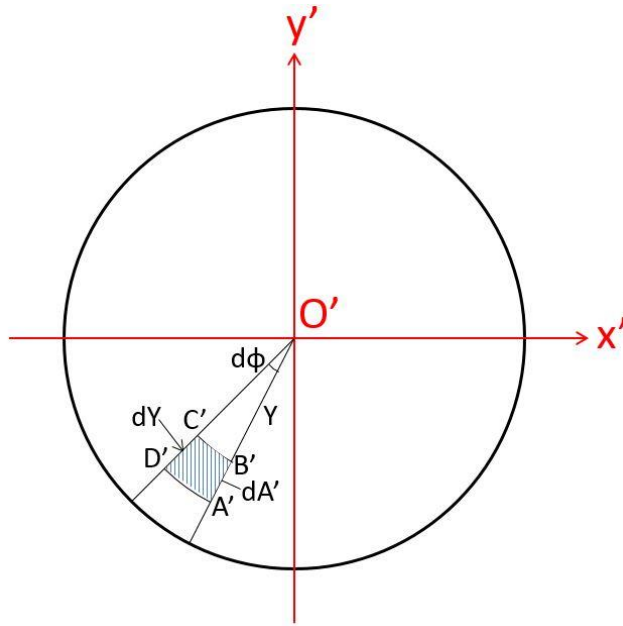


Figure 2.9. The image space of a fisheye lens system

Imagine the hemisphere in Fig 2.8 as the object plane of a 180-degree FOV fisheye lens, and the lens is centered at the origin. In this coordinate system, z axis is the optical axis. The polar angle θ corresponds to the incident field angle, from -90 degrees to +90 degrees. Angle ϕ is the azimuthal angle. The radius r is the distance between the object on the hemisphere to the fisheye lens at the origin. The shaded area ABCD on the surface of the hemisphere represents a very small area dA . Since dA is really small, line AB, AD, BC and CD are approximately straight lines. The corresponding polar and azimuthal angle of this area are small angles $d\theta$ and $d\phi$. Based on the small angle approximation, the following relationship holds:

$$AB = DC \approx r d\theta \quad (2.8)$$

$$BC \approx r \sin \theta d\phi \quad (2.9)$$

$$dA \approx AB \cdot BC = r^2 \sin \theta d\theta d\phi \quad (2.10)$$

Fig 2.9 shows the 2-D circular image transferred from the 3-D hemisphere in the object space by the fisheye lens. In this coordinate, the shaded area A'B'C'D' with the size of dA' is the

corresponding image of area ABCD in the object space. Y is the semi image height, which is the distance between the origin and the shaded area. Based on the small angle approximation, the following relationship holds:

$$B'C' \approx Yd\phi \quad (2.11)$$

$$A'B' = D'C' = dY \quad (2.12)$$

$$dA' \approx A'B' \cdot B'C' = Yd\phi dY \quad (2.13)$$

With these relations defined in both object and image space, the sagittal magnification M_s is defined by

$$M_s = \frac{A'B'}{AB} = \frac{D'C'}{DC} \quad (2.14)$$

Combine Eq. 2.14, Eq. 2.8 and Eq. 2.12, M_s is then defined by

$$M_s = \frac{dY}{r d\theta} \quad (2.15)$$

For similar derivation, the tangential magnification M_t is defined by

$$M_t = \frac{Y}{r \sin \theta} \quad (2.16)$$

The derivation result of sagittal and tangential magnification described in Eq. 2.15 and Eq. 2.16 shows that both of these magnifications depends on the semi image height Y. Since each projection methods defines Y differently, the sagittal and tangential magnification of each projection methods are different. These magnifications are discussed in detail in the next subsections.

2.2.2 Equidistant Projection

Recall the equidistant projection equation from Eq. 2.4

$$Y = f\theta$$

Take the derivative of this equation, then

$$dY = fd\theta \quad (2.17)$$

Combine Eq. 2.15 with Eq. 2.17, the sagittal magnification of the equidistant projection becomes

$$M_{s_ED} = \frac{f}{r} \quad (2.18)$$

Combine Eq. 2.4 with Eq. 2.16, the tangential magnification of the equidistant projection becomes

$$M_{t_ED} = \frac{f}{r} \left(\frac{\theta}{\sin \theta} \right) \quad (2.19)$$

Then compare Eq. 2.19 with Eq. 2.18, the relationship between tangential magnification and sagittal magnification can be expressed as

$$M_{t_ED} = M_{s_ED} \left(\frac{\theta}{\sin \theta} \right) \quad (2.20)$$

And

$$\begin{cases} M_{t_ED} = M_{s_ED}, & \theta = 0 \\ M_{t_ED} = 1.57 M_{s_ED}, & \theta = \frac{\pi}{2} \\ M_{t_ED} > 1.57 M_{s_ED}, & \theta > \frac{\pi}{2} \end{cases} \quad (2.21)$$

Eq. 2.18 shows that the sagittal magnification of this system depends on the focal length and the object distance of the system. It is constant across the field. The tangential magnification, on the other hand, is increasing towards the edge of the image according to Eq. 2.19. The

relationship between tangential magnification and sagittal magnification are shown in Eq. 2.20 and Eq. 2.21. To visualize this relationship, one can assume a small circle as the object. If the object is on-axis, its image is a circle with the radius of r' . If the same circle object is shifting off-axis, its image becomes an ellipse. The length of minor axis is constant and is always equal to r' . The major axis is increasing and reaches 1.57 times of the minor axis at field of 90 degrees. If the fisheye lens has semi field larger than 90 degrees, the major axis of the ellipse will keep increasing while the minor axis remains constant.

Equidistant projection is the most common projection method in fisheye lens design. Since the field angle and the image height are proportional, this projection method is often used for metrology purposes. This projection method was also popular for photographic fisheye lenses designed before the 1980s

2.2.3 Orthographic Projection

Recall the equidistant projection equation from Eq. 2.5

$$Y = f \sin \theta$$

Follow the same steps in the last subsection, the sagittal magnification, tangential magnification and the relationship between these magnifications become

$$M_{s_OG} = \frac{f \cos \theta}{r} \quad (2.22)$$

$$M_{t_OG} = \frac{f}{r} \quad (2.23)$$

$$M_{s_OG} = M_{t_OG} \cos \theta \quad (2.24)$$

Eq. 2.23 shows that the tangential magnification is constant across the field in the orthographic projection. Sagittal magnification, according to Eq. 2.22, is decreasing towards the

edge of the image, and becomes 0 when the semi field reaches 90 degrees. Assume a same circular object as in the last section. When the object is on-axis, the image is a circle with radius of r' . When the circle is shifting off-axis, the image is becoming an ellipse. The major axis of the ellipse remains the same, while the minor axis of the ellipse keeps decreasing. When the semi field reaches 90 degrees, the sagittal magnification decreases to 0 and the ellipse becomes a line towards tangential direction, with the length of r' .

The orthographic projection has the largest distortion at the edge of the image among all fisheye projection methods due to the sagittal magnification fall off to 0. Thus, the information near the edge of the image is nearly unusable. And it is impossible for an orthographic projection fisheye lens to achieve over 180-degree field of view. As a result, this projection method is rarely used for scientific purposes. However, the sacrifice of the information at the edge of the image ensures a less distorted image close to the center. And this method is adopted by some camera lens manufactures for their photographic fisheye lens design.

2.2.4 Stereographic Projection

Recall the equidistant projection equation from Eq. 2.6

$$Y = 2f \tan(\theta/2)$$

Follow the same steps in subsection 2.2.2, the sagittal magnification of stereographic projection becomes

$$M_{s,SG} = \frac{f}{r \cos^2(\theta/2)} \quad (2.25)$$

To write the tangential magnification in the similar form to the sagittal magnification, apply trigonometric-identities and rewrite Eq. 2.6

$$\begin{aligned}
Y &= 2f \tan(\theta/2) \\
&= \frac{2f \sin(\theta/2)}{\cos(\theta/2)} \\
&= \frac{2f \sin(\theta/2) \cos(\theta/2)}{\cos^2(\theta/2)} \\
&= \frac{f \sin \theta}{\cos^2(\theta/2)} \tag{2.26}
\end{aligned}$$

Combine Eq. 2.16 with Eq. 2.26, the tangential magnification of the stereographic projection becomes

$$M_{t_SG} = \frac{f}{r \cos^2(\theta/2)} \tag{2.27}$$

Then, the relationship between tangential magnification and sagittal magnification can be expressed as

$$M_{t_SG} = M_{s_SG} \tag{2.28}$$

And

$$\begin{cases} M_t = M_s = f/r, & \theta = 0 \\ M_t = M_s = 2f/r, & \theta = \frac{\pi}{2} \end{cases} \tag{2.29}$$

According to Eq. 2.28, for stereographic projection, the image has same tangential and sagittal magnification at any point on the image plane. Assume the same small circular object as before, the image is always a circle regardless where the object is. When the object is on-axis, the image is a circle with radius of r' . When the circle is shifting off-axis, the size of image is increasing in both tangential and sagittal direction at the same rate. When the object is placed at the polar angle of ± 90 degrees in the object space, the radius of the image circle is twice the radius

of the on-axis image circle. This projection method has the least distortion at the edge among the four fisheye projections and is rarely used in practical.

2.2.5 Equisolid Angle Projection

This projection method is named equisolid angle projection because same area in the image space corresponding to same solid angle in the object space. Recall the equidistant projection equation from Eq. 2.7

$$Y = 2f \sin(\theta/2)$$

Take the derivative of this equation, then

$$dY = f \cos(\theta/2)d\theta \quad (2.30)$$

The definition of the small solid angle $d\Omega$ corresponding to the small area dA on the hemisphere in object space is

$$d\Omega = dA/r^2 \quad (2.31)$$

Recall Eq. 2.10

$$dA \approx r^2 \sin \theta d\theta d\varphi \quad (2.32)$$

Then

$$d\Omega \approx \sin \theta d\theta d\varphi \quad (2.33)$$

In the image space, recall the expression for dA' in Eq. 2.13

$$dA' \approx Yd\varphi dY \quad (2.34)$$

Combine Eq. 2.7, Eq. 2.30 and Eq. 2.34, there is

$$dA' = f^2 \cdot 2 \sin(\theta/2) \cos(\theta/2) \cdot d\theta d\varphi \quad (2.35)$$

Apply trigonometric identities, then

$$dA' = f^2 \sin \theta d\theta d\varphi \quad (2.36)$$

Compare Eq. 2.36 with Eq. 2.33, and take the integral on both sides, the relationship between solid angle in object space and image size in image space become

$$A' = f^2 \Omega \quad (2.37)$$

Eq.2.37 tells that with equisolid angle projection, the same area in the image space corresponding to the same solid angle in the object space, despite the field angle of the object. Fisheye lenses designed using this projection can be used to measure the solid angle in the object space.

Follow the same steps in the previous subsections, the sagittal magnification and the tangential magnification become

$$M_{s_ES} = \frac{f \cos(\theta/2)}{r} \quad (2.38)$$

$$M_{t_ES} = \frac{f}{r \cos(\theta/2)} \quad (2.39)$$

The changing rate of sagittal magnification is the multiplicative inverse of the changing rate of tangential magnification. Assume a small circular object as before. When the circular object is on-axis, its image is also a circle. When the object is shifting off axis, the sagittal magnification is decreasing while the tangential magnification is increasing. Thus, the image becomes an ellipse, with the major axis along the tangential direction, and the minor axis along the sagittal direction.

The distortion is larger than the equidistant projection, but smaller than the orthographic projection at large field. This reduces the distortion of the center portion of the image while still maintaining good details at the edge of the image. Thus, this kind of fisheye projection method become popular recently for photographic fisheye lenses. Most of the photographic fisheye lenses that are currently on the market are designed based on the equisolid angle projection.

2.2.6 Projection Difference and their Practice Use

The relationship between the half image height and half field angle of different fisheye projection methods and the regular gnomonical projection method is shown in Fig 2.10. From this figure, all fisheye projections start to depart from the gnomonical projection at around 30-degree half field angle. The stereographic projection has the least barrel distortion, while the orthographic projection has the largest barrel diction. Equidistant projection and equisolid angle projection have similar medium amount of barrel distortion compare to the other two. Also note that the image height reaches its peak at 90-degree semi-field for orthographic projection. For that reason, the maximum FOV of an orthographic type fisheye lens is limited to 180 degrees.

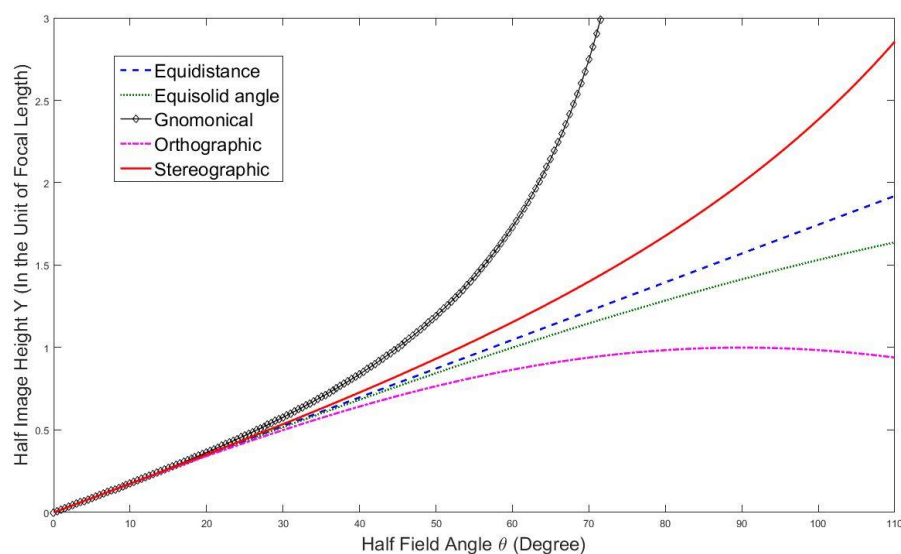


Figure 2.10. Image height vs. field angle for different fisheye projection system

Practically, photographic fisheye lenses are mostly designed based on equidistant and equisolid angle projections, with a few exceptions such as the Samyang 12mm f/2.8 fisheye lens designed using stereographic projection, and the Nikkor 10mm f/5.6 fisheye lens designed using orthographic projection. It is more challenging to maintain the stereographic and orthographic projection during the design, and aspherical elements are usually required. In fact, the Nikkor 10mm f/5.6 fisheye lens is the first aspherical lens for 35mm format camera [14]. Fig 2.11 shows the comparison between the same object under different fisheye projections. The differences are more noticeable around the edge, such as the shape of the palm tree around the top left of the photo and the gap between the building and the edge of the image. There is no easy judgement on which projection method is the best for photographic purpose. They all create different distortion effects and it is up to the photographer to choose the right projection they need.

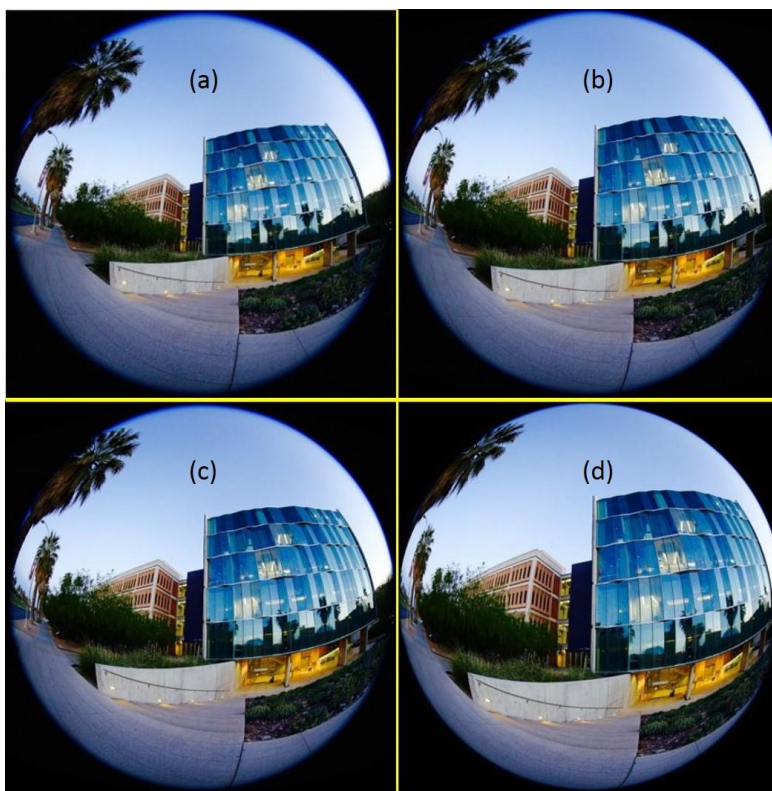


Figure 2.11. Same object under (a) stereographic projection, (b) equidistant projection, (c) equisolid angle projection and (d) orthographic projection

These four projection methods discussed in this section are the standard projection methods. However, for photographic fisheye lenses, image quality usually controls the design, and the projection is sacrificed to some extent. The small departure from the standard fisheye lens projection is usually allowed for the photographic fisheye lens. But slightly loosen the constrain on the image projection usually helps with the aberration control during the optimization stage of the fisheye lens design. The resulting projection can be described as

$$Y = af \sin(\theta/b) \quad (2.40)$$

where a and b are coefficients that define the projection. This projection is a modification of the standard equisolid angle projection. An example would be the NIKKOR 16mm F/2.8 fisheye lens. After a curve fitting applied to the lens projection data [Fig 2.12], it is clear that the projection method used by this lens was modified form equisolid angle projection, with coefficient a equals to 1.8, and b equals to 1.78.

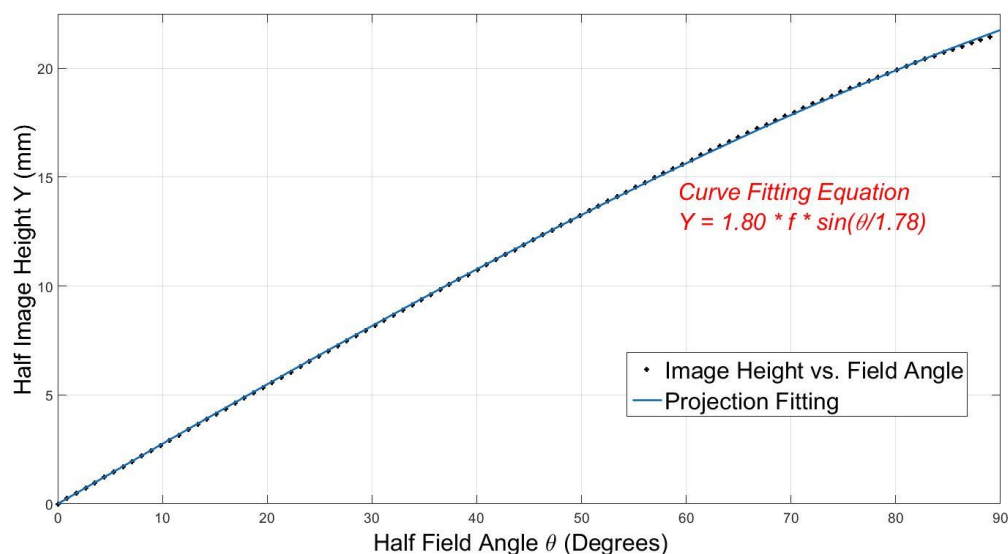


Figure 2.12. The projection curve fitting for the NIKKOR 16mm F/2.8D fisheye lens

2.3 Special Properties and Design Issues of Photographic Fisheye Lenses

As a unique type of photographic lens, fisheye lenses have some special properties compare to other ordinary photographic lenses. Some of these properties are beneficial while the others may create issues for the design and optimization of a fisheye lens. These special properties, along with some design issues, will be addressed in this section.

2.3.1 Negative Meniscus Lens and Pupil Shift

Since the aperture stop of a fisheye lens is on-axis and perpendicular to the axis, rays with incident angle larger than 90 degrees are impossible to enter the stop directly. Thus, a negative meniscus lens in the front is required for all fisheye lenses in order to direct the light from an entire hemisphere into the stop. The meniscus shape of the first element can be traced back to “the Hill sky lens” and is still used by every fisheye lens today. The meniscus lens reduces the chief ray angle so it can pass through the stop easily. For better aberration control, usually more than one negative element is used in the front group to further reduce the chief ray angle. Also, by using multiple meniscus lens and reduce the chief ray angle gradually, fisheye lenses with FOV larger than 180 degrees is possible. Figure 2.13 shows a Nikon 6mm F/2.8 fisheye lens that achieves a 220-degree FOV by using 3 meniscus lenses in the front.

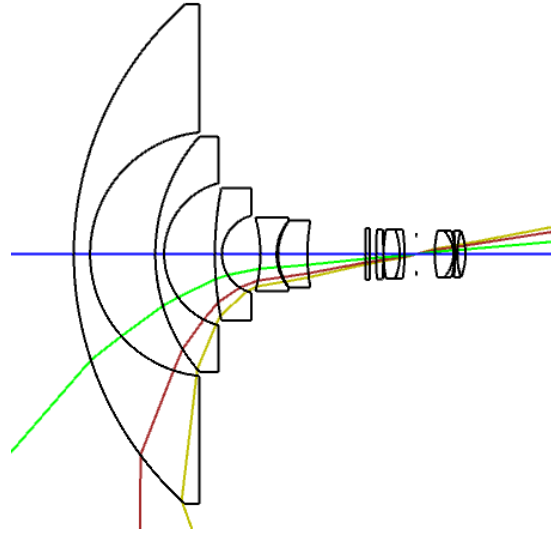


Figure 2.13. The Nikon 6mm F/2.8 220-degree fisheye lens with 3 negative meniscus lenses

The aperture stop in a fisheye lens is located near, or at the rear positive lens group. The image of the stop formed by the front lens group becomes entrance pupil. As the field of view increases, the real entrance pupil position may depart from the paraxial pupil position on axis. Such departure is not significant for lenses with small field of view. For lenses with extremely large field of view, such as the fisheye lens, the front negative lens group contributes a substantial amount of negative pupil spherical aberration \overline{W}_{040} . The consequence is that entrance pupil, as seen at oblique angles, appears to tilt and move forward, off the optical axis. This effect is usually referring as the pupil shift and is demonstrate with the Nikon 8mm F/8 fisheye lens in Fig 2.14. Effectively, in the meridional plane the entrance pupil follows the external caustic sheet for the entrance pupil's spherical aberration. This pupil shift is not only inevitable but is actually needed in order for the light from extreme angles to pass through entrance pupil. Also note that since the entrance pupil is tilted for off axis rays, it must be tilted at opposite angles for rays from opposite fields (e.g. +90-degree rays and -90-degree rays). This might be difficult to picture for a normal objective lens where the entrance pupils for rays from opposite fields are considered to share the

same virtual surface that is orthogonal to the optical axis. But it is the only logical explanation for a fisheye lens system.

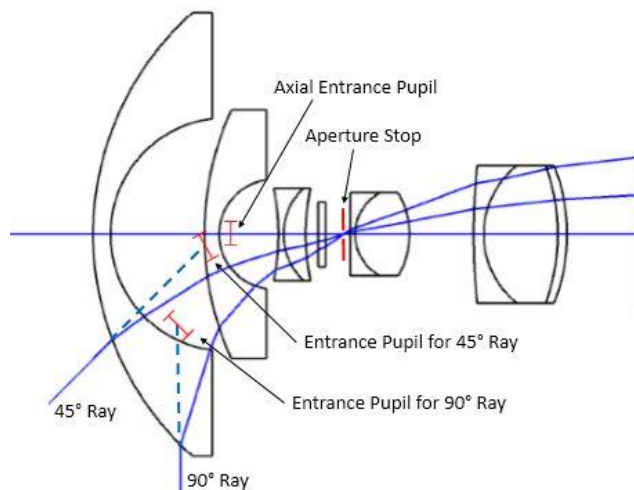


Figure 2.14. The pupil shift effect of the Nikkor 8mm F/8 fisheye lens

Although the shift of entrance pupil does not impact the lens physically since the entrance pupils are only virtual surfaces, it does affect both the sequential and non-sequential ray tracing in the optics CAD software. For sequential ray tracing software such as Zemax, the paraxial location and size for the entrance pupil is used to launch rays in the object space [18]. For ultra-wide angle lenses such as fisheye lens, ray aiming is required for rays to trace properly at large incident field. Fig.2.15 shows the difference of a simple fisheye lens [19] before and after the ray aiming is turned on. Ray aiming is an iteration process to find correct entrance pupil location to make sure that the chief ray passes through the center of the stop for each field. Such process took time and will slow down the ray tracing and lens optimization.

For non-sequential software such as FRED, since there is no definition of system stop nor chief ray, finding the correct entrance pupil with iteration is impossible. This creates a problem for stray light analysis. For stray light analysis of a lens, one useful technique is to define the entrance pupil as a region of interest. Only the rays scattering towards the entrance pupil is being traced.

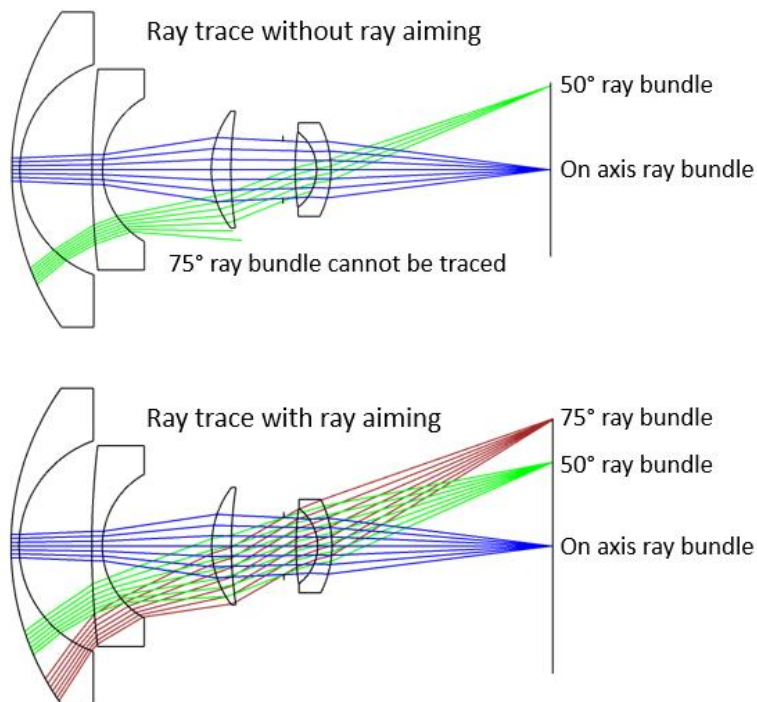


Figure 2.15. A fisheye lens with ray aiming turned on (top) and off (bottom) in Zemax

This significantly reduces ray trace time. However, for fisheye lenses, without locating the entrance pupil and the fact entrance pupil is different for each field, such technique to define the region of interest cannot be applied.

2.3.2 Inverted Telephoto Structure and Minimum BFD Requirement

Refer to Fig 2.14, a typical fisheye lens contains two lens groups, a front negative group to gradually reduce the chief ray angle and a negative rear group to focus the image, with the stop located between two groups. This is a typical inverted telephoto lens system. Fig 2.16 shows the structure difference between a telephoto lens and an inverted telephoto lens. Both lenses have the same lenses and same distance between the two lenses. Thus, the effective focal lengths (from principle plane P' to focal plane F') are same for both lenses. However, due to the rear principle plane being located differently, the inverted telephoto lens has longer BFD than the telephoto lens. And the BFD is longer than its effective focal length for the inverted telephoto lens.

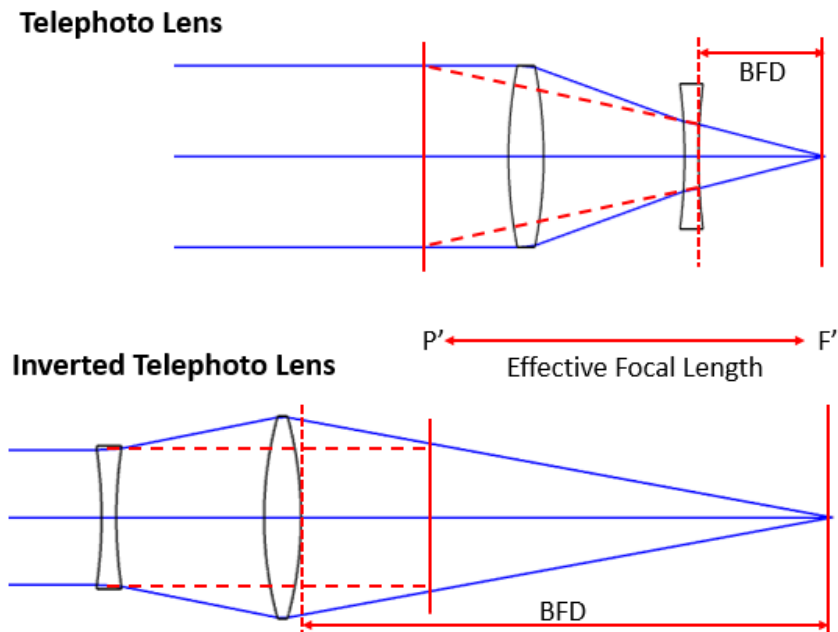


Figure 2.16. The structure of the telephoto lens and the inverted telephoto lens

For DSLR cameras, a certain clearance between the last surface of the lens to the image sensor is required for the folding mirror, shutter and other mechanisms. This clearance requirement also sets the minimum BFD requirement for the lenses. For typical 35mm DSLR cameras, a minimum BFD of 38mm is required. This creates a problem for fisheye lens designers since the focal length of the fisheye lenses for 35mm format cameras is much smaller than this minimum BFD requirement. Although the exact focal length of a fisheye lens depends on its projection method, for 35mm camera format, a typical focal length varies around 16mm for a diagonal fisheye lens, and around 9mm for a circular fisheye lens, which is smaller than one-fourth of the minimum required BFD. Even with an inverted telephoto structure, such BFD requirement is hard to meet, especially for circular fisheye lenses. A great example would be the Nikkor 7.5mm F/5.6 circular fisheye lens designed in 1960s. This lens could not meet the minimum BFD requirement, as a consequence, the folding mirror needs to be held in the upright position to attach this lens to the camera [Fig 2.15(a)]. An attachable viewfinder is also provided to use with the lens since the

original viewfinder is blocked [Fig 2.15(b)]. Today, even with the aid of computer optimization, this is still a design challenge. Fisheye lenses usually barely met the minimum BFD requirement, with the sacrifice of some optical performance.

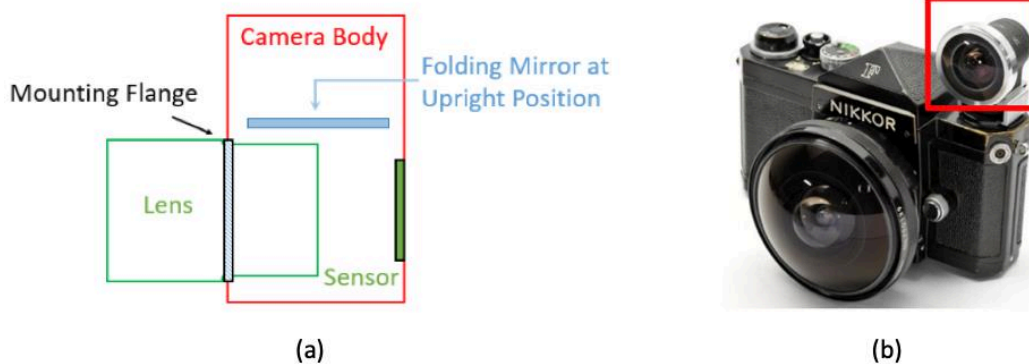


Figure 2.17. For a fisheye lens without sufficient BFD, (a) the folding mirror needs to be held at upright position and (b) an attachable viewfinder is needed to provide live view [20]

2.3.3 Depth of Field

Depth of field describes the distance between the nearest and farthest objects in a scene that appears acceptably sharp on the final image. Its corresponding distance in the image space is called depth of focus. Ideally, one image plane in the image space is conjugate with only one object plane in the object space. If the object distance is changed without changing the image distance, the image will be blurred. Practically, very small blur on the image is tolerable to human eyes. Typically, any small blur on the image beyond the human visual acuity is not noticeable and is considered to be sharp or in focus. And the limit of an unnoticeable blur on the image plane is called the circle of confusion, or CoC. The equations for the depth of field and hyperfocal distance is explained in this subsection. The detailed derivation of the depth of field can be found in author's master's thesis, so only the end result is shown in this subsection.

Refer to Fig. 2.18, C' is the circle of confusion on the nominal image plane, and C is the conjugate circle on the nominal object plane. The distance between object O' and O'' is the depth of field of this camera lens and is defined as L . And its corresponding depth of focus is defined by the distance between I' and I'' . D is the entrance pupil diameter, r is the nominal object distance, and f is the nominal focal length. The relationship between the depth of field L , circle of confusion C' , object distance r , focal length f , and the F-number N is

$$L = \frac{2NC'r^2f^2}{f^4 - N^2C'^2r^2} \quad (2.41)$$

Since C'^2 is very small compare to other parameters, the term $N^2C'^2r^2$ is neglectable, an approximation of the depth of field L is

$$L \approx \frac{2NC'r^2}{f^2} \quad (2.42)$$

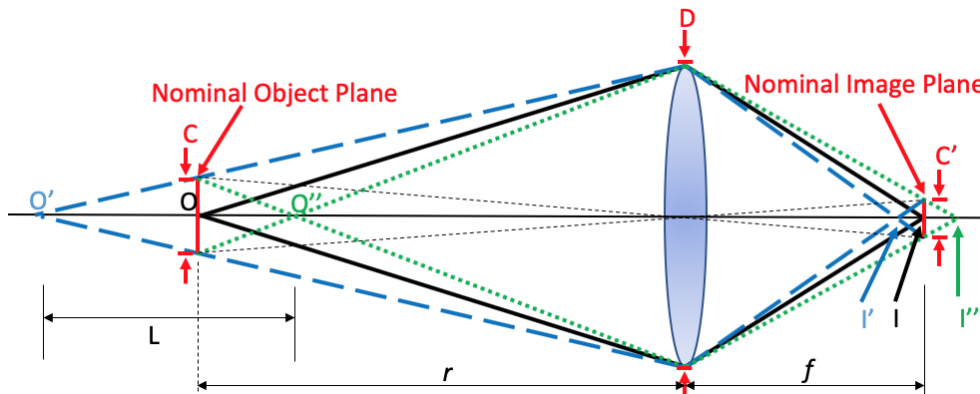


Figure 2.18. Illustration of depth of field L

The exact number of C' is hard to define as this is more of a subjective number based on different people's visual acuity. According to Carl Zeiss, $1/1500$ of the sensor diagonal, which is 0.029mm , is an appropriate number for C' for modern 35mm format cameras [21]. Since C' is a constant, according to Eq. 2.42, if same object distance is maintained, the depth of field is linear

to F-number and inverse quadratic with focal length. In another word, the depth of field increases with smaller aperture and longer focal length.

The derivation of Eq. 2.41 and Eq. 2.42 are based on the transverse magnification in the rectilinear image system (f -tan θ projection). For fisheye lenses, magnification is not constant across the field and is varied by its projection method. Nevertheless. Recall the relationship between different projection method in Fig 2.8, the magnifications of fisheye projections are the same with gnomonical projection on axis and are not deviate much from the gnomonical projection until the HFOV reaches about 55 degrees. Also, since majority of the information captured by a fisheye lens is within the center portion of the image, Eq. 2.42 is still a good approximation to calculate the depth of field for fisheye lenses.

Another concept that is related to the depth of focus is the hyperfocal distance, which describe the minimum object distance that allows everything beyond this distance to be in focus. The hyperfocal distance L_H is defined as

$$L_H \triangleq \frac{f^2}{NC'} \quad (2.43)$$

and the near focal limit L_{NEAR} is

$$L_H = \frac{f^2}{2NC'} \quad (2.43)$$

which is half of the hyperfocal distance. When a camera is focused at the hyperfocal distance, the objects from half of the hyperfocal distance to infinity are within the tolerable blur and are in focus.

For fisheye lenses, as discussed in the last subsection, usually has very short focal length. Compare to a standard prime lens with 50mm focal length, at the same object distance and under

the same aperture setting, a 15mm diagonal fisheye lens can achieve 11 times the depth of field. A 9mm circular fisheye lens can achieve 31 times the depth of field compares to the 50mm standard lens. Also, for a typical fisheye lens with a maximum aperture of F/2.8, the near focus limit is 1385mm for a diagonal fisheye lens, which is equal to the near focus limit for a 50mm standard lens with the aperture reduced to F/31. If the aperture is reduced to F/8, the near focus limit is 551mm for a diagonal fisheye lens and is only 175mm for a 9mm circular fisheye lens.

The large depth of field and short hyperfocal distance make fisheye lenses great choices for surveillance cameras, surrounding cameras for auto mobiles, and other applications that requires to capture large depth of field without refocusing. For photography, fisheye lenses are great for landscape photography to capture everything in focus. However, the large depth of field makes fisheye lenses almost impossible to achieve “bokeh” effect, which is a technique used by many photographers to intentionally blur the surroundings of the actual object.

2.3.4 Relative Illumination and Image Space Chief Ray Angle

Chief ray angle in image space directly affects the edge relative illumination of the image. For camera systems with no aberrations, the off-axis relative illumination follows the $\cos^4 \theta$ law that is state below:

$$E = E_0 \cdot \cos^4 \theta \quad (2.44)$$

where E = Off-axis illumination

E_0 = On-axis illumination

θ = Chief ray angle in image space

Practically, such relation is affected by aberrations in a real lens system [22]. However, since aberrations are usually well controlled in modern rectilinear photographic lenses, their relative illumination before vignetting obey the $\cos^4 \theta$ law well. As a rule of thumb, the edge relative illumination needs to be over 50% compare to the center of the image to be corrected digitally [23]. Thus, by the $\cos^4 \theta$ law, the image space chief ray angle needs to be smaller than 33 degrees in order to maintain at least 50% edge relative illumination. However, image space chief ray angle is usually controlled well under 33 degrees to allow room for vignetting, which helps reducing the off-axis aberrations.

For fisheye lenses, due to large barrel distortion, the light flux is distributed over increasingly smaller areas towards the edge of the image. Thus, illumination towards the edge is improved. This relative illumination improvement can also be explained by the entrance pupil coma aberration due to the following relationship

$$\overline{W}_{131} = W_{311} + \frac{1}{2} \mathcal{K} \cdot \Delta(\overline{u}^2) \quad (2.45)$$

where \overline{W}_{131} is the pupil coma coefficient, W_{311} is the image distortion coefficient, \mathcal{K} is the Lagrange invariant and \overline{u} is the chief ray angle. This equation shows that pupil coma aberration increases linearly with the image distortion. Pupil coma produces an aspect ratio change in the cross section of a beam at a pupil, which is possible to form a deformed pupil with a larger area than idea pupil thus accepts more light at off-axis field points [Fig 2.19]. Such pupil deformation to accept more light with the expense of image distortion is called Slyusarev effect [24]. An example of Slyusarev effect is shown is Fig 2.20, which a monochromatic fisheye lens with large image distortion and small image space chief ray angle produced a 104% relative illumination at the edge of the image compare to the center.

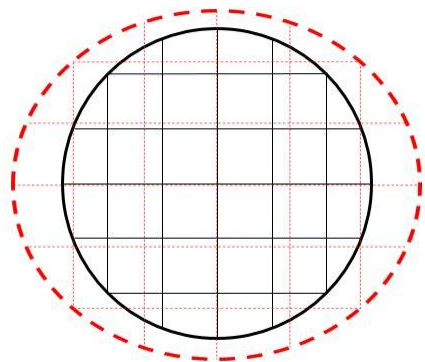


Figure 2.19. Coma aberration of the entrance pupil. Black solid lines indicate the paraxial entrance pupil with grid. The red dashed lines indicate the off-axis entrance pupil with corresponding grid.

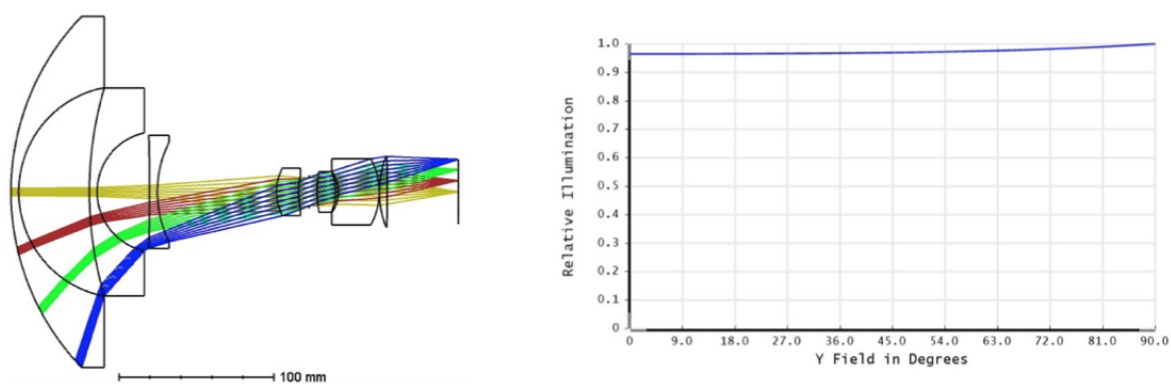


Figure 2.20. A monochromatic fisheye lens design with 104% edge relative illumination (compare to center illumination)

While the large amount of distortion benefits fisheye lens with less edge relative illumination issue, more vignetting may also be needed for fisheye lens to control the off-axis aberrations due to its large field of view. Thus, it is still necessary to maintain a small image space chief ray angle. Also, reducing the angle of chief ray hitting the image sensor also helps eliminating color crosstalk due to the structure of modern CMOS sensors [25].

2.4 Design of a Zoom Fisheye Lens for 35mm Format DSLR Cameras

Lens design details for zoom fisheye lenses are scarce in the literature. In author's master's thesis, a design of 9-16mm zoom fisheye lens with maximum aperture of F/3.2 to F/4.1 is briefly discussed. The study on zoom fisheye lens is carried on, and an improved zoom fisheye lens with

same focal length range but an increased maximum aperture of F/2.8 to F/3.5 is discussed in detail in this section. The highlights of the design are its simplicity, aberration control, and image quality. The design motivation of a zoom fisheye lens is explained. Then, the lens designed by the author is presented, along with the discussion on aberration control and design philosophy. The performance and tolerance are also evaluated. This design was published as “Photographic zoom fisheye lens design for DSLR cameras” on *Optical Engineering* [26].

2.4.1 Motivation and Current Designs of Zoom Fisheye Lenses

As mentioned in the previous sections, fisheye lenses can be categorized to two different types based on how the image fulfills the sensor. These are the diagonal fisheye lenses and circular fisheye lenses. To capture both the diagonal fisheye image and circular fisheye image usually requires photographers to switch between fisheye lenses with different focal lengths. However, a zoom fisheye lens with enough focal length coverage can provide both circular and diagonal fisheye image without changing lens.

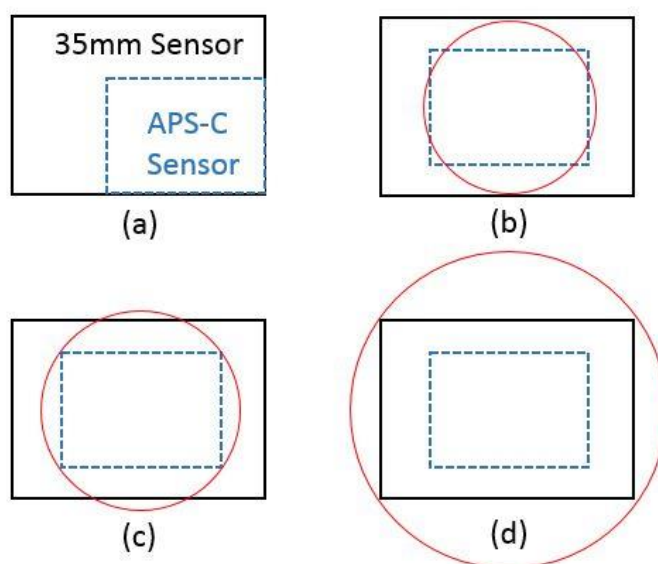


Figure 2.21. (a) Size comparison between a 35mm sensor and an APS-C sensor, (b) zoom fisheye lens at its shortest focal length, (c) zoom fisheye lens providing diagonal fisheye image for APS-C sensor, (d) zoom fisheye lens at its longest focal length.

For such zoom lens design, the fisheye lens should form an image circle with a diameter equal or slightly smaller than the width of 35mm format sensor to provide a circular fisheye image at its shortest focal length. Also, the lens should form an image circle with a diameter equal or slightly larger than the diagonal of a 35mm sensor to provide a diagonal fisheye image that fulfills the entire sensor at its longest focal length. In addition, this design can be used as a diagonal fisheye lens for APS-C format (a sensor format that is smaller than 35mm format and is often used in compact DSLR cameras) cameras at its intermediate zoom position where the image height is equal to the diagonal of an APS-C format sensor. Fig 2.21 (a) shows the size comparison between a 35-mm sensor and an APS-C sensor. Fig 2.21 (b) shows the image circle (red) at wide-angle zoom position. Fig 2.21 (c) shows the image circle at intermediate zoom position for a diagonal APS-C fisheye image. Fig 2.21 (d) shows the image circle at telephoto zoom position. For zoom lens terminology usage, the wide-angle zoom position and telephoto zoom position refer to the positions of the lens groups at the shortest and longest focal lengths. The term “telephoto” here does not imply that the lens has a telephoto construction since the fisheye lens is a inverted telephoto lens throughout the entire zoom range. The diagonal of an APS-C sensor is not standardized among different camera companies; the size of the Nikon DX sensor (23.5 mm × 15.6 mm) is used as the reference in this section.

A zoom fisheye lens can provide many benefits to photographers, however, the extreme FOV of a fisheye lens, its optical asymmetry, and the required long BFD make correcting off-axis aberrations, such as field curvature, oblique spherical aberration, and lateral color challenging. These challenges become greater when the lens must be optimized and balanced for different focal lengths. Over the last decade, a few zoom fisheye lens designs have been patented. For example, the lens in U.S. Patent #6,987,623 [27] assigned to Nikon, the lens in U.S. Patent #7,317,581 [28]

assigned to Pentax, and the lens in U.S. Patent #8,456,751 [29] assigned to Cannon. Among these patents, only the 8-15mm zoom design by Canon has been mass-produced at the time the author started to work on this project. The lens has 14 lens elements with one aspherical surface and a maximum aperture of F/4 throughout the entire zoom range. Recently, Nikon also released their first zoom fisheye lens with same focal range as the Canon lens. The lens has 15 elements with 2 aspherical lenses. And its maximum aperture is F/3.5 to F/4.5 depends on the current focal length. Both of these lenses have relatively small maximum apertures compare to fixed focal fisheye lenses (usually has maximum aperture at F/2.8). Also, these 2 lenses have large total element numbers. Thus, the motivation of this zoom lens design in this section is to achieve larger maximum aperture with less lens elements, while still maintaining good image quality.

2.4.2 Design Specifications and Lens Construction

The design specification is presented in Table 2.1. The specifications are showed at 3 critical zoom position, the wide angle zoom position that produces circular fisheye image, the telephoto zoom position that produces diagonal fisheye image, and an intermediate zoom position that produces diagonal fisheye image for selected APS-C format sensor (Nikon DX format). The focal length ranges from 9.2mm to 16.1mm, which is different from the 8-15mm focal length adopted by Canon and Nikon. As mentioned before in Section 2.2, a variation of equisolid-angle mapping is often used to characterize photographic fisheye lenses. This mapping varies depending on fisheye lens design, and therefore, to provide the same image size and field of view for fisheye lenses, slightly different focal lengths are possible. For the design that is presented in this section, a certain amount of freedom on the mapping and focal length is allowed in order to achieve better optical performance. However, the mapping is limited so the departure from standard equi-solid angle mapping is less than 10%.

Fig 2.22 shows the construction of the zoom lens at its extreme zoom position. The lens has a negative front group and a positive rear group and remains inverted telephoto structure throughout the entire zoom range. The front group consists of one doublet and two meniscus lenses; the rear group consists of a singlet lens, a doublet lens and a triplet lens. The lens prescription data are provided in Table 2.2. Linear units are in millimeters, and glass materials are chosen from the Schott glass catalogue.

The rear lens group, includes the aperture stop, acts as the variator and produces the majority of the lens movement to change the power of the lens, whereas the front group acts as the compensator that moves slightly to keep the image plane stationary. The physical motion of the lens groups, also refers as the cam curve, is shown in Fig 2.23. The rear group moves linearly, whereas the front group moves nonlinearly. The zoom is achieved by varying both BFD and space between front and rear groups.

Zoom Position	Wide angle	Intermediate	Telephoto
Focal Length (mm)	9.2	10.8	16.1
F/#	F/2.8	F/3	F/3.5
FOV (deg)	180	180	180
Half image height (mm)	12	14.1	21.6
Design Spectrum	Visible spectrum (F, d, C)		
Projection method	Equisolid angle to within 10% distortion difference		
BFD	38 mm		
Total track length	140 mm		
Maximum lens clear aperture	68.6 mm		
Object location	At infinity		

Table 2.1. Design specification of the zoom fisheye lens at different zoom positions

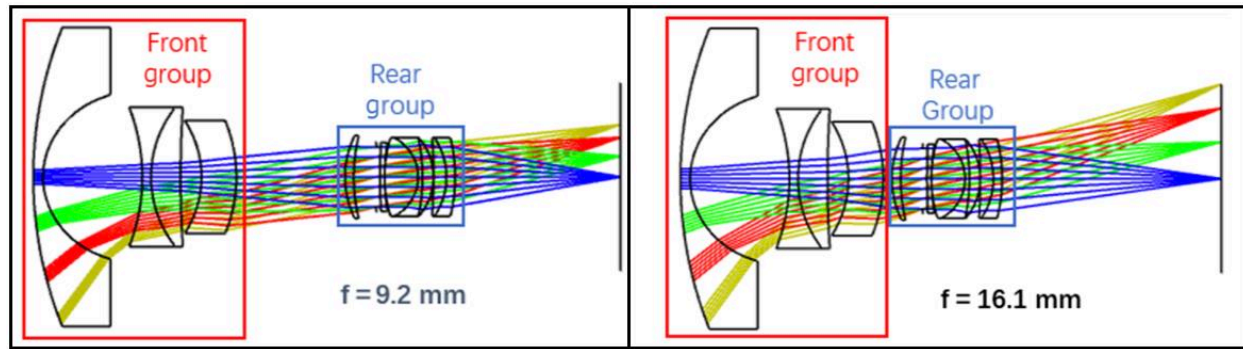


Figure 2.22. Lens structure at extreme zoom positions

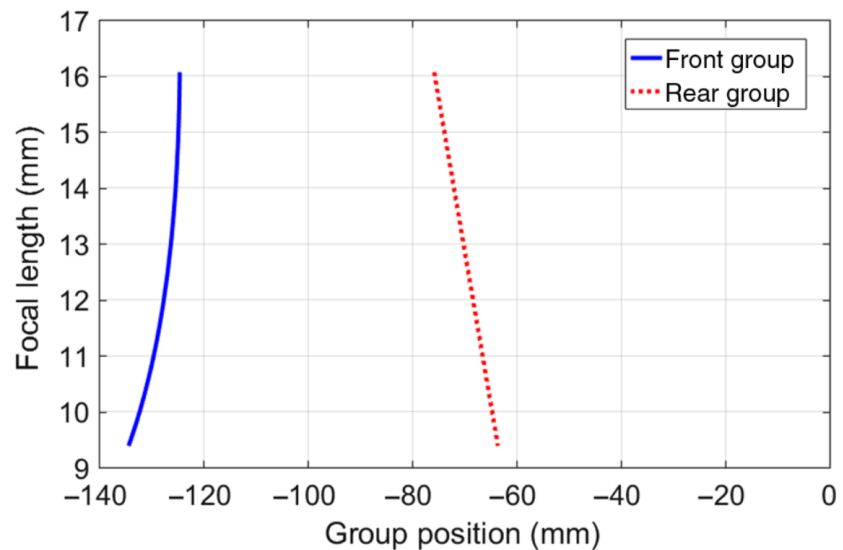


Figure 2.23. Cam curve of the zoom lens

Surface number	Radius of Curvature (mm)	Thickness (mm)	Material			
1	92.031	2.237	N-LAK34			
2 (aspherical)	17.647	22.819				
3	-43.924	1.999	N-PSK53A			
4	25.754	6.788	SF6			
5	245.219	4.811				
6	-23.732	8.001	N-LASF45			
7	-34.205	T7 (variable)				
8	21.396	2.000	N-SSK8			
9	40.422	5.122				
10 (stop)	Infinity	0.964				
11 (aspherical)	175.333	0.976	N-LAK10			
12	43.311	0.000				
13	29.529	7.749	N-BK10			
14	-10.137	0.999	N-LASF44			
15	-41.349	2.504	SF2			
16	-13.753	0				
17	-147.83	3.000	N-Pk52A			
18	-16.121	2.000	SF6			
19	-36.900	BFD (variable)				
Multiconfiguration	Wide angle	Intermediate	Telephoto			
Focal Length (mm)	9.2	10.8	16.1			
T7	24.985	17.300	2.009			
BFD	38	40.791	50.463			
Surface	Conic	4th	6th	8th	10th	12th
2	-0.183	-2.772E-06	1.760E-08	-1.188E-10	3.339E-13	-4.160E-16
11	0.000	-2.944E-05	-6.658E-08	2.457E-10	0.000	0.000

Table 2.2. Lens data with aspherical coefficients

2.4.3 Aberration Control

The final design of the zoom fisheye lens is shown in Fig 2.23. It consists, for maximum simplicity, of two zooming groups. The focal lengths of the front and rear group are -16mm and +30mm, respectively. Changing the group separation changes the focal length, and the focal plan is maintained by moving both groups. Since there are two groups, ideally, one should correct each group, or nearly correct, for its fourth-order aberrations, except distortion. Then the aberrations remain corrected through the focal range. To achieve such correction, two conditions have to be met. First, aperture size (F/#) needs to be varied with focal length to maintain same entrance pupil size. When this condition is met, light will pass through the front group about the same at different zoom position. Thus, the aberration control for the front group is maintained. Second, the rear group needs to be corrected for invariance of aberrations as its virtual object changes position. In this zoom lens with only 2 groups, the front group serves as the virtual object, and its position changes with the separation between two zoom groups during zooming. If somehow the aberrations of the rear group remain invariant, then the entire lens remains corrected through the entire zoom range.

$W_{040}^* = W_{040} + \left(W_{131} + \frac{1}{8} \mathcal{K}\Delta(u^2) \right) S + \left(\frac{3}{2} W_{222} + \frac{3}{8} \mathcal{K}\Delta(u\bar{u}) + W_{220P} \right) S^2$ $+ \left(W_{311} + \frac{3}{8} \mathcal{K}\Delta(\bar{u}^2) \right) S^3 + \bar{W}_{040} S^4$	(2.46)
$W_{131}^* = W_{131} + \left(3W_{222} + \frac{1}{2} \mathcal{K}\Delta(u\bar{u}) + 2W_{220P} \right) S$ $+ \left(3W_{311} + \mathcal{K}\Delta(\bar{u}^2) \right) S^2 + 4\bar{W}_{040} S^3$	(2.47)
$W_{220P}^* = W_{220P}$	(2.48)
$W_{222}^* = W_{222} + \left(2W_{311} + \mathcal{K}\Delta(\bar{u}^2) / 2 \right) S + 4\bar{W}_{040} S^2$	(2.49)
$W_{311}^* = W_{311} + 4\bar{W}_{040} S$	(2.50)

Table 2.3. Aberration coefficients upon object shift according to the object shift parameter S

The equations for the aberration coefficients upon object shift are given in Table 2.3 [24]. W_{040} , W_{131} , W_{220P} , W_{222} and W_{311} are coefficients for fourth order spherical aberration, coma, Petzval field curvature, astigmatism and distortion respectively before object shift. The coefficients with asterisk are the new coefficients after object shift. Note that the coefficients are a polynomial in the object shifting parameter S , which is

$$S = \frac{u^* - u}{\bar{u}} = \frac{y^* - y}{\bar{y}} \quad (2.51)$$

where u and \bar{u} are the marginal and chief ray angle respectively before shifting, y and \bar{y} are the marginal and chief ray height respectively before shifting, u^* and y^* are the marginal ray angle and marginal ray height after shifting. According to the degree of the polynomial, there are object positions for which no additional aberration is occurring. Take spherical aberration as an example. According to Eq 2.46, W_{040}^* is a polynomial of fourth degree on S , so there are four object positions where the spherical aberration remains invariant ($W_{040}^* = W_{040}$). Furthermore, for any of the fourth order aberration, if the coefficients of the polynomial are zero, then there would be no variation of that aberration. For example, to achieve invariance of astigmatism $W_{222}^* - W_{222} = 0$, according to Eq 2.49, there must be negligible pupil spherical aberration \bar{W}_{040} to eliminate polynomial term S^2 . Also, to eliminate polynomial term S , the rear lens group shall also have no image distortion W_{311} , and the chief ray must nearly pass by the nodal points as to have $\Delta(\bar{u}^2) = 0$, or alternatively $4W_{311} + \mathcal{K}\Delta(\bar{u}^2) = 0$.

Table 2.4 provides the fourth-order aberration coefficients of the front group, the rear group, and the complete zoom lens for the wide-angle and telephoto positions. The field of view used is 30 degrees as aberration coefficients depend on \bar{u} , which is undefined for $\theta = 90$ degree. The $F/\#$ used is $F/3.5$ for the wide-angle position and $F/6.1$ for the telephoto position. These F -numbers

make the passage of light in the front group about the same. Furthermore, for both positions, the rear group aberrations spherical aberration, coma, field curvature, and distortion are similar indicating that Eq 2.46, Eq 2.47, Eq 2.48 and Eq 2.50 in Table 3 are satisfied to some extent for invariance. Eq 2.49 in Table 2.3 for invariance of astigmatism is not satisfied as much compare to other aberrations. However, a second compensation mechanism takes place as there is stop shifting for the front group, which in the presence of coma changes the astigmatism from the front group to compensate the change of astigmatism upon zooming for the rear group. Note that except for inevitable distortion, the total fourth-order aberrations, for the 30-degree field of view and the corresponding F-numbers, are on the order of one wave or less, which is considered a small amount.

The above analysis about the invariance of fourth-order aberrations for the rear group explains how the aberrations can be controlled in such a simple two-group zoom lens. For this analysis, the sizes of the entrance pupil maintained the same for both zoom positions. In practice, the entrance pupil size varies and aberration balance between the front and rear groups is still necessary for sharp imaging. This balance is achieved by real ray tracing and optimization with computer software.

Group	Wide Angle			Telephoto		
	Front	Rear	Total	Front	Rear	Total
W_{040}	-0.017438	0.68148	0.664042	-0.0174	0.372954	0.355554
W_{131}	-0.978209	1.327662	0.349453	-1.020593	1.174717	0.154124
W_{222}	1.333673	0.422844	1.756517	0.069917	1.548848	1.618765
W_{220P}	-8.234249	8.418402	0.184153	-8.225243	8.409195	0.183952
W_{311}	143.42975	3.653452	147.083202	134.292114	7.697213	141.989327

Table 2.4. Zoom lens aberration coefficients in waves for a semi-field of 30 degrees

As mentioned before, fisheye lenses are constructed by inverted-telephoto structure thus are lack of symmetry about the aperture stop. This makes correcting lateral color challenging and requires special attention. Kumler and Bauer have shown that many fisheye lenses designed for 35-mm sensors have significant lateral color near the field edge, usually larger than 30 μm [30]. Since the distance between the zoom groups changes during the zoom, it is essential to achromatize each group independently. One method to control lateral color is by the use of achromatic doublets in both the front and rear group. Extra-low dispersion (ED) glass with large Abbe number also helps compensate the chromatic aberration. In this design, ED glass from the Schott glass catalogue (N-PK52A) was used.

Field curvature is difficult to be eliminate since Petzval curvature is purely a function of the lens power and its refractive index and is independent of stop position as other off-axis aberrations do. For example, in a Cooke triplet, the Petzcal radius can be about 2.4 times its focal length. The residual Petzval curvature, however, is balanced by some residual astigmatism to reduce the total field curvature aberration. Given the very large field of view of fisheye lenses, and the possible change of astigmatism upon zooming, then it is necessary to well correct Petzval curvature with zero or close to zero substantial residual to be balanced with astigmatism. Higher order field curvature also needs to be controlled, and one technique that is implemented into this design is the use of a conic surface in the front negative meniscus lens. Usually, such aspherical element is placed as close to the image sensor as possible and is known as the filed flattener. However, for SLR cameras, the use of field flattener is not allowed due to the minimum space clearance for the folding mirror. Thus, putting the aspherical surface in the most front element has the least impact to on-axis aberrations that heavily depend on marginal ray height, while efficiently

correct for off-axis aberrations. Field curvature aberration is also mitigated by the use of high index glass for the crown lenses and low index glass for the negative lenses.

The use of special glasses with very low dispersion is becoming popular for modern camera lens designs. Achromatic doublets made with such glasses can control lateral color effectively. However, these special glasses are usually much softer than normal crown glass and issues can arise due to manufacturability and durability. Also, these glasses cost much more than ordinary crown glasses. The size of the lens elements with special low dispersion glasses needs to be constrained to reduce cost. This can be done by putting such elements in the rear group close to the aperture stop. Another glass choice issue for fisheye lenses is the glass selection for the large negative meniscus lens in the front. Previous references suggest that regular crown glasses, such as BK7, should be used for the front element because of their low cost and low chromatic dispersion [31] [32]. However, the regular crown glasses are not the best glass choice today for modern fisheye lens design when lens size and weight are considered. Regular crown glasses have low index which reduce the lens power to bend the light and increases the diameter of the meniscus lens. From the layout of most photographic fisheye lenses, the front meniscus lens usually determines the maximum diameter of the entire lens and contributes significantly to the total lens weight. Using glasses with increasing index of refraction, such as flint glasses, for the front meniscus lens can result in a decreased diameter and weight at the expense of making lateral chromatic aberration harder to correct.

In this design, the aperture stop is located at the rear lens group. An aspheric surface is located close to the stop to effectively control spherical aberration. This aspherical surface is also used to control higher order coma W_{151} and oblique spherical aberration W_{240} as these aberrations also depend on the asphericity and can effectively be influenced. The Petzval radius of this design

is 1352 mm or more than 100 times the focal length, and as mentioned before, a conic surface is used in the front meniscus lens to control higher order Petzval field curvature.

2.4.4 Lens Optimization

For this project, Zemax OpticStudio was used to perform real ray tracing and lens optimization. The design philosophy and aberration control were explained in the last subsection. The error function first was defined with root mean square (RMS) optical path difference (OPD), and then with modulation transfer function (MTF) operands. Given the lens large field of view, 12 field positions were used during the lens optimization to properly sample the field. During the MTF optimization, the MTF verses field plot was used as an additional reference to adjust the weight of each field. Multiple configurations with different focal lengths were also used during the optimization to obtain even performance across the zoom range. Constrains on distortion aberration and to avoid physical lens interference were used. In addition, the chief ray angle (CRA) in image space was constrained to meet the maximum CRA requirement of digital sensor, which is no more than 30 degrees. This maximum image space CRA constraint must be followed throughout the entire zoom range since the relationship between FOV and CRA varies at different zoom positions. Fig 2.24 shows the plots of CRA versus HFOV in image space at different zoom positions. Furthermore, a constraint on image space CRA also benefits the relative illumination towards the edge of the image. Towards the end of the design stage, glass substitution was used with hammer optimization in Zemax OpticStudio to improve glass selection of the achromatic doublets.

2.4.5 Performance Evaluation

Optical performance of the zoom lens at 3 different zoom positions are evaluated in this subsection. The total aberration of the zoom lens was evaluated using wavefront OPD plots as shown in Fig 2.25. Plots of astigmatism, longitudinal aberration, distortion from equisolid angle projection, and lateral color were also used and are shown in Figs 2.26 – 2.29. Astigmatism and distortion are analyzed at 588nm wavelength (d-light). All evaluation in this section are analyzed at the maximum aperture setting for each zoom position.

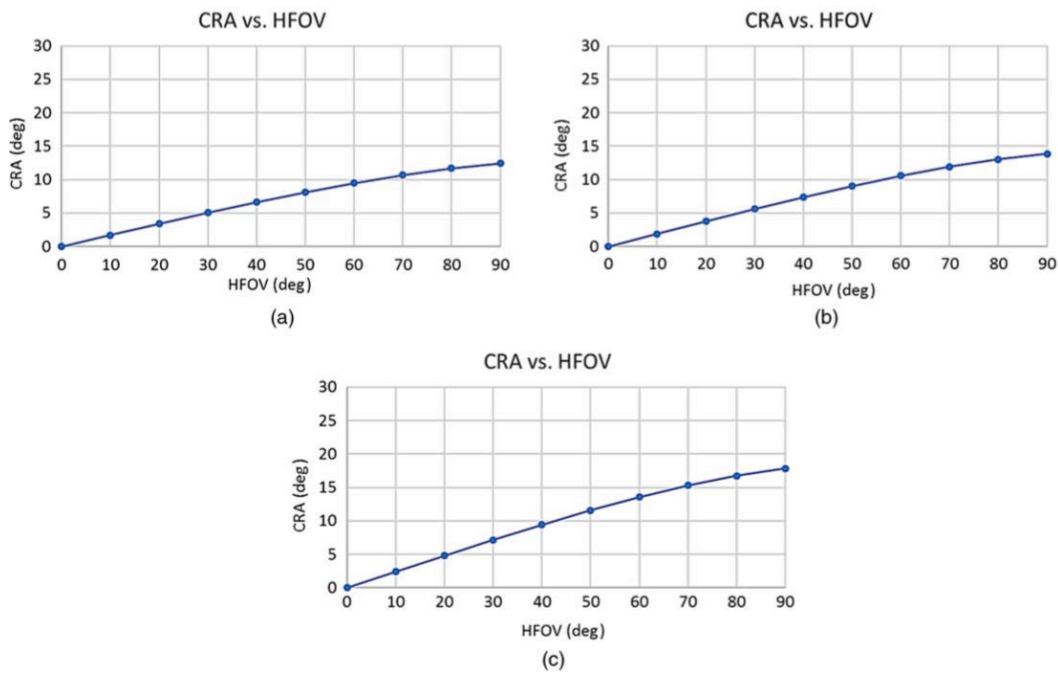


Figure 2.24. Image space CRA vs. HFOV at (a) wide-angle position, (b) intermediate zoom position, and (c) telephoto zoom position.

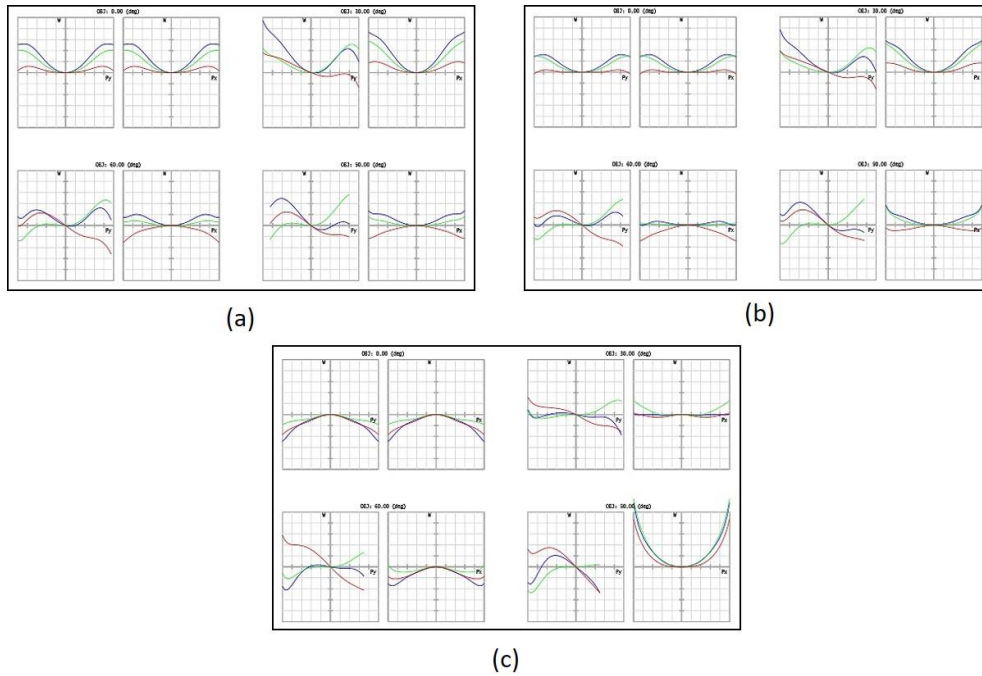


Figure 2.25. Optical path difference for 0 deg, 30 deg, 60 deg, and 90 deg half field at (a) wide angle zoom position, (b) intermediate zoom position, and (c) telephoto zoom position. Scale is ± 2 waves

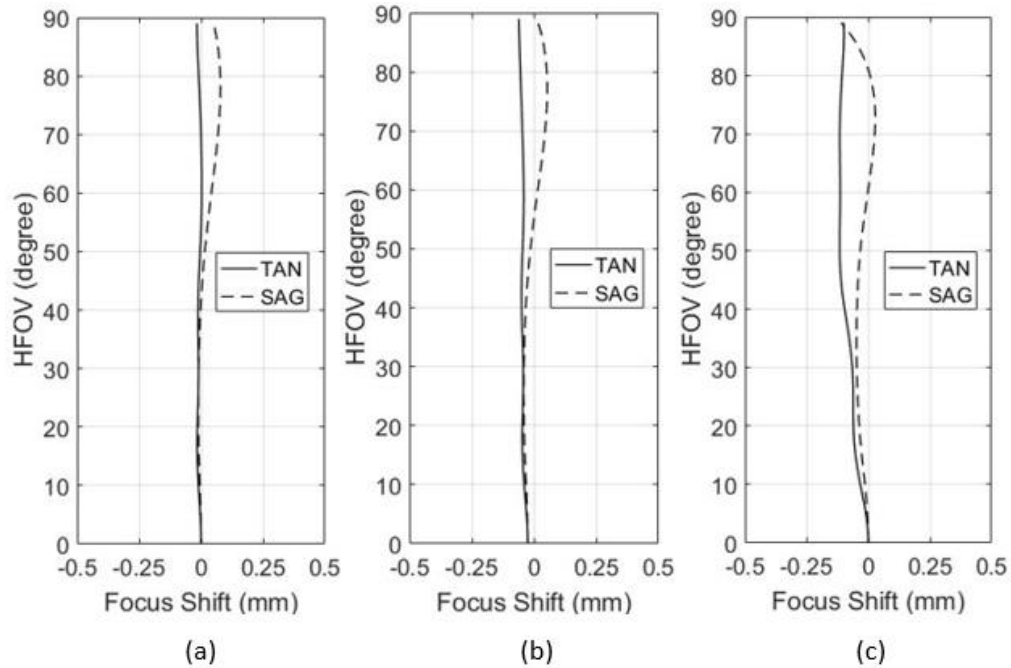


Figure 2.26. Astigmatic field curves at (a) wide angle zoom position, (b) intermediate zoom position, and (c) telephoto zoom position.

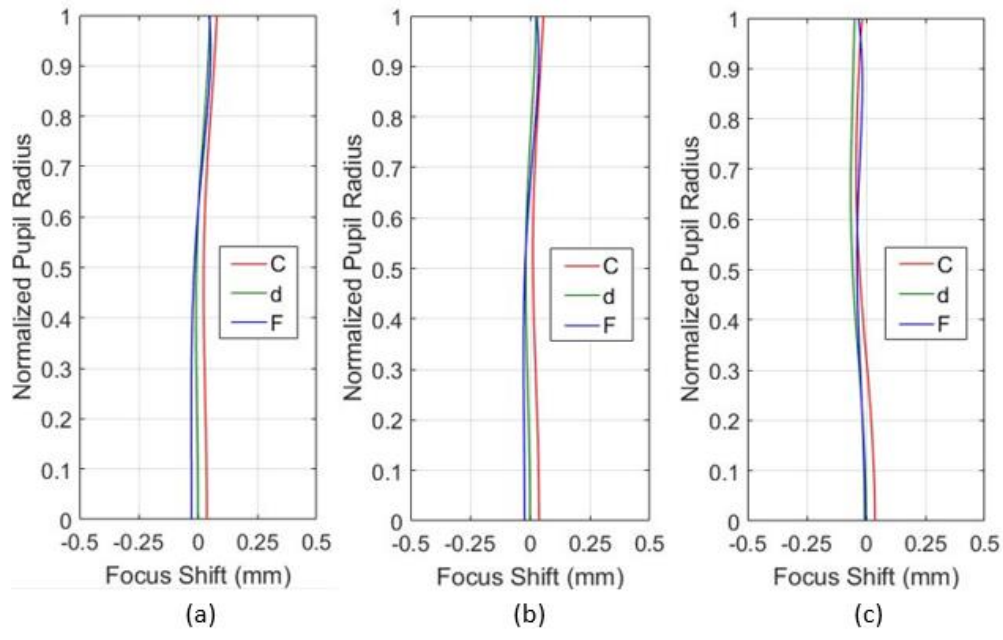


Figure 2.27. Longitudinal aberration at (a) wide angle zoom position, (b) intermediate zoom position, and (c) telephoto zoom position.

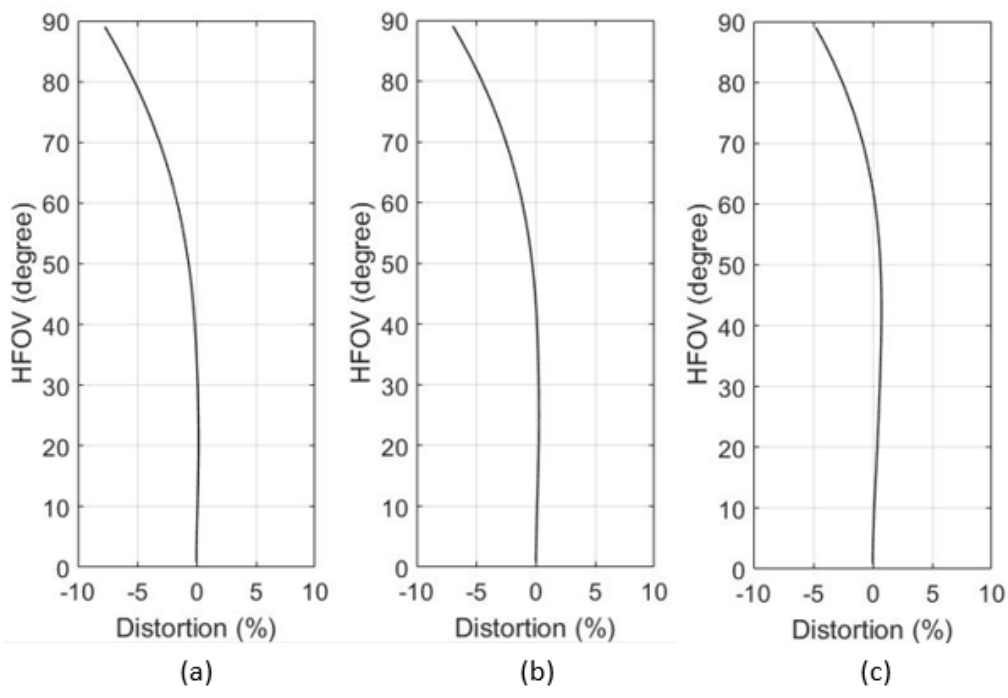


Figure 2.28. Longitudinal aberration at (a) wide angle zoom position, (b) intermediate zoom position, and (c) telephoto zoom position.

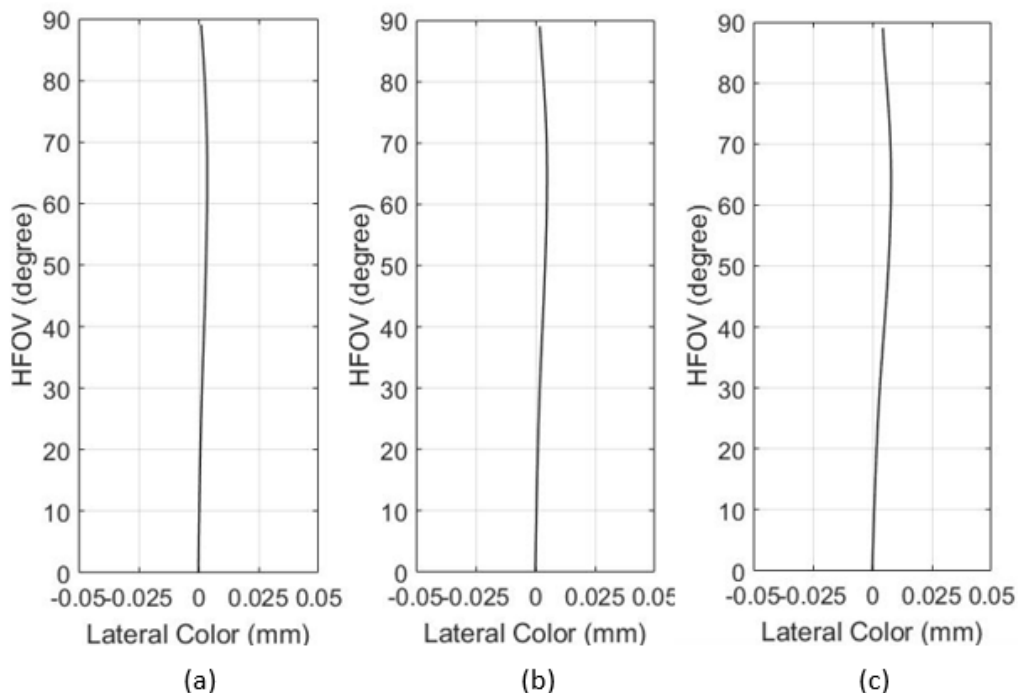


Figure 2.29. Lateral color at (a) wide angle zoom position, (b) intermediate zoom position, and (c) telephoto zoom position.

The peak to valley wavefront OPD deviations are mostly under two waves for all zoom positions. The lens shows better aberration control at the wide angle and intermediate zoom positions, where the focal lengths are smaller. At the telephoto zoom position, the image size is larger, and the aberration control becomes more difficult. Some vignetting is used to remove largely aberrated rays. The RMS wavefront error across the field is controlled under 0.5 waves at the wide angle and intermediate zoom positions and is under 1 wave at the telephoto zoom position.

Breaking down to individual aberrations, the lens has good field curvature and astigmatism performance at the wide angle and intermediate zoom positions. At the telephoto zoom position, astigmatism becomes more significant. Nevertheless, astigmatism and field curvature are balanced at the edge of the field during the optimization. So, the overall field curvature and astigmatism performance does not degrade significantly. The longitudinal aberration plot evaluates both

spherical aberration and axial color. The lens shows some spherochromatism, which is balanced with axial color aberration.

As mentioned before, the lens projection mapping of a photographic fisheye lens can be deviated from standard projection mapping for better image quality. However, the projection mapping is still maintained to some extent from equisolid angle projection. The distortion plot shows how much the lens projection is deviated from equisolid angle projection, which is maintained under 10% at the edge of the field. The lateral color performance of this lens is excellent. The lateral color plot is curved towards zero at the edge of the field, making the maximum lateral color smaller than 8 μm at the telephoto zoom position. At both the wide-angle zoom position and intermediate zoom position, the maximum lateral color is controlled under 5 μm , which is the size of a single pixel in many modern 35mm DSLR cameras.

Fig 2.30 shows MTF plots for the lens at all three zoom positions. 12 equal-area fields were used to analyze each zoom position. For photographic lenses, a different type of MTF plot is often used. This evaluates the contrast versus the field of view in image space at different spatial frequencies. This kind of MTF plot directly shows how contrast is varied from the center of the image towards the edge, and these data are often provided by photographic lens manufactures with their products. Spatial frequencies 10 and 30 lp/mm are typically used for this evaluation to cover the frequency range for normal photographic use. The MTF versus field plot is provided in Fig 2.31. Note that the field of view in image space is represented by the half image height.

At the telephoto zoom position, the contrast at high spatial frequency varies significantly over the field. The contrast is more uniform across the field at the wide-angle zoom position and at the intermediate zoom position. The MTF versus field plot gives a better understanding on how

contrast varies across the image. This lens has a consistent contrast across the field at the wide angle and intermediate zoom positions. However, at the telephoto zoom position, the contrast performance tends to degrade towards image edge. Practically, at this zoom position, only the image

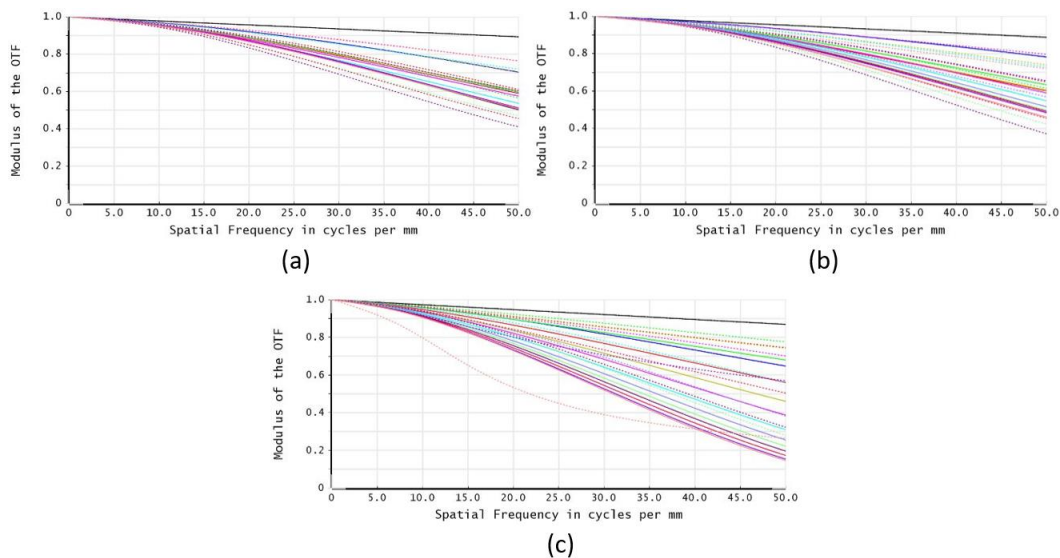


Figure 2.30. MTF versus spatial frequency at (a) wide angle zoom position, (b) intermediate zoom position, and (c) telephoto zoom position.

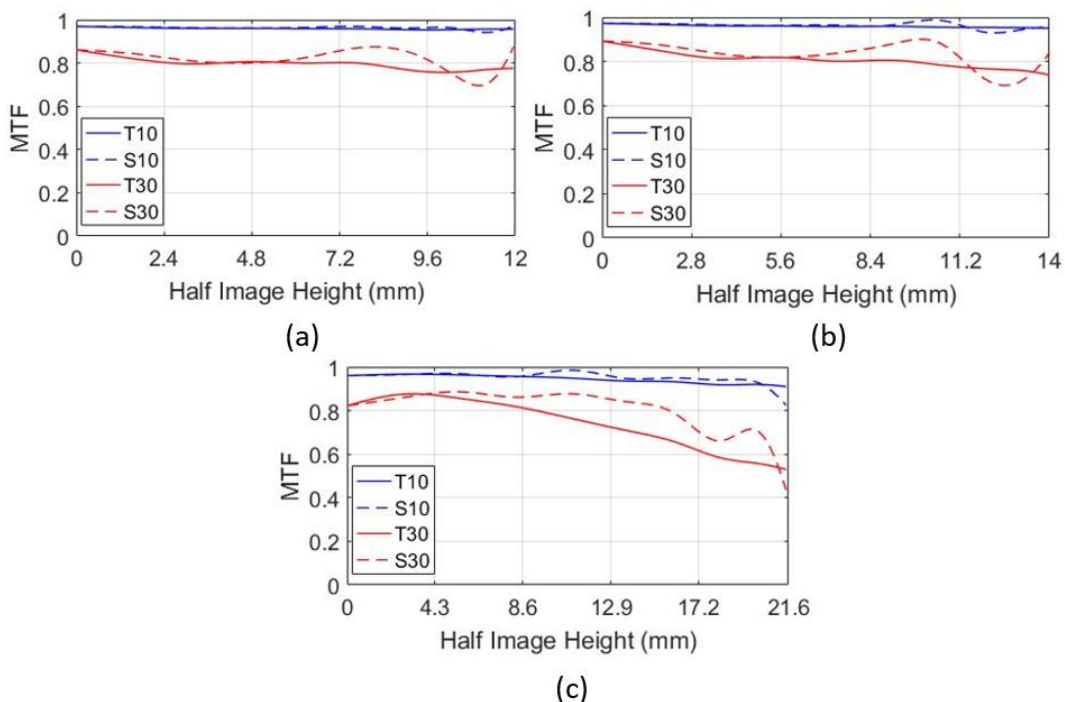


Figure 2.31. MTF versus field at (a) wide angle zoom position, (b) intermediate zoom position, and (c) telephoto zoom position.

diagonal achieves full 180-degree field of view, and most of the image portion at the large field is cut off by the rectangular shape of the sensor. Thus, some contrast performance at the edge of image circle is sacrificed during optimization to provide best contrast at the field center of the telephoto zoom position.

The relative illumination measures the illumination intensity level normalized to the maximum intensity across the field. It is highly dependent on image space chief ray angle, effective size of entrance/exit pupil, or equivalently on distortion aberration. The entrance pupil shape of this design and its angle dependence are presented in Fig 2.32. The total relative illumination is calculated by real ray tracing in Zemax OpticStudio and is based on the method that is described by Rimmer [33]. Such relative illumination plot is provided in Fig 2.33. Vignetting of the system is set to help reducing off-axis aberration while maintaining at least 50% of the relative illumination at the field edge.

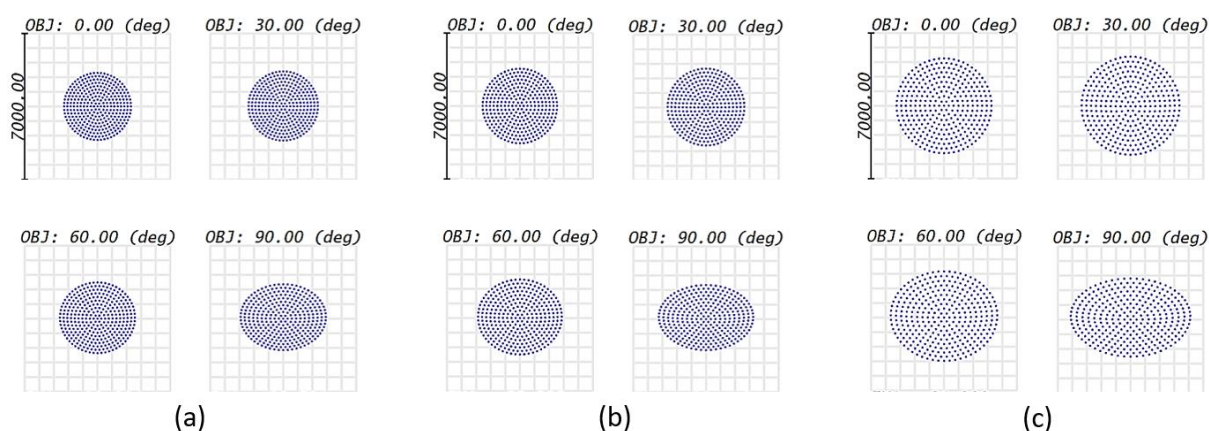


Figure 2.32. Entrance pupil shape at its maximum at (a) wide angle zoom position, (b) intermediate zoom position, and (c) telephoto zoom position.

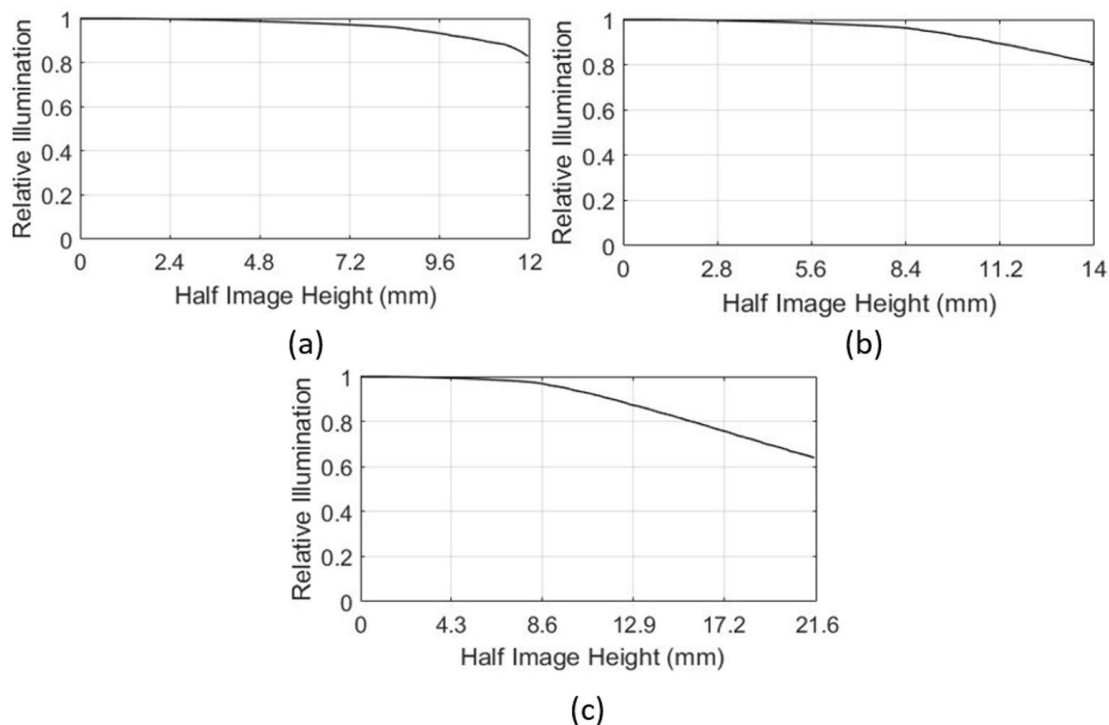


Figure 2.33. Relative illumination at (a) wide angle zoom position, (b) intermediate zoom position, and (c) telephoto zoom position.

2.4.6 Tolerance Analysis

During the manufacturing and assembling stage, tilt and decenter of surfaces and lens elements usually have the greatest effect on final lens performance. For the tolerance analysis, the effect of an element and surface decenter of $10\ \mu\text{m}$, and a tilt of 1 arc min were evaluated. The lens is axially symmetric, so only decenters along Y-axis and tilts about X-axis were evaluated for simplicity. 12 fields in both X and Y direction were used to sample the field of view. The estimated RMS wavefront changes based upon the root-sum-square method at each zoom position were calculated using Zemax OpticStudio and are summarized in Fig 2.34, Which shows the nominal RMS wavefront error in dark color and its estimated change in light color.

The sensitivity results show that the surface and element decenter impact most of the RMS wavefront lens performance. However, as two surfaces make a lens and are coupled, the element

decenter has less impact than the surface decenter. The impact from tilt and decenter is uniform across the zoom range. This sensitivity analysis provides a first estimate about how tilts and decenters would affect the RMS wavefront performance and provides a first useful estimate about the order of tolerances needed during manufacturing and assembly.

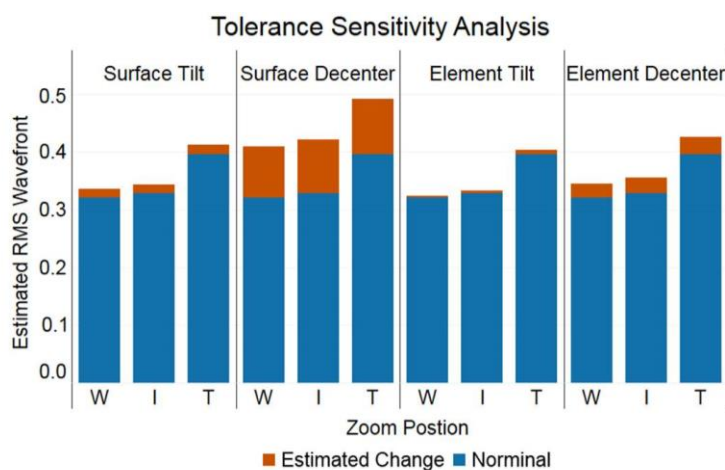


Figure 2.34. Effect of 1-arc min surface/element tilt, and 10- μ m surface/element decenter, at all three critical zoom positions, based upon the root-sum-square method

2.5 Conclusion

In this chapter, the author discussed the photographic fisheye lens design for 35mm DSLR in detail. This research is a continuous study from author's master's thesis, and a compact, large aperture zoom fisheye lens is presented with design approach and aberration control.

Fisheye imaging has been developed for over 100 years. It was originally designed for meteorological observation but is later become popular for creative photography. Section 1 gave an introduction of photographic fisheye lens and a brief discussion on the history of fisheye lens. Many useful design patterns, including the negative meniscus lens in the very front, and the use of achromatic doublets on both side of the stop are discovered during the development of fisheye lens and has been carried over to today's modern fisheye lens design. Some of the techniques used for

the development of fisheye lens also benefits other non-fisheye photographic lenses today, such as the use of aspherical surfaces. Recently, the development of zoom fisheye lens for photography is trending, with both Canon and Nikon issued their zoom fisheye lenses for 35mm DSLR cameras. The topic of zoom fisheye lens was covered in section 2.4.

Section 2 discussed different projection methods of fisheye lenses. Tangential and sagittal magnification across FOV of the four standard projection methods for fisheye lenses, including equidistant projection, orthographic projection, stereographic projection and equisolid angle projection, are derived mathematically. Among the four standard fisheye projections, stereographic projection produces least amount of barrel distortion towards the edge of FOV, while orthographic projection produces the most distortion and thus its full FOV is limited at 180 degrees. Equidistance projection and the equisolid angle projection produce similar intermediate amount of distortion. By analyzing the modern photographic fisheye lenses, the author also pointed out that projection for photographic fisheye lenses usually allows departure from standard projection method to some extent in exchange of better optical performance.

Special properties and design issues of a photographic fisheye lens were discussed in section 3. Fisheye lenses have large depth of field due to their short focal lengths from the largely distorted projection mapping, which make fisheye lenses being suitable for landscaping photography. Also, benefiting from large image distortion and pupil coma, fisheye lenses usually have better relative illumination performance compare to conventional lenses, with a possibility to exceed over 100% relative illumination at the image edge. Due to the mechanical constrain of a DSLR camera, sufficient BFDs are required for fisheye lenses. This constraint makes fisheye lens design challenging since the focal length of a typical fisheye lens is much shorter than the BFD requirement. Also, stray light analysis for fisheye lenses is also difficult due to the pupil shifting.

In section 4, the author discussed his philosophy behind the design of a zoom fisheye lens. Currently, zoom fisheye lens are rare on the market, and the existing lenses have relatively small apertures and contain many lens elements. The author presented a design with a large aperture of $F/2.8 - F/3.5$, with less lens element and good optical performance. A new approach to look at the aberration control of a two group zoom lens was also presented. Previously, aberrations were assumed to be balanced at different zoom settings for two group zoom lenses. However, by treating the front group as a virtual object and analyze the 3rd order aberration coefficients upon object shift, the author realized that invariance of 3rd order aberration between different zoom setting is possible under certain conditions. The aberration control challenges were also discussed in this chapter and the performance of the final zoom fisheye lens design was also presented and evaluated, with a short discussion on the tolerance analysis.

Overall, this chapter provides a comprehensive discussion on fisheye lens design. The references on fisheye lens design is lacking compare to other lens design topics, so this chapter can serve as a good reference for future scholars working on the topic of fisheye lens design. Also, some of the topics, such as the explanation of pupil aberration in section 2.3 and the discussion on aberration invariance for two group zoom lens in section 2.4 applies to lens design in general rather than just fisheye lenses.

3 Miniature Camera Lens Design with a Freeform Surface

Miniature camera lenses are widely used today and became one of the primary features on mobile platform electronics applications, such as cell phones and tablets. Lens designs for these miniature cameras have been rapidly developed in the past decade. Due to its extreme convenience and superior image quality, the development of miniature cameras significantly impacts the conventional digital camera market. According to CIPA (a statistical research joined by multiple major digital camera vendors such as Olympus, Canon and Nikon [34]), the global shipments of digital still cameras drops 84% [Fig 3.1] [35] since the year 2010 to 2018. As the award-winning photographer Chase Jarvis used to say, “the best camera is the one that’s with you” [36]. Today, more people choose to use miniature cameras that are integrated on their portable devices for photography instead of using conventional digital still cameras.

Although these miniature cameras in mobile devices are becoming ubiquitous in our daily lives, better optical performance is always demanded. However, improving optical performance for miniature cameras is always challenging. For example, to achieve good optical performance,

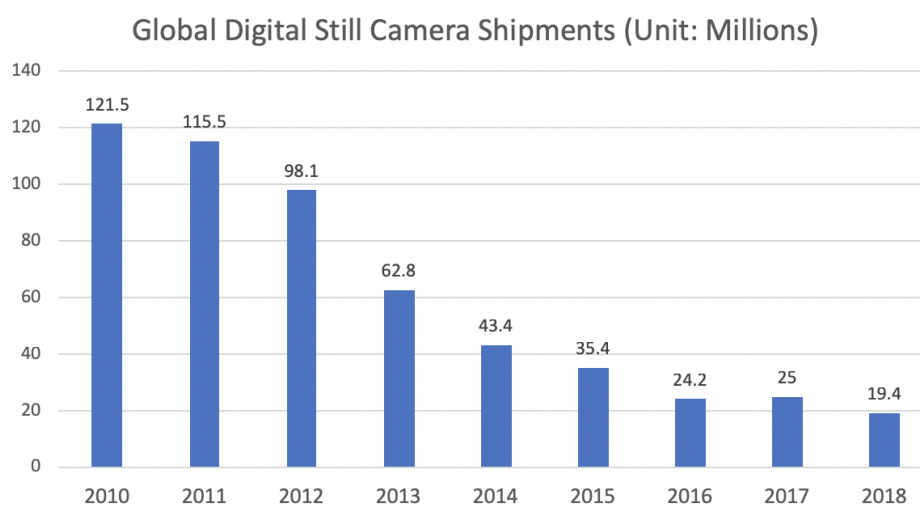


Figure 3.1. Global digital still camera shipments in pieces from 2010 to 2018

aspherical surfaces are extensively used during the miniature lens design, usually employing up to 16th order terms. Some latest designs contain aspherical surfaces even up to 20th order. The extensive use of aspherical surfaces creates issues on lens tolerancing, which leads to low yield. Maintaining high yield is important during the miniature camera lens design due to its large quantities. Over 1 billion smart phones are shipped each year [37]. To improve the lens yield, optical performance is usually compromised during the tolerance desensitization stage. Currently, the performance of the miniature camera lenses designed with conventional aspherical surfaces is approaching a limit. While lens designers are still pushing the limits of their designs with conventional even aspherical surfaces, a more efficient surface description is desirable for improvement. A paper published in 2016 [38] introduced a freeform surface that combines base surfaces of the pedal curve to the ellipse for light illumination control. Our study shows that this type of freeform surface can also benefit the miniature camera lens design. In this chapter, we discuss the benefits of using such pedal curve and its freeform combination for miniature camera lens optimization. Section 1 briefly explains some design challenges of miniature camera lenses. Section 2 discusses the form of pedal curve to the ellipse and its freeform combination. In section 3, a patented lens is optimized with both even aspheric surfaces and the pedal curve polynomial, and the performance comparison and tolerance analysis are provided. In section 4, another patented lens is optimized using Q-type polynomial surfaces along with the conventional even asphere, and the pedal polynomial surface. Then tolerance sensitivity and polynomial coefficient number are compared. In addition, the pedal surfaces from the freeform lens is replaced back to even aspherical surfaces to make a ‘reversed even asphere lens’ and then its performance is evaluated. In the end, section 5 concludes our studies on this freeform surface. The studies present in this chapter are

published as “Miniature camera lens design with a freeform surface” [39], and some of the materials are reused in this dissertation.

3.1 Design Challenges of a Miniature Camera Lens

When designing miniature camera lenses, lens designers are facing great challenges compare to designing conventional large-scaler camera lenses. The typical FOV of a primary camera lens on a portable device is about 70 to 75 degrees, with the focal length around 4 mm, and a maximum aperture around F/1.8. Fig 3.2 shows the comparison between a conventional camera lens designed by Nikon [40] and a miniature camera lens designed by Apple [41] with similar FOV and F/#. The detailed specs of these 2 lenses are shown in Table 3.1. Both designs are relatively up to date, with the Nikon patent filed in 2014 and the Apple patent filed in 2016. From Fig 3.2, it is clear that the design approaches and lens constructions are significantly different between a miniature camera lens and a conventional camera lens. Duo to the sensor size difference, the focal length of this miniature camera lens is about one-seventh of the focal length of the conventional camera lens with the same FOV and F/#. However, if the conventional camera lens was simply scaled down to the same focal length of the miniature lens, it would encounter many issues. The most severe issue is the limiting package size. Typically, the total track length (TTL) of a miniature camera today is around 5 mm to 6 mm in order to fit in the portable electronic devices. However, if the Nikon 28 mm lens was simply scaled down to the same focal length with the Apple 4 mm lens, its TTL would still be more than 3 times of the Apple lens and it would not be able to fit inside a modern portable electronic device such as cellphones and tablets. As mentioned in Chapter 2, wide-angle lenses for conventional cameras usually have an inverted telephoto structure with high telephoto ratio (ratio of TTL to focal length). To reduce the telephoto ratio and fit a wide-

angle lens in a much smaller package requires significant change in lens structure, which creates several challenges for the lens designers.

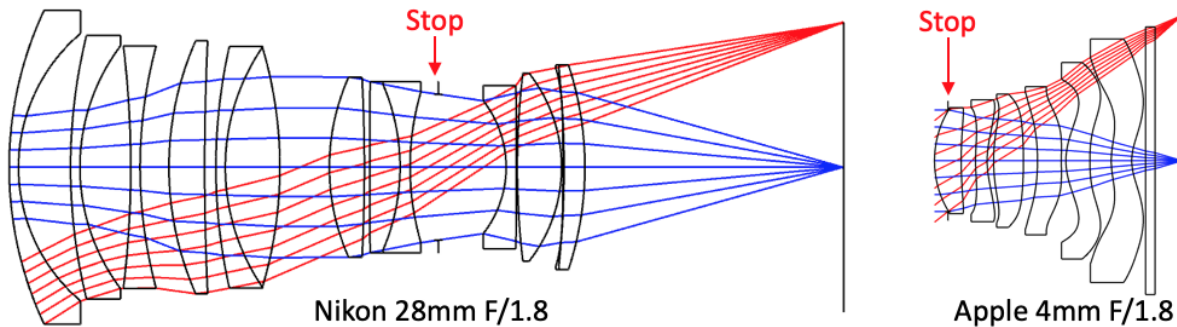


Figure 3.2. Layout comparison between the Nikon 28mm conventional camera lens and Apple 4mm miniature camera lens

	Nikon	Apple	Nikon Scaled
Focal Length	28.8 mm	4.0 mm	4.0 mm
F/#	F/1.8	F/1.8	F/1.8
FOV	75°	76°	75°
TTL	124.35 mm	5.45 mm	17.27 mm
Telephoto Ratio	4.32	1.36	4.32
Image Space CRA	17.4°	32.7°	17.4°
Elements Number	13	6	13
Materials Number	12	2	12
Aspherical Surface Number	1 surface, up to 8 th order	12 surfaces, up to 20 th order	1 surface, up to 8 th order

Table 3.1. Lens data for the Nikon lens, Apple lens and Nikon lens scaled to same focal length with the Apple lens

The first required design change is the stop position, which is showed in Fig 3.2. As mentioned in Chapter 2, the CMOS sensor used in a digital camera has a maximum allowed image space chief ray angle (CRA) to minimize color crosstalk [Fig 3.3]. To minimize image space CRA while significantly reducing the telephoto ration requires putting the aperture stop in the very front of the lens. It is shown in Table 3.1 that even the stop is positioned in the Apple miniature lens,

the image space CRA is still almost twice of the Nikon conventional lens due to its extremely small telephoto ratio. Such high image space CRA causes rapid drop of relative illumination towards the edge of image that requires digital compensation to the final image [Fig 3.4]. The low edge illumination also means using vignetting for off-axis aberration control like conventional camera lens design is almost impossible since this method further reduces the edge illumination. Putting the stop in the very front also means the miniature lens structure would completely lost symmetry. Maintain lens structure symmetry to some extent helps control third order coma, distortion, lateral color and any high order aberration that can be cancelled by flipping the sign of chief ray height. Without symmetry and the use of vignetting, correcting off-axis aberration for a miniature lens would be more challenging.

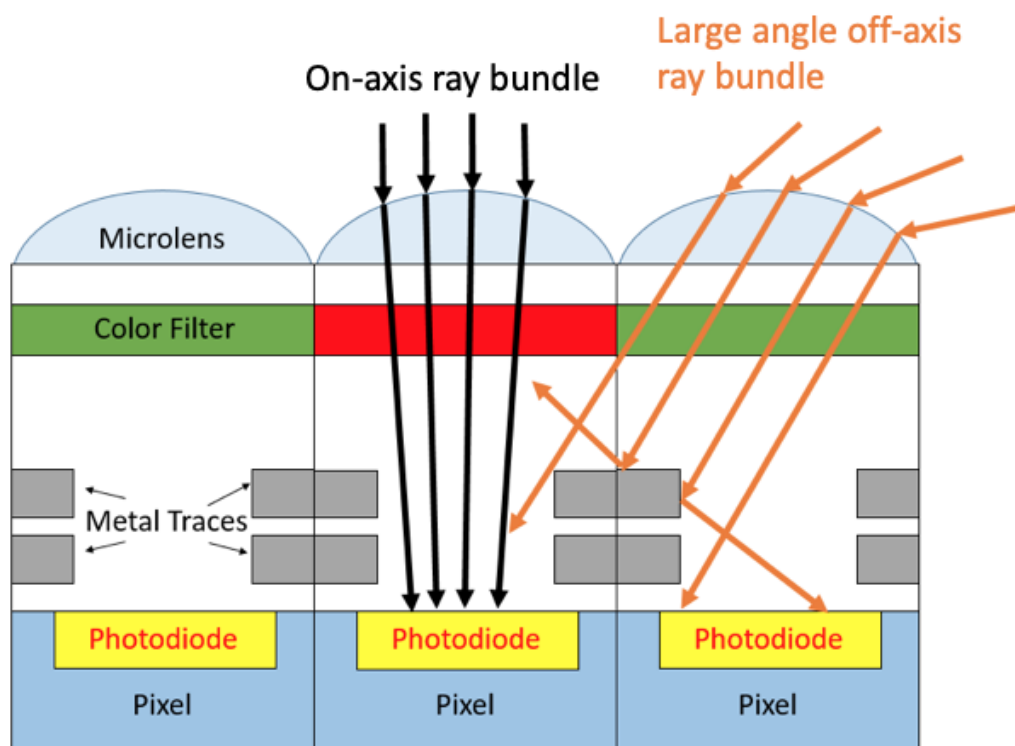


Figure 3.3. Sideview of a typical CMOS sensor, large angle off-axis ray bundle may cause light leakage into the neighboring pixels and results in color crosstalk

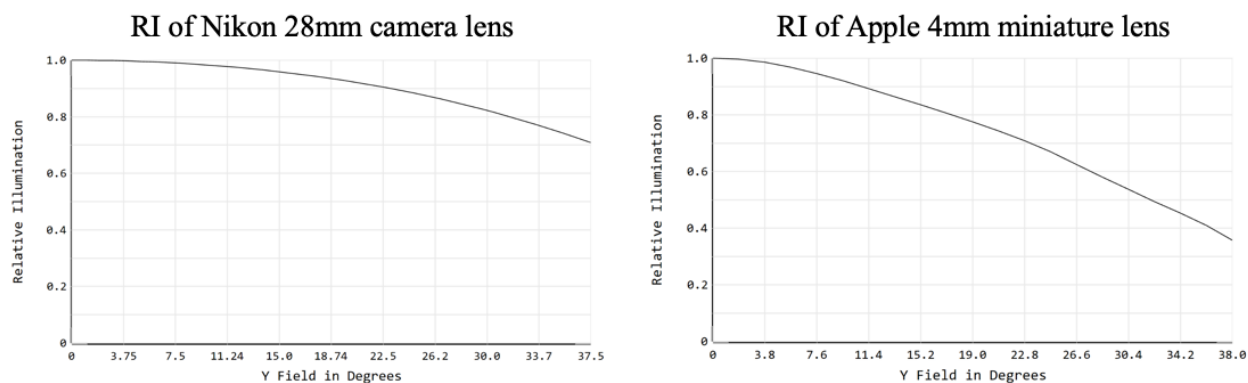


Figure 3.4. Comparison of relative illumination between Nikon 28mm camera lens and Apple 4mm miniature lens

Moving the stop to the front is not the only stumbling block for aberration control of a miniature lens. Due to the extremely short TTL, much fewer lens elements can be used on a miniature camera lens compare to a conventional camera lens. A typical miniature lens on the market has 5 elements. However, with the market demand of lower F/#, higher image quality and larger FOV, 6-element designs and even 7-element designs are appearing. On the other hand, conventional camera lenses usually have much less constraint on the element number. For example, the Nikon lens presented in Fig 3.2 and Table 3.1 has 13 lens elements, while the Apple lens only has 6. With more lenses, power can be split up to reduce aberrations, especially for 3rd order spherical aberrations. Reducing the element numbers would increase the power of an individual lens element, which further challenges the aberration control. Also, less lens element means less degree of freedom can be utilized for optimization. Thus, miniature lenses use aspherical surface extensively to provide enough degrees of freedom for aberration control. Finally, another key difference between designing a conventional camera lens and a miniature camera lens is the lens material. To design a conventional camera lens, lens designers can choose materials from massive materials catalogs from multiple vendors with a large range of refractive index and dispersion properties. Abundant selection of glass materials improves the optical performance, especially for the control of chromatic aberration. Achromatic doublets and ED glasses with very ultra-low

dispersion can effectively correct chromatic aberrations in the system. Special designed achromatic doublets, also known as “new achromatic doublets”, can benefit with the correction of field curvature as well [42]. For miniature lenses, injection molding is typically used to manufacture the small-scale lens elements with high order aspherical surfaces. In order to maintain the cost, plastics or optical polymers are usually used for injection molding. However, selections of plastic materials are very limited with no ultra-low dispersion option. For example, only 2 different materials (besides the IR filter) were used in the Apple lens design presented in Fig 3.2. The limited choice of lens materials and the lack of ultra-low dispersion plastics make correcting chromatic aberration difficult. In addition, plastic doublets are difficult to manufacture, this further challenges the correction of chromatic aberration and field curvature. Also, even though the extensive use of aspherical surfaces helps with some aberration control, it has no effect on chromatic aberrations either.

Besides the design challenges, miniature lenses at small scales also creates problems during manufacture. The most obvious impact is the tolerance budget. Scaling down a conventional camera lens requires spatial tolerances to scale down with the same ratio, which is about the factor of 7. This creates a huge problem on the tolerance budget of element and surface decenter. Usually a decenter tolerance within couple microns is required for miniature camera lenses. This requires very precise lens molding and system assembly. Angular tolerances such as lens tilt does not scale with the lens, but small defects on mechanical mounts will have a larger effect on tilt.

With the market pressure to make thinner electronic devices and add more cameras per device, the package size constrain gets tighter. However, better optical performance, smaller F/# and larger FOV are also favored by customers, which requires more lens elements to be used. The conflict between these two requirements are really challenging to optical designers. Newer

technologies are in development. For example, CMOS vendors are pushing the limit of their maximum acceptable of CRA by adding micro lenses on the sensor and reduce the distance between color filter and photodiode to reduce color cross talk. Also, lenses with less sensitivity to tolerance are desired by designers to increase manufacture yield. In this chapter, a new type of freeform surface is presented to reduce tolerance sensitivity of a miniature camera lens.

3.2 Aspherical and Freeform Surfaces

In miniature camera lens design, the rear group usually contains one or two elements that are strongly aspheric to efficiently correct field curvature, astigmatism and distortion. The shape of these lenses, however, cannot be easily explained by conventional aberration theory, as the aspheres become dominate at large field angles [25]. The shape of these surfaces is also rarely appeared in conventional camera lenses. Nevertheless, by reviewing current patents with 5 elements and 6 elements, one can realize that these strongly aspherical elements often contain surfaces with different curvature direction from the center of the surface to the edge (e.g., concave in the center and turning back to convex before the edge). Table 3.2 shows some example of such surfaces from various miniature camera lens patents.

Multiple different polynomials can be used to represent the sag of an aspherical surfaces. Among these polynomials, even aspherical polynomial and Q-type polynomial are the two typical ones used by lens designers for axial symmetric systems, like the miniature camera lens. Besides these typical polynomials, other polynomials may be more suitable for miniature camera design. In this chapter, conventional even aspherical polynomial and Q-type polynomial are explained. And a new polynomial defined based on pedal curve of ellipse is presented and its sag equation is derived

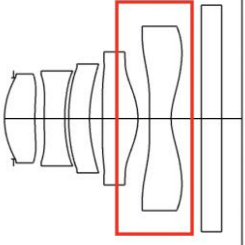
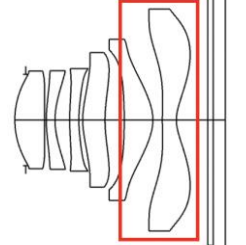
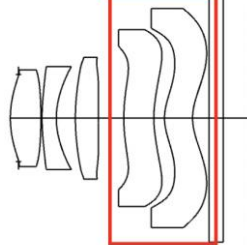
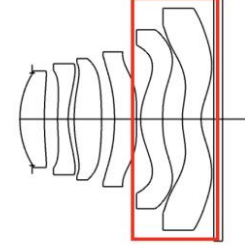
US 8,605,367 [43]	US 8,786,961 [44]	US 9,110,270 [45]	US 2017/0299845
			

Table 3.2. Some example patent lenses with strongly aspherical rear elements.

3.2.1 Conventional Aspherical Surfaces

The sag $z_{asp}(r)$ of a conventional even aspherical surface is

$$z_{asp}(r) = \frac{cr^2}{1 + \sqrt{1 - (1+k)c^2r^2}} + A_2r^2 + A_4r^4 + A_6r^6 + A_8r^8 \dots \quad (3.1)$$

where c is the vertex curvature of the surface, k is the conic constant, r is the radial distance from the optical axis, and aspherical coefficients are denoted as A_2 , A_4 , A_6 and A_8 . This well-known polynomial is the most common polynomial to describe an aspherical surface and is used in most of the lens design patents. However, lens designers also experience a few difficulties using even aspherical polynomial to fit the surface sag. These difficulties are mainly due to the problematic basis choice of even aspherical polynomial. The basis of even aspherical polynomial is not orthogonal, so a close fitting to the desired surface sag requires heavy cancellation between different orders of the polynomial. This makes the coefficient value very inefficient, and the accuracy of the fitting depend heavily on the number of digits. Small error on the coefficient thus significantly impacts the overall fitting. Since the final fitted sag is a result of heavy cancellation of different order aspherical terms, setting tolerances directly on the coefficients has very little meaning. During the process of lens design, since the polynomial basis are not orthogonal,

optimization is also inefficient since all the terms are required to vary when correcting higher order aberration.

To reduce the impact of these problems, an alternate polynomial called the Q-type polynomial was introduced in 2007 by G.W.Forbes [46]. In his paper, he introduced two different set of orthogonal aspherical basis, namely Q_m^{con} and Q_m^{bfs} for strong aspherical surfaces and mild aspherical surfaces respectively. For strong aspherical surfaces, the sag $z_{con}(r)$ is defined by

$$z_{con}(r) = \frac{cr^2}{1 + \sqrt{1 - (1+k)c^2r^2}} + D_{con}(u) \quad (3.2)$$

with

$$u := r/r_{max} \quad (3.3)$$

where r_{max} is the aperture size of the fitted surface. The sag is fitted by two parts. The first part defines the best fitting conic, which is same as the even aspherical polynomial. The second part defines the departure from the best fitting conic, and is a function of the normalized variable u . It is defined by

$$D_{con}(u) := u^4 \sum_{m=0}^M a_m Q_m^{con}(u^2) \quad (3.4)$$

where a_m is the aspherical coefficient. $Q_m^{con}(x)$ are the basis elements of the polynomial, and are chosen to be a particular case of the Jacobi polynomials [47] written as

$$Q_m^{con}(x) := P_m^{(0,4)}(2x - 1) \quad (3.5)$$

The chosen basis terms are not perfectly orthogonal in sag departure but is nearly so. Almost orthogonal basis terms significantly reduce the cancellation of different polynomial terms during the sag fitting, thus makes these basis terms more efficient than traditional even aspherical terms.

The second Q-type polynomial for mild aspheres is taking the considerations related to both fabrication and testing by limiting the transverse slop of the deviation between the surface and its best-fit sphere. Instead of making the sag departure orthogonal, the second Q-type polynomial has aspherical terms that are orthogonal in slop. Thus, this polynomial chooses the best fit sphere instead of best fit conic as the first term, then use the rest of the terms to describe the sag departure from its best fit sphere. The best-fitting sphere is chosen to coincident with the target surface at its axial point and around its perimeter. If the sag of the target surface at its perimeter is written as $z'(r_{\max})$, then the complete sag fitting equation is expressed as

$$z_{bfs}(r) = \frac{c_{bfs}r^2}{1 + \sqrt{1 - c_{bfs}^2r^2}} + D_{bfs}(u) \quad (3.6)$$

Where the curvature of the best-fit sphere c_{bfs} is defined by

$$c_{bfs} = \frac{2z'(r_{\max})}{r_{\max}^2 + z'(r_{\max})^2} \quad (3.7)$$

and the sag departure from the best-fit sphere $D_{bfs}(u)$ is defined by

$$D_{bfs}(u) := \frac{u^2(1 - u^2)}{\sqrt{1 - c_{bfs}^2r_{\max}^2u^2}} \sum_{m=0}^M a_m Q_m^{bfs}(u^2) \quad (3.8)$$

This departure is set up in a way to not impact on the best-fitting sphere as $D_{bfs}(u)$ is vanishing at the surface center ($u = 0$) and surface edge ($u = 1$). The aspherical terms $Q_m^{bfs}(x)$ are configured

so the weighted RMS slope of the departure along the normal is the sum of the squares of aspherical coefficients a_m . Then, the elements of the normal-departure slope are written as

$$\mathbf{S}_m(\mathbf{u}) := \frac{d}{d\mathbf{u}} \left\{ \mathbf{u}^2 (1 - \mathbf{u}^2) Q_m^{bfs}(\mathbf{u}^2) \right\} \quad (3.9)$$

and the final aspherical terms $Q_m^{bfs}(x)$ are chosen to make the normal-departure slope $\mathbf{S}_m(\mathbf{u})$ orthogonal by fulfilling the following condition

$$\langle \mathbf{S}_m(\mathbf{u}) \mathbf{S}_n(\mathbf{u}) \rangle = \delta_{mn} \quad (3.10)$$

Both of the Q-type are based on orthogonal basis terms, with the key difference on whether the sag departure is orthogonal, or the slope is orthogonal. However, in the end of his paper, Forbs stated that the second Q-type polynomial with terms $Q_m^{bfs}(x)$ retains most of the advantages of the first Q-type polynomial with terms $Q_m^{con}(x)$ while also facilitating the design of milder aspheres.

According to Forbs, Q-type polynomials have better representations of a sag fitting with the orthogonal basis terms. However, there are still some debate on which polynomial yield the best fit practically. As Forbs proved that Q-type polynomials yields better fit when a desired surface shape is known, during the actual optimization where global minimum is unknown and lens designers are settling into a local minimum, which aspherical polynomial produces the best fit depends on the specific applications [48]. A new polynomial that is more suitable for miniature lens designs is presented in the following section.

3.2.2 Freeform Surface based on Pedal Curve to the Ellipse

Recall figures from Table 3.2, different miniature cameras from various patents all includes 2 to 3 strong aspherical rear elements. These elements often contain surfaces with different curvature direction from the center of the surface to the edge. Currently these surfaces are

described by either conventional even aspherical polynomial or Q-type polynomial, which are superpositions of many aspherical terms with different coefficients. However, it is noted that this kind of surface profile can also be described by the pedal curve to the ellipse. The equation for the pedal curve to the ellipse on the x-y plane in a Cartesian coordinate system is

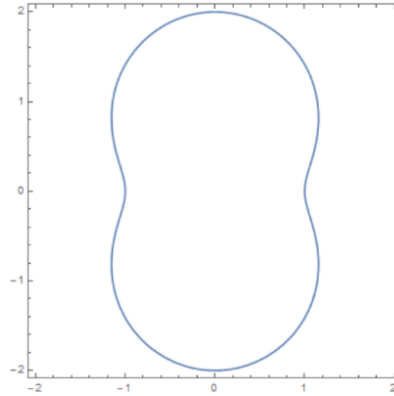


Figure 3.5. An example pedal curve to the ellipse, $a = 2$, $b = 1$

$$a^2 x^2 + b^2 y^2 = (x^2 + y^2)^2 \quad (3.11)$$

where a is the major axis of the ellipse, b is the minor axis, and r is the radial distance from the optical axis. Fig 3.5 shows an example pedal curve to the ellipse, note the similarity between this pedal curve and surface shapes of rear lens elements showed in Fig 3.2.

To use the pedal curve to construct an aspherical lens surface, the sag $z_{pedal}(r)$ needs to be derived from Eq. 3.11. Assume a random elliptical-like curve on the x-y plane in a Cartesian coordinate that is showed in Fig 3.6. The curve is symmetry about both x-axis and y-axis. The sag

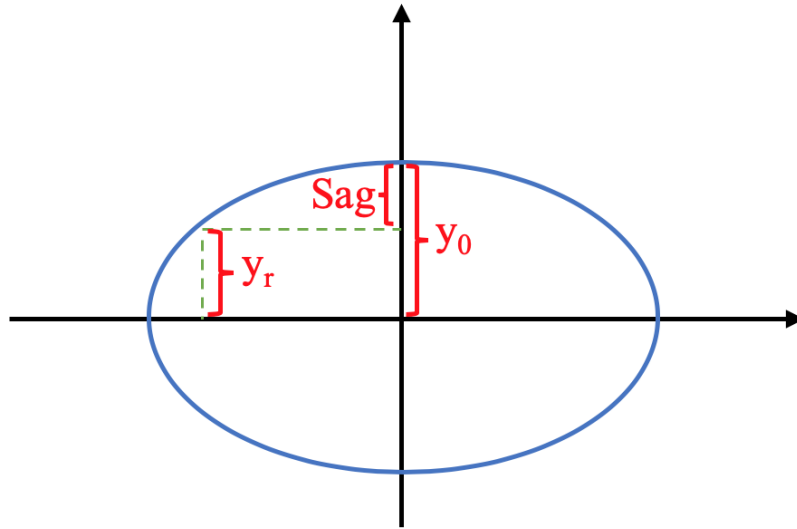


Figure 3.6. An elliptical-like curve on the x-y plane for sag equation derivation

of interest is defined along y-axis above x-axis. y_0 is the distance between the curve and x-axis at $x = 0$. y_r is the distance between the curve and x-axis at $x = r$. Then the sag $z(r) = y_0 - y_r$. If the elliptical-like curve is defined by Eq. 3.11, then y_0 is equal to the minor axis b . To calculate y_r , we start from the following relationship by substitute x in Eq. 3.11 with radial distance r :

$$a^2 r^2 + b^2 y_r^2 = (r^2 + y_r^2)^2 \quad (3.12)$$

Then, let $y_r^2 = m$

$$a^2 r^2 + b^2 m = (r^2 + m)^2$$

$$a^2 r^2 + b^2 m = r^4 + 2r^2 m + m^2$$

$$m^2 + (2r^2 - b^2)m + r^4 - a^2 r^2 = 0 \quad (3.13)$$

Solve for m , then

$$m = \frac{b^2 - 2r^2 \pm \sqrt{(2r^2 - b^2)^2 - 4(r^4 - a^2 r^2)}}{2}$$

$$m = \frac{b^2 - 2r^2 \pm \sqrt{b^4 + 4(a^2 - b^2)r^2}}{2} \quad (3.14)$$

Since $y_r^2 = m$, and y_r is a real number, the only real solution is

$$m = \frac{b^2 - 2r^2 + \sqrt{b^4 + 4(a^2 - b^2)r^2}}{2} \quad (3.15)$$

and the corresponding y_r above the x-axis is

$$y_r = \sqrt{\frac{b^2 - 2r^2 + \sqrt{b^4 + 4(a^2 - b^2)r^2}}{2}} \quad (3.16)$$

Thus, the sag $z_{pedal}(r)$ is

$$\begin{aligned} z_{pedal}(r) &= y_0 - y_r \\ &= b - \sqrt{\frac{b^2 - 2r^2 + \sqrt{b^4 + 4(a^2 - b^2)r^2}}{2}} \end{aligned} \quad (3.17)$$

Eq. 3.17 shows the sag of an aspherical surface based on a pedal curve to the ellipse. A freeform polynomial surface can then be written as a superposition of several pedal surfaces

$$\begin{aligned} z_{freeform}(r) &= A_1 z_{pedal1}(r) + A_2 z_{pedal1}^2(r) + A_3 z_{pedal1}^3(r) \\ &\quad + B_1 z_{pedal2}(r) + B_2 z_{pedal2}^2(r) + B_3 z_{pedal2}^3(r) \\ &\quad + \dots \end{aligned} \quad (3.18)$$

where $z_{pedal1}(r)$ and $z_{pedal2}(r)$ are different sets of pedal surfaces, $A_1 - A_3$ and $B_1 - B_3$ are coefficients. More sets of pedal surfaces or coefficients can be implant into the polynomial if needed.

This type of surface showed some benefits in a previous paper when used as LED encapsulation lens to provide better illumination uniformity [38]. However, it has never been used on an image system before. The similarity between the shape of a pedal surface and aspherical surfaces of the rear element of a miniature lens, and shallower surface slop towards the edge make

this type of surface a potentially better choice for miniature lens design. The performance of this surface is discussed in the following sections.

3.3 First Lens Comparison

In this section, a same patented miniature lens is constructed using both conventional even aspherical surface described in Eq. 3.1 and the freeform surface based on pedal curve to the ellipse described in Eq. 3.18. The nominal optical performance and tolerance sensitivity are then compared between the benchmark lens and the evaluation lens. The starting point for the benchmark lens design is from the first embodiment in U.S. Patent 9,110,270. The patent lens contains five lens elements with an IR-cut filter in front of the image sensor. The lens is re-optimized into our benchmark lens using only conventional even aspherical surfaces with the design specifications provided in Table 3.3. The number of aspheric coefficients for each surface remains the same in the patent specification. This optimization is not intended to change the patent lens construction or improve the performance but rather to fix the errors in the lens patent data. The evaluation lens, on the other hand, uses the pedal polynomial freeform surfaces to replace surface 7, 8, 9 and 10 in the rear lens group. The front group (with surface 1 – 6) are still even aspherical surfaces since their surface profiles do not align with the shape of pedal surface. The evaluation lens design uses the same specification as the benchmark lens, and the same merit function were used during the optimization to ensure an un-biased comparison. The detailed lens data for both lenses are showed in Appendix A.

Wavelength	f [mm]	F/#	FOV (deg)	TTL [mm]	Distortion	CRA (deg)	Edge RI
g, F, d, C	4.1	2.2	69.8	<5.2	<0.5%	<30	>50%

Table 3.3. Design specification of the first benchmark lens and evaluation lens

3.3.1 Nominal Performance Comparison

The layouts and the optical path difference (OPD) referenced to the chief ray of benchmark lens and evaluation lens are shown in Fig 3.7 and Fig 3.8 with maximum scale of ± 1 wave. The structural difference between these two lenses are minimal. On the performance side, the evaluation lens with the freeform surface provides a smoother OPD plot across the pupil and has overall better aberration control. In addition, the evaluation lens has a more consistent aberration control across its field of view, this can also be observed in the MTF plots in Fig 3.9. The MTF of the evaluation lens shows a more uniform contrast performance across the field of view. For example, at 200 lp/mm frequency, while the on-axis contrasts of both lenses do not differ much from each other, the evaluation lens shows better contrast at the maximum field of view compare to the benchmark lens.

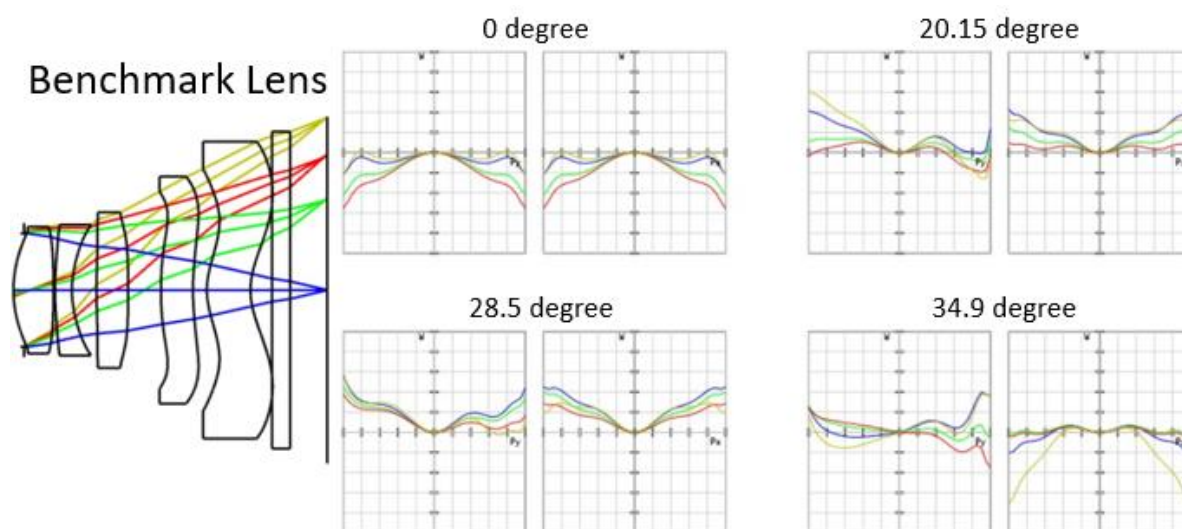


Figure 3.7. Layout and OPD plots of the benchmark lens. The maximum scales of OPD plots are ± 1 wave

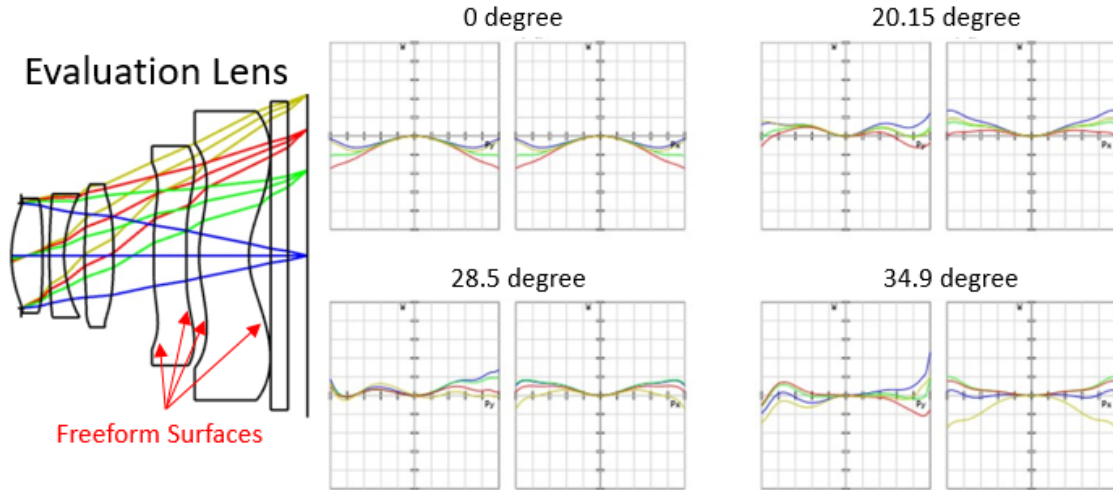


Figure 3.8. Layout and OPD plots of the evaluation lens. The maximum scales of OPD plots are ± 1 wave

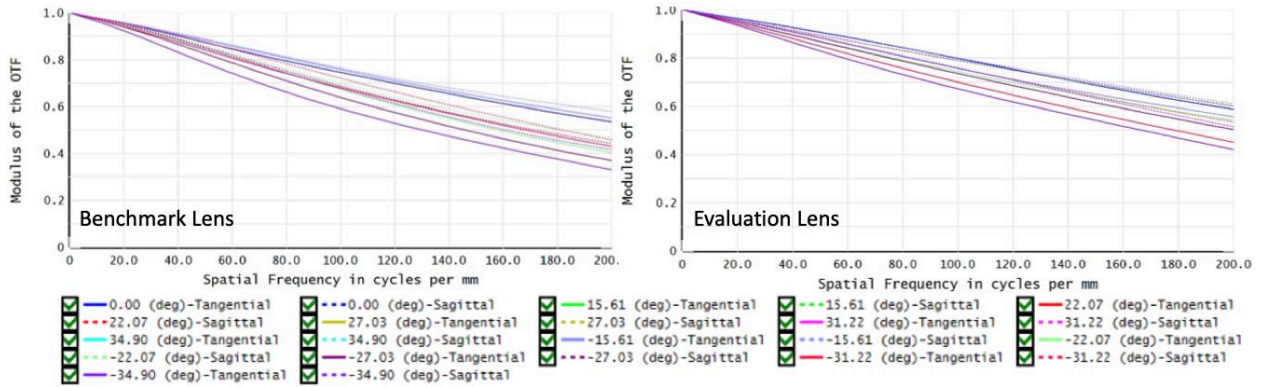


Figure 3.9. Nominal MTF plots of benchmark lens (left) and evaluation lens (right)

3.3.2 Tolerance Sensitivity

Tolerancing errors, such as decenter and tilt during manufacturing and assembly, are the most challenging problem for lens designers when designing miniature lenses. As mentioned in section 3.1, decenter of both surface level and element level has significant impact on the final performance due to the tighter tolerance budget that scales down with the lens package size. Furthermore, high order aspherical surfaces are usually more sensitive to decenter as a single surface or as a part of a lens element. Thus, tolerance desensitization, especially on surface and element decenter, is critical during the miniature camera design. Since tolerance desensitization

usually results in a down grade of nominal lens performance, a less sensitive design before desensitization is always desired.

In this section, the surface and element decenter sensitivities on the rear lens elements for both benchmark lens and evaluation lens are tested. MTF plot is used for evaluation since it directly reflects the optical contrast. Incident fields of view are set up along Y direction. Since the direction of surface and element decenter impacts the image contrast differently, the field of view is sampled in both the positive Y direction and the negative Y direction in a single MTF plot to sufficiently analyze the impact of decenter. The target surfaces and elements are first shifted 5 μm in Y direction for both lenses. The resulted MTF plots are presented in Fig 3.10 – 3.15.

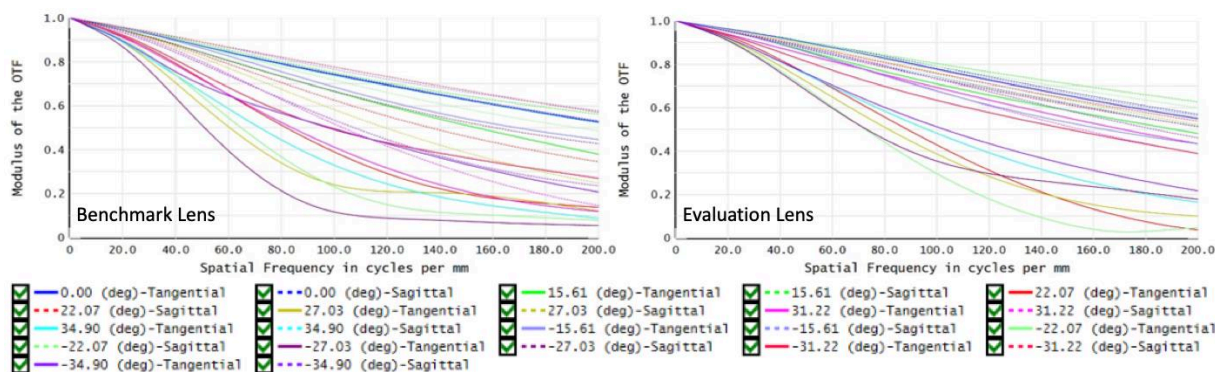


Figure 3.10. MTF plots of benchmark lens (left) and evaluation lens (right) under 5 μm decenter of surface 7 in Y direction

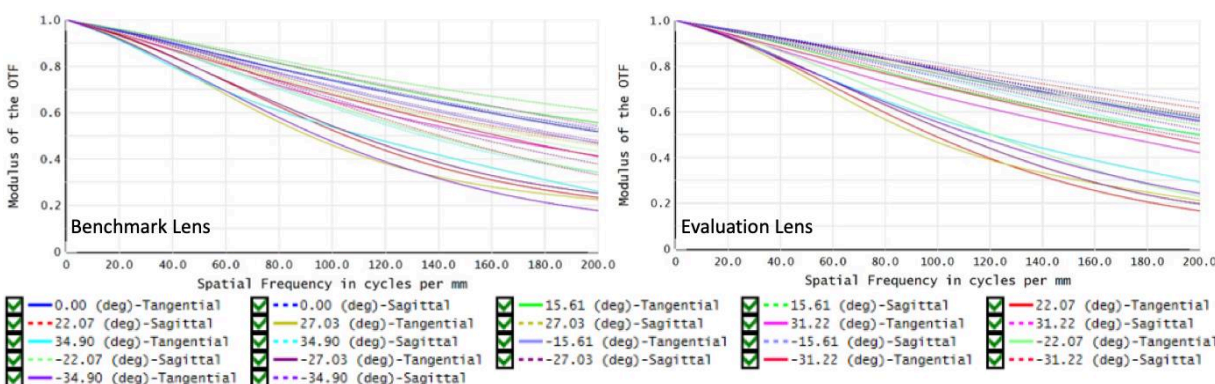


Figure 3.11. MTF plots of benchmark lens (left) and evaluation lens (right) under 5 μm decenter of surface 8 in Y direction

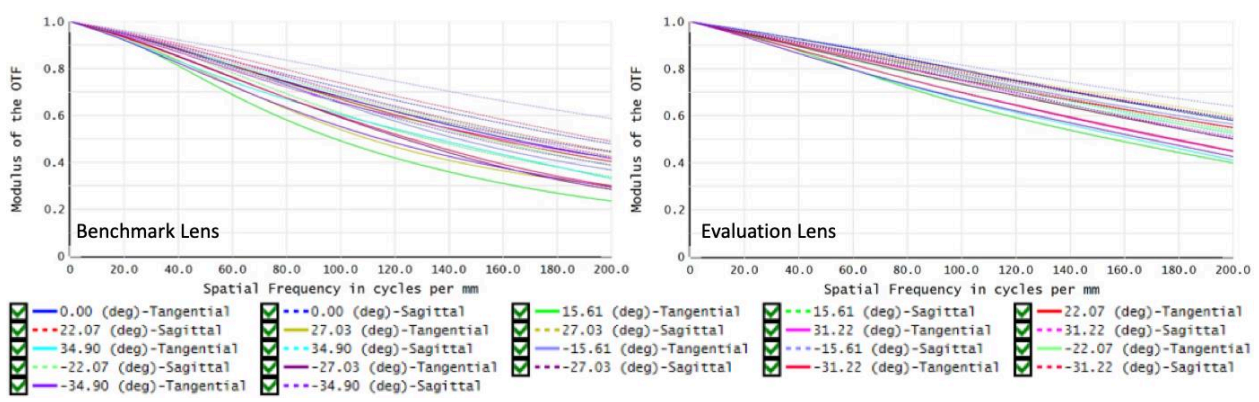


Figure 3.12. MTF plots of benchmark lens (left) and evaluation lens (right) under 5 μm decenter of surface 9 in Y direction

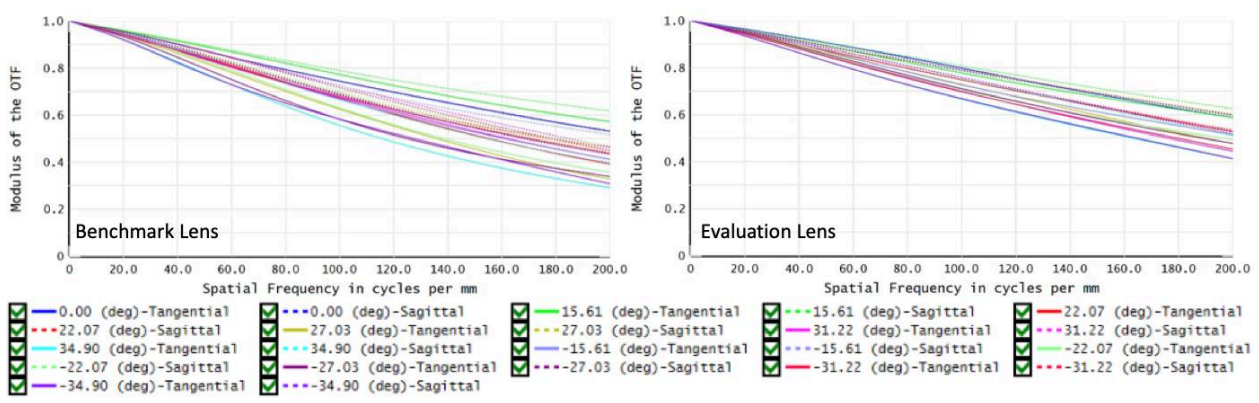


Figure 3.13. MTF plots of benchmark lens (left) and evaluation lens (right) under 5 μm decenter of surface 10 in Y direction

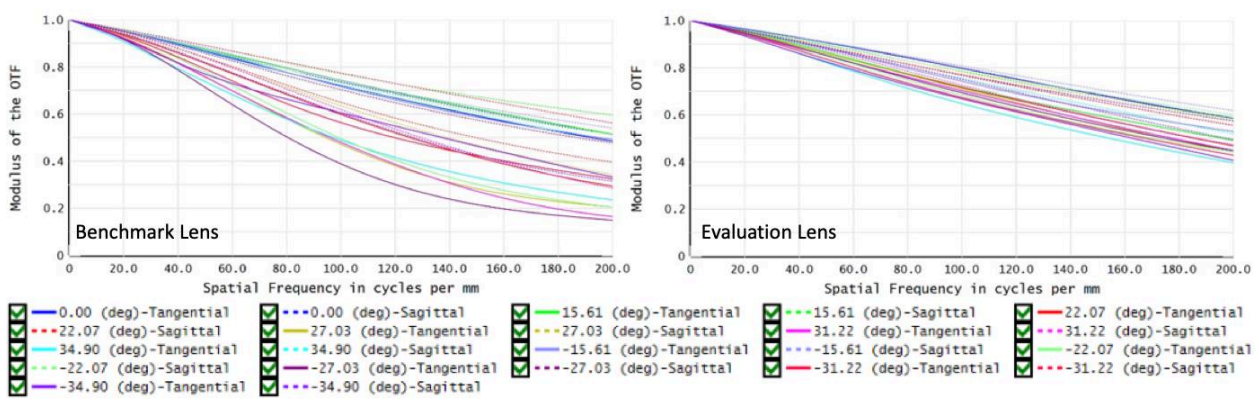


Figure 3.14. MTF plots of benchmark lens (left) and evaluation lens (right) under 5 μm decenter of element 4 in Y direction

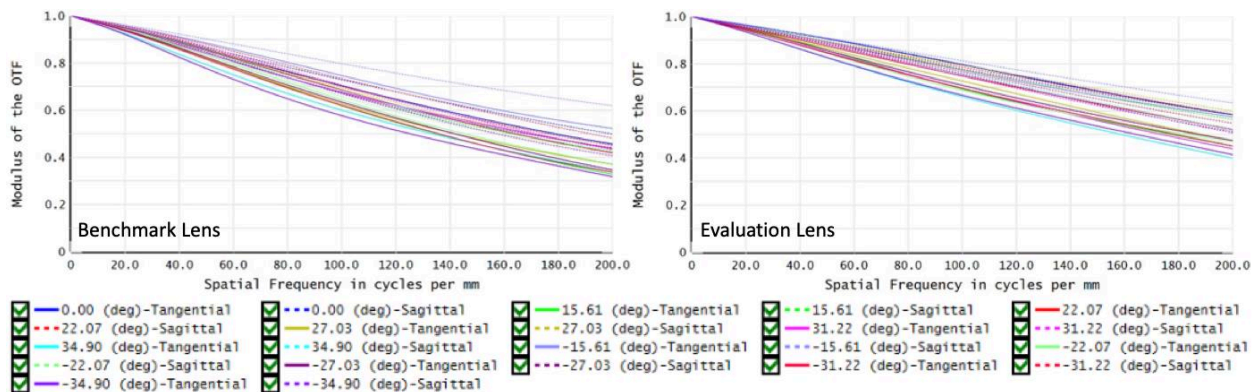


Figure 3.15. MTF plots of benchmark lens (left) and evaluation lens (right) under 5 μm decenter of element 5 in Y direction

Then, each surface and element are also shifted 5 μm in X direction to analyze the impact on image quality when the surface or element is decentered in the orthogonal direction of the incident fields. And the results are showed in Fig 3.16 – 3.21.

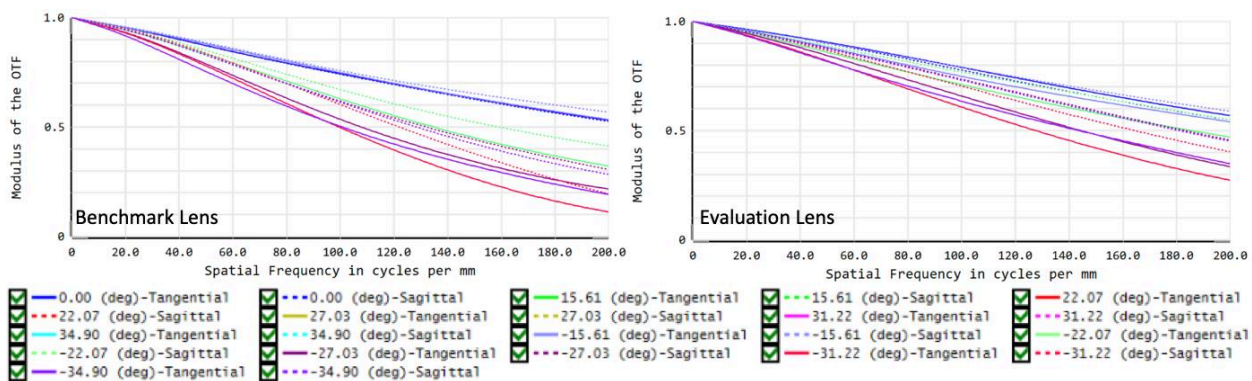


Figure 3.16. MTF plots of benchmark lens (left) and evaluation lens (right) under 5 μm decenter of surface 7 in X direction

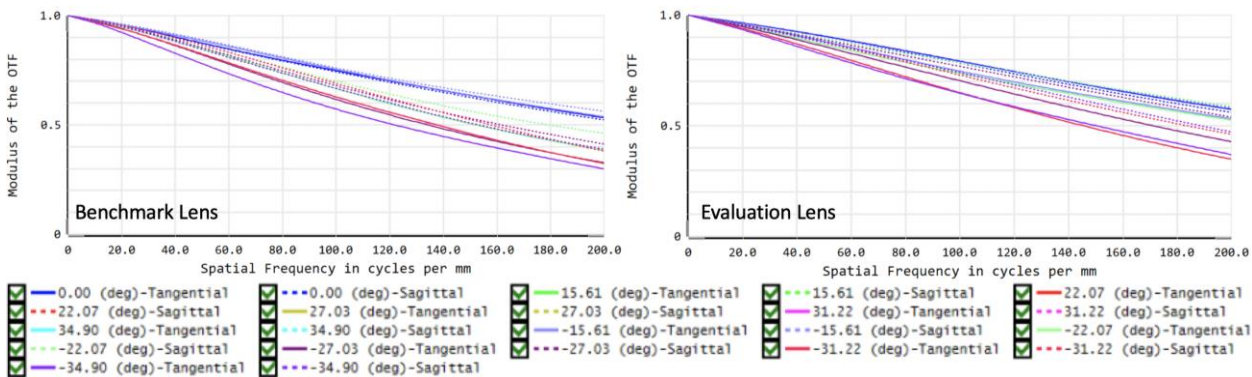


Figure 3.17. MTF plots of benchmark lens (left) and evaluation lens (right) under 5 μm decenter of surface 8 in X direction

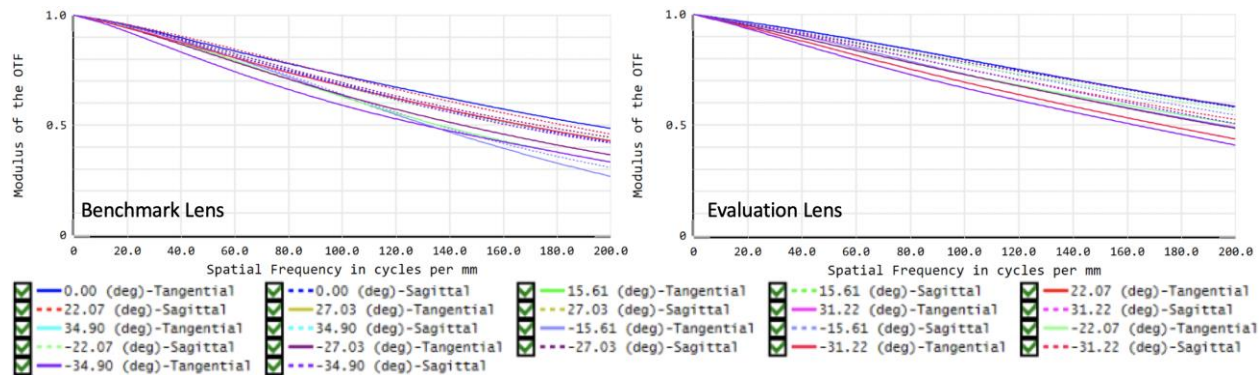


Figure 3.18. MTF plots of benchmark lens (left) and evaluation lens (right) under 5 μm decenter of surface 9 in X direction

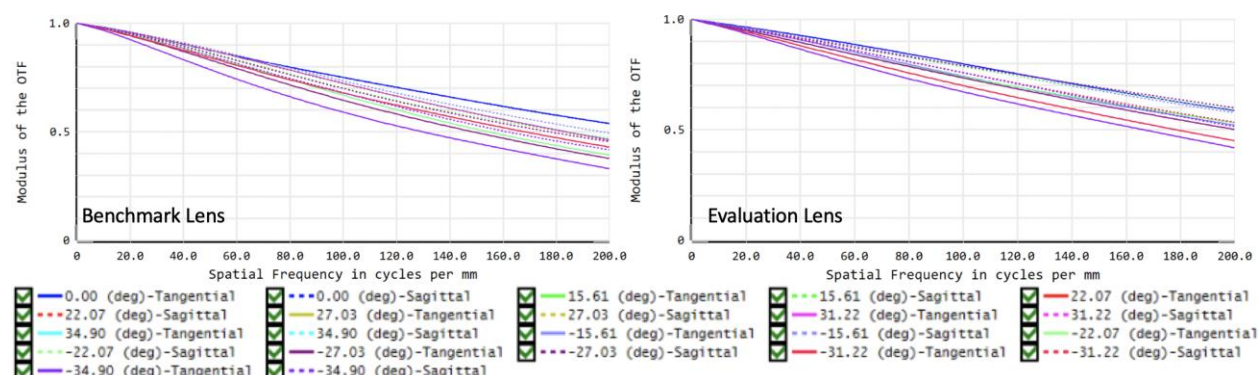


Figure 3.19. MTF plots of benchmark lens (left) and evaluation lens (right) under 5 μm decenter of surface 10 in X direction

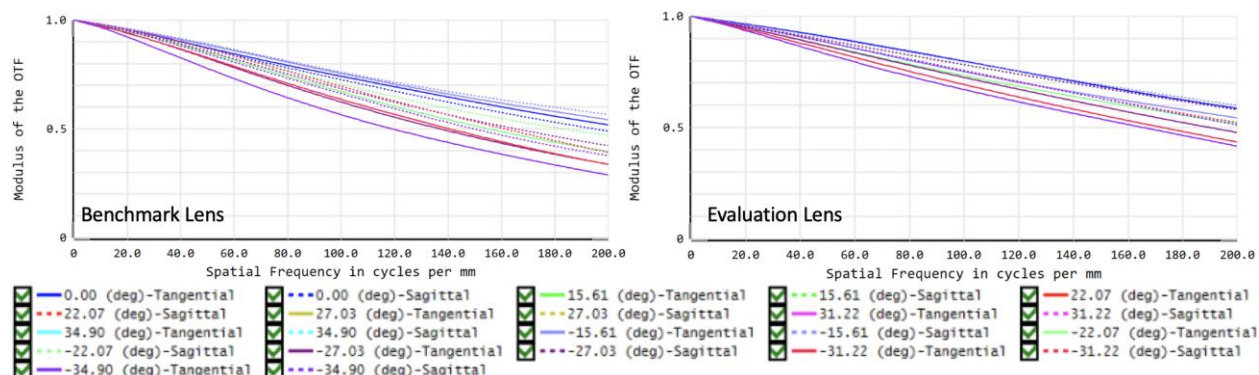


Figure 3.20. MTF plots of benchmark lens (left) and evaluation lens (right) under 5 μm decenter of element 4 in X direction

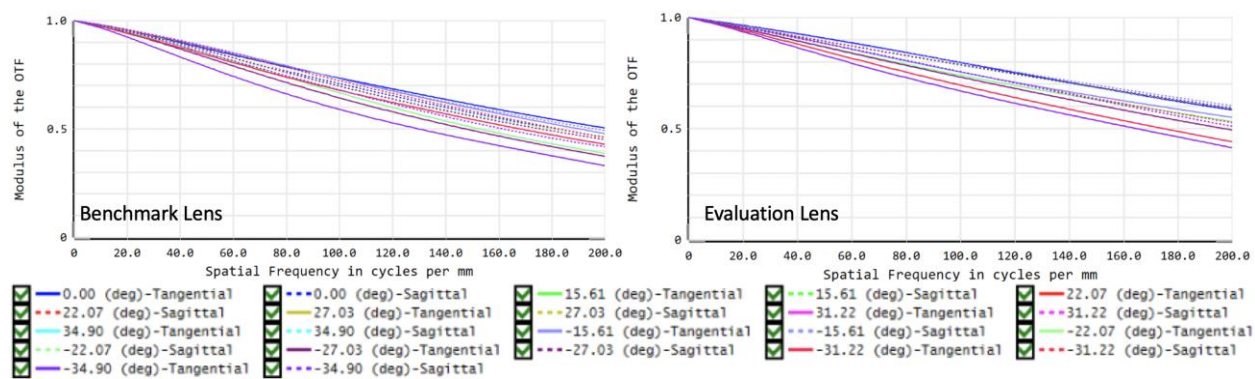


Figure 3.21. MTF plots of benchmark lens (left) and evaluation lens (right) under 5 μ m decenter of element 5 in X direction

From the MTF plots, both the benchmark lens and evaluation lens suffer more from surface/element decenter in the direction of sampled incident fields (Y direction). For decenter in orthogonal direction of sampled fields (X direction), only small impact to contrast can be observed except when surface 7 (the most sensitive surface) is decentered. However, The MTF plots for surface/element decenter in Y direction show that the benchmark lens suffers more from surface decenter than the evaluation lens. This difference behavior comes from surfaces 7, 9 and 10. Surface 8 on both lenses is equally sensitive. Also, decenter of 4th lens element has a significant impact on the benchmark lens, while the 5th lens element has a similar impact on both lenses. Overall, the evaluation lens with the freeform surfaces has less decenter tolerance sensitivity than the benchmark lens.

3.4 Second Lens Comparison

In this section, a second set of lenses from a different patent file is constructed to verify the result from the first lens comparison. The starting point for the second benchmark lens is from U.S. Patent 8,605,367. we re-optimized the patent lens with conventional even aspherical surfaces to fix minor errors in the patent data and keep our comparison un-biased. An evaluation lens is also re-optimized by replacing the rear group elements (surfaces 7, 8, 9 and 10) with pedal freeform

surfaces. In addition, we set up another benchmark lens with Q-type polynomial surfaces. As discussed in section 3.2, Q-type polynomial uses orthogonal basis that provides better manufacturability and may make the design process more efficient. A previous paper also explains how a Q-type polynomial can potentially increase the yield of miniature camera lenses [49]. Thus, this benchmark lens with Q-type surfaces can serve as another reference to assess the performance of the evaluation lens. Up to 8 coefficients (including the conic constant) are used for the Q-type polynomial in the benchmark lens. There are two optional types of basis for the Q-type polynomial, Q_m^{bfs} is used since it has more benefits than Q_m^{con} . Design specifications of these three lenses are provided in Table 3.4.

Wavelength	f [mm]	F/#	FOV [deg]	TTL [mm]	Distortion	CRA [deg]	Edge RI
g, F, d, C	1.9	2.4	67	<2.4	<1%	<30	>50%

Table 3.4. Design specification of the even asphere lens, the Q-type polynomial lens, and the pedal freeform lens

3.4.1 Performance Comparison

Lens layouts for the even asphere lens, the Q-type polynomial lens and the pedal freeform lens are shown in Fig 3.22. From this figure, the even asphere lens and the Q-type polynomial lens share similar construction, while the pedal freeform lens shows some surface shape change for the rear lens group. To compare the nominal performance between these three lenses, OPD plots are showed in Fig 3.23 – 3.25, and the MTF plots are provided in Fig 3.26.

From the OPD plots, the overall aberration control of these lenses does not show significant differences. The lens with pedal freeform surfaces shows slightly better on-axis aberration control, the OPD across the pupil is smoother and more uniform, but the differences are minimal. This can be confirmed by the MTF plots. While the lens with pedal freeform surface has better MTF

performance on-axis, the contrast performances are almost identical at larger field of view for all three lenses.

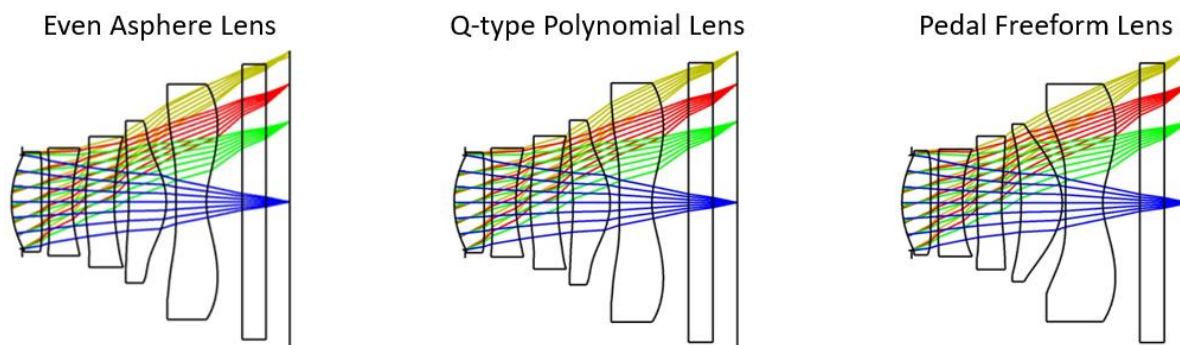


Figure 3.22. Lens layout of the even asphere lens, the Q-type polynomial lens and the pedal freeform lens

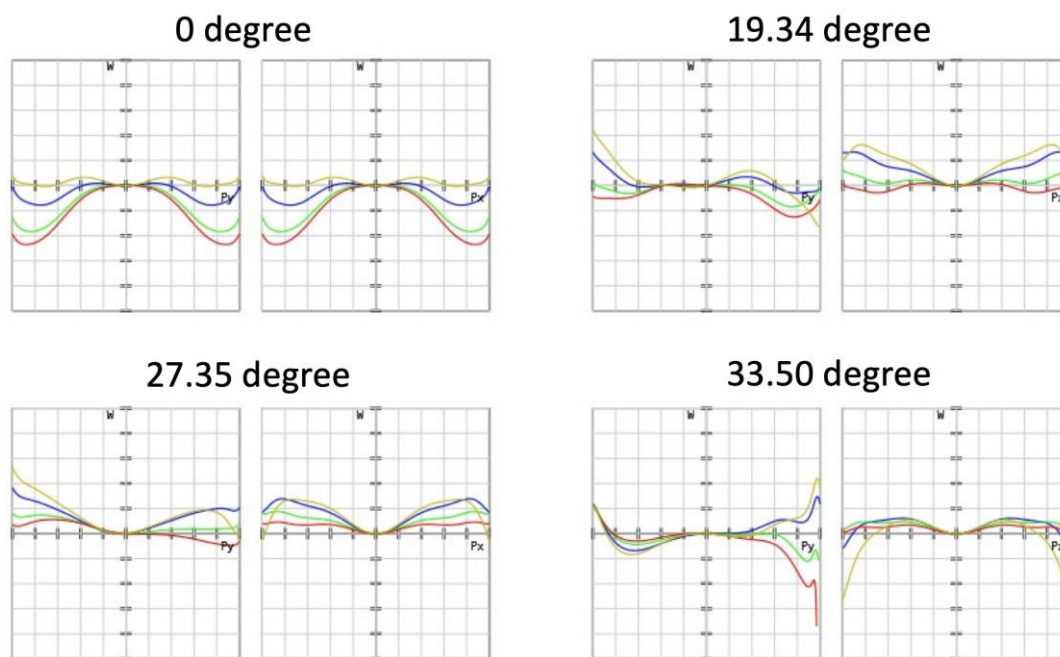


Figure 3.23. Nominal OPD plots of the even sphere lens

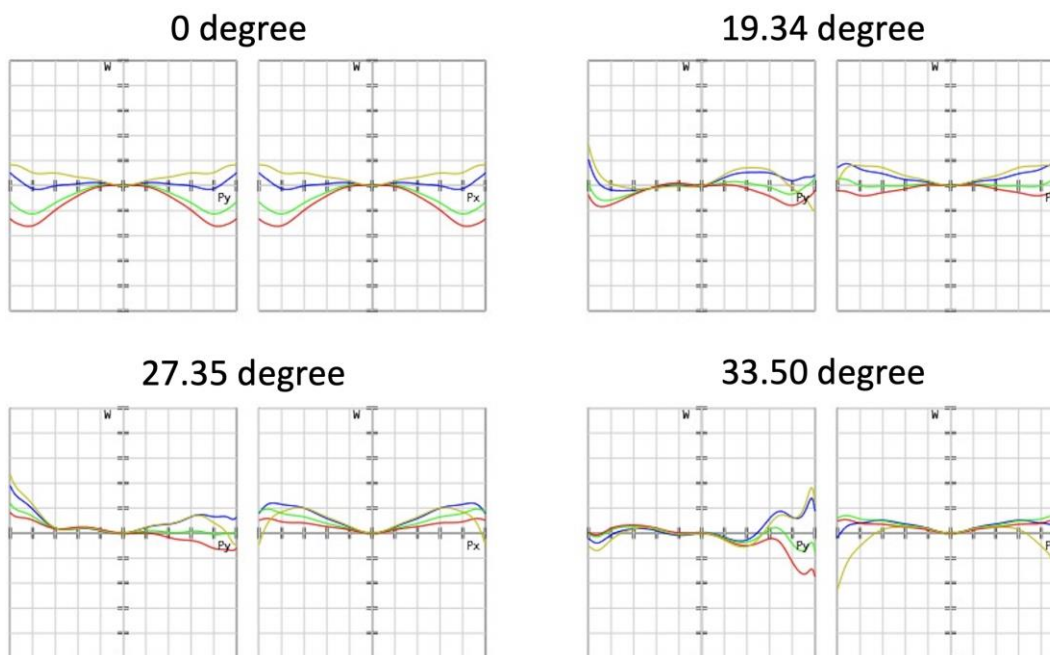


Figure 3.24. Nominal OPD plots of the Q-type polynomial lens

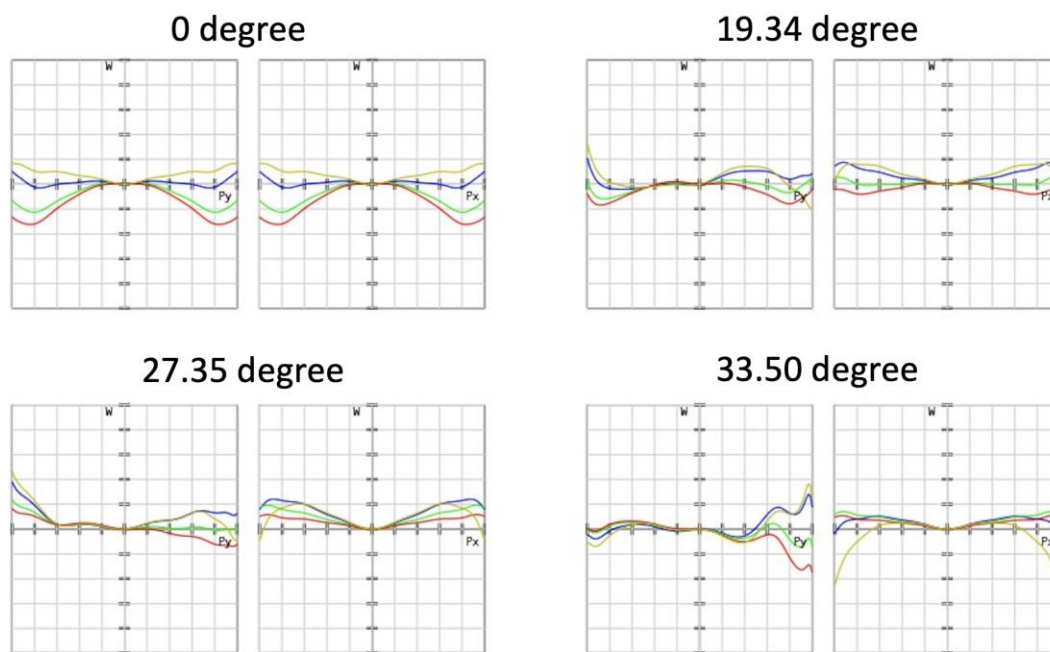


Figure 3.25. Nominal OPD plots of the pedal freeform lens

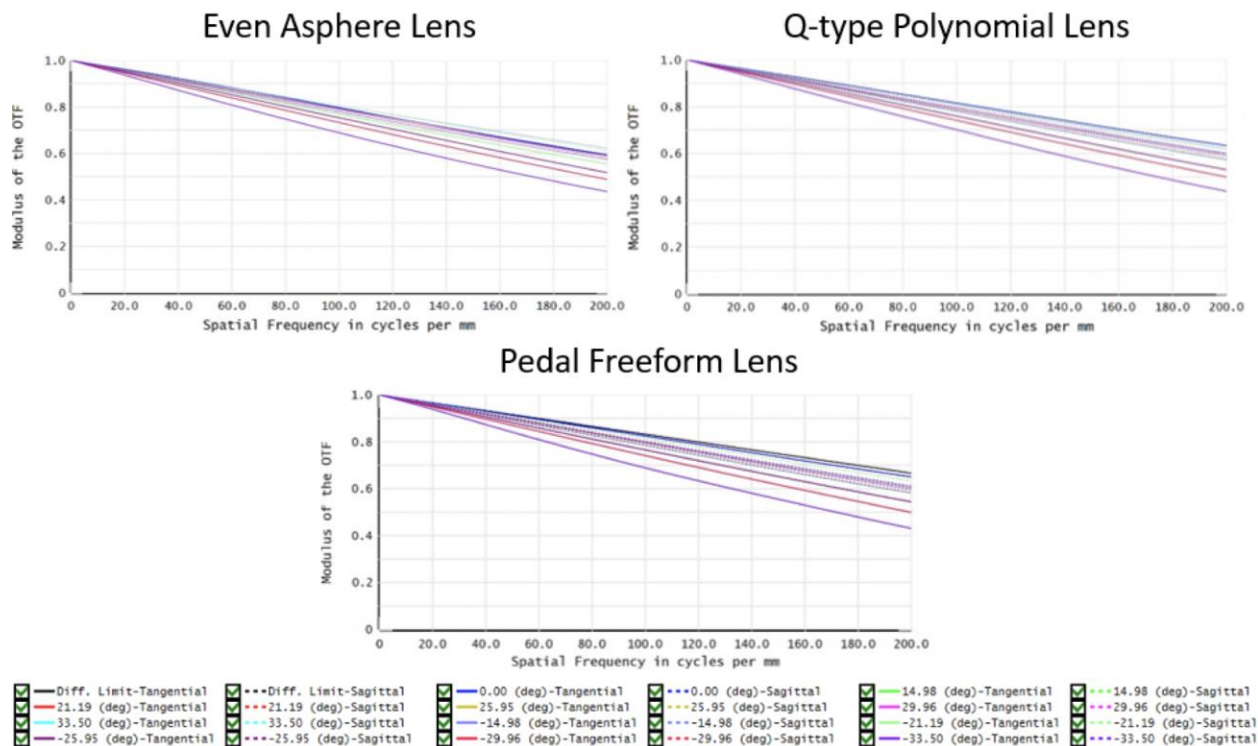


Figure 3.26. Nominal MTF plots of the even asphere lens, the Q- type polynomial lens and the pedal freeform lens

To test the tolerance sensitivity of these lenses, similar procedures were used to evaluate the MTF performance under the influence of 5 μm surface and element decenter. According to the results from section 3.3, surface and element decenter orthogonal to incident fields has much smaller impact to optical performance compare to decenter parallel to incident fields. Thus, surface and element decenter are evaluated along the direction of incident fields (Y direction) in this section. The results of the decenter sensitivity test are shown in Fig 3.27 – 3.32.

From the MTF plots, the contrast after surface and element decenter are almost identical for the even asphere lens and the Q-type polynomial lens. The Q-type polynomial lens shows slightly advantage with decenter of surface 8 (Fig 3.28) and element 4 (Fig 3.31). On the other hand, the pedal freeform lens shows significant better performance during surface and element decenter. This result correlates with the first lens comparison discussed in section 3.3.

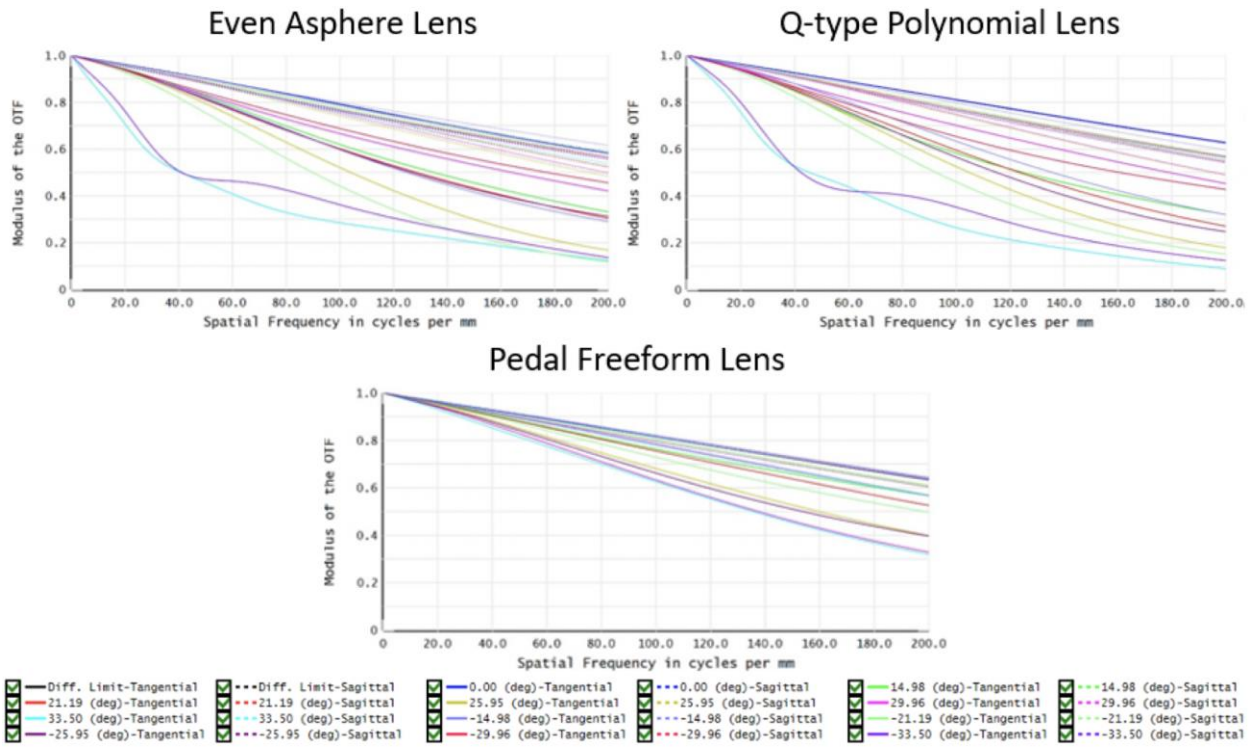


Figure 3.27. MTF plots under 5 μ m decenter of surface 7 in Y direction for the even asphere lens, the Q- type polmyomial lens and the pedal freeform lens

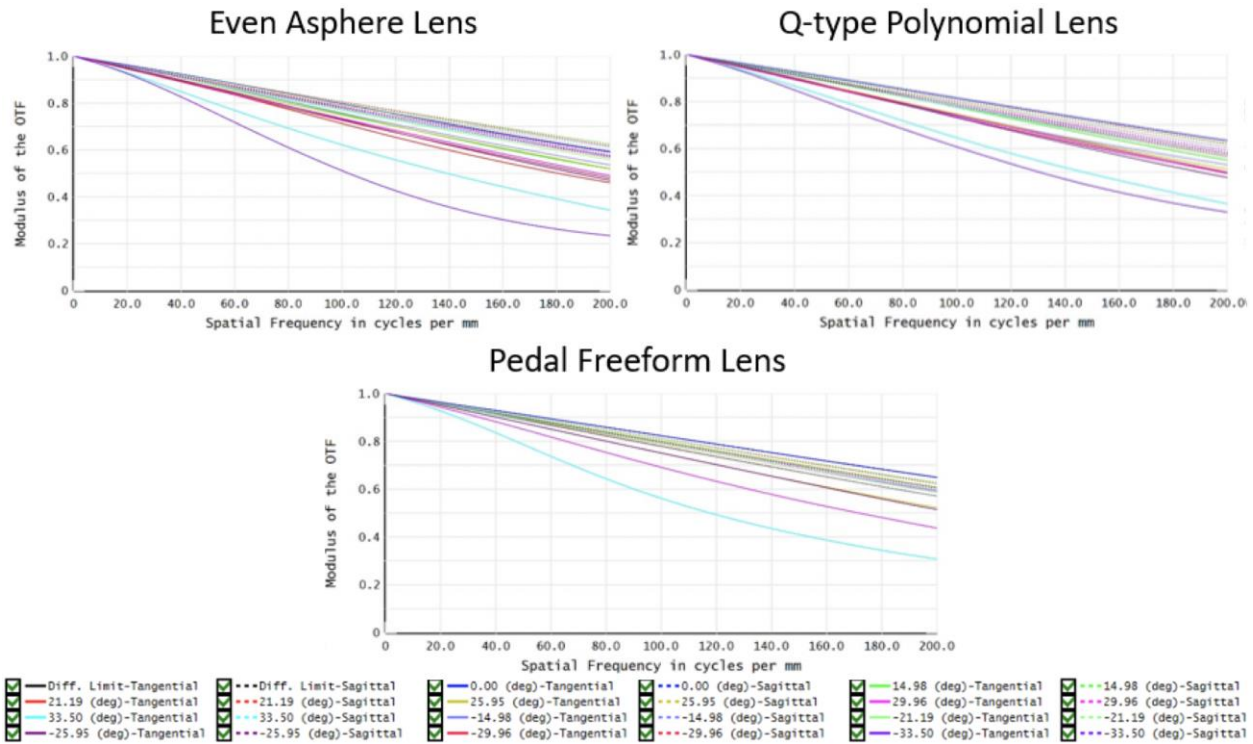


Figure 3.28. MTF plots under 5 μ m decenter of surface 8 in Y direction for the even asphere lens, the Q- type polmyomial lens and the pedal freeform lens

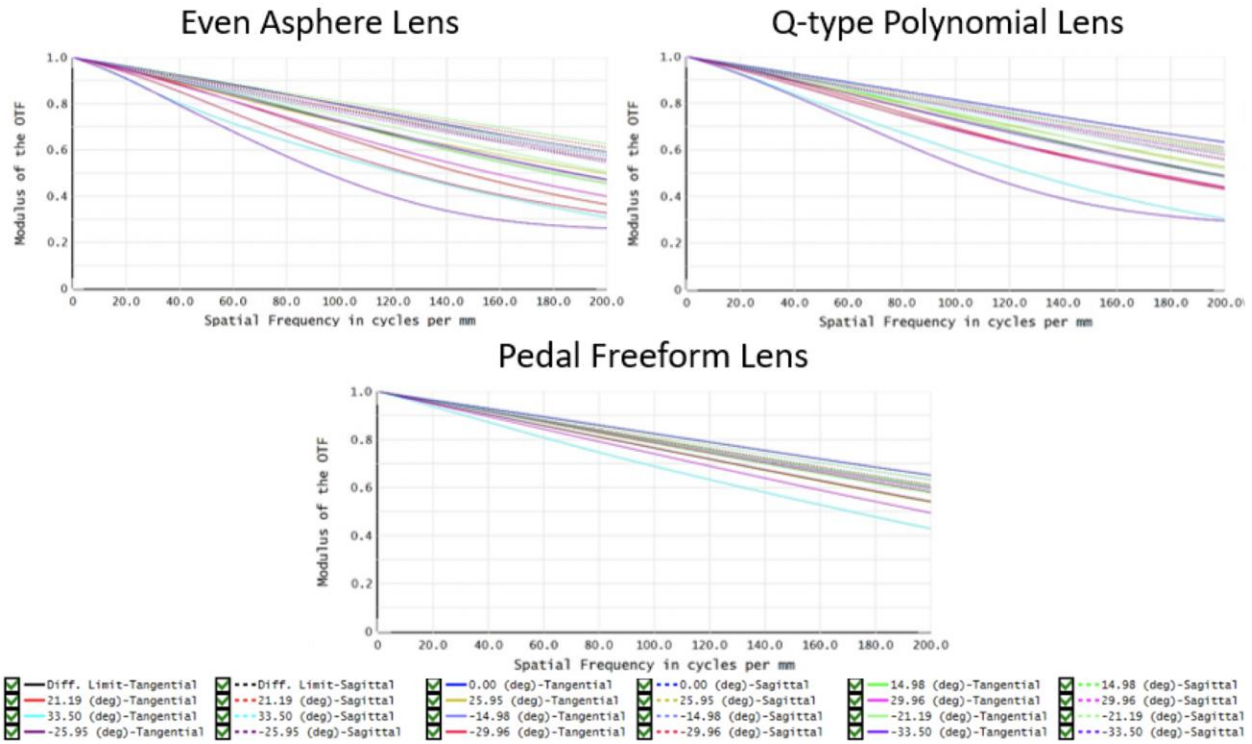


Figure 3.29. MTF plots under 5 μm decenter of surface 9 in Y direction of the even asphere lens, the Q- type polynomial lens and the pedal freeform lens

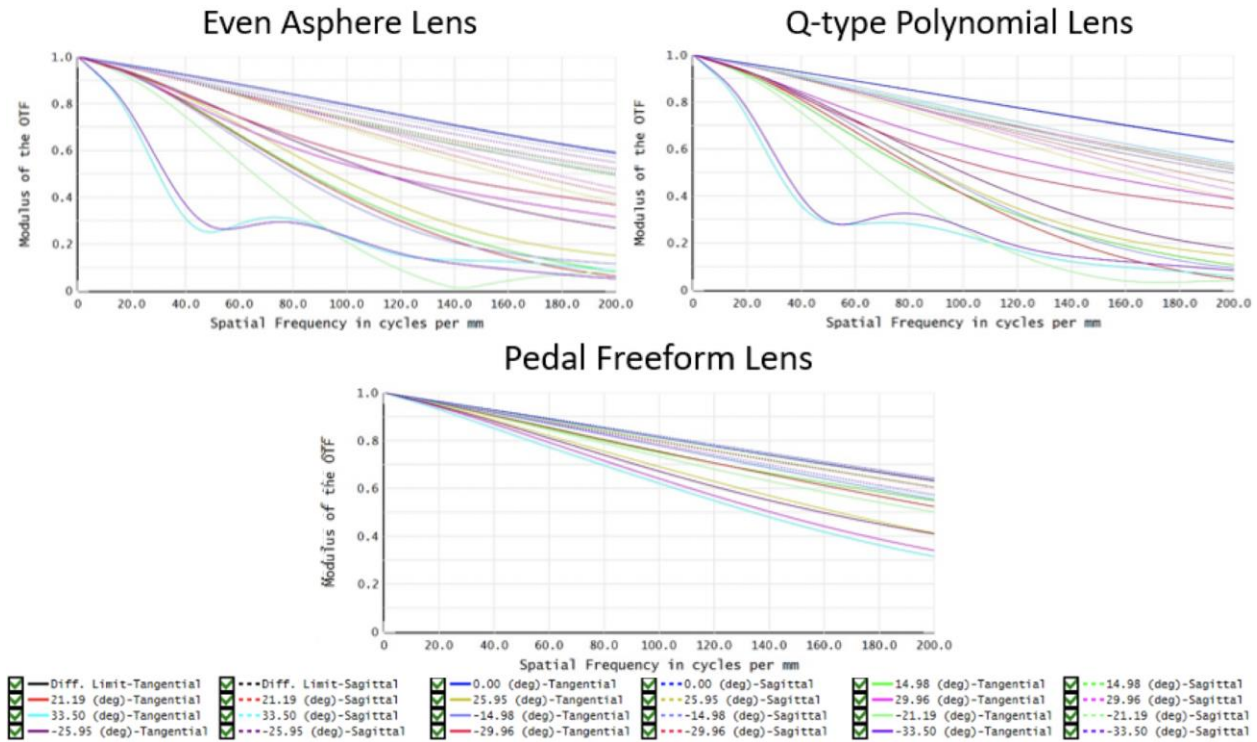


Figure 3.30. MTF plots under 5 μm decenter of surface 10 in Y direction of the even asphere lens, the Q- type polynomial lens and the pedal freeform lens

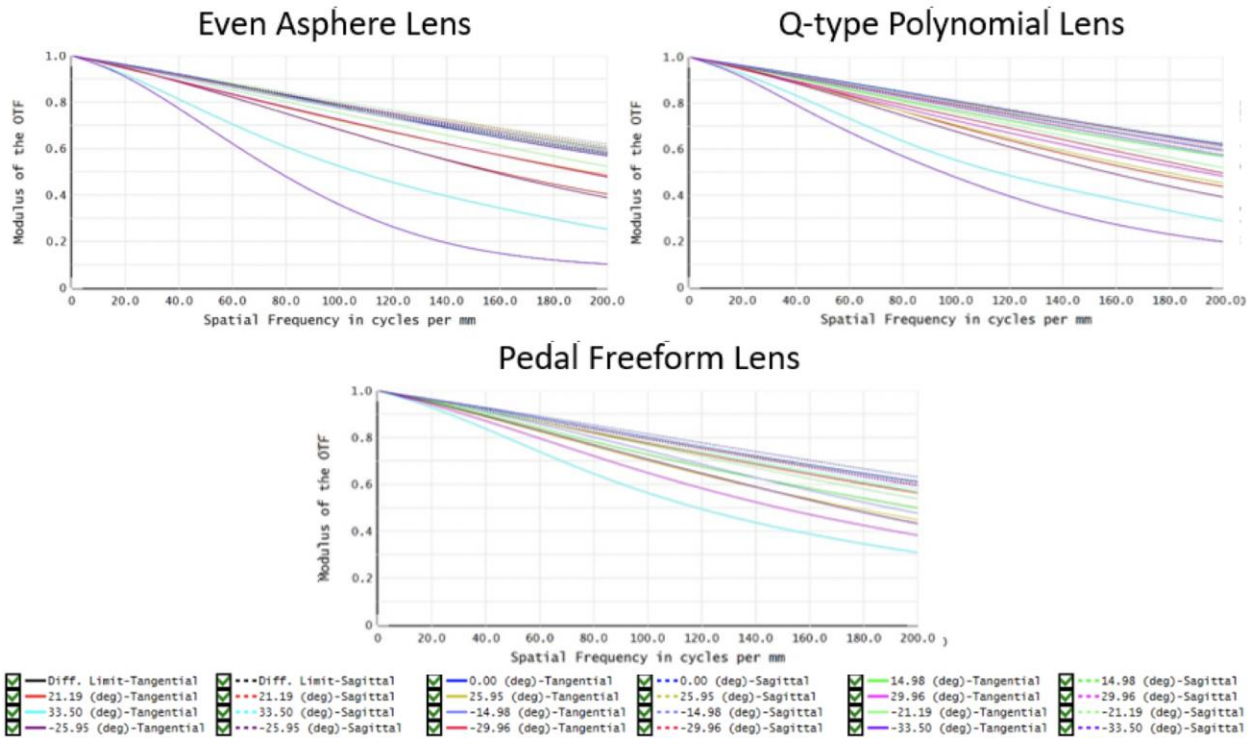


Figure 3.31. MTF plots under 5 μm decenter of element 4 in Y direction of the even asphere lens, the Q- type polynomial lens and the pedal freeform lens

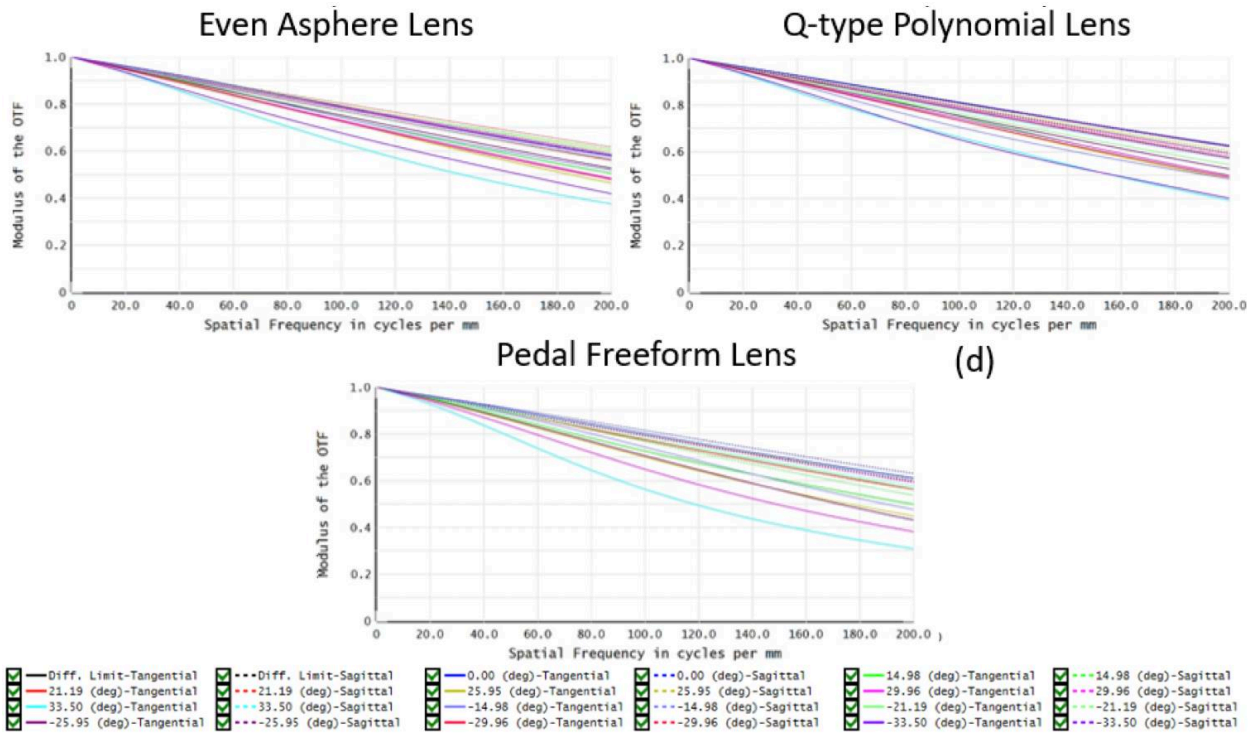


Figure 3.32. MTF plots under 5 μm decenter of element 5 in Y direction of the even asphere lens, the Q- type polynomial lens and the pedal freeform lens

Another way to assess an aspherical/freeform design is by its total number of polynomial coefficients for each surface. While more coefficients provide more degrees of freedom, and usually benefit the optical performance, too many coefficients often appear to be redundant. Also, the extensive use of aspheric terms often leads to wiggles and unnecessary variation on a surface; the variations can add error rather than cancel error. Keeping the same optical performance while reducing the number of polynomial coefficients is usually a goal for lens designers. Less coefficients make the design cleaner and result in a more efficient design. Table 3.5 shows the number of polynomial coefficients, including the conic constant, of the surfaces in the rear lens group of each lens. The freeform design can achieve the same nominal performance and better sensitivity performance with significant reduced number of coefficients.

Surface	Even Asphere Lens	Q-type Polynomial Lens	Pedal Freeform Lens
7	Up to 16 th order, 8 Coefficients	8 Coefficients	1 set of pedal polynomial, 3 coefficients
8	Up to 16 th order, 8 Coefficients	8 Coefficients	1 set of pedal polynomial, 3 coefficients
9	Up to 16 th order, 8 Coefficients	8 Coefficients	1 set of pedal polynomial, 3 coefficients
10	Up to 16 th order, 8 Coefficients	8 Coefficients	2 sets of pedal polynomial, 6 coefficients

Table 3.5. Number of polynomial coefficients, including the conic number, of all 3 lenses under evaluation.

3.4.2 Reversed Asphere Design

In the last subsection, we verified the less tolerance sensitivity of the pedal freeform surfaces. However, from the lens layout comparison showed in Fig 3.22, the shape of the rear elements in the pedal freeform lens slightly differs from the even asphere lens and the Q-type polynomial lens. This may raise the debate among whether the reduced tolerance sensitivity is

actually due to the use of pedal polynomial surface, or due to the new lens shape discovered during optimization. Thus, it is important to check the origin of the reduced sensitivity. A good way to test this is to reconstruct the freeform design with even aspherical surfaces and evaluate its performance. Since we are changing pedal surfaces back to aspherical surfaces, we call this reconstructed lens the ‘reversed asphere lens’. Fig 3.33 shows the lens layout of the reversed asphere lens and the pedal freeform surface. The nominal MTF performance of these two lenses are showed in Fig 3.34. The detailed lens data of the reversed asphere lens can also be found in Appendix B.

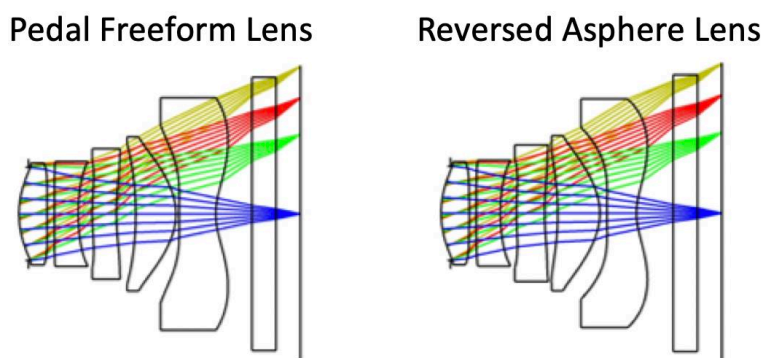


Figure 3.33. Layout of the pedal freeform lens (left) and the reversed asphere lens (right)

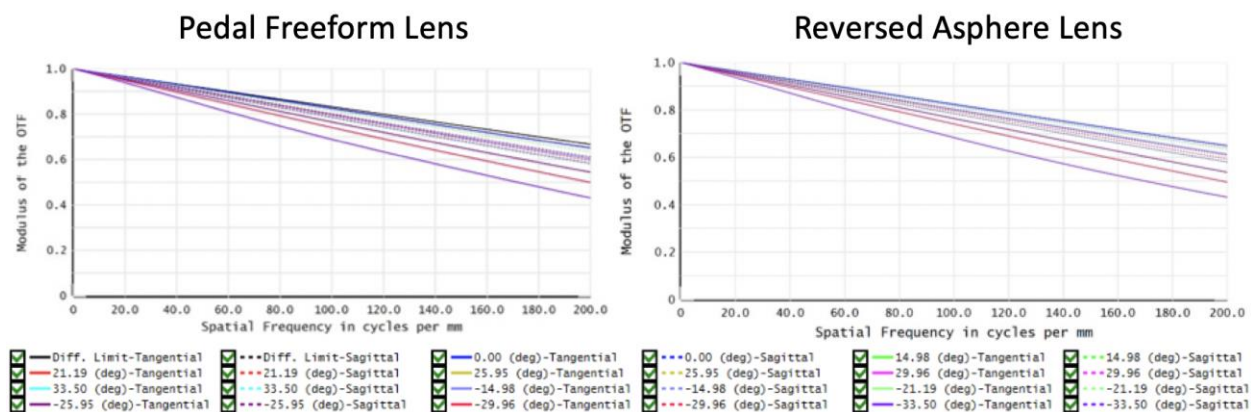


Figure 3.34. Nominal MTF plots of the pedal freeform lens (left) and the reversed asphere lens (right)

According to Fig 3.33, after reconstructing the pedal freeform lens with conventional asphere surfaces, the lens layout of two lenses are close. The nominal MTF performances of both

lenses are also identical to each other. An exact same procedure used in last subsection is applied to evaluate the tolerance sensitivity of the reversed asphere lens. The comparison of MTF performances under surface and element decenter between the pedal freeform lens and reversed asphere lens is showed in Fig 3.35 – 3.40.

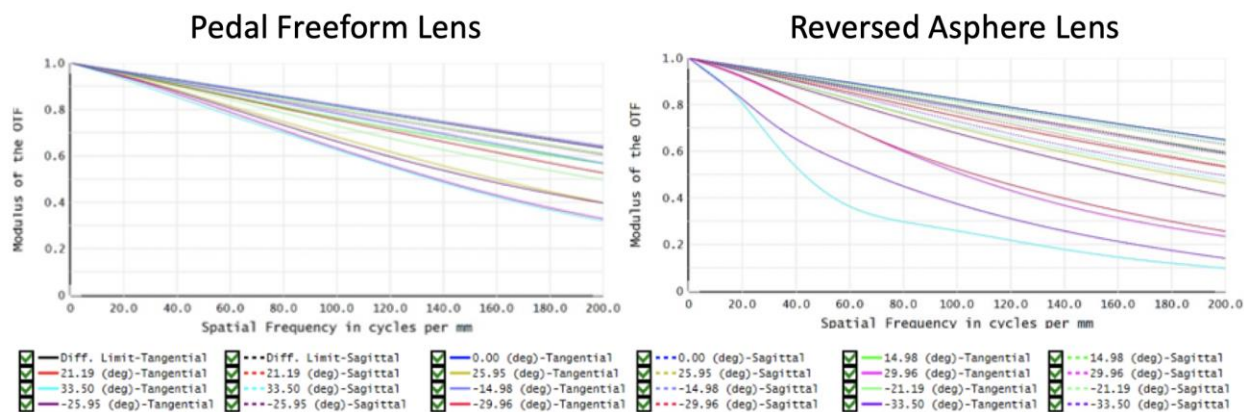


Figure 3.35. MTF plots of the pedal freeform lens (left) and the reversed asphere lens (right) under 5 μm decenter of surface 7 in Y direction

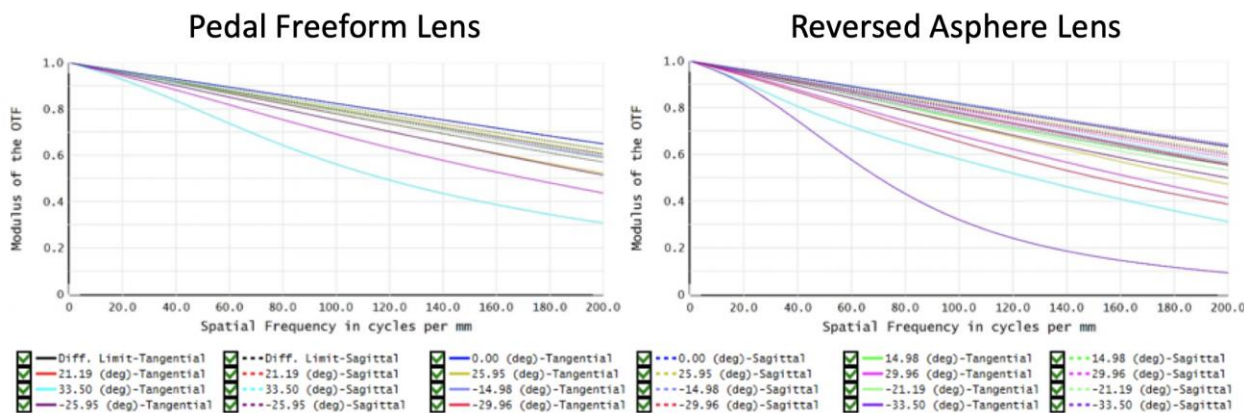


Figure 3.36. MTF plots of the pedal freeform lens (left) and the reversed asphere lens (right) under 5 μm decenter of surface 8 in Y direction

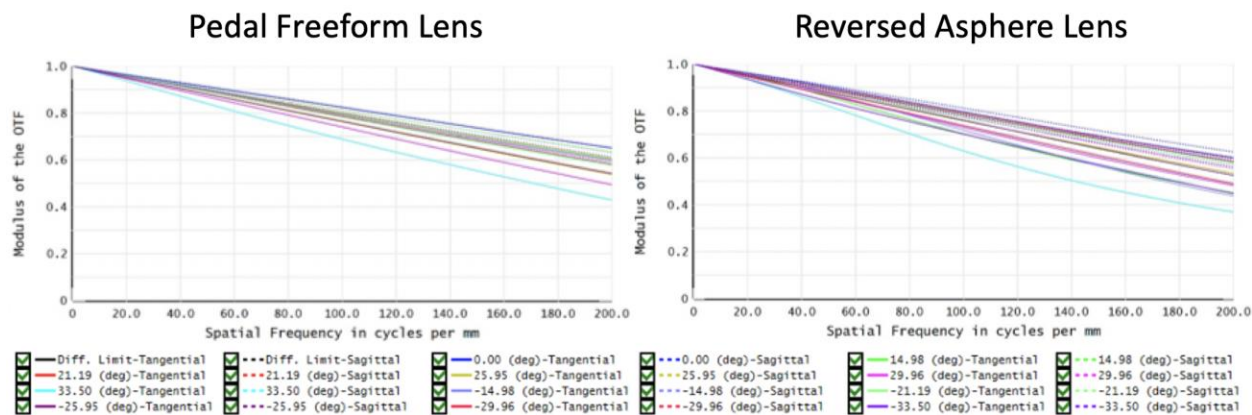


Figure 3.37. MTF plots of the pedal freeform lens (left) and the reversed asphere lens (right) under 5 μm decenter of surface 9 in Y direction

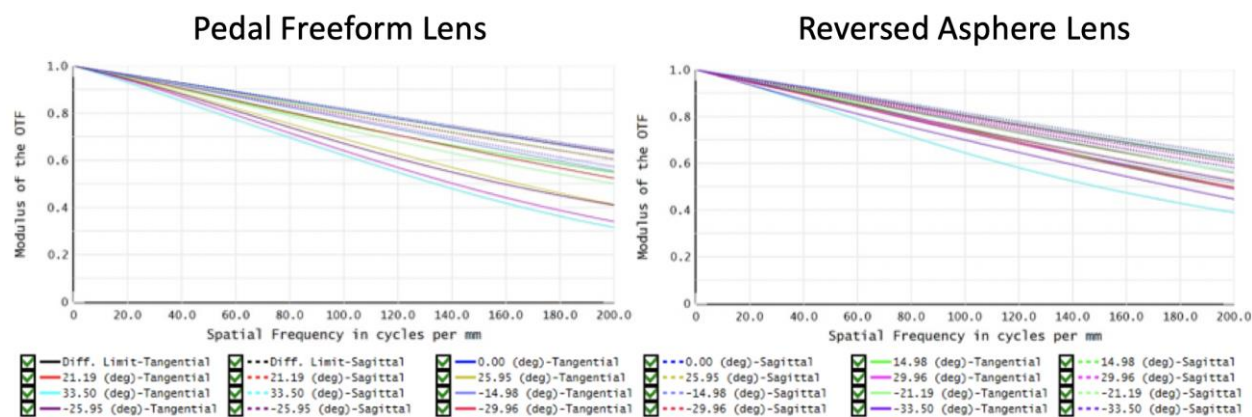


Figure 3.38. MTF plots of the pedal freeform lens (left) and the reversed asphere lens (right) under 5 μm decenter of surface 10 in Y direction

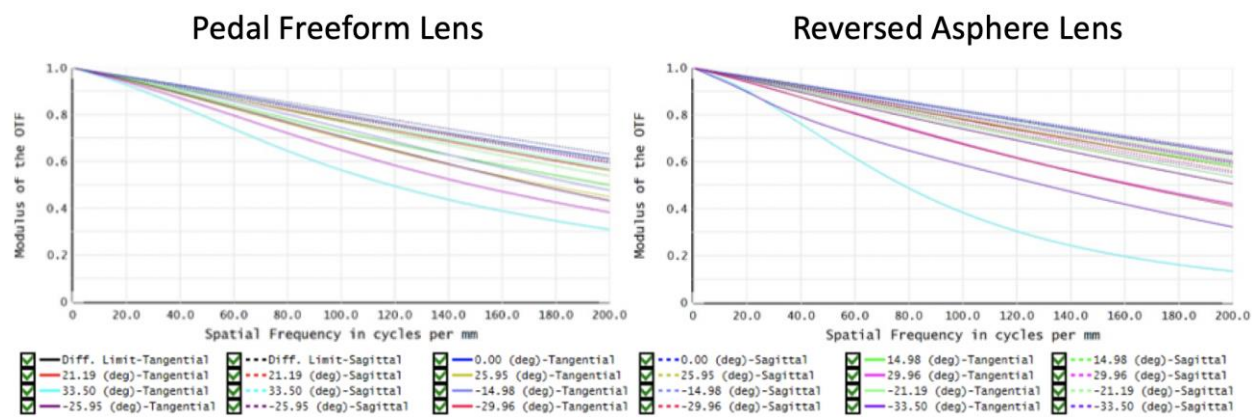


Figure 3.39. MTF plots of the pedal freeform lens (left) and the reversed asphere lens (right) under 5 μm decenter of element 4 in Y direction

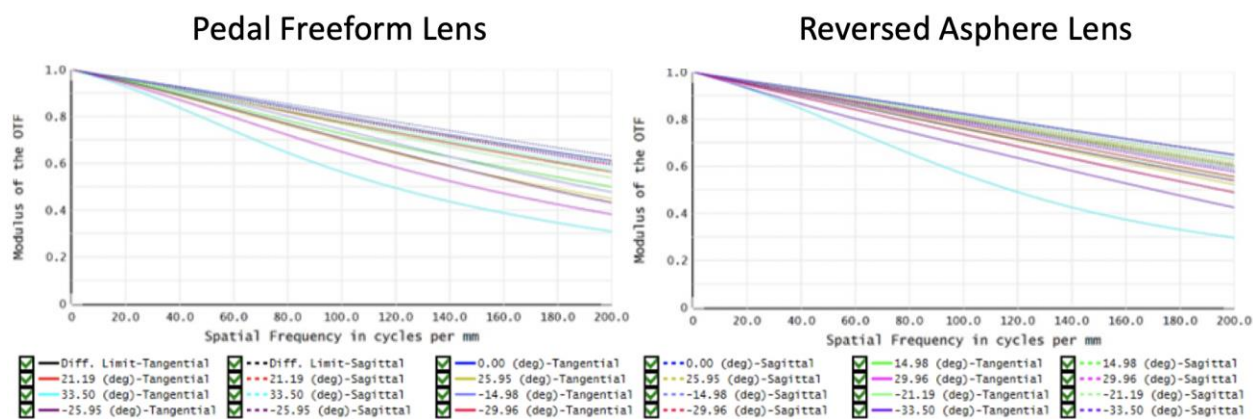


Figure 3.40. MTF plots of the pedal freeform lens (left) and the reversed asphere lens (right) under 5 μm decenter of element 10 in Y direction

From the MTF comparisons, it is clear that the reversed asphere surface has larger tolerance sensitivity than the pedal freeform lens. This means, despite that the overall construction of the pedal freeform design being visually identical to the reconstructed system with even asphere surfaces, the detailed surface profile of the freeform design cannot be 100% reproduced by the even asphere surfaces to achieve the same level of tolerance sensitivity. The decreased sensitivity of the pedal freeform surface is indeed due to the surface profile.

3.5 Conclusion

In this chapter, the author discussed the design of miniature lens using a freeform surface based on the pedal of ellipse. 2 sets of comparison were presented and the benefits of using this type of freeform surface in miniature lens design is analyzed.

Section 3.1 gave a brief discussion on the miniature lens design. A conventional camera lens and a miniature camera lens with same equivalent focal length are compared to show the difference in design of a conventional lens and a miniature lens. While the miniature lenses may benefit from the extensive use of aspherical surfaces, the package size limitation and lack of

material choices made the miniature lens design challenging. Also, the small scale of miniature lens limits its tolerance budget, thus a less sensitive design is always desired.

In section 3.2, the author first provided a discussion on the 2 most common aspherical surface type that are currently used for miniature camera lens, including the even asphere surface and Q-type polynomial. Q-type polynomial have a theoretical advantage over the even asphere surface when the global optimized surface shape is known because of its almost orthogonal basis. However, it does not necessarily have better performance than even asphere surface during the local optimization stage. Then the author discussed the freeform surface based on the pedal curve to the ellipse, including the motivation to use this surface for miniature camera and derivation of its sag.

Section 3.3 provided a set of comparison between the miniature lens designed by conventional even asphere surface and the proposed freeform surface. Miniature lens designed by the freeform surface showed better nominal performance by producing smoother OPD plots and more uniform contrast across the field. In addition, the lens with freeform surface showed significant improvement in surface and element decenter compare to the lens designed with even asphere surfaces.

In section 3.4, the author used another patent lens for comparison. Q-type polynomial surface was added into the comparison. The simulation results showed that while the difference in nominal performance is small, the lens constructed with proposed freeform surface again showed significant decenter sensitivity improvement compare to both the lens constructed with Q-type polynomial surfaces and even asphere surfaces. Also, the freeform surfaces utilize less asphere coefficients compare to the other two surface types. In this section, the author also converted the freeform lens back with even asphere surfaces, but the reversed lens was not able to maintain the

low decenter sensitivity. This proved that the improvement in sensitivity was due to the surface type, rather than the slight difference in lens construction between the freeform lens and other two lenses.

Overall, in this chapter, the author showed that the decenter sensitivity of a miniature lens may be improved by replacing the aspherical surface with the proposed freeform surface based on the pedal curve to the ellipse by two set of comparison. Also, the lens optimized with the freeform surface may also improve the nominal optical performance slightly.

4 Applications and Optical Performance Consideration of Liquid Lenses

Focus tunable lens (FTL) is a type of adaptive optical element with a tunable range of focal length that can be tuned either electronically or mechanically. The modern FTLs has been developed since late 1970s, but the history of FTL can be traced back to almost 1000 years ago from Song dynasty in China. Focal length tuning of a single optical element can be achieved by two major ways either by changing the refractive index of the element or by changing the lens shape. This categorizes modern FTLs into two types, including liquid crystal (LC) lens with a tunable refractive index and liquid lens with a tunable lens shape. Compare to the LC lens, liquid lens provides a larger focus tunable range, faster response time and suffers less from optical birefringence of liquid crystal [50]. In addition, liquid lenses can be treated as conventional optical lenses with multiple configurations during ray tracing simulation, thus is favored by many optical engineers.

Due to the benefits provided by the liquid lens, a wide range of applications were being developed recently utilizing the liquid lenses. Many applications are using liquid lenses to replace moving optical elements in conventional optical systems to achieve little to wide range of system focal length change, including auto focus, move-free zoom lens and 3D scanning microscopy. Besides that, liquid lenses are also being used for some creative applications, such as beam steering device and image stabilizer. Among all the applications, 3D scanning microscopy is one of the most trending application and draws attention of many scholars and companies. By inserting a tunable lens into a microscope, move-free 3D scanning can be achieved, which is beneficial to medical research. However, when putting the liquid lens inside a diffraction limited microscope system, inevitable downgrade in optical performance will appear. The downgrade in optical

performance could be caused by aberration, material dispersion and gravity. A comprehensive quantitatively analysis on the impact of optical performance from liquid lens is needed.

In this chapter, a brief discussion on the development and principle of FTLs is presented in section 4.1. Then in section 4.2, the author provides a survey on the applications utilizing liquid lenses, including focus sweep, zoom optical system and beam steering. In section 4.3, the author presents a comprehensive optical performance evaluation on 3D microscopy with liquid lenses. A set of ray tracing simulation and evaluation on chromatic aberration and on-axis MTF are first discussed, then the results are compared to the experimental data. In addition, gravity effect is also evaluated during the lab experiment. In section 4.4, the author provides a novel approach to correct chromatic aberration of a liquid lens with conventional lens design. All the materials presented in this chapter will be concluded in section 4.5.

4.1 Development and Principles of Focus Tunable Lenses

The development of focus tunable lens can be traced back to Song dynasty (920 – 1279) in China. A device called “butterfly cup” or “fish cup” was recorded by several references [51] [52]. This device served as a wine cup with a butterfly or fish painted in the bottom of the cup that can only be seen when the cup is filled up with wine or other liquid. The principle of such device is demonstrated in Fig 4.1. A positive singlet is put near the bottom of the cup. A butterfly or any other interesting object is painted underneath the positive lens. The object is painted further than the focal plane of the single lens, thus the rays coming from the object are converging after passing through the positive lens. Such converging rays cannot be compensated by our eyes, causing the image to focus in front of the retina, so the image cannot be seen clearly when the cup is empty. When the cup is filled with liquid, the liquid became a negative lens. The entire cup forms a compound doublet and the focal length is extended so the object is within the focal plane of the

compound lens. The rays become diverging or parallel after the doublet thus can be captured by human eye and focus on retina. Then the object can be seen clearly when the cup is filled up. To the author’s knowledge, this is the first focus tunable device in the history.

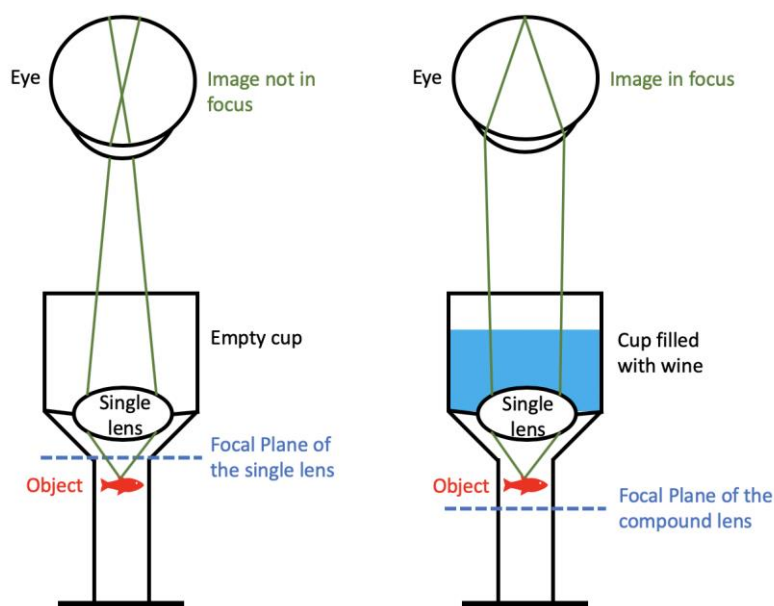


Figure 4.1. Working principle of the “butterfly cup” from Song dynasty.

The development of modern FTLs went down two different paths. The first type of FTL is LC tunable lens, which is based on large optical birefringence property of the nematic liquid crystal. The concept of LC tunable lens, which was a LC lens with an inhomogeneous cell gap, was first proposed by Susumu Sato in 1979 [53]. Figure 4.2 demonstrates the principle of the LC tunable lens with inhomogeneous cell gap. Assume a linear polarized ray bundle with polarization along Y direction incident on a LC lens. If the optical axis of the LC is perpendicular to the incident ray polarization (in X direction), the incident ray bundle will be governed by the ordinary refractive index n_o of the LC, then the system focal length is the ordinary focal length f_o . If the optical axis of the LC is rotated so that it is parallel to the incident ray polarization (in Y direction). Then the incident ray bundle will be governed by the extraordinary refractive index n_e of the LC, then the system focal length is change to the extraordinary focal length f_e . By applying either magnetic

field or electric field around the LC cell, the orientation of the LC molecule can be controlled, so the focal length can be tuned between ordinary focal length f_o and extraordinary focal length f_e .

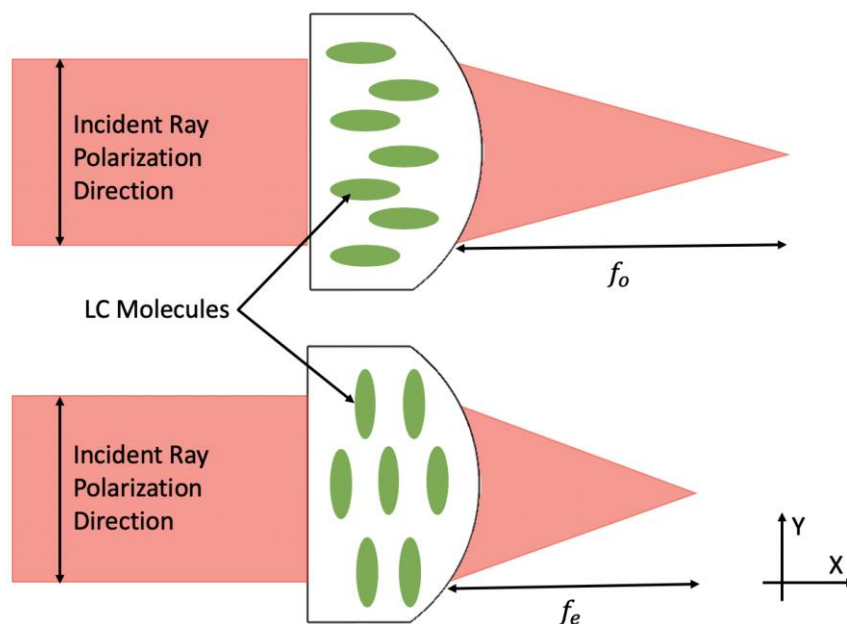


Figure 4.2. Working principle of LC tunable lens with inhomogeneous cell cap

The LC tunable lens proposed by Susumu Sato was with an inhomogeneous cell cap, which means the LC molecules are concealed inside a lens-shaped cell, and the orientation of the molecules are being tuned together. Due to the inhomogeneous of the cell gap, the alignment of the LC directors is difficult. Another LC tunable lens concept with more compact design was introduced by Stephen T. Kowel in 1984 [54]. He proposed a LC lens with a homogeneous cell gap, where the LC molecules are essentially concealed inside a plan parallel plate. Figure 4.2 demonstrates the principle of such LC lenses. To achieve the lens effect, the LC molecules are tuned differently across its cross section, resulting a phase difference between the center of the lens and edge of the lens, thus producing a converging or diverging wavefront. To achieve the correct distribution of the LC molecules, complicated electrode designs are required. Three major electrode designs for the LC lenses with homogeneous cell cap, including hole-patterned electrode,

curved electrode and planar electrodes constructed by 2 materials with different dielectric constant ϵ_1 and ϵ_2 are illustrated in Figure 4.3.

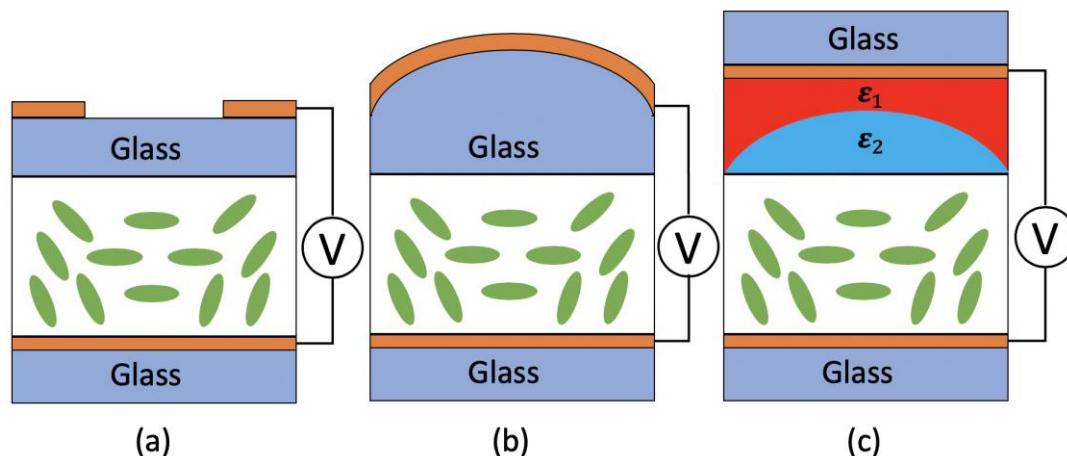


Figure 4.3. Electrode designs for LC lenses with homogeneous cell gap, including (a) hole-patterned electrode, (b) curved electrode and (c) planar electrodes.

The biggest issues of LC tunable lenses are their slow response time and polarization dependency. The response time of a typical LC tunable lens is around 500 ms to 1s [55]. And since the fundamental principle of a LC lens is the birefringence of LC molecules, polarization of incident light needs to be strictly controlled, thus cause a limitation on the applications. Another approach with faster response time and no polarization dependency is liquid lens. B. Berge and J. Peseux first discussed a liquid lens based on electrowetting in 2000 [56]. Electrowetting describes a physics phenomenon that the surface tension of a liquid droplet can be controlled by applying external voltage. This was first discovered by M. G. Lippmann in 1875. This technology has been developed for years and was eventually used by optical engineers to tune the curvature of a liquid lens. Fig. 4.4 illustrate the principle of a liquid lens based on electrowetting. A lens cell contains two non-miscible liquids, usually water and oil. The liquids are transparent with different refractive index but same density. These two liquids form a natural liquid-liquid interface, which the curvature can be tuned by applying external voltage. By tuning the interface curvature, the

effective focal length can also be tuned. The most drawback for this type of liquid lens is its sensitivity to temperature. At its ideal design temperature, two liquids in the lens cell have same density, so the lens shape would not be impacted by gravity. However, different liquids would have different thermal expansion coefficients, and the densities of the two liquids would not be able to match at a different temperature. The thermal effects of the liquid-liquid lens were discussed by Jerome Crassous [57]. He concluded that the gravity effect caused by thermal issues is significant, so the maximum aperture of such a lens is limited. The idea of a liquid lens based on electrowetting was adopted by a company named Varioptic (now a part of Corning) and actually went to mass production. However, their largest aperture liquid lens only has a clear aperture of 3.9 mm [58].

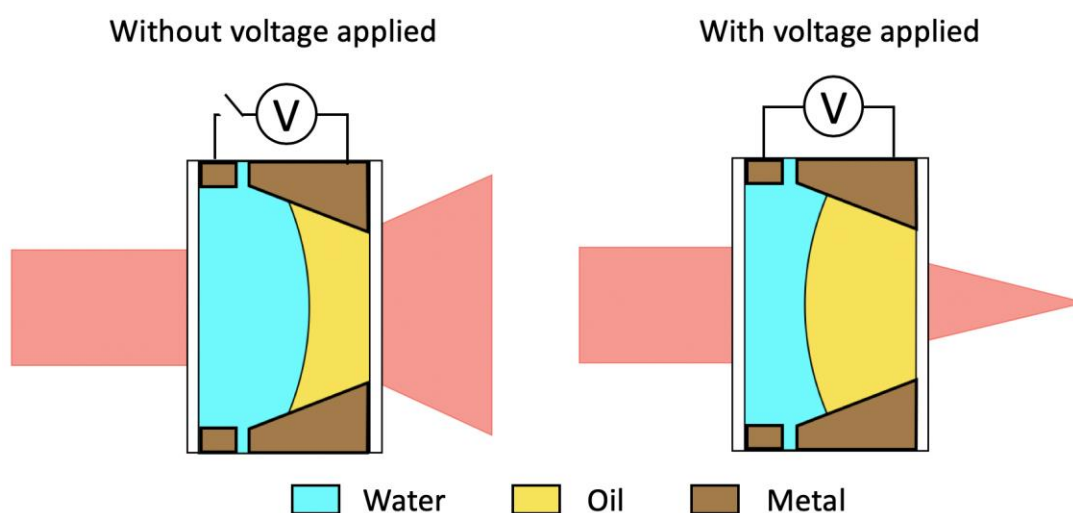


Figure 4.4. Working principle of a liquid lens based on electrowetting.

To increase the aperture, the interface between liquids needs to be stiffer. This can be done by inserting a thin polymer membrane between the two liquids. Figure 4.5 demonstrates the principle of a liquid lens with a membrane. Similar to a liquid lens based on electrowetting, two liquid chambers with liquids of different refractive indexes are used to tune the lens power. The membrane serves as the interface between two liquid chambers, and its shape can be changed by applying pressure either mechanically or with an electrical actuator. Furthermore, with the

boundary defined by the membrane, two liquids are not required and only one liquid is needed. The other liquid chamber can be replaced by air to increase the index difference between two chambers and provide a larger tunable range with more compact size. A company named Optotune is currently the biggest vendor of the liquid lenses with polymer membrane. The clear aperture of their liquid lens is up to 10 mm if it is electrical controlled and is up to 25 mm if it is mechanically controlled. The clear aperture of Optotune lenses with polymer membrane are significantly larger than the Varioptic lenses based on electrowetting. In addition, liquid used for the lenses with polymer membrane has less restriction on its density, which results in a larger material choice range. Liquids with larger Abbe number can be used to reduce color dispersion.

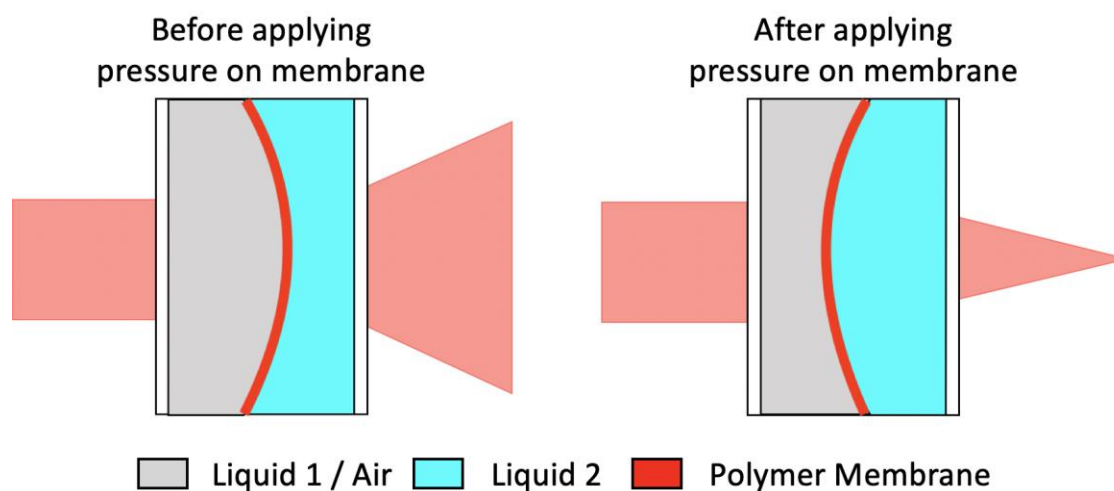


Figure 4.5. Working principle of a liquid lens with polymer membrane, lens shape is changed by applying pressure on membrane.

Even though the polymer membrane is stiffer than the liquid-liquid interface, the tunable lenses with membrane still suffers from gravity effect, especially when the lens is positioned in a horizontal direction. Also, since liquid lenses are usually used as an adaptive optical component, large spherical aberration and chromatic aberration introduced by inserting liquid lenses are big concerns for real application. Recently, some gravity immune liquid lenses and aspherical liquid lenses are being researched [59] [60] [61]. Unfortunately, none of these lenses are mass produced

nor available on the market. Also, chromatic aberration correction for liquid lenses are rarely discussed. This topic will be covered in section 4.4.

4.2 A Review of Application Utilizing Liquid Lenses

For the past two decades, many different applications were discovered by scientists and engineers that utilized liquid lenses in different ways. In this section, the author will give a review on three major applications with liquid lenses.

4.2.1 Focus Sweeping

One of the most common application of a liquid lens is focus sweeping. The general idea of focus sweeping is to control the focal plane position in small magnitude by slightly adjusting the system focal length. This can be done by inserting a liquid lens in front of the focal plane directly or by adding one or more liquid lens inside the optical system. Several different applications can utilize the concept of focus sweeping. The first and most straight forward application is a variable focus ophthalmic lens. This is done by simply replacing a conventional bifocal glass with a liquid lens. Many papers and patents have talked about this concept, and Fig 4.6 shows the structure of such device from a sample patent. Although such devices are suitable for multiple purposes, one of the biggest motivations behind a variable focus ophthalmic lens is to correct presbyopia. Presbyopia is a medical condition describes the irreversible loss of the accommodative ability of the eye due to aging. When a fully corrected human eye (without other types of refractive error) is relaxed, the lens in the eye focus objects far away or at infinity onto retina. To focus a closer object onto the retina, the lens in the eye provides accommodation by changing the lens shape. However, the ability to adjust the eye lens accommodation is weakening with the increasing of age. According to a study [62], the maximum accommodation of the eye

lens is usually stable at around 7 diopters before the age of 20 but may decrease to under 0.5 diopter at the age of 50 and dropped to 0.01 (complete loss of accommodation) at the age of 69. Presbyopia is an inevitable age-related eye condition that is prevalent across the world. In 2005, over 1.04 billion people were estimated to suffer from presbyopia. And this number is expected to rise to 1.37 billion in 2020 [63]. In addition, presbyopia is independent of other refractive errors such as myopia, hyperopia and astigmatism.

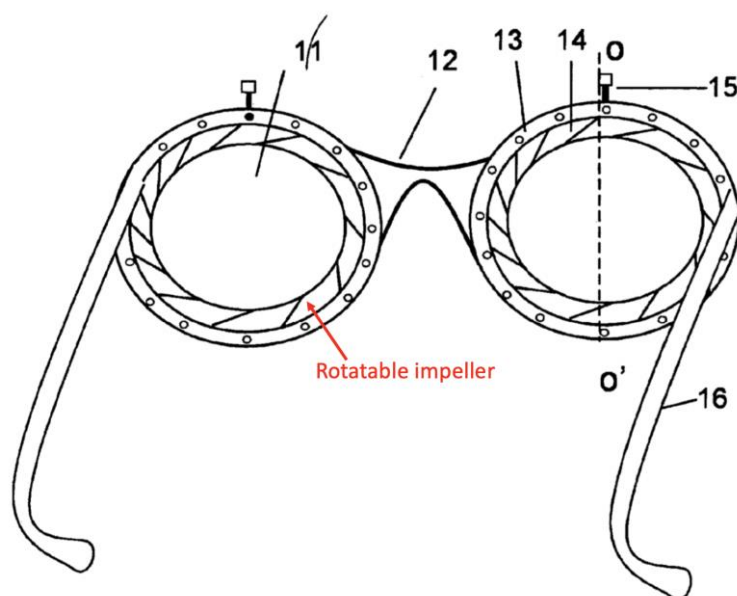


Figure 4.6. Figure of an example patented variable focus liquid ophthalmic lens. Optical power of liquid lens is tunable by adjusting the rotatable impeller

Previously, presbyopia was treated by using bifocal or trifocal glasses to provide 2 or 3 fixed focal lengths. Nevertheless, this solution is not very satisfactory as it only brings objects at two fixed distance into focus, usually one for far distance objects and one for book reading. A focus tunable liquid lens can provide extra levels of accommodation and more flexibility. Figure 4.7 illustrated an example of using liquid lens for correcting presbyopia and comparing to a normal eye with good accommodation. The liquid lens chosen by the author is the Optotune ML-20-37. The focal length tuning range of this liquid lens is from $-\infty$ to -55 mm and from $+55$ mm to ∞ . The

lens is put roughly at the front focal plane of the eye (about 15mm in front of the eye) to avoid any visual magnification change. The eye is modeled by using Arizona eye model and is assumed to be otherwise healthy except without lens accommodation (relaxed eye). Fig. 4.7 (a) demonstrates the relaxed eye looking at an object at infinity. Liquid lens provides no power and serves as a plan parallel plate. Fig. 4.7 (b) demonstrates the relaxed eye looking at a near object at 80 mm in front. At this state, the liquid lens provides maximum positive power to focus the image on retina. Fig. 4.7 (c) and Fig. 4.7 (d) demonstrate eye with good lens accommodation looking at same object at infinity and at 80 mm in front of the eye. The eye lens is required to accommodate 12.5 diopters in order to focus the near object on retina. Thus, the chosen liquid lens has enough tunable range to correct presbyopia, even for eyes that completely lost their powers for accommodation. However, the currently liquid lenses have a limitation on clear aperture. The Optotune ML-20-37 used in this comparison only provides a 50% vignetted FOV of $\pm 18^\circ$ with a 20mm clear aperture. To increase FOV, larger aperture is required thus creates more difficulty for manufactures.

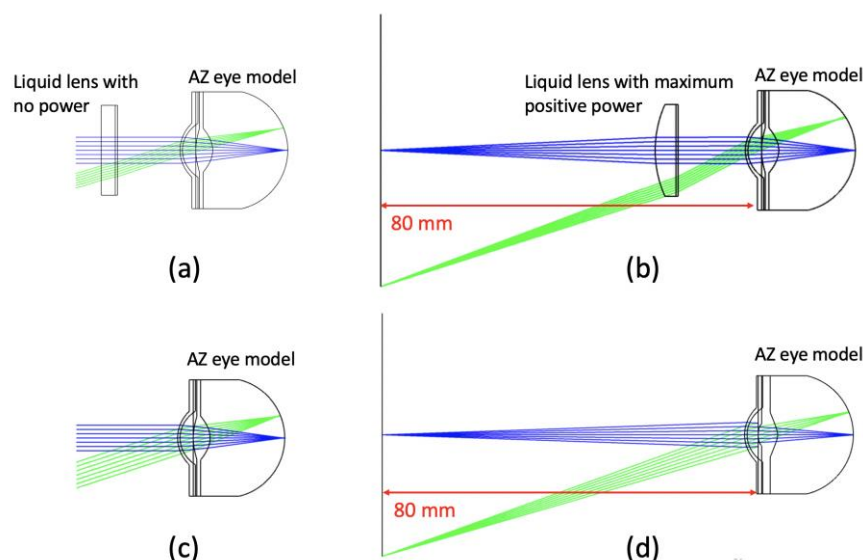


Figure 4.7. Example of presbyopia correction using liquid lens. (a) A relaxed eye looking at infinity through liquid lens, (b) a relaxed eye looking at a near object through liquid lens, (c) a relaxed eye looking at infinity without liquid lens, (d) an eye looking at a near object with eye lens accommodation.

Another application based on the focus sweeping ability of liquid lens is resolving the vergence-accommodation conflict (VAC) in head mount displays (HMDs). VAC describes the mismatch of accommodation and convergence between the 2D image plane and the 3D virtual object rendered in a stereoscopic display. Currently, most 3D stereoscopic displays are based on the concept of binocular disparity, where a pair of images with a disparity between them are rendered one for each eye to facilitate stereo parallax. The optics between the display and human eyes are usually fixed, resulting a rendered 3D object to appear at a fixed distance in front of the human eyes, regardless of the assumed object distance. Fig 4.8 demonstrates the VAC in a 3D stereoscopic HMD. Assume the HMD is rendering a near object (the basketball) and a farther object (the tree) both in 3D using the same optics. These objects are rendered at the same object plane at a fixed vergence distance in front of the eye. However, looking at the farther object and the near object should require different eye lens accommodation in nature. The difference between the accommodation distances and vergence distance creates a conflict named VAC. The VAC is a major contribution to viewing discomfort for HMDs [64]. Despite the tremendous developments in VR/AR technology recently, correcting VAC for better viewing comfort still remains a challenge today. An efficient method to reduce VAC is urgently needed.

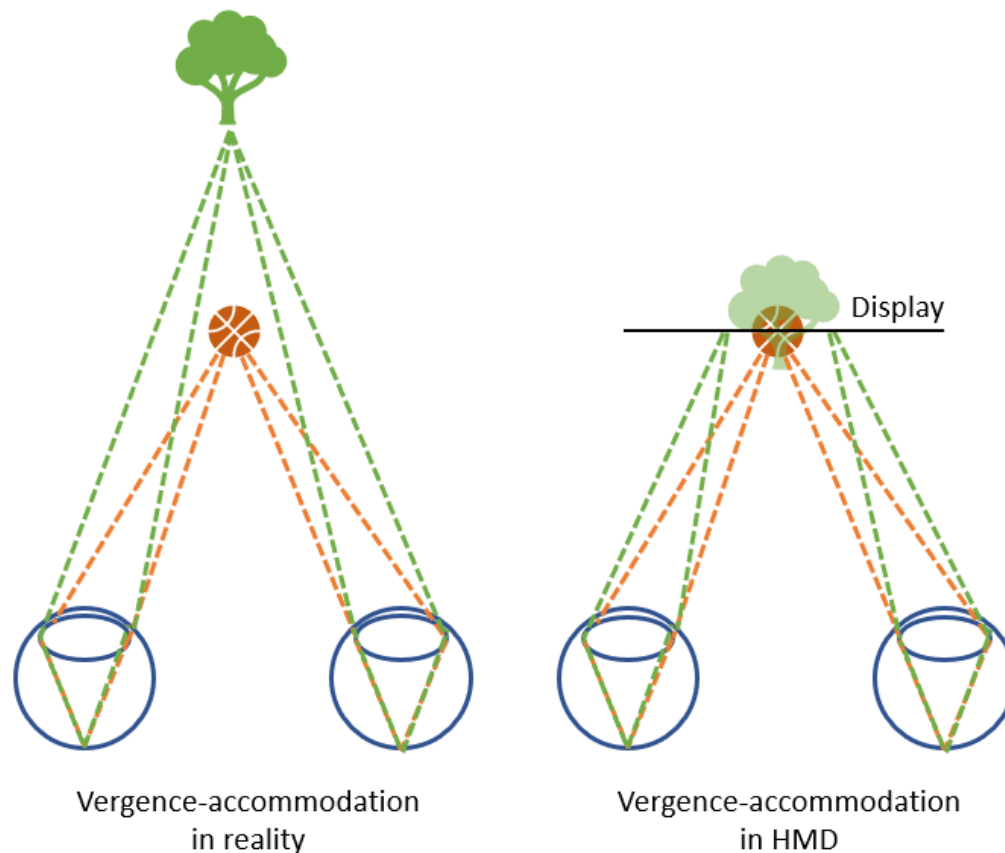


Figure 4.8. Demonstration of VAC in HMDs.

Since the 1990s, many methods to reduce VAC were proposed through scientific conferences and research papers, including Maxwellian view display with spatial light modulator (SLM) [65], multifocal plane displays [66], light-field displays [67], computational multilayer displays [68] and vari-focal approach. Among all these methods, the vari-focal approach adds least hardware complexity to an HMD. Several solutions with mechanical moving parts were proposed [69] [70], but the response times were simply too slow. A liquid lens with tunable focal length range can be an alternate solution. In 2008, Sheng Liu from the University of Arizona discussed an optical see-through head mounted display with addressable focal planes with the use of liquid lens [71]. The proposed system used a set of objective lenses to image the light from micro display to an intermediate image plane. The intermediate image is then re-projected with a “bird bath combiner”, where a beam splitter and a spherical mirror are used to redirect light into the eye

without blocking the scene in front of the eye. A custom-made liquid lens is inserted near the stop of the objective lens in an HMD system to address the focal distance of the HMD from infinity (0 diopter) to the near point (5 diopter) of the eye [Fig 4.9]. This proposed prototype achieves a diagonal FOV of 28° . Fig 4.10 demonstrates a wide-angle system designed by the author of this dissertation with an off-the-shelf liquid lens. A liquid lens from Optotune (EL-10-30-TC) with a focus tunable range between 50 mm to 120 mm is used to match eye lens accommodation from 0 diopter to 8 diopters, which positioned the virtual object at from infinity to 125 mm in front of the eye. The system can provide a diagonal FOV of 45° . Since the liquid lens is placed near the stop of the objective lens thus does not limit the FOV, larger FOV is also possible with more optical elements for better off-axis aberration control.

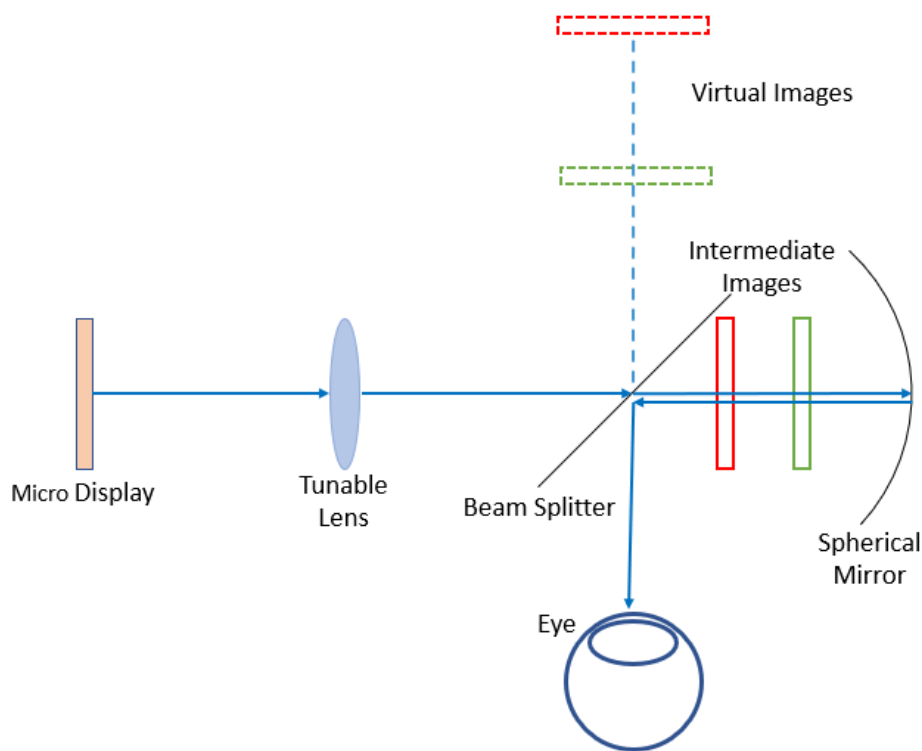


Figure 4.9. A “bird bath” type HMD with a tunable lens to reduce VAC

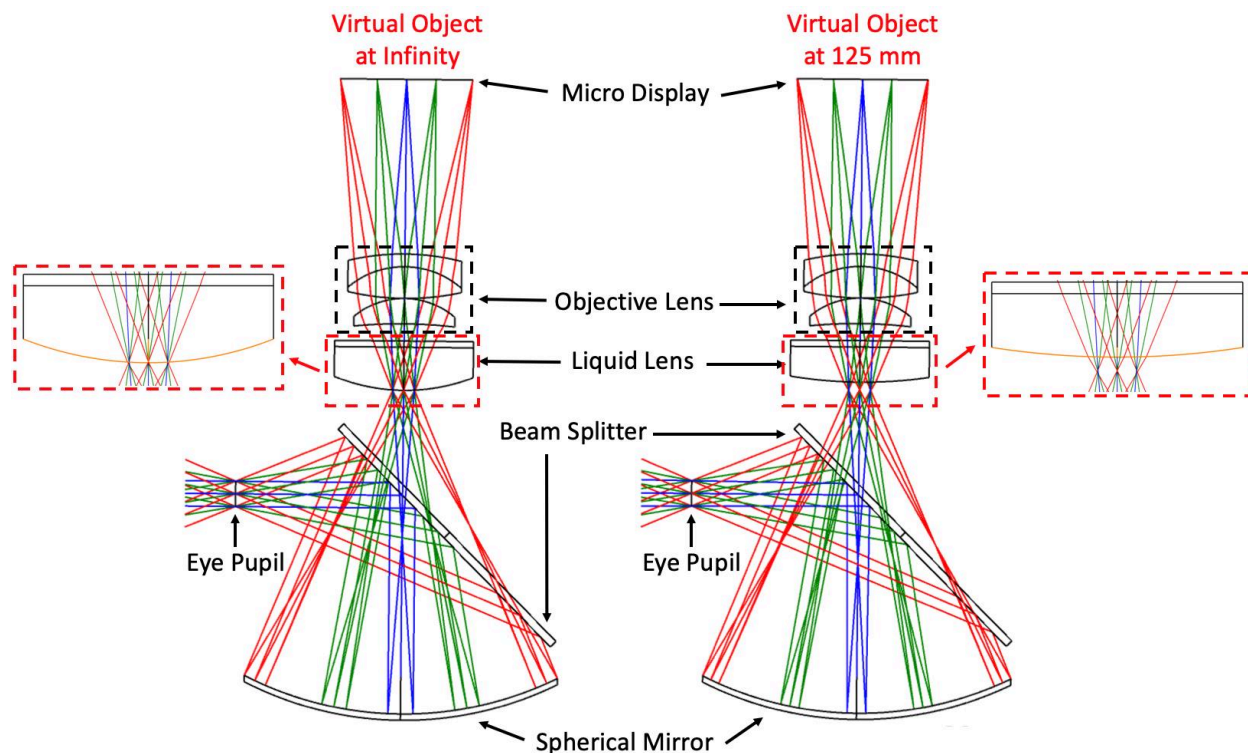


Figure 4.10. A wide FOV HMD with commercial off-the-shelf liquid lens

Compare to mechanical moving vari-focus solution, liquid lens adds even less hardware complexity and can even be implant directly to an existing HMD system. In a recent paper published by Robert Konrad from Stanford University demonstrated an HMD with reduced VAC simply by attaching 2 off-the-shelf liquid lenses from Optotune onto a commercially available HMD (Oculus Rift DK2) [72] [Fig. 4.11]. The setup achieved an accommodation range from 10.5 cm to infinity with a fast response time of 15 ms at room temperature. The biggest drawback of this setup is the small clear aperture of the liquid lens. Compare to the systems showed in Fig 4.9 and Fig 4.10, since the liquid lens is now positioned away from the stop of objective lens, the clear aperture of the liquid lens now becomes the limiting factor of FOV. The system proposed in Robert's paper with a 10 mm clear aperture liquid lens attached on the HMD only achieved a maximum FOV of approximately 26° , which is a significant reduction from its original 100° FOV.

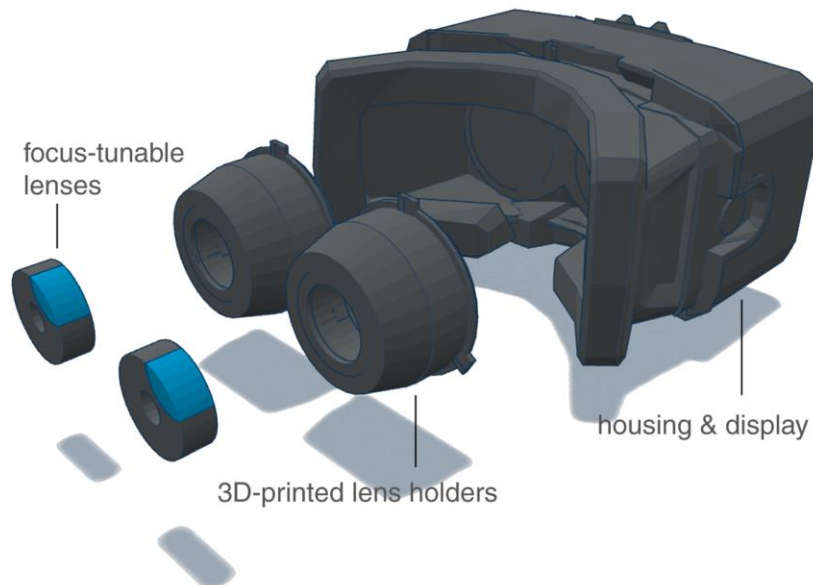


Figure 4.11. A focus-tunable near-eye HMD based on commercially off-the-shelf components [72]

Other than the focus tunable ophthalmic lenses and HMDs, another application of 3D microscopy that is enabled by liquid lens is also trending lately. For a nominal infinite conjugate microscope setup, the illumination light is focused on the specimen placed at the front focal plane of the microscope objective as shown in Fig. 4.12(a). In order to image the specimen at different depths, either the objective or the specimen traditionally must be moved mechanically along Z-axis, thus significantly reducing the imaging speed. In recent years, as shown in Fig. 4.12(b), a liquid lens setup with a tuning range from negative to positive focal length has been developed to focus and image the specimen at different depths. Compare to the mechanical scanning, motion-free scanning with liquid lens reduces vibration to the specimen during the movement, and the scanning speed could be faster. One major drawback of this setup is that the new objective loses its telecentricity, which is standard for most of the high-end refractive infinite conjugate objectives. However, since now the objective scans through multiple focal planes, the impact caused by the non-telecentric nature of the system is not significant. An alternate solution is to relay the system with a 4F system and put the liquid lens at its conjugate pupil. Nevertheless, this solution is much

less practical than putting the liquid lens directly above the objective since a relatively large space to insert the relay system between the objective lens and tube lens is required [Fig. 4.13].

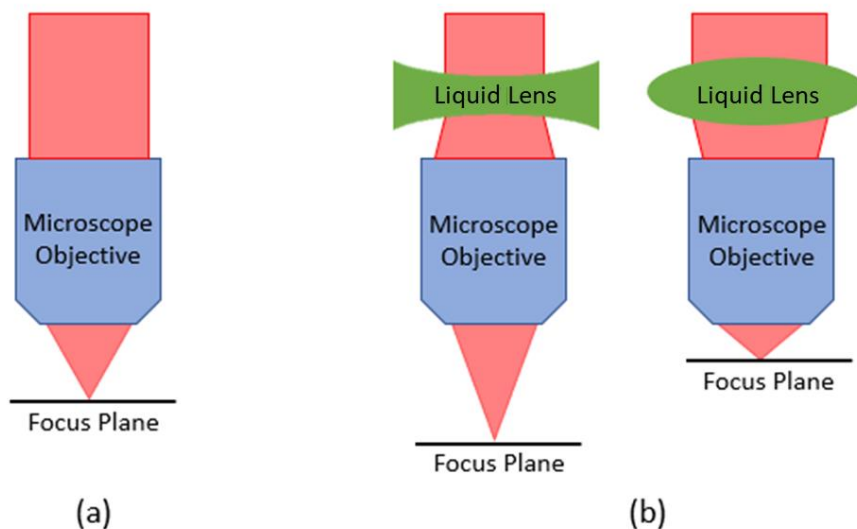


Figure 4.12. Light propagation through (a) a conventional infinite conjugate objective with a fixed focus plane and (b) an infinite conjugate objective pairs with a liquid lens

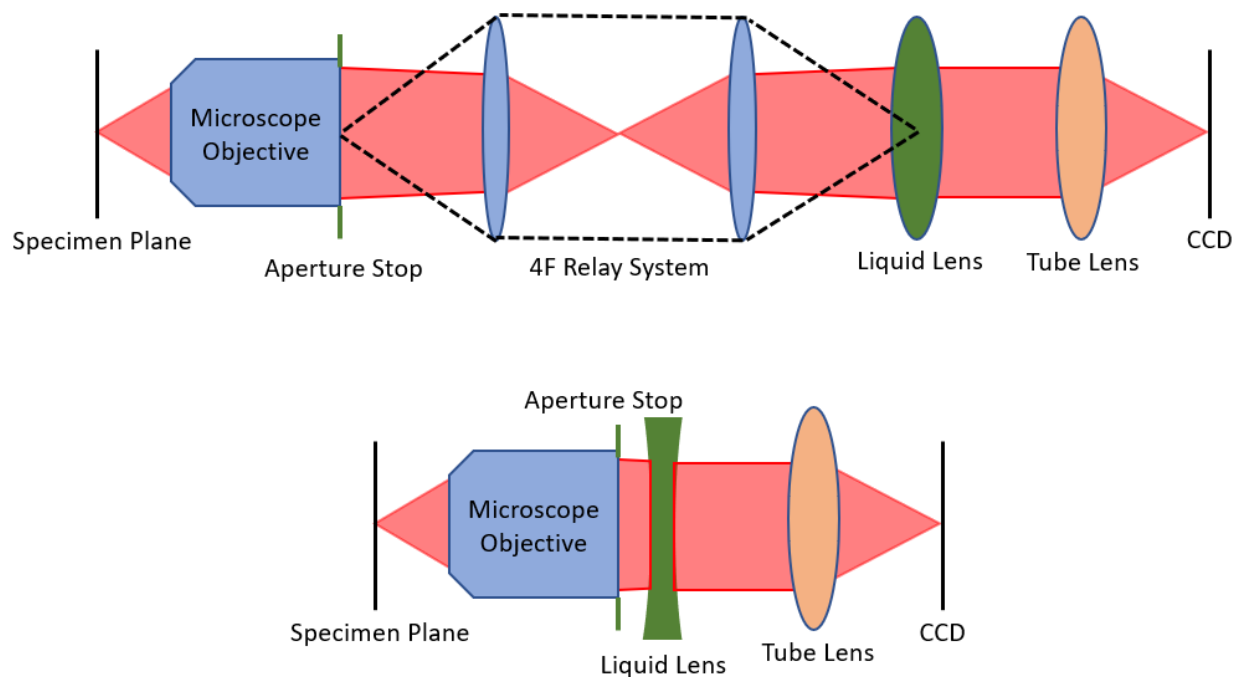


Figure 4.13. System comparison between putting liquid lens at conjugated pupil of aperture stop (top) and putting liquid lens directly above microscope objective close to the aperture stop (bottom).

Recently, a number of studies on motion-less 3D microscopy using liquid lenses are published [73, 74, 75]. However, the image quality impact from adding the liquid lenses into the microscope system is rarely discussed. In addition, methods to correct chromatic aberration for liquid lenses are also missing in previous published references. These problems will be discussed in detail in the next section.

Besides the above 3 applications, focus sweeping using liquid lenses are also integrated in many other applications, such as machine vision, laser processing and focus sweep videography [76]. The fundamentals behind these applications are all similar, which is to acquire image at different field depth. The integration of liquid lens into these applications are relatively straight forward as only small depth change and single liquid lens element is required. To enable large focus change, usually more complicated systems and multiple liquid lenses are required. This will be discussed in the next sub-section.

4.2.2 Zoom System based on Liquid Lens

Zoom systems are often found in numerous fields of optics. Conventional zoom systems utilize physical movements between different optical element groups to change the system's optical power via mechanical motion. However, traditional zoom systems with mechanical moving parts have many limitations, such as system large packaging size and slow zooming speed. Zoom system based on liquid lens can achieve much faster zooming speed with a smaller packaging size due to no mechanical moving parts. Liquid lenses also offer more degrees of freedom during zooming by varying focal length of individual liquid lens rather than changing the separation between fixed focus lenses. In addition, from manufacture standpoint, lens designers do not have to concern about element misalignment during zooming for zoom systems based on liquid lenses.

For over a decade, these benefits drove engineers and researchers to develop various types of optical zoom system using liquid lenses.

Among different optical systems that are based on focus changing of liquid lenses, perhaps the most straight forward application is the telescope. From fundamental geometric optics, we know the magnification of an afocal telescope is

$$M = \frac{f_o}{f_e} \quad (4.1)$$

where f_o is the focal length of the objective, and f_e is the focal length of the eyepiece. For conventional telescopes, since the focal length of the objective is fixed, difference magnification can only be achieved by changing eye piece with different focal lengths. In 2013, Nickolaos Savidis introduced a Keplerian telescope with two plano-convex liquid lenses [77][Fig.4.14]. The focal length of the objective ranges from approximately 32.5 to 340 mm. The focal length of eye piece can change accordantly to maintain the common focal point between objective and eyepiece. The magnification ranges from 0.1x to 10x, provides a 100x full range of magnification. However, the design and experiment in this paper only demonstrate the first order optics concept of an afocal zoom system using liquid lenses. No aberration control is applied in the design and image quality is rather poor. The author also points out the vignetting problem caused by small aperture of the liquid lenses.

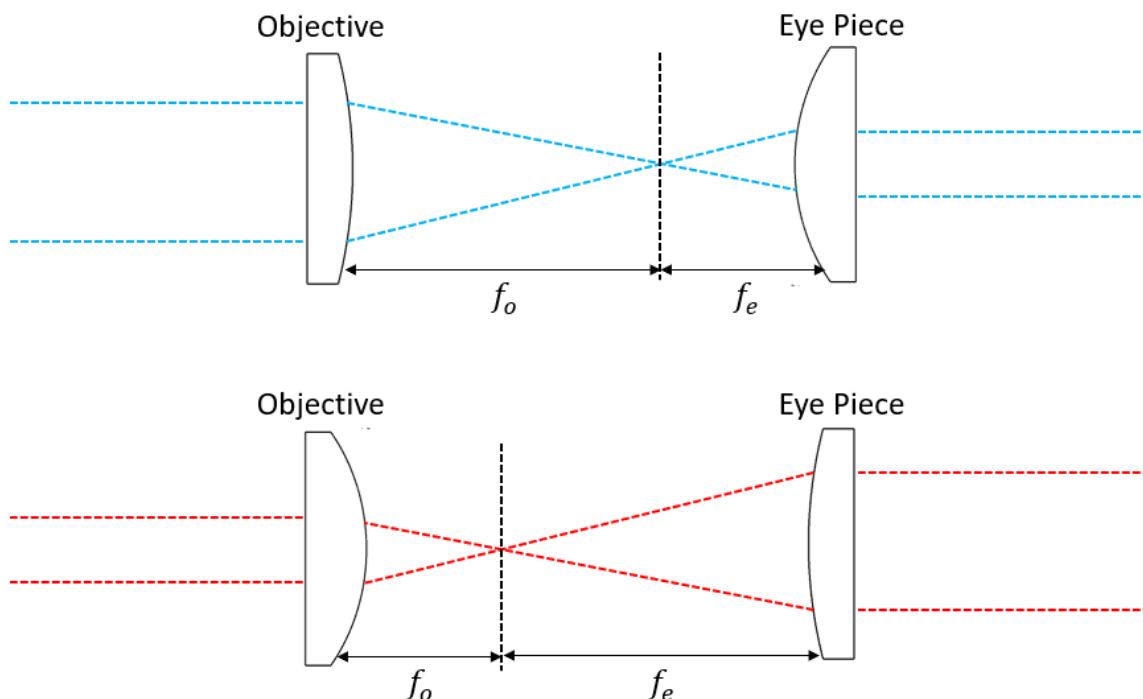


Figure 4.14. An afocal zoom system. Both objective and eye piece are liquid lenses introduced by Nickolaos Savidis

While Savidis's design is based on an afocal system, he did also propose to add another lens behind the afocal system to focus the image on a CCD sensor, then the system becomes a zoom imaging system. However, having an intermediate image plane is not ideal for most of the imaging systems. Many efforts have been spent by numerous researchers to utilize liquid lenses in imaging systems. One great example is the 4x zoom laparoscope presented by Seungwan Lee in 2013 [78][Fig 4.15]. Conventional laparoscopes themselves do not have mechanical zoom capability due to the limited packaging size. A zoom adapter between the lens and the sensor is needed for zooming purpose and the magnification is usually very limited. In this paper, the author designed a 3-group 3D laparoscope that is capable of changing its effective focal length from 3.24 mm to 12.94 mm to achieve a 4x zoom. The first group contains a meniscus lens to reduce chief ray angle and accept wide angle FOV. It also contains one liquid lens and one achromatic doublet. The second group contains one positive lens and a liquid iris to adjust stop size. The third group contains another pair of liquid lens and achromatic doublet. Two additional aspherical lenses were

also included in the third group to further correct off-axis aberration. In addition to the 2 doublets, to further correct chromatic aberration, the author also designed a diffractive optical element (DOE) on the surface of liquid iris. The entire system contains no mechanical moving parts but provides a larger magnification range compare to conventional laparoscope. From the paper, the simulated optical performance is promising. However, no lab validation was presented in this paper, so the actual performance is unknown.

Another critical field for liquid-lens-based zoom system is photographic lens, specifically miniature zoom lens for mobile devices. Mechanical zoom lenses have been used for conventional cameras for decades, however, it has not been successfully integrated into mobile devices yet due to limited packaging size and alignment difficulty. Thus, engineers and researchers are eager to develop miniature zoom lens with liquid lenses for smaller packaging size and minimum mechanical moving parts. In 2007, S. Kuiper from Philips Research presented a 1.7x zoom camera based on two liquid lenses and three plastic aspherical lenses [79] [Fig 4.16]. The zoom lens can support 60° FOV at wide angle position and 37° FOV at telephoto position. This lens was manufactured, and image quality was evaluated by Kuiper. The image is rather noisy, and contrast is lower compare to image taken by commercial miniature camera. Low transmission due to Fresnel loss at 16 uncoated lens surfaces were identified as the root cause for image quality degrade by Kuiper. He also commented on the difficulty of chromatic aberration correction for this system. Despite the low dispersion of liquid lens material, correcting chromatic aberration for a system contains liquid lens is actually very challenging. This topic will be discussed in detail later in section 4.4.

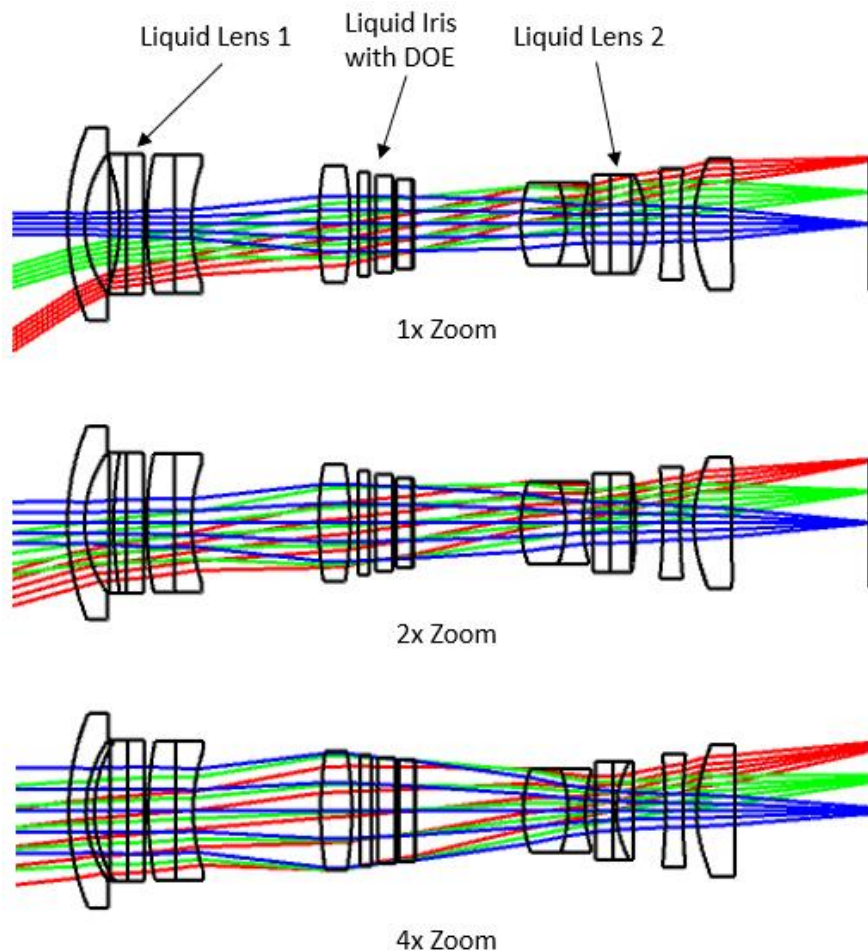


Figure 4.15. A 4x zoom laparoscope presented by Lee.

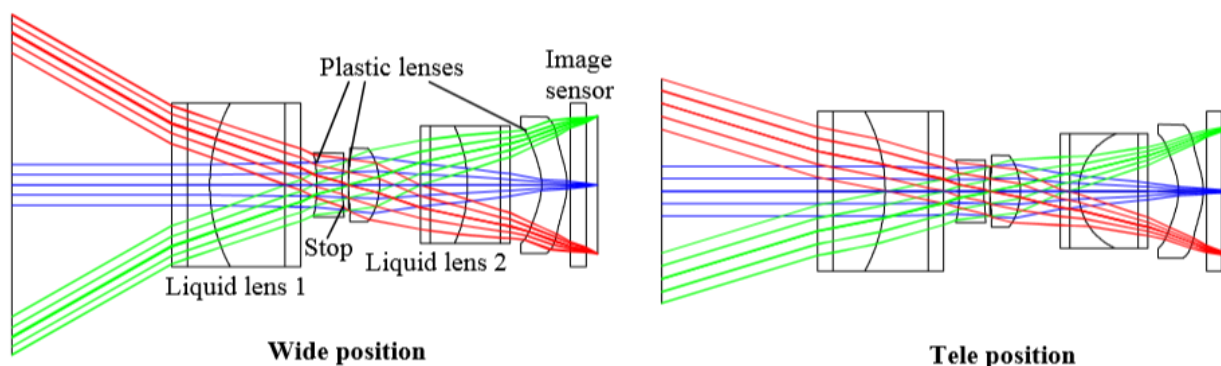


Figure 4.16. A 1.7x zoom camera lens presented by Kuiper [79].

Another attempt to make a miniature zoom lens with liquid lenses were presented by Pengpeng Zhao in 2018 [80] [Fig 4.17]. In his design, 2 liquid lenses were used along with 3 static lenses to achieve 2x optical zoom. A folding mirror is also used after the first lens element to reduce lens thickness along z direction. The entire system dimension is 5 mm x 6.5 mm x 17 mm.

The focal length of the first liquid lens changes from 24.9 mm to 7.1 mm, and the second liquid lens has a focal length range from -28 mm to -5.3 mm. The effective focal length (EFL) of the system changes from 4.5 mm to 9 mm, with a FOV ranging from 40° to 20° respectively. Compare to Kuiper's design, Zhao's design achieves slightly larger zoom ratio and FOV range. But the real novelty of Zhao's design are the special designed gravity immune liquid lenses. Between the focal range of 6.1 mm to 9 mm where the two liquid lenses have relative smaller curvature, both of these them exhibits gravity-immunity. Besides that, the liquid lenses used for this system are made to be aspherical to reduce spherical aberration. Although almost diffractive limited performance was claimed for this system, aperture information was not revealed in the paper. From the cutoff frequency of the MTF plots, the system $F/\#$ is likely to be larger than $F/5$ at wide angle position and larger than $F/8$ at telephoto position. This level of aperture sizes is too small for practical mobile devices today. Chromatic aberration correction was also not mentioned in this paper.

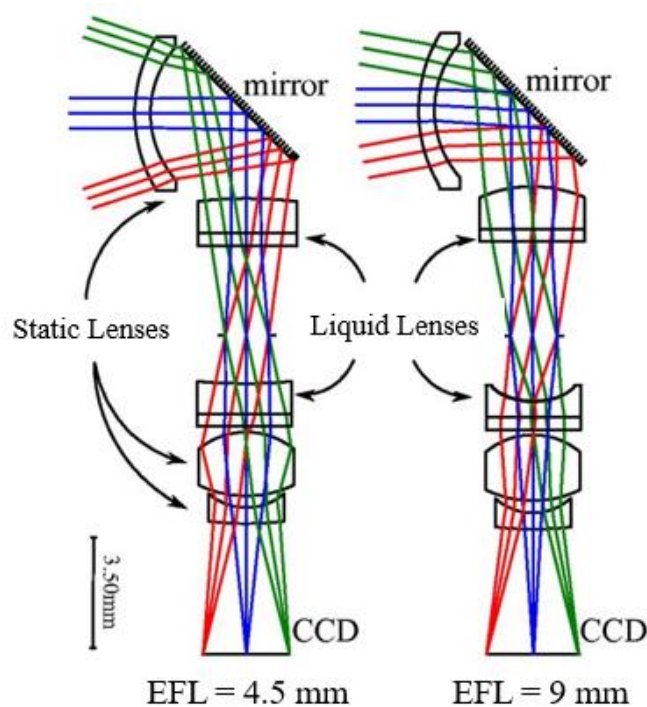


Figure 4.17. A 2x zoom camera lens presented by Zhao [80].

The miniature zoom lenses published previously showed great design challenges. First, to reduce impact of gravity, liquid lenses usually have small aperture. To construct a zoom lens, a variation group and compensation group are needed, which means at least two liquid lenses are required for such system. Thus, to minimize the chief ray heights at liquid lens surfaces, the stop is usually placed between two liquid lenses. This does not agree with the design philosophy of a modern miniature lens where the stop is placed in the very front for small packaging size. Also, current liquid lenses have very small focus tuning range, which makes zoom ratio small within limited packaging size, usually no more than 2x. In addition, aberration correction, especially for chromatic aberration, is very hard compare to conventional zoom lens design. In Fig 4.18, an aberration corrected 2x miniature zoom lens system designed by the author of this dissertation is presented. 5 static lenses with spherical surfaces and 2 liquid lenses with focal length ranging from -17 mm to +17 mm (in red boxes) were used to achieve a focal range from 2 mm to 4mm. The lens is designed to achieve 56° FOV at wide angle position and 28° at telephoto position. The maximum aperture is F/2.8 at wide angle position and F/4 at telephoto position. Both FOV and F/# are more practical than previous designs. The optical performance of this system is presented in Fig 4.19. The system can achieve almost diffractive limited performance at telephoto position and still maintain very good contrast at wide angle position. Also, from the focal shift plots in Fig 4.19, the system is achromatic at both telephoto zoom position and wide angle zoom position, which has never been done in previous literatures. The packaging size without mounts is 12.5 mm x 7.5 mm. This size is reasonable to be integrated in modern mobile devices.

When Kuiper first presented his design in 2007, he was very optimistic about the future of miniature zoom lens based on liquid lenses and projected mass production to be soon. However, despite many efforts from the industry [81, 82], such lenses were never made into mass production

until today. The biggest bottleneck perhaps is the small optical zoom range and bulk packaging size compare to conventional miniature lenses. Today, most of the modern mobile devices have multiple miniature lenses with different focal lengths combining with digital crop to provide relatively large zoom range. A miniature zoom lens with liquid lenses is very unlikely to be integrated with mobile devices in the near future until a significant increase in zoom ratio.

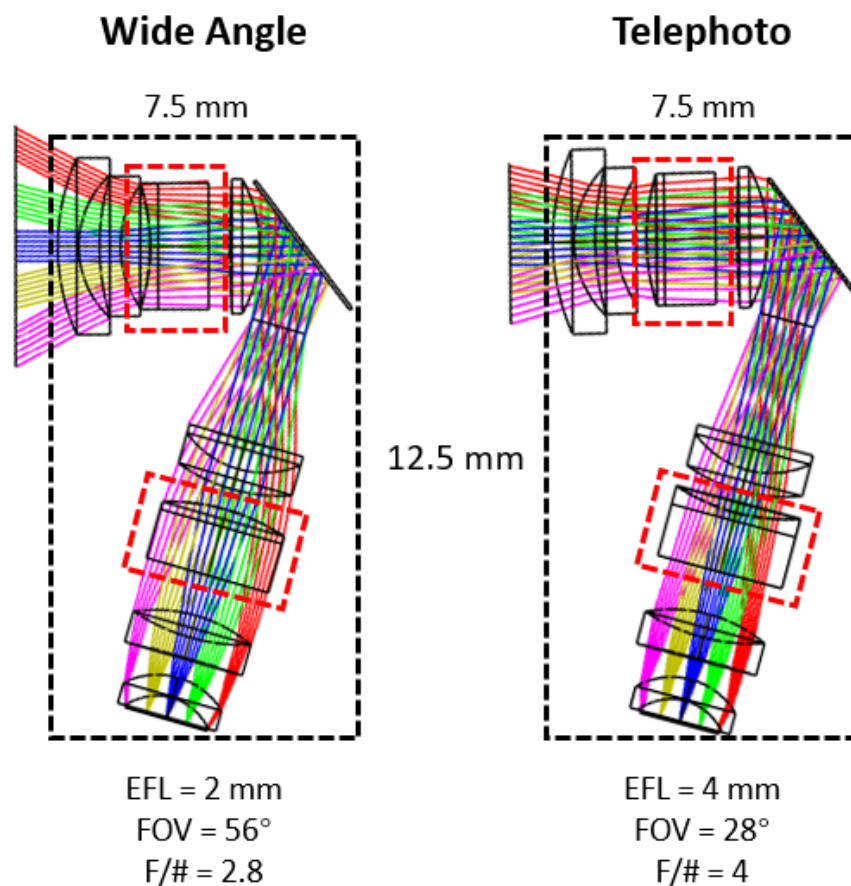


Figure 4.18. A 2x zoom camera lens with chromatic aberration correction.

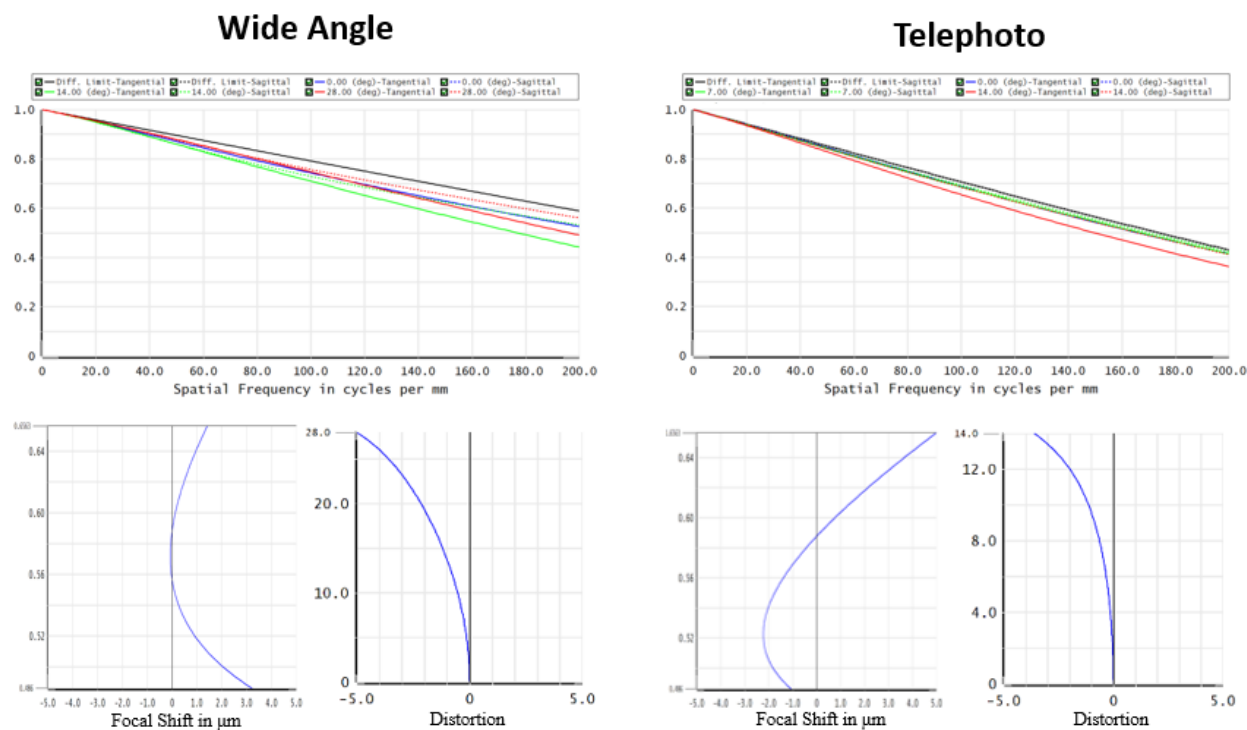


Figure 4.19. Optical performance of the 2x zoom lens based on liquid lenses

Since photographic zoom lenses purely based on liquid lenses are challenging, some hybrid designs that combines mechanic zoom lens and liquid lens together were proposed, such as the 2.5x miniature zoom lens presented by F. C. Wippermann [83] in 2006 and the 2.6x miniature zoom lens presented by Jung-Huang Sun in 2009 [84] [Fig. 4.20]. These systems offer slightly larger zoom ratio and better optical performance than the zoom lenses discussed above with no mechanical moving parts. The tradeoffs are larger packaging size with more complexity in structure. In 2013, Canon patented several hybrid zoom-lens designs for APS-C DSLR cameras, with maximum zoom ratio up to 9.8x [85][Fig. 4.21]. With the assistance of liquid lenses, these zoom lenses are able to maintain same track length during moving. Olympus and Eastman Kodak also filed similar patents [86, 87]. Nevertheless, these lenses were never made to mass production.

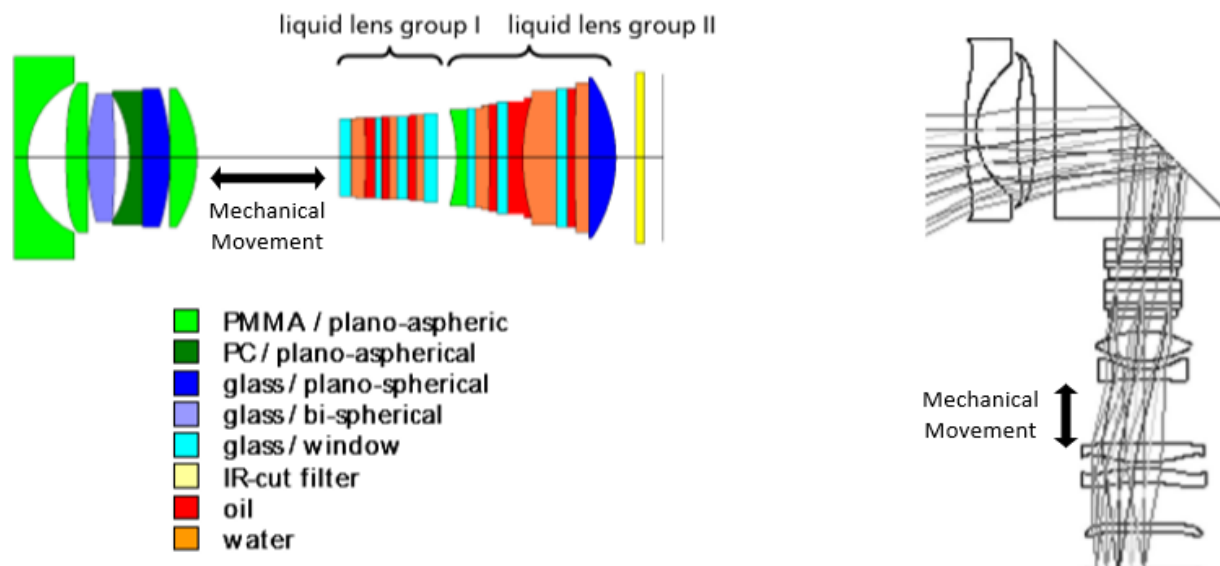


Figure 4.20. 2.5x hybrid zoom lens presented by Wippermann (left) and 2.6x hybrid zoom lens presented by Sun [83, 84]

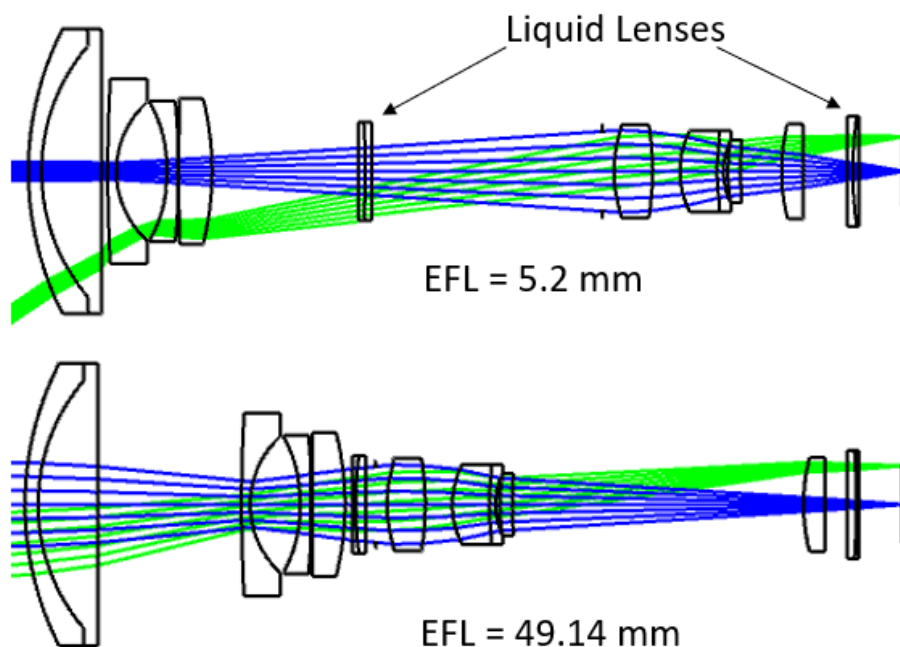


Figure 4.21. A 9.8x hybrid zoom lens patented by Canon [85]

4.2.3 Nonmechanical Beam Steering

Another innovative application based on liquid lens is beam steering. In previous sections, liquid lenses were placed on axis within an axial symmetric optical system. If a liquid lens is decentered from system optical axis intentionally, nonmechanical beam steering can be achieved.

Fig 4.22 illustrate such concept with 2 liquid lenses. Ray bundle can be steered using the decentered liquid lens. The steering angle is controlled by adjusting surface curvature of the decentered liquid lens. However, during the curvature change, system focal length is also changed. Then an additional on-axis liquid lens can be added into the system to maintain the desired focus. Compare to conventional mechanical beam steering method such as using MEMS mirror, this method is more reliable, response faster and consume less power.

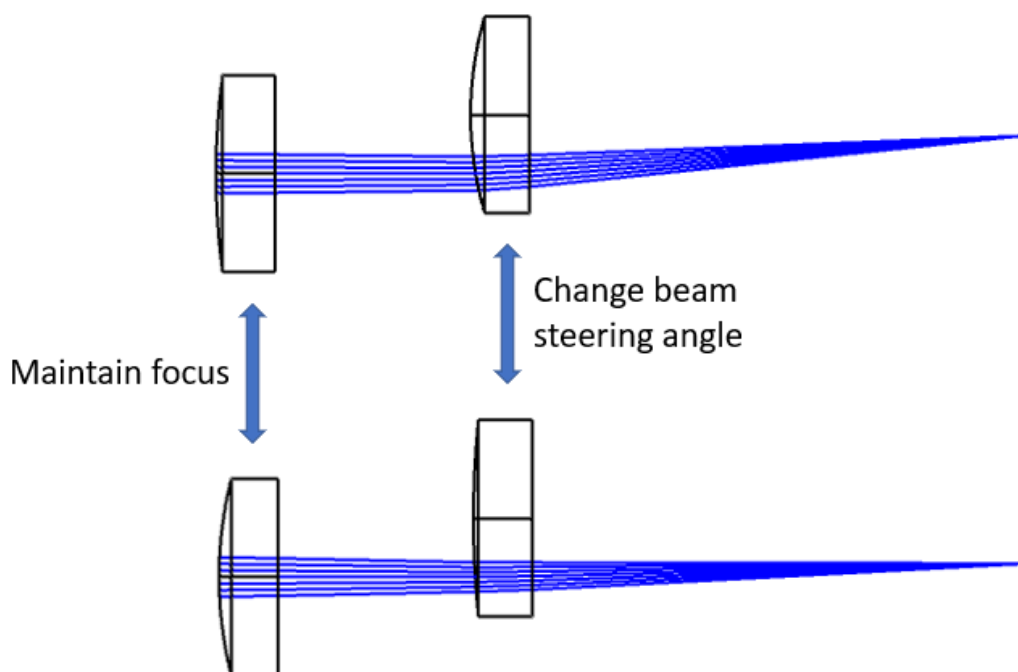


Figure 4.22. A non-mechanical beam steering system using liquid lenses

In 2016, Mo Zohrabi proposed a wide-angle non-mechanical beam steering system based on liquid lenses [88]. The system utilized 2 decentered tunable lenses to shift beam in both X and Y direction while maintaining system power with an additional 3rd liquid lens on axis. By adding a relay lens and pair the optical system with other conventional objective lenses, higher steering angle range can be achieved. An ultra-wide angle optical beam steering system that pairs liquid lenses with an existing fisheye lens is also demonstrated by Zohrabi to provide $\pm 90^\circ$ 2D beam scanning in all direction [Fig 4.23].

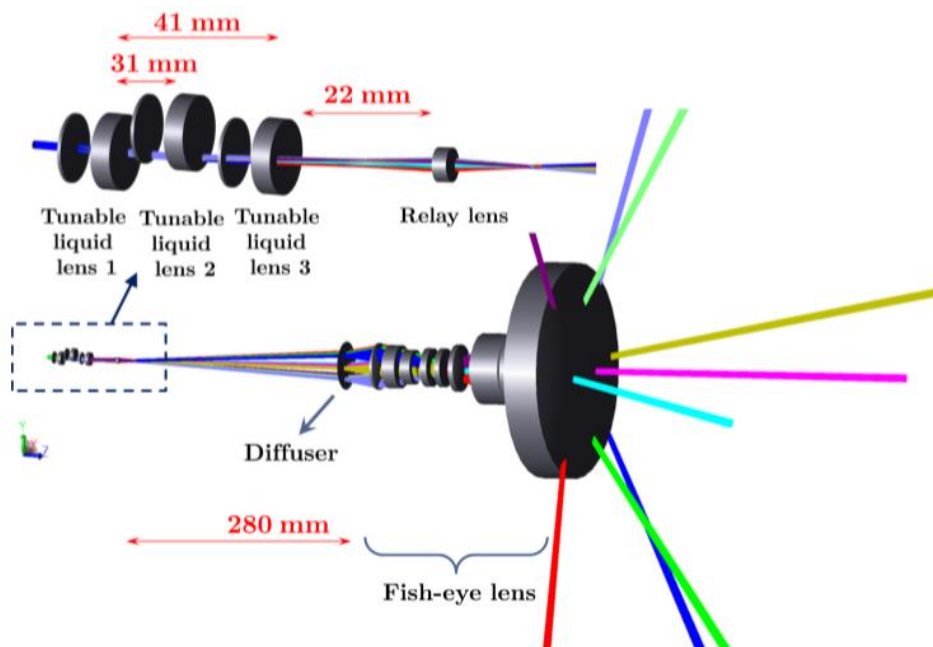


Figure 4.23. An ultra-wide angle non-mechanical beam steering system using liquid lenses presented by Zohrabi [88]

The ultra-wide angle beam steering system presented by Zohrabi can be a potential candidate for LIDAR applications in autonomous driving systems where wide angle beam steering is crucial. Similar method was also be adopted by conventional photographic lenses for image stabilization. Conventional image stabilization for modern DSLR and mirrorless camera depends on the movement of compensation optical element in the lens or CMOS sensor in camera body. In 2017, Blackeye Optics LLC was granted a patent that utilizing liquid lenses for image stabilization [89][Fig 4.24]. In this design, four liquid lenses were used to slightly shift image in both X and Y direction and maintain the focus. MTF plots were also presented in the patent file that indicates very minor image quality downgrade with the change of surface curvatures of liquid lenses. This design concept shows great potential to replace conventional image stabilization due to its low cost, compact size and significantly lower noise level, which is critical for professional video shooting.

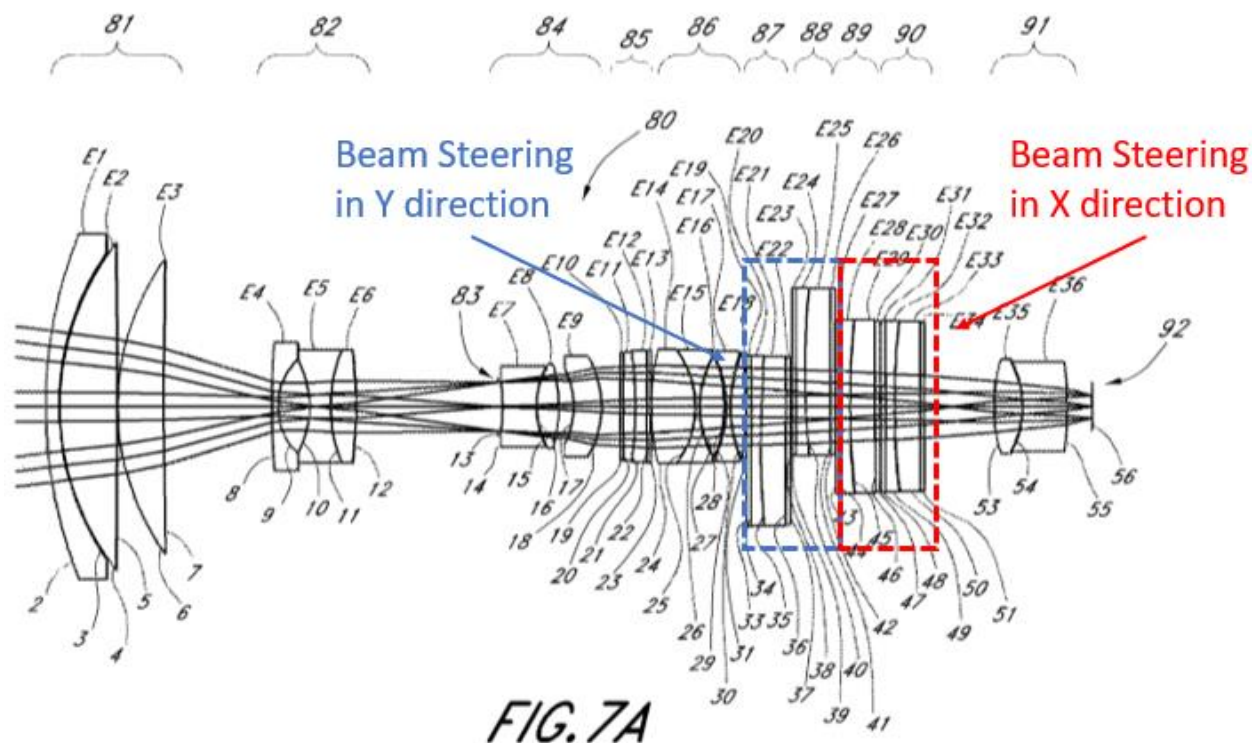


Figure 4.24. A camera lens with liquid lens optical image stabilizer [89]

4.3 Optical Performance Evaluation of Liquid Lens used for 3D microscopy

A brief introduction of 3D microscopy utilizing liquid lenses were given in section 4.2.3, and the corresponding drawings were illustrated in Fig 4.16 and Fig 4.17. Recently, there are a number of studies on motion-less 3D microscopy using liquid lenses [90, 91, 92]. Nevertheless, most papers seem to focus on the capability of 3D scanning rather than the optical performance. Since high-end microscope objectives are mostly diffraction limited, and the liquid lenses are designed without the consideration of aberration control, attaching liquid lens on the objective will certainly impact the optical performance of the objective. Also, chromatic aberration correction was rarely discussed. It seems the manufacturers of liquid lenses are purely relying on the low dispersion material for maintaining low chromatic aberration without any further color correction [93]. Furthermore, when discussing the applications of liquid lenses in general, the impact caused by gravity when positioning liquid lenses in the horizontal direction is often overlooked by

designers. In this section, these issues are addressed by providing a comprehensive evaluation on optical performance of 3D microscopy using liquid lens. We perform the evaluation both in software simulation and experiment. In addition, a novel method for correcting chromatic aberration of liquid lens is proposed in the next section.

4.3.1 Simulation and Experiment Setup

Fig. 4.24 demonstrates the setup for the simulation. The liquid lens used in the simulation is the Optotune EL-10-30-TC. The theoretical power tuning range of this lens is +8.3 dpt to +20 dpt (+120 mm to +50 mm in focal length). However, the lens shape loses stability at the extreme of its tuning range, so the power tuning range is limited between +9 dpt and +16 dpt. Note that power tuning range of this lens is entirely positive, so an offset lens (OL) is paired with the liquid lens to shift the tuning range to include both positive and negative power. A -75mm focal length plano-concave lens is used as the OL, which brings the power tuning range of the combined setup to from -3.65 dpt to 4 dpt (-274 mm to $-\infty$ mm and +250mm to $+\infty$ mm in focal length). It will be ideal to evaluate the performance with real lens data of microscope objectives, however almost all of the microscope objective vendors do not disclose the lens data for their infinite conjugate objectives. With the best effort, the author is able to acquire 4 “black box” Zemax files from Thorlabs, including a 2X (TL2X-SAP, NA = 0.1) and a 4X (TL4X-SAP, NA = 0.2) refractive apochromatic objectives, a 15X (LMM-15X, NA = 0.3) and a 40X (LMM-40X, NA = 0.5) reflective objectives for our simulation. Visible spectrum (F, d, C) are used as the wavelengths in the simulation. Input beam diameter is set to fulfill the full numerical aperture of each objective. For each set of simulation, on-axis MTF, chromatic aberration (longitudinal focal shift) and focal plane scanning range are evaluated. The MTF and chromatic aberration are evaluated at 5 different

FTL power settings at 9 dpt, 11 dpt, 12.43 dpt, 14 dpt and 16 dpt. 12.43 dpt is chosen because at this power, the combination of FTL and OL is afocal.

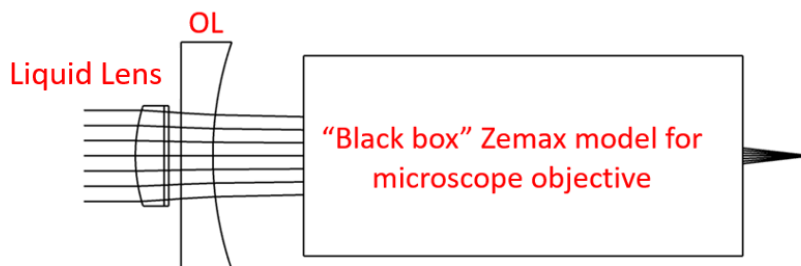


Figure 4.25. Simulation setup in Zemax

Figure 4.25 demonstrates the setup to evaluate the spherical aberration and chromatic focal shift introduced by the liquid lens. A Twyman-Green type interferometer is constructed and positioned vertically to minimize the gravity effect caused to the liquid lens. The polarization camera essentially provides phase shift and capture the interferogram at four different phases. A 5X Mitutoyo plan apochromatic objective with $NA = 0.14$ is used in this experiment. A collimated laser beam with enough beam diameter to cover the entire objective NA is used as light source. Perfect collimation is checked with shear plate for each wavelength. All the data measured in this experiment went through reproducibility test, where 5 sets of data were measured and averaged for each data point, with the objective and spherical mirror being re-aligned for every measurement. The measured wavefront is estimated from the final image and fit with Zernike polynomials in Matlab. Same as in the simulation, the spherical aberration and chromatic focal shift are evaluated at 5 liquid lens power settings at 9 dpt, 11 dpt, 12.43 dpt, 14 dpt and 16 dpt. Also, the objective without liquid lens is evaluated to serve as a reference.

While spherical aberration is straight forward and can be extract from the ninth Zernike coefficient Z_8 , the focus shift between different wavelengths is more complicated to measure. First, 3 Lasers with different wavelengths across the visible spectrum (488nm, 543nm and 633nm) are

used as the light source. Zernike coefficients are measured for each wavelength without changing the distance between the spherical mirror and objective. Then the field-independent wavefront aberration coefficient for focus is calculated by

$$W(r, \varphi)_{focus} = r^2(2Z_3 - 6Z_8 \pm \sqrt{Z_4^2 + Z_5^2}) \quad (4.2)$$

where ρ is radial distance, Z_3 , Z_4 , Z_5 and Z_8 are the fourth, fifth, sixth and ninth Zernike coefficient, and the sign is chosen to minimize the magnitude of the coefficient [94]. To accurately get the linear relationship between the field-independent wavefront aberration coefficient and the focus in mm, the system is calibrated for each wavelength independently by intentionally defocus the spherical mirror and record its new coefficient. Then the focus shift between different wavelengths can be calculated.

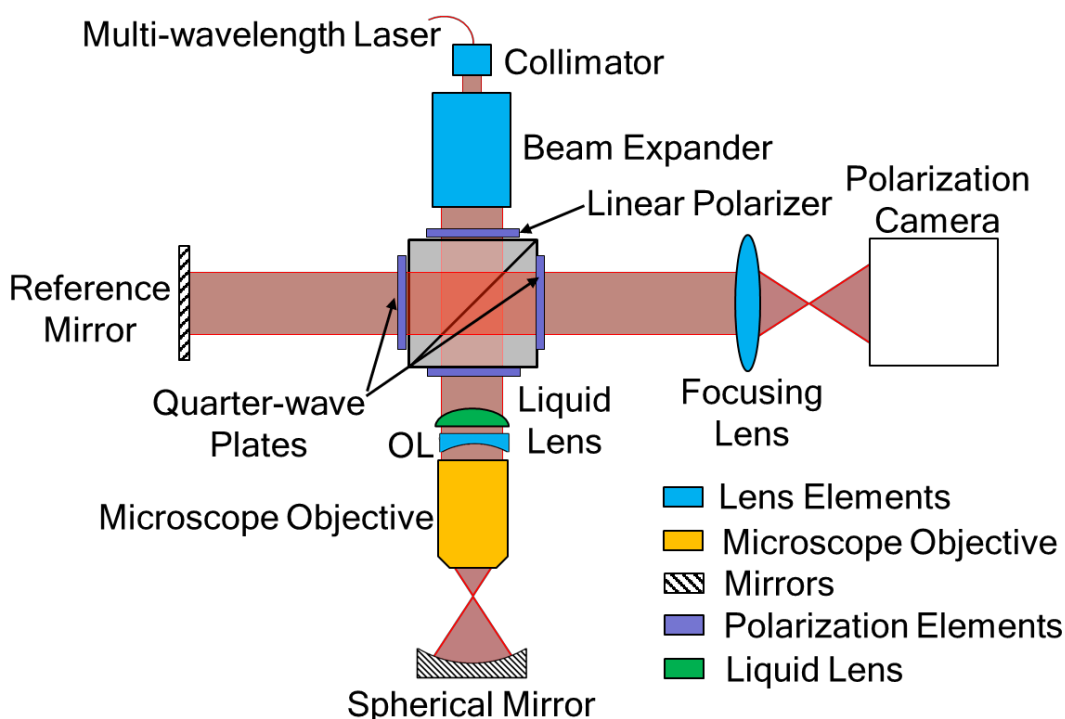


Figure 4.26. A Twyman-Green interferometer to measure the spherical aberration and chromatic focal shift of the 3D microscopy setup in vertical direction.

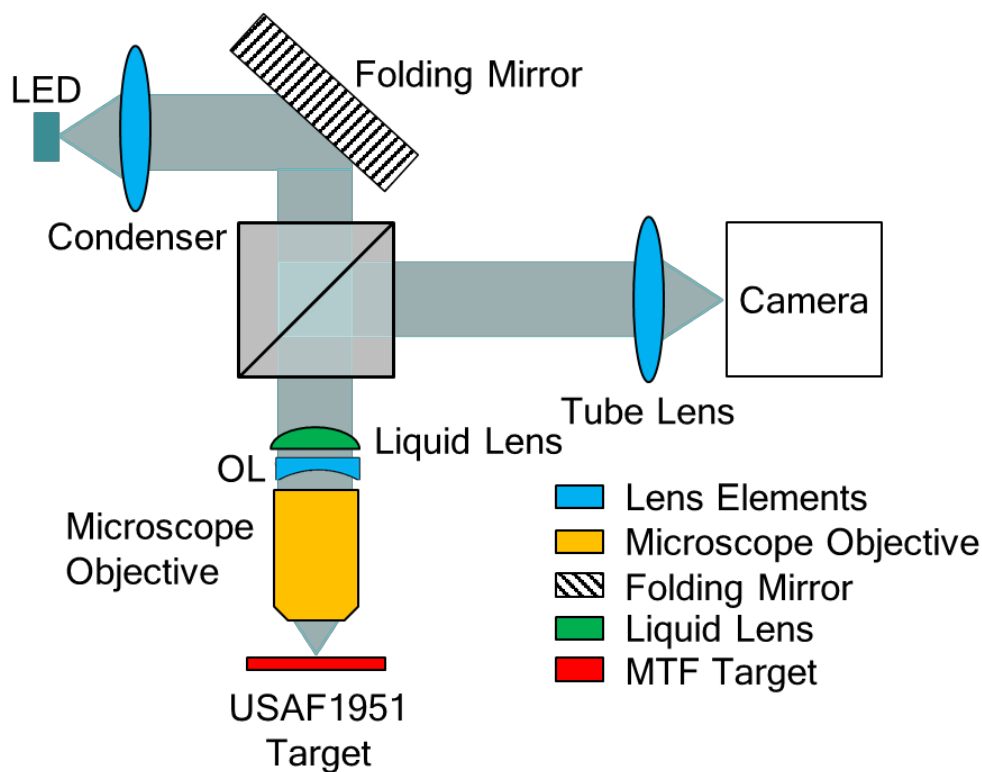


Figure 4.27. Setup to measure the image contrast with a USAF 1951 target to evaluate system resolution.

Figure 4.26 is the setup to test the impact caused to system resolution by the liquid lens setup. This is done by evaluating the image contrast with an USAF1951 target up to 9th group. A blue LED (peak at 455 nm) is used as the light source. A condenser lens is placed after the LED to collimate the divergent beam from the LED to fill the pupil of the objective. The illuminated target is imaged by the objective and a 200 mm tube lens to the camera. The image contrast is evaluated at 5 liquid lens power settings at 9 dpt, 11 dpt, 12.43 dpt, 14 dpt and 16 dpt, and is also evaluated without liquid lens as a reference.

Figure 4.27 shows two setups to evaluate the gravity effect with the FTL setup positioned in horizontal direction. Both interferogram and image contrast are evaluated with procedure similar to the previous evaluations. When the liquid lens is positioned in the horizontal direction, significant coma will appear due to the gravity pulling the polymer lens towards the ground. For

interferometric measurements, only 632.8 nm laser is used since chromatic aberration has no significant impact on monochromatic aberrations. Spherical aberration (Z_8) and coma in both directions (Z_8 and Z_8) are calculated from the interferograms. Both the aberration coefficients and the image contrast are compared with the data measured in the previous experiments where liquid lens is positioned in the vertical direction.

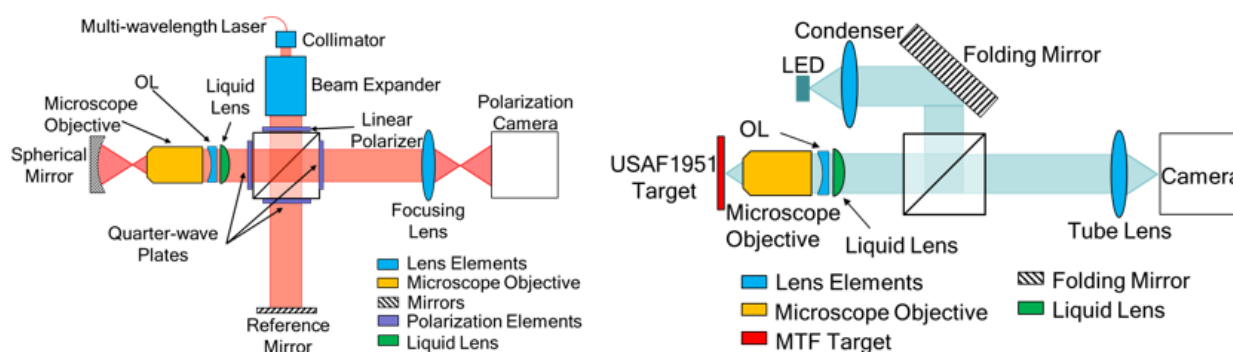


Figure 4.28. Setup to measure aberration and contrast of the 3D microscopy in horizontal direction to exam gravity effect.

4.3.2 Simulation and Experiment Results

Fig. 4.28 - 4.31 shows the scanning range and the on-axis MTF plots of the 4 chosen microscope objectives at 5 liquid lens power settings: 9 dpt, 11 dpt, 12.43 dpt, 14 dpt and 16 dpt. On-axis MTFs for the objective themselves without attaching the liquid lens are also provided as references. All of the 4 objectives are able to produce diffraction-limited performance before attaching the liquid lens. After the liquid lens is attached, on-axis MTF performance downgrades as expected. The decrease in contrast is more significant when paring the liquid lens with low magnification objectives. Contrast suffers less but still is noticeable when higher magnification objective lenses are used. At the same time, scanning range decreases when the objective magnification is increased. Between different power settings of the liquid lens, it seems for all the

objectives, the optimal contrast is achieved when the power of liquid lens is 12.43 dpt, where the total power of the liquid lens and OL is 0 dpt (afocal).

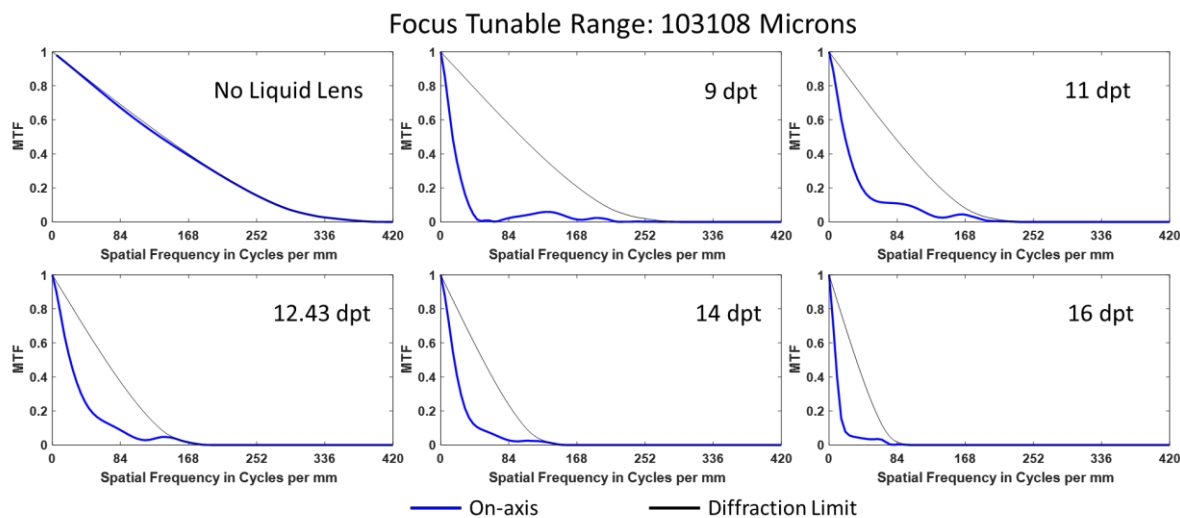


Figure 4.29. On-axis MTF of the liquid lens and OL paired with Thorlabs 2X refractive objective.

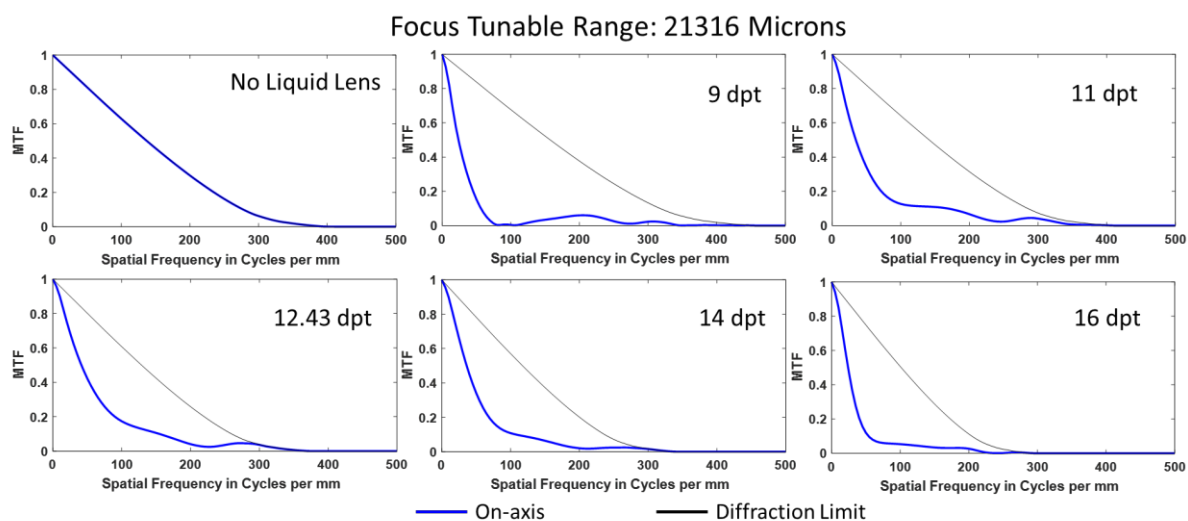


Figure 4.30. On-axis MTF of the liquid lens and OL paired with Thorlabs 4X refractive objective.

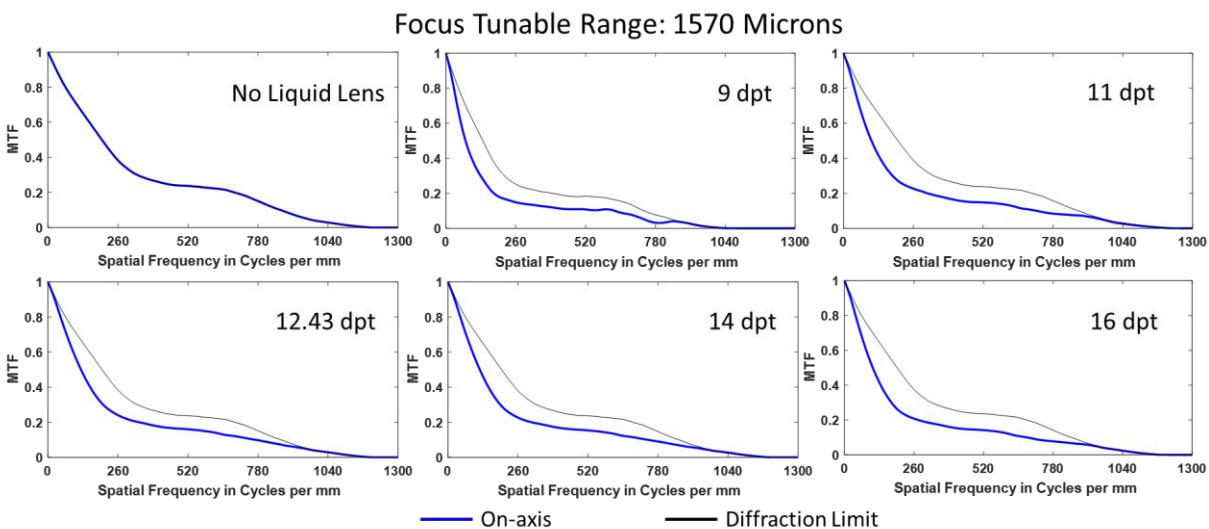


Figure 4.31. On-axis MTF of the liquid lens and OL paired with Thorlabs 15X reflective objective.

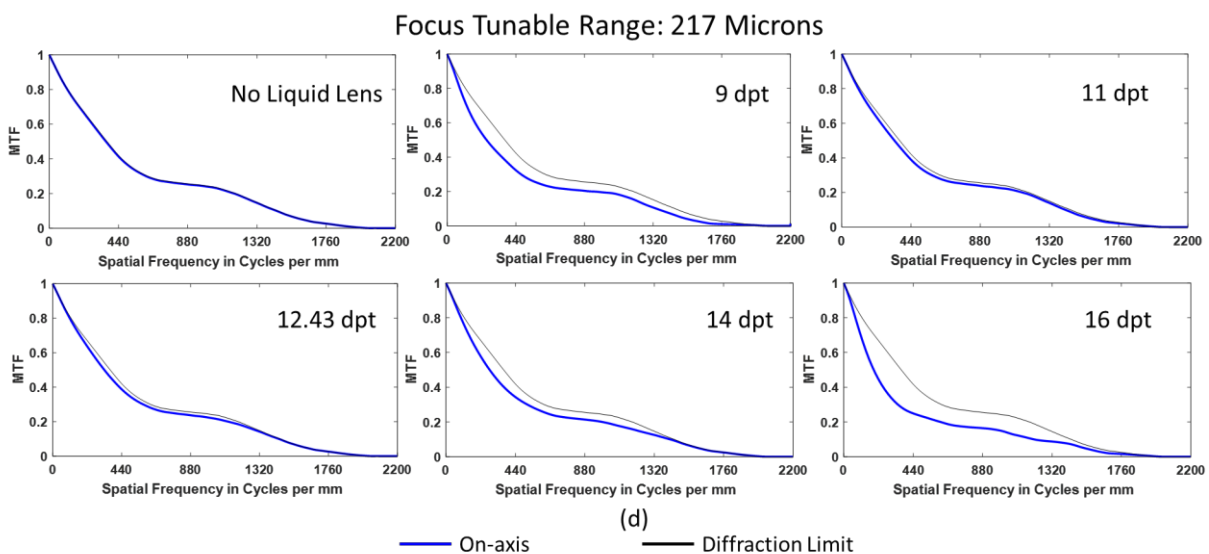


Figure 4.32. On-axis MTF of the liquid lens and OL paired with Thorlabs 40X reflective objective.

Fig. 4.32 shows the chromatic focal shift within the visible spectrum of the 4 chosen microscope objectives at the same 5 power settings. Focus shifts between the F-line and d-line (486nm and 588nm) and between the F-line and C-line (486nm and 656nm) are recorded at each liquid lens power setting. Significant chromatic shift is observed. As the power of the liquid lens increases, the effective focal length of the entire objective setup decreases, and the chromatic focal

shift reduces with the effective focal length. Another way to assess the chromatic aberration correction is to read the plot of chromatic focal shift vs. focal length. Fig. 4.33 compares the chromatic focal shifts between the objectives without liquid lens and with liquid lens set to 12.43 dpt. The evaluation spectrum is extended to 365 nm – 750 nm to further evaluate the chromatic focal shift. Both refractive objectives show clear sign of apochromatic correction while both reflective objectives have no chromatic focal shift due to their reflective nature. However, after attaching the liquid lens, the relationships between chromatic focal shift and wavelength are almost linear for all the objectives. This means, despite the low dispersion of the material used by for the liquid lens (Abbe Number ~ 105), the objective setup with the liquid lens shows no achromatic correction at all.

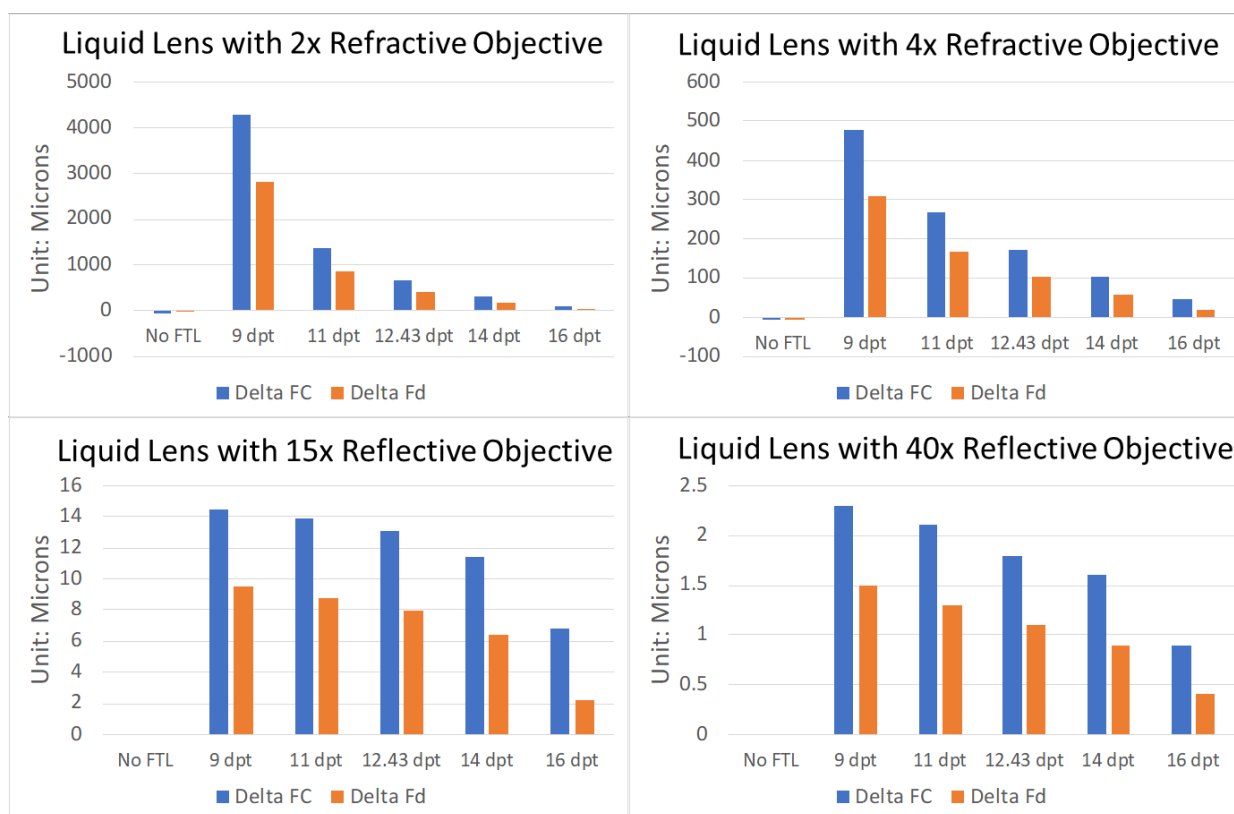


Figure 4.33. Chromatic focal shifts between F-line and C-line (blue bar) and between F-line and d-line (orange bar) for 4 chosen objectives with liquid lens and OL.

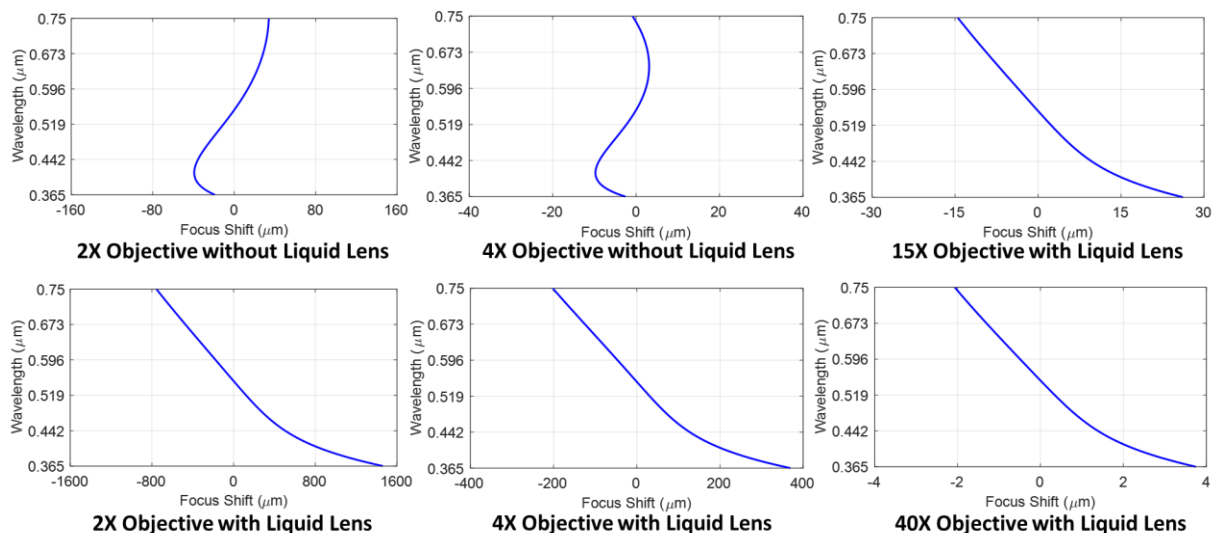


Figure 4.34. Chromatic focal shift plots for the objectives with and without liquid lens.

Fig. 4.34(a) shows the spherical aberration at each liquid lens power setting by measuring the 9th Zernike coefficient Z_8 using out Twyman-Green interferometer. The liquid lens setup is placed vertically so the gravity effect is minimum, and the surface shape of the liquid lens remains almost spherical within the clear aperture. Significant spherical aberration is observed in the experiment. Since the microscope objective without liquid lens setup is diffraction limited, spherical aberration observed in the experiment is contributed almost entirely by the liquid lens and OL. As we increase the power of the liquid lens, the curvature of the curved surface of liquid lens is also increasing, resulting a rapid increase of spherical aberration. In addition, the system shows noticeable spherochromatism, which is the color variation of the spherical aberration, at each liquid lens power setting.

To further investigate the chromatic aberration, color variation of the focal plane, also known as the focal shift, is evaluated by measuring the defocus of each wavelength using the interferometer. The results are showed in Fig. 4.34(b). Compared to the simulation result showed in Fig. 4.32, similar trend is observed. Chromatic focal shift with up to 58 times larger is observed when the power of liquid lens is set at 9 dpt, compared to the original microscope objective without

liquid lens attached. As the power of liquid lens increases, system focal length decreases, resulting in a reduction of chromatic focal shift. However, even at the largest liquid lens power setting of 16 dpt, the chromatic focal shift between the two extreme wavelengths (488 nm and 633 nm) is still more than 5 times larger than that of the original microscope objective.

Fig. 4.34(c) shows the contrast evaluation of the original microscope objective and the objective with liquid lens and OL attached at 5 liquid lens power settings. The images of USAF target are cropped to focus on groups 6, 7, 8 and 9. Fig. 4.34(d) shows the quantitative evaluation on the average contrast (sagittal and tangential) of the line pairs of group 7 element 1. A 50% to 80% contrast reduction, depending on the power setting of liquid lens, is observed after liquid lens and OL are attached. The highest contrast is observed when the liquid lens has a power of 12.43, which agrees with the finding from the simulation.

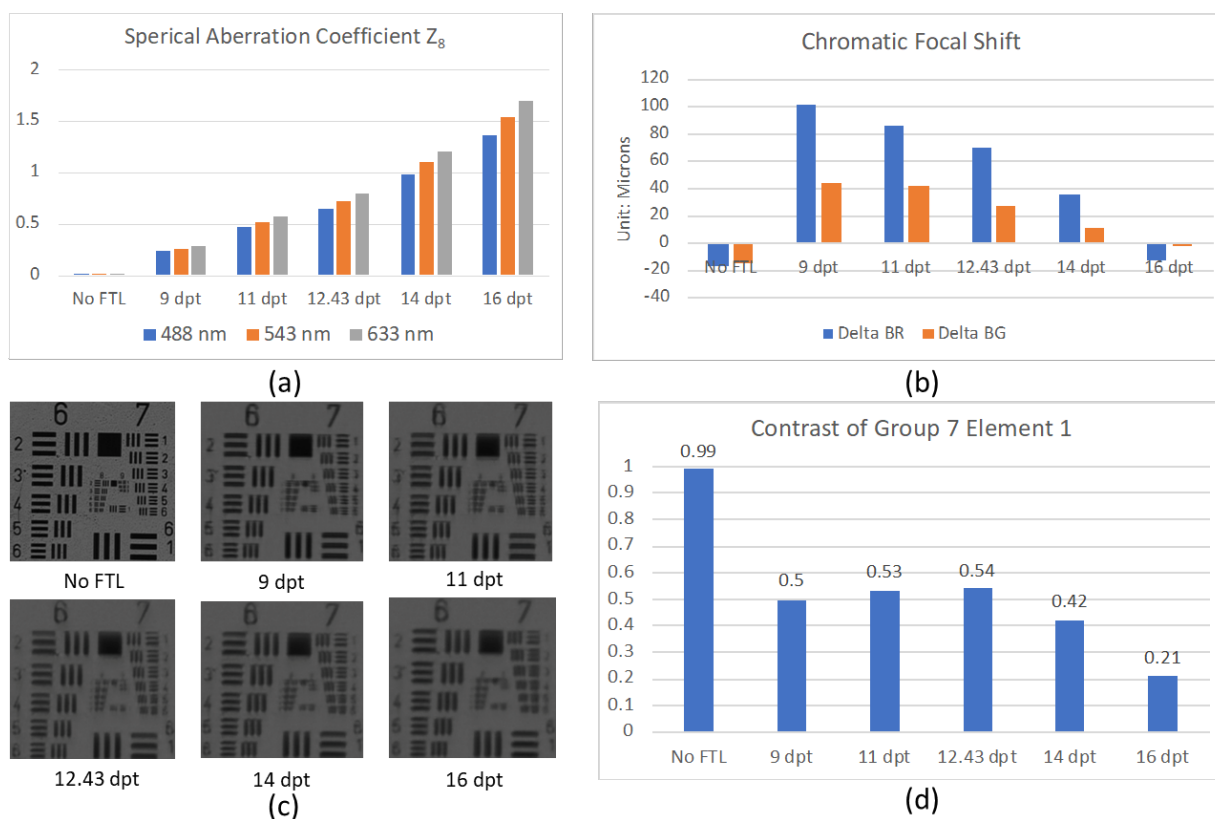


Figure 4.35. Optical performance evaluation of 3D microscopy setup in vertical direction

The evaluation of the liquid lens setup with gravity effect is shown in Fig. 4.35. The wavefront map calculated from the interferogram shows that coma becomes the dominate aberration when liquid lens setup is positioned horizontally. The Zernike coefficient of 3rd order spherical aberration Z_8 , and 3rd order coma Z_6 and Z_7 are presented in Fig. 4.35(a). The orientation of the liquid lens is set up so that Z_7 indicates the coma along the direction of gravity, where Z_6 is the coma orthogonal to the direction of gravity. Spherical aberration has small change compared to the vertical liquid lens setup. Coma coefficient Z_7 reduces slightly with the increase of liquid lens power, but the difference is not significant. Note the presence of coma orthogonal to the direction of gravity, this may be caused by the imperfection of the liquid lens itself. This effect can also be observed from the wavefront map in Fig. 4.35(b), where the direction of coma has a 6-degree departure from the direction of gravity. The presence of coma caused by gravity has a large impact on the image contrast. Fig. 4.35(c) shows the images of 1951 USAF resolution target with 5 liquid lens settings. The image quality is degraded significantly. Fig. 4.35(d) plots the corresponding average contrasts, showing the contrast decreases rapidly as the power of FTL increases. This experiment indicates that this type of FTL cannot be used horizontally.

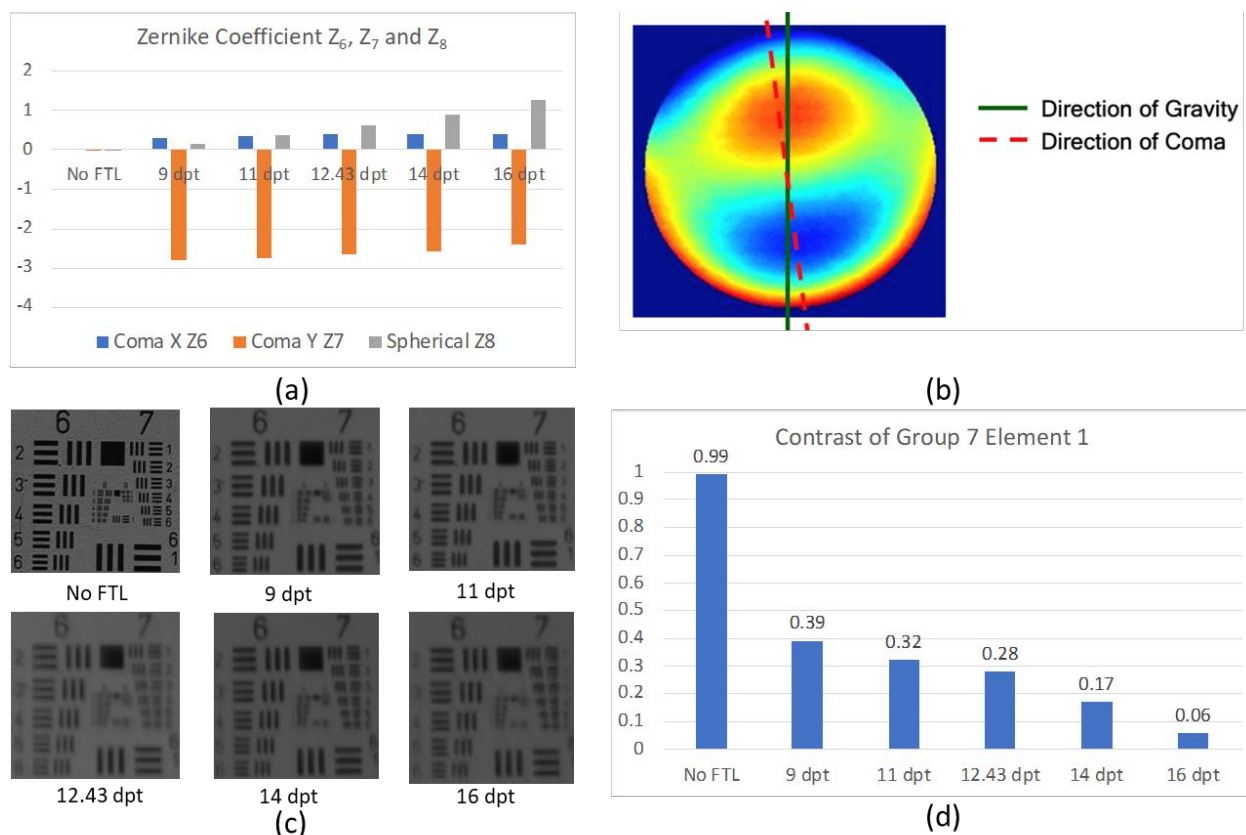


Figure 4.36. Optical performance evaluation of 3D microscopy setup in horizontal direction

4.4 Correction of Chromatic Aberration

From both simulation and experiment results, we come to conclusion that despite the low dispersion of liquid lens material, the induced chromatic aberration is too severe to be ignored and must be corrected. There are two different types of chromatic aberrations to be corrected: chromatic change of magnification (lateral color) and chromatic change of focus (axial color). The chromatic change of magnification is the color variation of the image magnification, and it can be partially corrected through the post image processing. Since changing the focal length will result a magnification change of image during the scanning, post processing to adjust magnification at each liquid lens setting is necessary. Chromatic change of focus, on the other hand, is hard to eliminate during the post processing, thus requires to be corrected before the image is taken.

Correcting chromatic change of focus for liquid lenses are more complicated than conventional lenses. Axial color for conventional lenses can be easily corrected by an achromatic doublet that is designed with specific combination of lens materials and lens powers. However, for liquid lenses, lens power changes with different current settings, but the lens material, specifically the Abbe number remains constant. That means if an achromatic doublet is designed to correct axial color at one liquid lens power setting, the correction will be not effective once the liquid lens power is changed. Currently, the correction of chromatic aberration of liquid lens has rarely been discussed due to this difficulty. Philipp Waibel proposed an achromatic liquid system with multi-chamber membrane lenses [95]. However, this method requires designing the liquid lens with optimal refractive index and Abbe number, which is not entirely practical. In this section, we propose a method to correct axial color of FTLs with conventional lens design technique.

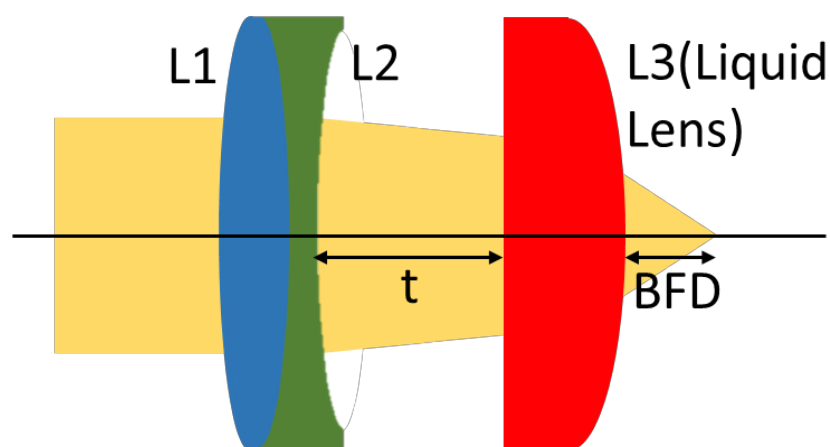


Figure 4.37. Optical setup for equation derivation

Figure 4.36 describes the problem we are trying to solve. Assume we are putting an achromatic doublet in front of the liquid lens to bring F-line and C-line into a common focus, this means the back focal distance (BFD) for F-line and C-line must be the same. To derive conditions to fulfil this requirement, we assume all elements in this figure are thin lenses, start with basic Gaussian reduction

$$\Phi_{total} = (\Phi_1 + \Phi_2) + \Phi_3 - (\Phi_1 + \Phi_2)\Phi_3 t \quad (4.3)$$

$$BFD = \frac{1}{\Phi_{total}} + d' \quad (4.4)$$

$$d' = -\frac{\Phi_1 + \Phi_2}{\Phi_{total}} t \quad (4.5)$$

$$\Phi_{nC} = \Phi_{nF} - \frac{\Phi_{nd}}{V_n} \quad (4.6)$$

where Φ_1 and Φ_2 are the powers of 2 lens elements of the doublet, Φ_3 is the power of the liquid lens, Φ_{total} is the power of the system, t is the distance between the doublet and liquid lens, d' is the distance between liquid lens and rear principle plane, Φ_{nC} , Φ_{nd} and Φ_{nF} are the powers of n th element regarding to the specific wavelengths, and V_n is the Abbe number of the n th element. According to Eq. 4.3, we have

$$\Phi_{Ftotal} = (\Phi_{1F} + \Phi_{2F}) + \Phi_{3F} - (\Phi_{1F} + \Phi_{2F})\Phi_{3F} t \quad (4.7)$$

$$\Phi_{Ctotal} = (\Phi_{1C} + \Phi_{2C}) + \Phi_{3C} - (\Phi_{1C} + \Phi_{2C})\Phi_{3C} t \quad (4.8)$$

Insert Eq. 4.6 to Eq. 4.8,

$$\begin{aligned} \Phi_{Ctotal} = & \left[\left(\Phi_{1F} - \frac{\Phi_{1d}}{V_1} \right) + \left(\Phi_{2F} - \frac{\Phi_{2d}}{V_2} \right) \right] + \left(\Phi_{3F} - \frac{\Phi_{3d}}{V_3} \right) \\ & - \left[\left(\Phi_{1F} - \frac{\Phi_{1d}}{V_1} + \Phi_{2F} - \frac{\Phi_{2d}}{V_2} \right) \left(\Phi_{3F} - \frac{\Phi_{3d}}{V_3} \right) t \right] \end{aligned} \quad (4.9)$$

then

$$d'_F = -\frac{\Phi_{1F} + \Phi_{2F}}{\Phi_{Ftotal}} t \quad (4.10)$$

$$d'_C = -\frac{\Phi_{1C} + \Phi_{2C}}{\Phi_{Ctotal}} t \quad (4.11)$$

and

$$\begin{aligned}
 BFD_F &= \frac{1}{F_{Ftotal}} - \frac{F_{1F} + F_{2F}t}{F_{Ftotal}} \\
 &= \frac{1 - (F_{1F} + F_{2F}t)}{F_{Ftotal}} \\
 &= \frac{1 - (F_{1F} + F_{2F}t)}{(F_{1F} + F_{2F}) + F_{3F} - (F_{1F} + F_{2F})F_{3F}t}
 \end{aligned} \tag{4.12}$$

$$\begin{aligned}
 BFD_C &= \frac{1}{F_{Ctotal}} - \frac{F_{1C} + F_{2C}t}{F_{Ctotal}} \\
 &= \frac{1 - (F_{1C} + F_{2C}t)}{F_{Ctotal}} \\
 &= \frac{1 - \left(F_{1F} + F_{2F} - \frac{F_{1d}}{V_1} - \frac{F_{2d}}{V_2} \right) t}{(F_{1F} + F_{2F}) + F_{3F} - \left(F_{1F} + F_{2F} - \frac{F_{1d}}{V_1} - \frac{F_{2d}}{V_2} \right) \left(F_{3F} - \frac{F_{3d}}{V_3} \right) t - \frac{F_{1d}}{V_1} - \frac{F_{2d}}{V_2} - \frac{F_{3d}}{V_3}}
 \end{aligned} \tag{4.13}$$

Then, the difference between BFDs of F-line and C-line can be calculated and simplified

$$\begin{aligned}
 DBFD &= BFD_F - BFD_C \\
 &= \frac{F_{3d} \left[(F_{2d}V_1ta) + (F_{1d}V_2ta) - (V_1V_2a^2) \right] - F_{2d}V_1V_3 - F_{1d}V_2V_3}{D}
 \end{aligned} \tag{4.14}$$

where α is

$$a = -1 + F_{1F}t + F_{2F}t \tag{4.15}$$

and D is the denominator that is expanded as

$$\begin{aligned}
 D &= \left[-F_{3F} + F_{1F}(-1 + F_{3F}) + F_{2F}(-1 + F_{3F}) \right] \cdot \\
 &\quad \left\{ F_{2d}V_1(F_{3d}t + V_3 - F_{3F}tV_3) + F_{1d}V_2(F_{3d}t + V_3 - F_{3F}tV_3) \right. \\
 &\quad \left. - V_1V_2[F_{3d}a + V_3(F_{1F} + F_{2F} + F_{3F} - F_{1F}F_{3F}t - F_{2F}F_{3F}t)] \right\}
 \end{aligned} \tag{4.16}$$

To bring F-line and C-line into common focus for all tunable settings, we need to have ΔBFD equal 0 and independent on Φ_{3d} . Then the following two conditions must be fulfilled:

$$\Phi_{2d}V_1V_3 + \Phi_{1d}V_2V_3 = 0 \quad (4.17)$$

and

$$(\Phi_{2d}V_1t\alpha) + (\Phi_{1d}V_2t\alpha) - (V_1V_2\alpha^2) = 0 \quad (4.18)$$

Simplify the first condition and apply it to the second condition, the two conditions become:

$$\Phi_{2d} = -\frac{\Phi_{1d}V_2}{V_1} \quad (4.19)$$

and

$$-V_1V_2 + V_1V_2\Phi_{1F}t + V_1V_2\Phi_{2F}t = 0 \quad (4.20)$$

The second condition can be further simplified with the following approximation:

$$\begin{aligned} \Phi_{2d} &\approx \Phi_{2F} \\ \Phi_{1d} &\approx \Phi_{1F} \end{aligned} \quad (4.11)$$

Then the second condition becomes:

$$\Phi_{1d}t = \frac{V_1}{V_1 - V_2} \quad (4.22)$$

If both conditions in Eq. 4.19 and Eq. 4.22 are met, then the correction for axial color is achieved for the visible range. This correction is independent of the liquid lens power.

Next, this condition is verified in Zemax. The setup of the system is shown in Fig. 4.36.

The liquid lens is same with the previous simulation. The merit function is to have achromatic

condition for visible spectrum throughout the entire tunable range of the liquid lens. For optimization, surface curvatures of the doublet and the distance between the doublet and liquid lens are set as variables. In addition, the glass materials of the doublet are set as substitution and hammer optimization is used in Zemax to find various glass combinations. Then each system is evaluated to check how well it follows the derived conditions. The results are shown in Table 4.1. Condition 1 from Eq. 4.19 is highlighted in red and condition 2 from Eq. 4.22 is highlighted in green.

	L1	L2	Φ_{2d}	$-\frac{\Phi_{1d}V_2}{V_1}$	$\Delta 1$	$\Phi_{1d}t$	$\frac{V_1}{V_1 - V_2}$	$\Delta 2$
1	N-PSK53A	P-SF68	-0.000648	-0.000648	0.00%	1.490	1.495	0.34%
2	N-BK7	P-SF68	-0.000391	-0.000389	-0.51%	1.462	1.486	1.64%
3	N-SSK2	N-LAK33B	-0.047492	-0.047469	-0.05%	54.086	53.273	-1.50%
4	N-BAK1	N-LAK33B	-0.013024	-0.013035	0.08%	10.819	11.057	2.20%
5	N-BAK1	P-LASF50	-0.005378	-0.005389	0.20%	3.308	3.382	2.24%

Table 4.1. Comparison between Zemax solution and derived conditions.

From Table 4.1, we can see that each solution found by Zemax meets the 2 derived conditions within 3% error. This study validates that if the two conditions are met, the chromatic focal shift can be corrected and is independent of liquid lens power. However, note that for all the solutions that Zemax finds, the combined focus tunable ranges are very small, and the liquid lens is positioned close to the image plane. To explain this, we start with calculation of the BFD for intermediate wavelength d-line:

$$\begin{aligned}
 BFD_d &= \frac{1}{F_{dtotal}} - \frac{F_{1d} + F_{2d}}{F_{dtotal}} t \\
 &= \frac{1 - (F_{1d} + F_{2d})t}{(F_{1d} + F_{2d}) + F_{3d} - (F_{1d} + F_{2d})F_{3d}t}
 \end{aligned} \tag{4.23}$$

Insert the first condition from Eq. 4.19,

$$\begin{aligned}
 BFD_d &= \frac{1 - \left(F_{1d} - F_{1d} \frac{V_2}{V_1} \right) t}{\left(F_{1d} - F_{1d} \frac{V_2}{V_1} \right) + F_{3d} - \left(F_{1d} - F_{1d} \frac{V_2}{V_1} \right) F_{3d} t} \\
 &= \frac{1 - F_{1d} t \left(1 - \frac{V_2}{V_1} \right)}{F_{1d} \left(1 - \frac{V_2}{V_1} \right) + F_{3d} \left(1 - F_{1d} + F_{1d} \frac{V_2}{V_1} t \right)}
 \end{aligned} \tag{4.24}$$

Then insert the second condition from Eq. 4.22,

$$\begin{aligned}
 BFD_d &= \frac{1 - \frac{V_1}{V_1 - V_2} \left(1 - \frac{V_2}{V_1} \right)}{F_{1d} \left(1 - \frac{V_2}{V_1} \right) + F_{3d} \left(1 - \frac{V_1}{V_1 - V_2} + \frac{V_1}{V_1 - V_2} \cdot \frac{V_2}{V_1} \right)} \\
 &= \frac{1 - \frac{V_1 - V_2}{V_1 - V_2}}{F_{1d} \left(1 - \frac{V_2}{V_1} \right) + F_{3d} \left(1 - \frac{V_2 - V_1}{V_1 - V_2} \right)} \\
 &= 0
 \end{aligned} \tag{4.25}$$

The above result show that when the required conditions are met to bring F and C to common focus, the BFD happened to be equal to 0. In real system, the BFD is very small, and the tunable lens is almost at focal point, so changing the focal length of the tunable lens has small impact on the focal length of overall system. In other words, to correct the axial color while maintaining a reasonable focus tunable range with one achromatic doublet is impractical. Additional lens elements are required to provide extra degrees of freedom.

Figure 4.37 shows an achromatic focus tunable system with one liquid lens and 2 doublets. For simulation purpose, the full tunable range of the liquid lens (8.33 dpt to 20 dpt) is sampled with 5 even increments and thin lenses are used for the doublets. The chromatic focal shift of this system is also shown in Fig. 4.37, the system is able to maintain achromatic correction at all liquid lens power settings. And the tunable range for the combined system is reasonable from 8.33 dpt to 16.5 dpt.

Another perk of using 2 doublets is to achieve apochromatism. A previous paper discussed a method to easily achieve apochromatism with 2 doublets. Figure 4.38 shows an apochromatic tunable microscope objective setup. A paraxial surface with 10mm focal length is used to simulate a 20X diffraction limited objective, and the design spectrum expands from visible spectrum to 400 nm – 700nm. Note that the system achieves apochromatism at each liquid lens power setting. Also, the on-axis MTF is diffraction limited at most of the liquid lens power setting except the largest liquid lens power setting, where the spherical aberration starts to lose control and results in a downgrade in image quality.

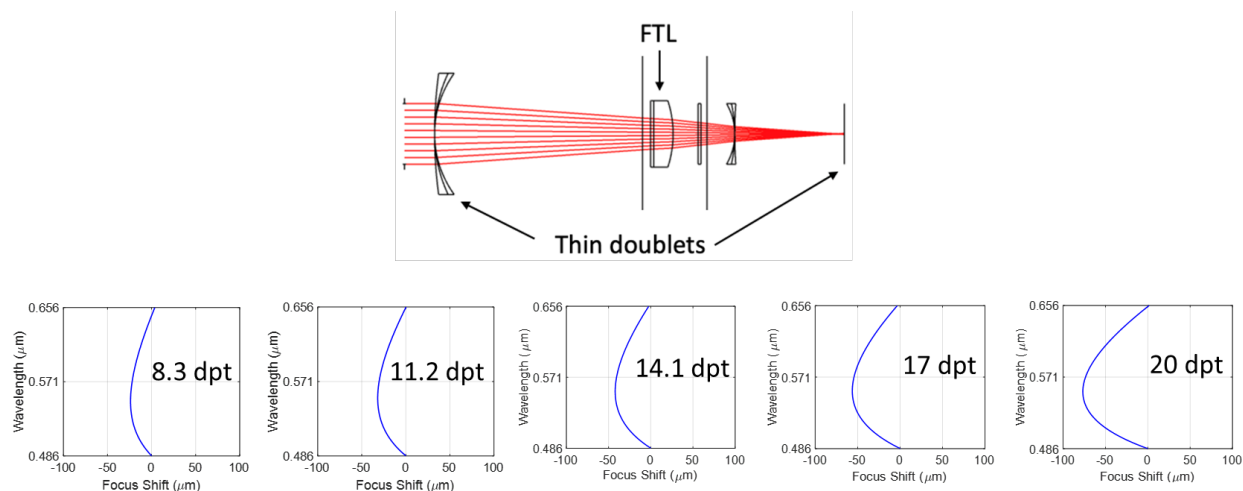


Figure 4.38. An achromatic liquid lens system with 2 thin doublets

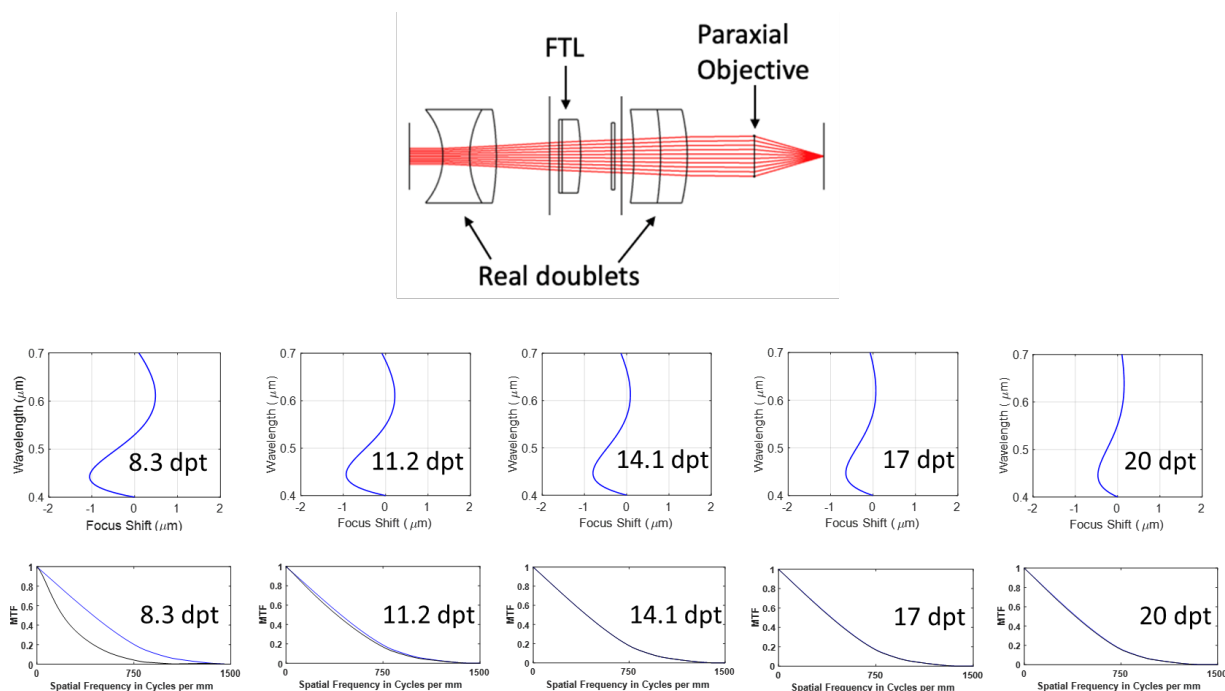


Figure 4.39. An apochromatic 3D microscopy system.

4.5 Conclusion

In this chapter, a detailed discussion of applications and aberration consideration for applications with liquid lenses are discussed.

Section 4.1 provides a brief introduction and history behind focus tunable lenses. Different types of focus tunable lenses, including FTLs based on liquid crystal, early generation liquid lenses based on electrowetting and modern liquid lenses with polymer membrane are compared. Due to small tunable range of liquid crystal lenses and small aperture of liquid lenses based on electrowetting, liquid lenses with polymer membrane is more desired for modern optical design.

Section 4.2 provides a survey on major applications of liquid lenses. 3 different applications, including focus sweep, zoom optical system and beam steering were discussed. An HMD display with dynamic eye compensation to reduce VAC and a 2X optical zoom miniature lens with no mechanical moving parts designed by the author are also provided as examples. The

ability to adjust the focus of an optical system without moving mechanical parts makes liquid lens great candidate for many applications such as head mount display, auto focus system and 3D microscopy. And beam steering with decentered liquid lens is ideal for applications such as wide angle laser scanning system and image stabilization. A mechanical motion free zoom lens is also possible with multiple liquid lenses, but it is still facing challenge due to relatively small achievable zoom ratio.

Section 4.3 evaluates impact to optical performance when paring a liquid lens with microscope objective for 3D microscopy. The evaluation was done in both Zemax simulation and lab experiment with a custom built Twyman-Green interferometer. Significant image quality down grade is observed both in simulation and experiment. The root causes are mainly due to strong spherical aberration and chromatic aberration introduced by the liquid lens to the original microscope objective. Impact from gravity was also evaluated in this section with lab experiment. Strong coma and some astigmatism were discovered when the liquid lens was positioned horizontally. This shows liquid lenses suffer from severe deformation due to gravity. The author would not recommend using liquid lens in horizontal direction.

In section 4.4, the author proposed a novel method to correct axial chromatic aberration of liquid lens independent of its optical power. This is a very critical finding since no other methods to correct chromatic aberration with liquid lens were proposed in previous literatures. Though derivation of equation from first order optics, conditions to maintain common focus for different wavelength independent of lens power was found. An example of an achromatic liquid lens setup and an apochromatic microscope objective is also provided in this section.

In general, liquid lenses provide more degree of freedoms for optical designers thus provide many opportunities for novel optical design. However, liquid lenses are also facing great

challenges such as small aperture, impact from gravity and aberration correction independent of lens power. Nevertheless, these challenges should not stop researchers and engineers exploring the possibilities with liquid lenses. The author wishes that the method to correct chromatic aberration present in this chapter can be a small step on the path to achieve great success of optical designs utilizing liquid lenses.

5 Conclusion

This dissertation presented of a collection of three topics that provide examples of novel optical system designs, introduce innovative new optical design methods and optical performance assessments on novel optical components. Each topic has been discussed independently as a self-contained chapter.

Chapter 2 gives a comprehensive discussion on photographic fisheye lenses. A detailed historic background not only gives an introduction on the photographic fisheye lens, but also gave readers an idea of fisheye lens design philosophy via the evolution of fisheye lens structures. Different fisheye projection methods, including equi-distance, orthographic, stereographic and equisolid angle projection were discussed in detail in this chapter. Tangential and sagittal magnifications of each projection were derived from the correlation between object space and image space. The results show that different projection methods not only provide different distortion curve, but also have different characteristic in how the image is distorted. Special properties and design challenges such as pupil shift and long BFD requirements were then explained. In the end of the chapter, the author presented a large aperture zoom fisheye lens design. A new method for aberration control of a two group zoom lens is explained. By treating the front group as a moving target, it is possible for the designers to achieve aberration invariant during the zoom instead of balancing aberration between front and rear group. The design example was then evaluated on both optical and tolerance performance.

Chapter 3 discussed tolerance improvement of miniature lenses by using a new freeform surface based on pedal curve of ellipse. Two sets of comparison between the freeform surface and conventional aspherical surface, including even aspherical surface and Q-type polynomial surface, are presented in this chapter. For each comparison, the results show even though the patented lens

optimized by different surface type has very similar structure and nominal contrast performance, the lens optimized using the freeform surface shows better MTF curves under surface and element decenter. An attempt to reverse fit the freeform surface back to even asphere surface proved that the improvement in tolerance is caused by the surface type, not the slightly difference of the lens structure. The author believes that based on this study, the pedal freeform surface can improve the manufacturing yield of miniature camera lenses.

In Chapter 4, the author discussed about utilization of liquid lens. A survey on the different applications of liquid lens, including focus sweeping, motion free zoom lens and beam steering was given. The image quality impact caused by paring liquid lens with microscope objectives to achieve 3D microscopy was evaluated by the author both in simulation and experiments. Both simulation and experiments suggest that the liquid lens can cause significant image quality downgrade due to large spherical aberration of the liquid lens. The experiments also indicated that strong coma would appear due to gravity when the liquid lens was positioned horizontally. Also, strong chromatic focal shift can also be observed. To correct the chromatic change of focus, the author derived the condition to correct the focal shift independent of the liquid lens power. An achromatic example and an apochromatic example using the derived condition were demonstrated in the end of this chapter.

The theoretical results and practical examples describe in this dissertation serve to offer new insights into the novel optical design for various applications, to introduce new perspectives in aberration control and to provide design considerations when using newly innovative optical components.

APPENDIX A – LENS DATA I

Lens data of the benchmark lens and evaluation lens discussed in section 3.3 are showed in the following tables.

Surface	Radius of Curvature (mm)	Thickness (mm)	Refractive Index	Abbe Number
1(STOP)	Infinity	-0.1700		
2	1.9802	0.6549	1.535	56.16
3	-14.1844	0.0230		
4	4.1950	0.2781	1.614	25.58
5	1.7205	0.4023		
6	11.7761	0.5156	1.535	56.16
7	-24.3458	0.5365		
8	6.5341	0.5220	1.535	56.16
9	3.2161	0.2267		
10	1.1315	0.7123	1.535	56.16
11	1.1461	0.3500		
12	Infinity	0.3000	1.517	64.20
13	Infinity	0.6068		

Table A.1. Lens data for benchmark lens in section 3.3

Surface	Conic	4 th order	6 th order	8 th order
2	0.00000000E+00	-1.14459337E-02	8.06834715E-03	-2.24438250E-02
3	0.00000000E+00	-1.40832782E-02	-3.50134681E-02	3.62506569E-02
4	0.00000000E+00	-1.12652734E-01	6.83235244E-02	-1.40402257E-02
5	0.00000000E+00	-1.19004339E-01	8.66261989E-02	-3.57619858E-02
6	0.00000000E+00	-1.99184976E-02	-4.58974220E-02	5.08366541E-02
7	0.00000000E+00	-2.01586565E-02	-6.01361830E-02	4.67510400E-02
8	0.00000000E+00	8.11547845E-02	-1.01016975E-01	5.24101544E-02
9	-1.60439064E+02	3.95468150E-02	-2.70680457E-02	2.67991019E-03
10	-7.04568130E+00	-3.94731423E-02	-3.27592751E-02	1.23315039E-02
11	-3.90131724E+00	-5.63799049E-02	1.01881107E-02	-2.36615912E-03
Surface	10 th order	12 th order	14 th order	16 th order
2	-4.39386007E-04	0.00000000E+00	0.00000000E+00	0.00000000E+00
3	-2.17917711E-02	0.00000000E+00	0.00000000E+00	0.00000000E+00
4	3.48099416E-03	0.00000000E+00	0.00000000E+00	0.00000000E+00
5	1.29384048E-02	0.00000000E+00	0.00000000E+00	0.00000000E+00
6	-2.18382271E-02	-1.17096861E-02	2.41520078E-02	-7.42026455E-03
7	-1.40026881E-02	-3.97302294E-03	5.05660009E-03	-5.36908692E-04
8	-1.93694656E-02	2.95109954E-03	0.00000000E+00	0.00000000E+00
9	5.38193913E-05	0.00000000E+00	0.00000000E+00	0.00000000E+00
10	-3.35287334E-04	-2.20055934E-04	-1.69866807E-05	5.73357578E-06
11	4.09723496E-04	-8.81918571E-06	-5.79990532E-06	4.39869064E-07

Table A.2. Aspherical coefficients for benchmark lens in section 3.3

Surface	Radius of Curvature (mm)	Thickness (mm)	Refractive Index	Abbe Number
1(STOP)	Infinity	-0.1700		
2	2.1115	0.5492	1.535	56.16
3	-10.8802	0.1154		
4	7.2955	0.2591	1.614	25.58
5	1.9430	0.3608		
6	6.8454	0.5093	1.535	56.16
7	-7.6617	0.7051		
8	N/A	0.5752	1.535	56.16
9	N/A	0.2217		
10	N/A	0.8748	1.535	56.16
11	N/A	0.3845		
12	Infinity	0.3000	1.517	64.20
13	Infinity	0.3455		

Table A.3. Lens data for evaluation lens in section 3.3

Surface	a_A	b_A	A_1	A_2	A_3	a_B	b_B	B_1	B_2	B_3
8	6.968	10.018	-16.677	7318.840	2.233E05	6.751	13.033	0.555	0.097	-2.650
9	6.609	9.599	-23.020	3183.602	1.162E05	4.357	11.9	0.334	-0.306	-0.439
10	4.400	6.493	-10.122	-51.276	934.067					
11	4.982	7.536	-12.316	-104.055	-834.645					

Table A.4. Pedal Surface data for evaluation lens in section 3.3

APPENDIX B – LENS DATA II

Lens data of the benchmark lens and evaluation lens discussed in section 3.4 are showed in the following tables.

Surface	Radius of Curvature (mm)	Thickness (mm)	Refractive Index	Abbe Number
1(STOP)	Infinity	-0.090		
2	0.8049	0.2515	1.544	55.90
3	18.0275	0.0615		
4	9.0938	0.1962	1.634	23.80
5	1.3576	0.1112		
6	1.7528	0.2396	1.634	23.80
7	1.7209	0.1221		
8	-2.8926	0.3142	1.544	55.90
9	-0.5513	0.0808		
10	8.2372	0.2548	1.544	55.90
11	0.6079	0.3000		
12	Infinity	0.2000	1.517	64.20
13	Infinity	0.2000		

Table B.1. Lens data for the even asphere lens in section 3.4

Surface	Conic	4 th order	6 th order	8 th order
2	-6.160170970006175E-001	1.023836708225658E-001	1.735566474569875E-001	1.491583402130984E+000
3	1.571881017972249E+003	1.736313913128300E-002	-5.021259485123550E+000	1.763877416614461E+001
4	3.212726089457453E+002	-1.917620288390619E-001	-3.933335107489270E+000	3.612461221370640E+000
5	4.448386938530537E+000	-2.767925024453586E-001	-2.784289815383411E+000	4.120510864805106E+000
6	-9.979245673050464E+000	-2.448130164141417E-001	-1.699337776885191E+000	2.304387498681645E+000
7	-1.161113085934044E+000	-1.400251679605974E-001	-8.560243917991763E-001	4.986017691536522E-001
8	-2.930541999176889E+001	5.797044078031328E-002	-7.259813065419654E-002	4.061000577109866E+001
9	-2.909346223942523E+000	-2.759156857618746E-001	1.024871925670994E+000	1.796455381525980E+001
10	3.548224405617754E+001	-1.950844984865909E+000	7.842954109636196E+000	-1.805578488221025E+001
11	-6.492318051541923E+000	-1.253253067772189E+000	3.782609651909794E+000	-8.585017963496384E+000
Surface	10 th order	12 th order	14 th order	16 th order
2	-4.233155392036432E+001	4.745174386992058E+001	0.000000000000000E+000	0.000000000000000E+000
3	-9.418837952763629E+001	2.013024675037215E+002	0.000000000000000E+000	0.000000000000000E+000
4	-4.481470419330914E-001	1.659919090495261E+002	0.000000000000000E+000	0.000000000000000E+000
5	0.000000000000000E+000	0.000000000000000E+000	0.000000000000000E+000	0.000000000000000E+000
6	2.161374144656372E+001	-1.177051450322211E+002	0.000000000000000E+000	0.000000000000000E+000
7	6.065762600235678E+000	1.042362209006220E+001	0.000000000000000E+000	0.000000000000000E+000
8	-3.935710384529049E+002	1.702565404566384E+003	-3.774548183215493E+003	3.446868457400165E+003
9	-4.664742332173191E+001	-3.117176271282559E+001	1.778674255637286E+002	-1.396399229299091E+002
10	2.784821186091452E+001	-2.771879777791267E+001	1.537613926431594E+001	-3.633582271510425E+000
11	1.283420943285990E+001	-1.208219603010521E+001	6.467654090916510E+000	-1.509468509343585E+000

Table B.2. Aspherical coefficients for the even asphere lens in section 3.4

Surface	Radius of Curvature (mm)	Thickness (mm)	Refractive Index	Abbe Number
1(STOP)	Infinity	-0.090		
2	0.7999	0.2445	1.544	55.90
3	-7.3650	0.0656		
4	-9.0771	0.1952	1.634	23.80
5	1.5448	0.1177		
6	3.7891	0.2244	1.634	23.80
7	1.9147	0.1255		
8	-4.7386	0.3033	1.544	55.90
9	-0.7275	0.0762		
10	-6.3720	0.2662	1.544	55.90
11	355.5210	0.3000		
12	Infinity	0.2000	1.517	64.20
13	Infinity	0.2000		

Table B.3. Lens data for the Q-type polynomial lens in section 3.4

Surface	Conic	A0	A1	A2
2	-6.095575235262221E-001	5.765451355372000E-003	-3.140406578326000E-003	7.786988626266000E-004
3	1.623539137667746E+002	2.811516125673000E-002	-3.372536049232000E-003	-1.294666249117000E-003
4	-5.088337032464850E+002	1.003765803640000E-002	7.305244110170000E-003	-4.468770789667000E-003
5	-1.876843847054599E+000	1.155067627324000E-002	1.452661195457000E-003	-1.424938046608000E-003
6	-7.785690298008008E+001	5.274687491096000E-002	-1.018385557716000E-002	3.721809979744000E-003
7	-6.388454151170719E+000	-2.693614801011000E-002	2.097953523768000E-002	-6.613095917935000E-003
8	-1.112811007071853E+002	-1.698552817254000E-002	8.378426059457000E-004	-9.246909825964000E-003
9	-5.457409671942098E+000	-2.178627620652000E-002	-6.791385588743000E-002	2.756599292649000E-002
10	4.076892750758425E+001	-4.447777682844000E-002	-2.021905597155000E-003	2.371164558817000E-002
11	-6.772233993299750E+012	3.290398549437000E-001	3.558008835978000E-002	3.896426375921000E-002
Surface	A3	A4	A5	A6
2	-7.364575412664000E-005	5.743585664727000E-006	-2.959024502350000E-005	3.533483556988000E-005
3	5.932501215314000E-004	-1.857585109495000E-004	1.351383824882000E-004	-1.130797667073000E-004
4	8.529359533291000E-004	3.554574214000000E-005	9.605402427039001E-006	-5.818619179469000E-005
5	2.976398542695000E-004	3.304007321407000E-005	0.000000000000000E+000	0.000000000000000E+000
6	-1.099368316936000E-003	1.131619344705000E-004	1.070315923616000E-005	3.359327462159000E-005
7	8.075371227388000E-004	-9.502614893717999E-005	3.826593380972000E-005	2.163634104755000E-004
8	8.405073201910000E-003	-3.631003354717000E-003	1.761989084670000E-003	8.330412771666000E-005
9	4.217834971665000E-003	-1.947998850312000E-003	-1.190124134722000E-003	9.423742466450001E-004
10	4.945034481598000E-003	1.558266785817000E-003	-5.857599106993000E-004	-3.145241192292000E-004
11	8.554206902007000E-003	1.028044725569000E-002	1.935144483999000E-004	2.168453409555000E-003

Table B.4. Aspherical coefficients for the Q-type polynomial lens in section 3.4

Surface	Radius of Curvature (mm)	Thickness (mm)	Refractive Index	Abbe Number
1(STOP)	Infinity	-0.0774		
2	0.7774	0.2331	1.544	55.90
3	-34.0446	0.0606		
4	-29.1770	0.1971	1.634	23.80
5	1.5577	0.1160		
6	1.9260	0.1996	1.634	23.80
7	1.7232	0.1599		
8	N/A	0.3332	1.544	55.90
9	N/A	0.0258		
10	N/A	0.3028	1.544	55.90
11	N/A	0.3000		
12	Infinity	0.2000	1.517	64.20
13	Infinity	0.2000		

Table B.5. Lens data for the freeform lens in section 3.4

Surface	a_A	b_A	A_1	A_2	A_3	a_B	b_B	B_1	B_2	B_3
8	3.1249	4.8216	3.3935	0.8918	2482.0993					
9	1.9845	3.0414	11.5249	-7.6366	8000.5933					
10	3.0997	5.2689	-0.5287	-93.8744	-739.6468					
11	1.9633	2.9471	-8.9771	-43.2004	-717.2674	0.8362	2.0107	-0.1542	-0.05517	2.8035

Table B.6. Pedal Surface data for the freeform lens in section 3.4

Surface	Radius of Curvature (mm)	Thickness (mm)	Refractive Index	Abbe Number
1(STOP)	Infinity	-0.0754		
2	0.7749	0.2310	1.544	55.90
3	-12.0579	0.0572		
4	380.2226	0.1977	1.634	23.80
5	1.4516	0.1325		
6	2.1516	0.2309	1.634	23.80
7	2.0394	0.1070		
8	-2.0784	0.3450	1.544	55.90
9	-0.4981	0.0582		
10	3.4315	0.2419	1.544	55.90
11	0.5115	0.3000		
12	Infinity	0.2000	1.517	64.20
13	Infinity	0.2000		

Table B.7. Lens data for the reversed even asphere lens in section 3.4

Surface	Conic	4 th order	6 th order	8 th order
2	-6.641726760372720E-001	7.781839460409228E-002	-1.407064554312676E+000	2.205999553728279E+000
3	-2.219070038773028E+002	1.158900163014764E-001	-4.907468531972230E+000	1.247908688612758E+001
4	-1.987630833427081E+036	4.125766522138427E-001	-1.116016121926126E+000	-1.068991252315753E+000
5	8.160008420992295E+000	-3.892309353958376E-001	2.485417198350974E+000	-7.023320454743756E+000
6	-1.066363267986735E+002	-7.591181743222000E-001	-3.183274870556654E+000	7.646332082342918E+000
7	-3.785496713906750E+001	-3.826569946765784E-001	-9.783727493513916E-001	3.481775337532207E+000
8	-1.851516381099496E+001	3.619892521483346E-002	-4.803100507624958E-001	8.612240187921989E-001
9	-4.899761768428384E-001	1.845312436531721E+000	-4.960136858895774E+000	1.193566159723761E+001
10	-4.472521687310797E+002	-1.773877747846477E+000	1.079278707753436E+000	8.821675768550929E+000
11	-6.303536404546549E+000	-1.324760584697902E+000	2.945730388742025E+000	-5.090567717322975E+000
Surface	10 th order	12 th order	14 th order	16 th order
2	-2.656837649499798E+001	-2.277317053164147E+002	0.000000000000000E+000	0.000000000000000E+000
3	-9.513854369076316E+001	1.313201059467801E+002	0.000000000000000E+000	0.000000000000000E+000
4	-1.578878183022909E+001	2.331938577682804E+002	0.000000000000000E+000	0.000000000000000E+000
5	0.000000000000000E+000	0.000000000000000E+000	0.000000000000000E+000	0.000000000000000E+000
6	6.093071720524443E+001	-2.521139932490704E+002	0.000000000000000E+000	0.000000000000000E+000
7	1.022901572103860E+001	-1.921587902493959E+001	0.000000000000000E+000	0.000000000000000E+000
8	3.141722322043772E+000	5.058661239310373E+000	-8.476404219151386E+000	0.000000000000000E+000
9	2.425685987068149E+001	-1.372428705533351E+002	1.797721321304469E+002	0.000000000000000E+000
10	-3.332817527875586E+001	4.835667319479916E+001	-2.561578020867785E+001	0.000000000000000E+000
11	5.329878478302482E+000	-3.066451599060840E+000	6.944573999446649E-001	0.000000000000000E+000

Table B.8. Aspherical coefficients for the reversed even asphere lens in section 3.4

REFERENCES

- [1] H. Robin, "A lens for whole sky photographs," *Quarterly Journal of the Royal Meteorological Society*, vol. 50, no. 211, pp. 227-235, 1924.
- [2] M. Laikin, *Lens Design, 4th Edition*, CRC Press, 2006.
- [3] W. J. Smith, *Modern Lens Design; 2nd Edition*, McGraw Hill Professional Engineering, 2004.
- [4] Y. Yan, *Photographic fisheye lens design for 35mm format cameras*, Tucson: The University of Arizona, 2016.
- [5] Market Research Future, January 2019. [Online]. Available: <https://www.marketresearchfuture.com/reports/panoramic-camera-market-2301>.
- [6] C. Wang, H. Zhang, M. Yang, X. Wang, L. Ye and C. Guo, "Automatic Parking Based on a Bird's Eye View Vision System," *Advances in Mechanical Engineering*, vol. 2014.
- [7] Samsung, [Online]. Available: <https://www.samsung.com/us/mobile/virtual-reality/gear-360/gear-360-sm-r210nzwaxar/>.
- [8] R.W.Wood, "XXIII Fish-eye views, and vision under water," *Philosophical Magazine Series 6*, vol. 12, no. 68, pp. 159-162, 1906.
- [9] W.N.Bond, "A wide angle lens for cloud recording," *Philosophical Magazine Series 6*, vol. 44, no. 263, pp. 999-1001, 1922.
- [10] R. Kingslake, *A History of the Photographic Lens*, Academic Press, 1989.
- [11] Germany Patent 620538.
- [12] "History of Nikon Rangefinder Cameras," Nikon, [Online]. Available: <http://imaging.nikon.com/history/>.
- [13] K. Miyamoto, "Fish Eye Lens," *Journal of the Optical Society of America*, vol. 54, no. 8, pp. 1060-1061, 1964.

-
- [14] Japan Patent 438,664.
- [15] US Patent 3,524,697.
- [16] US Patent 3,737,214.
- [17] R. Cicala, "Lensrentals," 19 February 2019. [Online]. Available: <https://www.lensrentals.com/blog/2019/02/assembling-the-c-4-optics-hyperfisheye-prototype/>.
- [18] Zemax, OpticStudio 15.5 SP1 Help Files, 2015.
- [19] US Patent 4,525,038.
- [20] R. d. Stoutz. [Online]. Available: https://www.destoutz.ch/lens_7.5mm_f5.6_750139.html.
- [21] K. J. Fleischer, *Camera Lens News No.1*, Oberkochen: Carl Zeiss Camera Lens Division, 2007.
- [22] D. Reshidko and J. Sasian, "The role of aberrations in the relative illumination of a lens system," in *Noval Optical Systems Design and Optimization XIX*, San Diego, 2016.
- [23] J. Bereau and P. P. Clark, "The Optics of Miniature Digital Camera Modules," in *International Optical Design Conference 2006*, Vancouver, 2006.
- [24] J. Sasian, *Introduction to Aberrations in Optical Imaging Systems*, Cambridge University Press, 2013.
- [25] P. P. Clark, "Mobile Platform Optical Design," in *International Optical Design Conference*, Kohala Coast, 2014.
- [26] Y. Yan and J. Sasian, "Photographic zoom fisheye lens design for DSLR cameras," *Optical Engineering*, vol. 56, no. 9, 2017.
- [27] US Patent 6,987,623.
- [28] US Patent 7,317,581.

-
- [29] US Patent 8,456,751.
- [30] J. J. Kumler and M. L. Bauer, "Fish-eye lens designs and their relative performance," in *Current Developments in Lens Design and Optical Systems Engineering*, San Diego, 2000.
- [31] M. Laikin, "Wide angle lens systems," in *1980 International Lens Design Conference*, 1980.
- [32] Y. Wang, *Fisheye Lens Optics*, Beijing: China Science Publishing and Media, 2006.
- [33] M. P. Rimmer, "Relative illumination calculations," in *Optical system design, analysis, production for advanced technology systems*, 1986.
- [34] "List of Members participating in CIPA Statistical Research," September 2018. [Online]. Available: http://www.cipa.jp/stats/documents/e/list_e.pdf.
- [35] CIPA, "Total Shipments of Cameras and Interchangeable Lenses," [Online]. Available: <http://www.cipa.jp/stats/documents/common/cr200.pdf>.
- [36] C. Jarvis, *The best camera is the one that's with you: iPhone photography* by Chase Jarvis, New Riders, 2009.
- [37] "Smartphone shipments expected to drop for the third consecutive year in 2019, according to IDC," 6 March 2019. [Online]. Available: <https://www.idc.com/getdoc.jsp?containerId=prUS44903419>.
- [38] J. Sasian, D. Reshidko and C.-L. LI, "Aspheric/freeform optical surface description for controlling illumination from point-like light sources," *Optical Engineering*, vol. 55, no. 11, 2016.
- [39] Y. Yan and J. Sasian, "Miniature camera lens design with a freeform surface," in *International Optical Design Conference 2017*, 2017.
- [40] JP Patent 2015-152812.
- [41] US Patent 2017/0299845.
- [42] J. Bently and C. Olson, *Field Guide to Lens Design*, Bellingham: SPIE Press, 2012.

-
- [43] US Patent 8,605,367.
- [44] US Patent 8,786,961.
- [45] US Patent 9,110,270.
- [46] G. W. Forbes, "Shape specification for axially symmetric optical surfaces," *Optical Express*, vol. 15, no. 8, pp. 5218-5226, 2007.
- [47] M. Abramowitz and I. Stegun, *Handbook of Mathematical Functions*, Dover, 1978.
- [48] K. Hawkins, "Comparing Forbes asphere model to the even asphere," 19 August 2015. [Online]. Available: <https://customers.zemax.jp/os/resources/learn/knowledgebase/comparing-forbes-asphere-model-to-the-even-asphere.aspx>.
- [49] B. Ma, K. Sharma, K. P. Thompson and J. P. Rolland, "Mobile device camera design with Q-type polynomials to achieve higher production yield," *Optics Express*, vol. 21, no. 15, pp. 17454-17463, 2013.
- [50] M. Ventura, M. Bueler, C. Gratzel and M. Aschwanden, "Compact optical design solutions using focus tunable lenses," in *Proceedings Volume 8167 Optical Design and Engineering IV*, Marseille, France, 2011.
- [51] Y. He, Chun Zhu Ji Wen, Zhonghua Book Company, 1983.
- [52] Y. Zhang, Yuan Jian Lei Han, Shanghai Ancient Books Publishing House, 2008.
- [53] S. Sato, "Liquid-Crystal Lens-Cells with Variable Focal Length," *Japanese Journal of Applied Physics*, vol. 18, 1979.
- [54] S. T. Kowel, D. S. Cleverly and P. G. Kornreich, "Focusing by electrical modulation of refraction in a liquid crystal cell," vol. 23, no. 2, pp. 278-289, 1984.
- [55] H.-C. Lin, M.-S. Chen and Y.-H. Lin, "A Review of Electrically Tunable Focusing Liquid Crystal Lenses," *Transactions on Electrical and Electronic Materials*, vol. 12, no. 6, pp. 234-240, 2011.

-
- [56] B. Berge and J. Peseux, "Variable Focal Lens Controlled by an External Voltage: An Application of Electrowetting," *The European Physical Journal E*, vol. 3, no. 2, pp. 159-163, 2000.
- [57] J. Crassous, C. Gabay, G. Liogier and B. Berge, "Liquid Lens based on Electrowetting: A New Adaptive Component for Imaging Applications in Consumer Electronics," in *Proceedings Volume 5639, Adaptive Optics and Applications III*, Beijing, China, 2004.
- [58] "Corning Varioptic Lenses," [Online]. Available: <https://www.corning.com/worldwide/en/innovation/corning-emerging-innovations/corning-varioptic-lenses/variable-focus-lenses-a-series.html>. [Accessed 2019].
- [59] P. Zhao, C. Ataman and H. Zappe, "Gravity-Immune Liquid-Filled Tunable Lens with Reduced Spherical Aberration," *Applied Optics*, vol. 55, no. 28, pp. 7816-7823, 2016.
- [60] K. Wei, H. Huang, Q. Wang and Y. Zhao, "Focus-Tunable Liquid Lens with an Aspherical Membrane for Improved Central and Peripheral Resolutions at High Diopters," *Optics Express*, vol. 24, no. 4, pp. 3929-3939, 2016.
- [61] H. Yu, G. Zhou, H. M. Leung and F. S. Chau, "Tunable Liquid-Filled Lens Intergrated with Aspherical Surface for Spherical Aberration Compensation".
- [62] H. A. Anderson, G. Hentz, A. Glasser, K. K. Stuebing and R. E. Manny, "Minus-Lens-Stimulated Accommodative Amplitude Decreases Sigmoidally with Age: A Study of Objectively Measured Accommodative Amplitudes from Age 3," *Investigative Ophthalmology & Visual Science*, vol. 49, no. 7, 2008.
- [63] Frick KD, Joy SM, Wilson DA, Naidoo KS and Holden BA, "The Global Burden of Potential Productivity Loss from Uncorrected Presbyopia," *Ophthalmology*, pp. 1706-10, 2015.
- [64] G.Kramida, "Resolving the Vergence-Accommodation Conflict in Head-Mounted Displays," *IEEE Transactions on Visualization and Computer Graphics*, vol. 22, no. 7, pp. 1912-1931, 2016.
- [65] K. Y. M. O. T. M. a. E. S. T. Ando, "Retinal projection display using holographic optical element," in *Proc. SPIE*, 2000.

-
- [66] Q. W. Y. W. a. G. J. D. Cheng, "Lightweight Spatial-multiplexed Dual Focal-Plane Head-Mount Display using Two Freeform Prisms," *Chin. Opt. Lett.*, vol. 11, no. 3, p. 031201, 2013.
- [67] Y. W. D. C. a. Y. L. W. Song, "Light Field Head-Mounted Display with Correct Focus Cue Using Micro Structure Array," *Chin. Opt. Lett.*, vol. 12, no. 6, pp. 060-010, 2014.
- [68] A. M. a. H. Fuchs, "Computational augmented reality eyeglasses," in *Proc. ISMAR*, 2013.
- [69] K. O. a. F. S. Shiwa, "Proposal for a 3-D display with accommodative compensation: 3DDAC," *J. Soc. Inf. Display*, vol. 4, no. 4, pp. 255-261, 1996.
- [70] T. Shibata et al., "Stereoscopic 3-D display with optical correction for the reduction of the discrepancy between accommodation and convergence," *J. Soc. Inf. Display*, vol. 13, no. 8, pp. 665-671, 2005.
- [71] D. C. a. H. H. S. Liu, "An Optical See-Through Head Mounted Display with Addressable Focal Planes," in *Proc. ISMAR*, 2008.
- [72] R. Konrad, E.A. Cooper and G. Wetzstein, " Novel Optical Configurations for Virtual Reality: Evaluating User Preference and Performance with Focus-tunable and Monovision Near-eye Displays," in *Proceedings of the ACM Conference on Human Factors in Computing Systems*, 2016.
- [73] B. Grewe, F. Voigt, M. Van't Hoff and F. Helmchen, "Fast two-layer two-photon imaging of neuronal cell populations using an electrically tunable lens," *Biomed. Opt. Express*, vol. 2, no. 7, pp. 2035-2046, 2011.
- [74] M. Bathe-Peters, P. Annibale and M. Lohse, "All-optical microscope autofocus based on an electrically tunable lens and a totally internally reflected IR laser," *Opt. Express*, vol. 26, no. 3, pp. 2359-2368, 2018.
- [75] K. Lee, E. Chung, S. Lee and T. J. Eom, "High-speed dual-layer scanning photoacoustic microscopy using focus tunable lens modulation at resonant frequency," *Opti. Express*, vol. 25, no. 22, pp. 26427-26436, 2017.
- [76] "Publications," [Online]. Available: <https://www.optotune.com/publications-2>. [Accessed 2019].

-
- [77] N. Savidis, G. Peyman, N. Peyghambarian and J. Schwiegerling, "Nonmechanical zoom system through pressure-controlled tunable fluidic lenses," *Appl Opt.*, vol. 52, no. 12, pp. 2858-2865, 2013.
- [78] S. Lee, M. Choi, E. Lee, K.-D. Jung, J.-h. Chang and W. Kim, "Zoom lens design using liquid lens for laparoscope," *Opt. Express*, vol. 21, no. 2, pp. 1751-1761, 2013.
- [79] S. Kuiper, B. Hendriks, J. Suijver, S. Deladi and I. Helwegen, "Zoom camera based on liquid lenses," in *Proceedings Volume 6466, MOEMS and Miniaturized Systems VI*, San Jose, 2007.
- [80] P. Zhao, C. Ataman and H. Zappe, "A miniaturized camera objective with 2X optical zoom," in *Proceedings Volume 10545, MOEMS and Miniaturized Systems XVII*, San Francisco, 2018.
- [81] US Patent 7,725,016.
- [82] US Patent 2016/0202455 A1.
- [83] F. Wippermann, P. Schreiber, A. Brauer and B. Berge, "Mechanically assisted liquid lens zoom system for mobile phone cameras," in *Proc. SPIE 6289, Novel Optical Systems Design and Optimization IX*, San Diego, 2006.
- [84] J.-H. Sun, B.-R. Hsueh, Y.-C. Fang, J. MacDonald and C.-C. Hu, "Optical design and multiobjective optimization of miniature zoom optics with liquid lens element," *Appl. Opt.*, vol. 48, no. 9, pp. 1741-1757, 2009.
- [85] JP Patent 2014-145883A.
- [86] US Patent 7,265,911.
- [87] US Patent 6,924,944.
- [88] M. Zohrabi, R. Cormack and J. Gopinath, "Wide-angle nonmechanical beam steering using liquid lenses," *Opt. Express*, vol. 24, no. 21, pp. 23798-23809, 2016.
- [89] US Patent 9,581,736.

-
- [90] K. Lee, E. Chung, S. Lee and T. Fom, "High-speed dual-layer scanning photoacoustic microscopy using focus tunable lens modulation at resonant frequency," *Opt. Express*, no. 25, pp. 26427-26436, 2017.
- [91] F. Fahrhach, F. Voige, B. Schimid, F. Helmchen and J. Huisken, "Rapid 3D light-sheet microscopy with a tunable lens," *Opt. Express*, no. 21, pp. 21010-21026, 2013.
- [92] B. Grewe, F. Voige, M. v. Hoff and F. Helmchen, "Fast two-layer two-photon imaging of neuronal cell populations using an electrically tunable lens," *Biomed. Opt. Express*, no. 2, pp. 2035-2046, 2011.
- [93] H. Li, X. Cheng and Q. Hao, "An electrically tunable zoom system using liquid lenses," *Sensors*, vol. 16, no. 45, 2016.
- [94] J. Wyant and K. Creath, "Basic wavefront aberration theory for optical metrology," in *Applied Optics and Optial Engineering*, 1992, pp. 1-53.
- [95] P. Waibel, D. Mader, P. Liebetraut, H. Zappe and A. Seifert, "CHromatic aberration control for tunable all-silicone membrane microlenses," *Opt. Express*, no. 19, pp. 18584-18592, 2011.
- [96] Y. Wang, Yu Yan Jing Tou Guang Xue, China Science Publishing and Media, 2006.
- [97] Y. Shimizu, "Wide angle fisheye lens". US Patent 3737214A, 5 June 1973.
- [98] C. B. Martin, "Design issues of a hyperfield fisheye lens," in *Novel Optical Systems Design and Optimization VII*, Denver, CO, 2004.
- [99] R. Juergens, "Image Quality," 2014. [Online]. Available: <http://fp.optics.arizona.edu/sasian/2015opti517>.
- [100] CMOSIS nv, "24 MPixel 36 x 24 mm² 14 bit image sensor in 110/90 nm CMOS technology," in *2013 INTERNATIONAL IMAGE SENSOR WORKSHOP*, 2013.
- [101] US Patent 8,456,751.
- [102] [Online]. Available: <http://www.nikkor.com>.

[103] US Patent 5,434,713.

[104] Japan Patent 63-017,421.

[105] Japan Patent 02-248,910.

[106] US Patent 3,589,798.

[107] Canon, [Online]. Available: <http://www.usa.canon.com>.

[108] Nikon, [Online]. Available: <http://www.nikonusa.com/>.

[109] Sigma, [Online]. Available: <http://www.sigmaphoto.com/>.

[110] Sony, [Online]. Available: <http://www.sony.com/>.

[111] S. Sato, "Liquid-crystal lens-cells with variable focal length," *Japanese Journal of Applied Physics*, vol. 18, no. 9, 1979.